Serpentinite Dehydration in Subduction Zones: A Multiscale Process

Kumulative Dissertation

zur Erlangung des Grades
Doktor der Naturwissenschaften (Dr. rer. nat.)

am Fachbereich Geowissenschaften
Institut für Geologische Wissenschaften
der Freien Universität Berlin

vorgelegt von

Konstantin Huber

Berlin, 2024

"Zögernd, bald hier bald dort, erwacht das Gebirge, schlägt die Augen auf und beginnt zu reden, zu reden in der Sprache, die der fieberhaft Gespannte in den Büchern und Bergen der Heimat Wort für Wort gelernt, damit er hier und heute die Erde verstünde. Er starrt und späht und – versteht."

H. Cloos

Eigenständigkeitserklärung

Ich erkläre hiermit, dass ich die vorliegende Dissertation selbstständig und ohne unerlaubte Hilfe angefertigt habe. Jegliche verwendeten Hilfsmittel und Quellen sind im Literaturverzeichnis vollständig aufgeführt. Die aus den benutzten Quellen wörtlich oder inhaltlich entnommenen Stellen sind als solche kenntlich gemacht. Des Weiteren erkläre ich, dass die Arbeit bisher weder in gleicher noch in ähnlicher Form einer Prüfungsbehörde vorlag.

Declaration of Academic Honesty

I hereby certify that this thesis has been composed by me and is based on my work unless stated otherwise. All references have been quoted, and all sources of information have been specifically acknowledged. I further declare that I have not submitted this thesis at any other institution in order to obtain a degree.

Konstantin Huber
Hamburg, 31.05.2024

Supervisors

1st supervisor: Prof. Dr. Timm John
2nd supervisor: Dr. Johannes C. Vrijmoed

Dates of Submission and Defense

Submitted: 31.05.2024
Defense: 05.07.2024

Diese Arbeit wurde vom Promotionsausschuss des Fachbereichs Geowissenschaften am

_____ genehmigt.

Abstract

Dehydration of oceanic lithosphere in subduction zones is a crucial geodynamic factor on Earth and is linked to various geological phenomena. Efficient recycling of fluids liberated at depth back to the surface is essential to maintain the deep volatile cycle in balance over geological timescales. Rock dehydration itself is a multiscale process involving multiple physical processes, each acting on different time and length scales.

Natural examples of exhumed meta-serpentinites comprise a channelized network of olivine-rich veins that formed during dehydration and have served as a pathway for fluid escape at depth during dehydration. These vein networks can provide information about the processes that led to their formation and hence about the fluid release mechanisms. Previous studies have shown the importance of chemical heterogeneities for microscale channelization, and numerical models can successfully reproduce slab-scale fluid flow focusing that is observed using geophysical methods. However, the strikingly high content of metamorphic olivine and the intrinsic rock properties that lead to channelization going towards the slab scale, are not yet well understood.

This dissertation systematically studies rock dehydration as a multi-scale process. By combining a dataset of fully hydrated serpentinite with a numerical model, we aim to reproduce and explain the formation of a channelized, olivine-rich vein network observed in nature. The model thus connects the microscale mineral dehydration reactions to the macroscale fluid escape from the slab into the mantle.

The first scientific chapter presents a multiscale dataset of a serpentinite from the Mirdita ophiolite in Albania. The dataset includes geological, chemical, and structural data from the sub-micrometer up to the outcrop scale. Chemical heterogeneities are demonstrated to be scale invariant over at least four spatial orders of magnitudes. Thermodynamic modeling along the subduction zone P-T path shows porosity to be spatially heterogeneous on each scale during the P-T window of a dehydration reaction.

As a first step towards a dynamic model, the third chapter presents a numerical model for reactive fluid flow in an existing vein network. The model investigates the effects of chemical heterogeneities on the composition of the released fluid. A fluid released in a low-silica environment has a low content of dissolved silica. Fluid flow from a low-silica to a relatively higher-silica environment can trigger the dehydration reaction of antigorite to olivine, even at constant temperature. The model shows that local metasomatism can produce veins of almost pure olivine in a matrix that still contains abundant antigorite.

In the fourth chapter, the reactive fluid flow model is formulated in GENERIC (General Equation for Non-Equilibrium Reversible-Irreversible Coupling) to mathematically analyze the

underlying system of equations. This is the first application of GENERIC to a geoscience problem. The analysis shows that the system is well-posed and confirms the existence of a general solution for the system of equations.

The outlook presents preliminary results of a reactive porosity wave model, which is a logical and promising next step in combining the findings of the previous chapters into a single numerical model. Porosity waves are a mechanical fluid flow focusing mechanism and thus one possible mechanism for slab-scale channelized fluid fluxes. The model couples mechanical porosity waves with the effects of silica transport in the fluid and thermal effects. It serves as a large-scale model for fluid escape from the slab. Based on the findings of scale-invariant occurrence of chemical heterogeneities, it uses chemical mappings from the multiscale dataset as initial conditions and as a proxy for kilometer-scale chemical heterogeneities. This is the first time that a reactive porosity wave model has been combined with data from natural rock samples.

Zusammenfassung

Die Entwässerung von ozeanischer Lithosphäre in Subduktionszonen ist ein entscheidender geodynamischer Faktor auf der Erde und steht mit zahlreichen anderen geologischen Phänomenen in Verbindung. Die effiziente Rückführung der in der Tiefe freigesetzten Fluide zurück zur Erdoberfläche ist essenziell, um das Gleichgewicht des tiefen Volatilkreislauf der Erde über geologische Zeiträume aufrechtzuhalten. Die Entwässerung von Gesteinen ist ein Multiskalenprozess, der eine Vielzahl physikalischer Prozesse beinhaltet, die jeweils auf verschiedenen Zeit- und Längenskalen wirken.

Natürliche Beispiele obduzierter Meta-Serpentinite zeigen häufig ein kanalisiertes Netzwerk olivinreicher Adern, die sich während der Entwässerung gebildet und die als Wegsamkeit für die in der Tiefe während der Entwässerung entweichenden Fluide gedient haben. Diese Adernetzwerke können Aufschluss geben über die Prozesse, die zu ihrer Entstehung geführt haben. Bisherige Studien zeigen die Bedeutung von chemischen Heterogeneitäten für die Kanalisierung auf der Mikroskala, und numerische Modelle können erfolgreich großskalige Fluidfokussierung reproduzieren, die mit Hilfe geophysikalischer Methoden entdeckt wurde. Für den hohen Gehalt an metamorphem Olivin in den Adern sowie die intrinsischen Gesteinseigenschaften, die zur Kanalisierung auch auf größeren Skalen führt, fehlt bisher jedoch ein umfassendes Verständnis.

Diese Dissertation untersucht Gesteinsentwässerung systematisch als einen Multiskalenprozess. Durch die Kombination von einem Datensatz eines vollständig hydratisierten Serpentinits mit einem numerischen Modell reproduziert und erkärt sie die Entstehung eines kanalisierten olivinreichen Adernetzwerkes wie es in der Natur vorkommt. Das Modell ver-

bindet daher kleinskalige Entwässerungsreaktionen mit großskaligen Fluidbewegungen von der subduzierten Platte in den darüberliegenden Mantel.

Im zweiten Kapitel wird ein Multiskalen-Datensatz eines Serpentinits aus dem Mirdita-Ophiolit in Albanien präsentiert. Der Datensatz beinhaltet geologische, chemische und strukturelle Daten von der sub-Mikrometer- bis zur Aufschlussskala. Er zeigt, dass chemische Heterogenitäten über mindestens vier Größenordnungen skaleninvariant auftreten. Thermodynamische Berechnungen entlang eines Subduktions-P-T-Pfads zeigen die räumlich heterogene Verteilung von Porosität auf jeder Skala während des P-T-Fensters einer Entwässerungsreaktion.

Als ersten Schritt hin zu einem dynamischen Modell zeigt das dritte Kapitel ein numerisches Modell für reaktive Ströumngen in einem bestehenden Adernetzwerk. Das Modell untersucht die Effekte von chemischen Heterogenitäten auf die Zusammensetzung des freigesetzten Fluids. Ein in einer siliziumärmeren Umgebung freigesetztes Fluid hat auch einen niedrigen Gehalt an gelöstem Silizium. Strömungen aus einer siliziumarmen in eine relativ dazu siliziumreichere Umgebung können auch bei konstanter Temperatur Entwässerung durch die Reaktion von Antigorit zu Olivin hervorrufen. Das Modell zeigt, dass sich durch lokalen Metasomatismus Adern aus beinahe reinem Olivin in einer noch antigoritreichen Matrix bilden können.

Im vierten Kapitel der Dissertation wird das vorangegangene Modell für reaktive Strömungen in GENERIC (General Equation for Non-Equilibrium Reversible-Irreversible Coupling [Allgemeine Gleichung für Nichtgleichgewichts-Reversibel-Irreversibel-Kopplung]) formuliert, um das zugrundeliegende Gleichungssystem mathematisch zu analysieren. Dies ist die erste Anwendung von GENERIC auf eine geowissenschaftliche Fragestellung. Die Analyse zeigt, dass System korrekt gestellt ist und bestätigt die Existenz einer allgemeinen Lösung für das Gleichungssystem.

Im Ausblick werden vorläufige Ergebnisse eines reaktiven Porositätswellenmodells präsentiert. Das Modell ist ein logischer und vielversprechender nächster Schritt, um die Erkenntnisse der vorherigen Kapitel in ein einziges numerisches Modell zu verbinden. Porositätswellen sind ein mechanischer Mechanismus zur Strömungsfokussierung und somit ein möglicher Mechanismus für kanalisierte Strömungen auf der slab-Skala. Das Modell koppelt mechanische Porositätswellen mit den Effekten von Siliziumtransport in Fluiden und Temperatureffekten. Es dient als großskaliges Modell für das Entweichen von Fluiden aus der subduzierten Lithosphäre. Unter Einbeziehung der Ergebnisse über die Skaleninvarianz von chemischen Heterogenitäten werden die chemischen Kartierungen als Anfangsbedingungen und als Proxy für chemische Heterogenitäten auf der Kilometerskala verwendet. Hier wird erstmals ein reaktives Porositätswellenmodell mit Daten von natürlichen Gesteinsproben kombiniert.

Acknowledgements

This work would not have been possible without the support of my supervisors, colleagues, many friends, and my family. I'm grateful for the support I received from many people throughout the past years and for the experiences that came along with doing this Ph.D.

First of all, I would like to thank my first supervisor Timm John. Thank you for giving me the opportunity to work on such an exciting topic in the interdisciplinary environment of the CRC 1114. You encouraged me to grow out of my comfort zone and learn new concepts, ideas, and methods. The work in the CRC and my time as a member of the mineralogy-petrology group has been enriching. Thank you for your support over the years and your help, especially in difficult times.

Next, I would also like to thank my second supervisor, Hans Vrijmoed. Thank you very much for all your support over the years, not only during the time of this thesis. You sparked my enthusiasm for equations and numerical modeling right from my first course in Berlin. More than seven years later, I'm very grateful that I could learn so much from you.

I would also like to thank Yury Y. Podladchikov, who has been closely associated with the project throughout and who invited me as a guest in his research group at the University of Lausanne in the summer of 2023. Together with Liudmila Khakimova, we developed an important part of the reactive porosity wave model during this time. I very much enjoyed the time with you and had a lot of fun during our modeling sessions. Thanks!

Further thanks go to Jan Pleuger for his support with the fieldwork in Albania in 2019 and for the many great conversations during my time at the Geocampus. Working at the SFB gave me the opportunity to conduct research in a unique interdisciplinary environment. I would like to thank the CRC team and especially Marita Thomas for their support and scientific discussions over the last few years. A special thanks also goes to Andrea Zafferi for the great collaboration in Project C09 and for exchanging many great ideas over the years. Thanks also to Robert Polzin for the great discussions and your support.

I would also like to thank Marco Scambelluri; on the very first day of the project, you introduced us to the Erro Tobbio outcrops and it will end with you as reviewer for this thesis.

I highly appreciate your time and effort in this project.

I very much enjoyed my time at the Geocampus and I'm grateful to have met many great colleagues and friends who supported me in many ways. Thanks, Caroline Brachmann, Philip Kingsberry, Charlotte Läuchli, Arthur Borzi, Saskia Bläsing, Marc Grund, Julian Hülscher, Lorenzo Gemignani, Iris Wannhof, Anselm Loges, Xin Zhong, Shilei Quiao, Julia Schmidt, Sara Vulpius, Lisa Kaatz, and Christiane Behr.

During my time in Berlin, I gained much support and strength from the friendships at H1. You have made Berlin home, thanks for all the great times together. A special thanks to Linus and Cinzia, Andrea, Saskia, Pawel, Jacky, Wieland, Sia, Hagen, Sheila, Caro, and Isa. I also want to thank Paul, Adrian, Lorenz, Simon, Elias, Maxi, and Vinzenz for their long-lasting friendship.

This thesis concludes my geology studies, which would not have been possible in this form without the support of my family. I thank my parents for supporting me in pursuing my interests and my grandparents for their support, especially during the early years of my studies. They knew before I did that I was going to write a doctoral thesis.

Finally, I would especially like to thank Julia for enriching my life over the last few years.

Contents

List of Figures

List of Tables

Listings

Thesis Outline

This thesis consists of six chapters. Chapters 3 and 4 have been published in peer-reviewed journals; Chapter 2 has been submitted to a peer-reviewed journal and has received a decision of major revisions. At the time of submission, the reviewers' feedback is incorporated and the chapter will be re-submitted; Chapter 6 is currently being prepared for submission. The following provides an overview of the thesis structure and explains each chapter's author contributions.

Chapter 2 deals with the occurrence of chemical heterogeneities over at least four orders of magnitudes and investigates their effects on dehydration reactions and fluid production rates. Chapter 3 presents a reactive transport model that shows how reactive fluid flow, resulting from the aforementioned chemical heterogeneities, leads to dehydration and olivine enrichment within an existing vein-like porosity structure. Chapter 4 is a joint publication between mathematicians and geoscientists and presents a mathematical analysis of the system of equations used in Chapter 3. Chapter 6 presents the preliminary results of a reactive porosity wave model that combines the effects of reactive transport (Chapters 3 and 4) with mechanical effects and uses data from the multiscale dataset (Chapter 2) as initial conditions.

Chapter 1: Introduction

This chapter introduces the thesis topic and provides background information on the subduction zone dehydration processes. It outlines the theoretical framework within which the study was conducted, including the methodology used. It also explains how this dissertation fits into the CRC 1114 research program.

Chapter 2: Pulsed fluid release from subducting slabs caused by a scale-invariant dehydration process

K. Huber, T. John, J. C. Vrijmoed, J. Pleuger, and X. Zhong
Submitted to Earth and Planetary Science Letters (Major Revisions)

Chapter 2 presents a field-based multiscale serpentinite dataset and demonstrates the scale-invariant occurrence of similar chemical heterogeneities over at least four orders of magnitudes. These heterogeneities cause a scale-invariant dehydration behavior of the subducting hydrated oceanic slab mantle with distinct peaks for porosity production at every scale.

Konstantin Huber selected the Mirdita ophiolite in Albania as the field site, conducted the on-site fieldwork (mapping, sampling), obtained the data, wrote the codes to compile all data into a single dataset, performed the thermodynamic calculations, wrote the manuscript, and prepared all figures.

Timm John assisted during the fieldwork and provided ideas for data compilation and processing. Timm John was also involved in designing the structure of the manuscript. Johannes C. Vrijmoed, together with Konstantin Huber, performed the SEM element mappings, provided codes for SEM data processing, and assisted during the development of the codes. Jan Pleuger provided valuable expertise on local geology and, during the fieldwork in Albania, helped with the selection of local outcrops and improved the knowledge of the geological background section. Xin Zhong performed the Raman spectroscopy measurements and the Raman data processing. All authors interpreted and discussed the data set.

Chapter 3: Formation of olivine veins by reactive fluid flow in a dehydrating serpentinite

K. Huber, J. C. Vrijmoed, and T. John
Published in G^3 – Geochemistry, Geophysics, Geosystems

Chapter 3 presents a numerical model for reactive fluid flow in a dehydrating serpentinite. It builds on the previous chapter by showing how certain chemical domains described in Chapter 2 release a silica-poor fluid that can trigger dehydration and cause olivine enrichment within a vein.

Konstantin Huber wrote the reactive transport code, prepared the lookup tables, wrote the manuscripts, and created all figures. Johannes C. Vrijmoed supervised the development of the reactive transport code and preparation of the lookup tables. The code is written in

the then-unpublished Thermolab framework developed by Johannes C. Vrijmoed and Yury Y. Podladchikov. Johannes C. Vrijmoed and Timm John contributed to the discussion of the results. Timm John helped to draft the manuscript's outline and structure the discussion.

Chapter 4: A porous-media model for reactive fluid-rock interaction in a dehydrating rock

A. Zafferi, K. Huber, D. Peschka, J. C. Vrijmoed, T. John, M. Thomas
Published in the Journal of Mathematical Physics

Chapter four is a joint publication of all members of the C09 project. The Chapter presents a mathematical analysis of the system of equations and the lookup table data of the reactive transport model of Chapter 3. The system of equations is rewritten in terms of GENERIC (General Equation for Non-Equilibrium Reversible-Irreversible Coupling) formalism, allowing for a better mathematical analysis of the equations.

Andrea Zafferi, Marita Thomas, and Dirk Peschka carried out the mathematical analysis and formulation of the system in GENERIC. Andrea Zafferi wrote large parts of the manuscripts. Konstantin Huber wrote the section about the relevance of reactive fluid flow during rock dehydration. In addition, Konstantin Huber provided plots of system properties based on the lookup tables of the model used in Chapter 3. Johannes C. Vrijmoed assisted with the data processing and improvements for necessary recalculations. All authors provided feedback during the scientific discussions and contributed to improving the manuscript.

Chapter 5: Conclusions

This chapter summarizes the overall findings of this dissertation.

Chapter 6: Outlook: Towards the Slab Scale – Fluid Escape from a Dehydrating Slab by Reactive Porosity Waves

This chapter presents an outlook by showing a possible further development towards a reactive porosity wave model that combines the effects of reactive transport from Chapter 3 with viscous rheology to study large-scale fluid escape from the slab. The model is ready to use data from the multiscale dataset Chapter 2 as initial conditions.

A porosity wave model was proposed as work package four in the C09 project proposal. Konstantin Huber prepared the lookup tables and spent four weeks in summer 2023 as a guest at the University of Lausanne. During that time, Liudmila Khakimova, Yury Y. Podladchikov, and Konstantin Huber developed the first versions of the transport code. Johannes C. Vrijmoed helped prepare the lookup tables, greatly benefiting from his and Yury Y. Podladchikov's latest developments for ternary systems in the Thermolab software. Liudmila Khakimova's and Yury Y. Podladchikov's efforts helped to improve computation efficiency significantly. Konstantin Huber created all the Figures and wrote great parts of the chapter with help from Liudmila Khakimova, especially in the section about the mathematical model formulation. Timm John contributed valuable conceptual ideas, especially in the discussion. Marco Scambelluri contributed to defining the outline of the overall goal by providing the geological background information from the field perspective.

Chapter 1

Introduction

1.1 Rock Dehydration in Subduction Zones

Earth's lithospheric plates move constantly at rates of several millimeters per year. At convergent plate boundaries, subduction zones form where denser oceanic lithosphere sinks beneath a less dense overriding plate into the Earth's mantle.

The subducting plate carries significant amounts of volatile and fluid mobile elements such as halogens (Scambelluri et al., 2004b; John et al., 2011; Barnes et al., 2018) and sulfur (Alt et al., 2013; Li et al., 2020), which are structurally bound in the crystal lattice of hydrous minerals and carbonates (Pagé and Hattori, 2019; Scambelluri et al., 2019; Deschamps et al., 2013). Most of these volatile compounds are released as or dissolved in a free fluid phase during devolatilization reactions (Rüpke et al., 2006; Spandler and Pirard, 2013; van Keken et al., 2011) and will eventually migrate back toward the Earth's surface, thus closing the deep Earth's volatile cycle. This deep volatile cycle has far-reaching consequences for Earth's geodynamic evolution, and subduction zones play a crucial role in this cycle by being one of the main sites for element recycling on Earth (Spandler and Pirard, 2013; Scambelluri et al., 2004a; Faccenda, 2014; Deschamps et al., 2013).

Hydration of the oceanic plate, i.e. the formation of hydrous minerals by fluid-rock interaction at relatively low temperatures, occurs as the oceanic lithosphere moves away from its origin at mid-ocean ridges and seawater can percolate through the rock column (Faccenda, 2014; Godard et al., 2013; Prigent et al., 2020). Additional, deep-reaching hydration likely occurs at bend faults in the proximity of the trench [Figure 1.1 *near trench hydration*, Ranero et al. (2003); Fujie et al. (2013); Naif et al. (2015); Grevemeyer et al. (2018)].

Serpentinization, i.e. the formation of serpentine by the reaction of the primary mantle

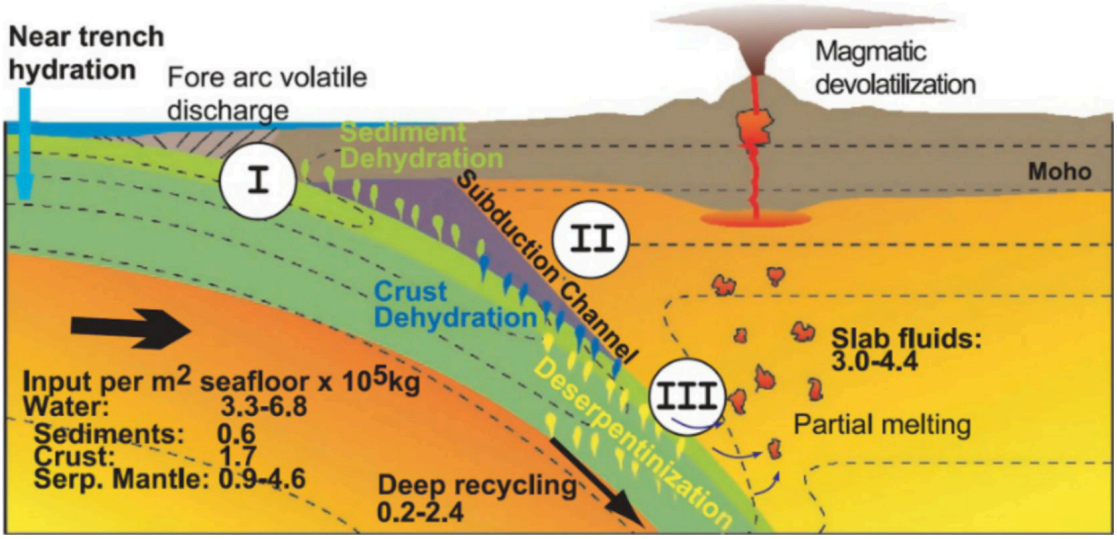

Figure 1.1: H_2O fluxes in a subduction zone, from Rüpke et al. (2004). A partially hydrated slab undergoes dehydration during subduction. The H_2O input estimates underline the significance of serpentinites as the main carrier of rock-bound H_2O into the subduction zone. Deserpentinization (III) liberates significant amounts of water as a free fluid phase, impacting a variety of other subduction zone processes.

minerals olivine and pyroxene with (sea)water, is important because of the large H_2O storage capacity of serpentinites. A fully serpentinized mantle consists of up to 13 wt. % of H_2O (Schmidt and Poli, 1998; Evans et al., 2013; Carlson and Miller, 2003; Evans, 2004), making serpentinites by far the main carriers of solid-bound H_2O into subduction zones. The presence of serpentinites also affects mantle rheology by lowering the rock strength and supporting shear localization in subduction zones (Raleigh and Paterson, 1965; O'Hanley, 1996; Hirth and Guillot, 2013; Guillot et al., 2015), and porous flow in the oceanic plate could have initiated subduction in the first place (Dymkova and Gerya, 2013). Furthermore, serpentinization is linked to the formation of deep-sea vents, so-called black smokers, where the percolating seawater exits the rock column, heated up by the geothermic gradient and the exothermic serpentinization reaction, with a high pH and rich in reduced gases such as hydrogen and sulfides. These vents provide a heat source and a unique chemical environment at the seafloor and might have been one of the places for the origin of life on Earth (e.g. Hannington et al., 2005; Martin et al., 2008; Georgieva et al., 2021).

As a result of different degrees of crust hydration and serpentinization, the slab entering a subduction zone is hydrated to various degrees (Kodolányi et al., 2012; Grevemeyer et al., 2018). H_2O contents lie on the order of several 100 tons per m^2 of oceanic plate [Figure 1.1,

Deschamps et al. (2013); Rüpke et al. (2004); van Keken et al. (2011)]. Due to their high H_2O storage capacity, the degree of serpentinization is the main factor controlling the H_2O influx into subduction zones (Figure 1.1).

Most of the water carried into the subduction zone is expelled from the slab during dehydration and eventually returns to the surface. At the onset of subduction, pore water is expelled from the sediments into the forearc (Figure 1.1I, Figure 1.3D). With ongoing subduction, pressure (P) and temperature (T) conditions increase (Syracuse et al., 2010) and trigger a series of dehydration reactions (Schmidt and Poli, 1998; Ulmer and Trommsdorff, 1995; Hacker et al., 2003a; Schmidt and Poli, 2014) that liberates the structurally bound H_2O as a free fluid phase filling up porosity created by densification of the rock (e.g. John et al., 2012; Taetz et al., 2018).

When reaction-induced fluid production is limited, compaction leads to the expulsion of the fluid from the slab into the mantle wedge and to the closing of porosity. A minor amount of H_2O is retained in the mantle (Figure 1.1 *deep recycling*) and is transported further down into the deep mantle where it can be stored in small quantities in so-called nominally anhydrous minerals (NAMs) such as olivine (Demouchy and Bolfan-Casanova, 2016; Williams and Hemley, 2001).

1.1.1 Geodynamic Significance of Rock Dehydration

Slab dehydration in subduction zones is a key geodynamic process and is linked to many other well-known geological phenomena. The liberated fluids play a key role in arc magmatism (Elliott et al., 1997; John et al., 2012) by inducing partial melting in the mantle wedge. Along with other factors such as shear heating, slab dehydration is also one of the causes of subduction zone seismicity (Peacock, 2001; Yokoyama et al., 2002; Hacker et al., 2003b; Ferrand, 2019) because of the reaction-induced volume changes and dehydration embrittlement of the solid slab and because the presence of a free fluid phase reduces effective stresses.

The transient transformation of the downgoing slab into a porous medium (Miller et al., 2003; Zack and John, 2007; Morishige and van Keken, 2018; Taetz et al., 2018) during dehydration results in the densification of the solid and a drastic change in petrophysical rock properties (Faccenda, 2014), whereas reactive fluid flow in the porous network leads to mass transfer in subduction zones (Zack and John, 2007; John et al., 2012; Chen et al., 2019; Clarke et al., 2020). Solid densification allows the slab to sink further into the mantle by a downward-directed slab pull force that is one of the driving mechanisms for the movement of tectonic plates. The slab-derived fluids migrate upwards from the slab into the subduction zone interface and eventually into the mantle wedge. Here, the presence of a free fluid phase

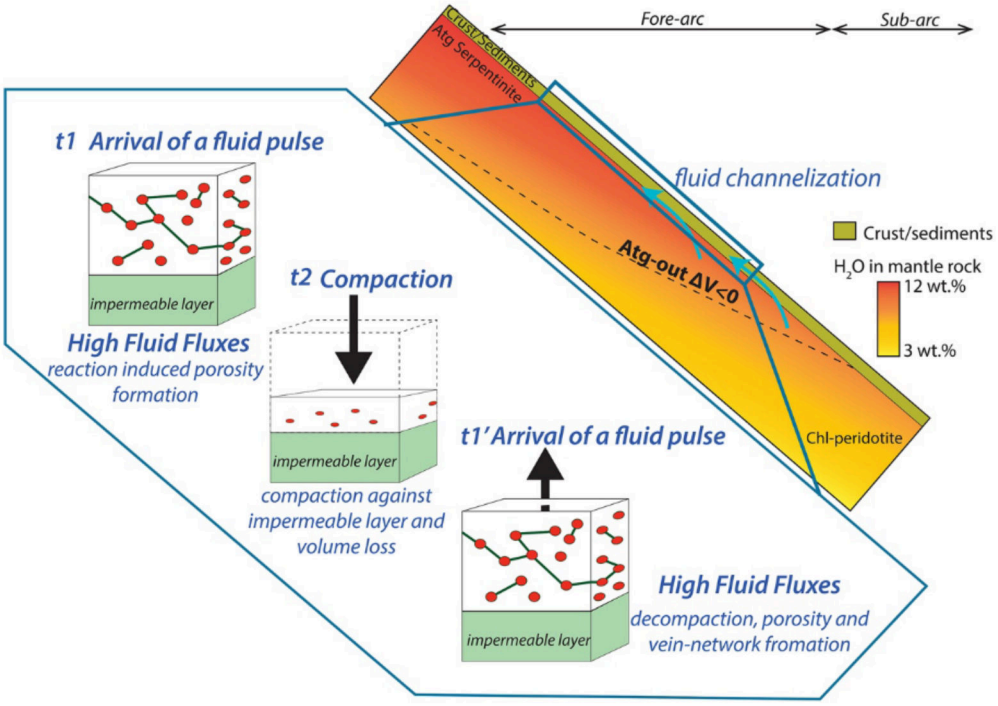

Figure 1.2: Schematic view of the pulse-like evolution of a transient high porosity network in a subducting slab, from Piccoli et al. (2021). During P-T conditions where a dehydration reaction occurs, a transient highly permeable porosity network in the rock evolves. When the reaction is terminated, compaction closes the porosity and the fluid is expelled upwards.

causes partial melting of the mantle by lowering the solidus (e.g. Grove et al., 2006; Ulmer and Trommsdorff, 1995; Ulmer, 2001). These hydrous melts migrate further upwards (McKenzie, 1984) and eventually feed arc volcanoes (Elliott et al., 1997; Hattori and Guillot, 2003; Yokoyama et al., 2002; Schmidt and Poli, 1998; Walowski et al., 2015). Element recycling from the mantle back to the surface over geological time scales is critical to sustaining an equilibrium between the presence of volatiles on the Earth's surface and the mantle (Plümper et al., 2017; van Keken et al., 2011; Parai and Mukhopadhyay, 2012), and, on the one hand, for sustaining plate tectonics on the other hand, thus for sustaining life on Earth (e.g. Brovarone et al., 2020).

1.1.2 Evolution of a Transient Porosity Network

During dehydration, the slab transiently transforms from a rock with a low background porosity into a highly permeable rock that allows fluid flow in the transient porous network

before compaction causes closure of the compliant porosity and initiates fluid expulsion (Figure 1.2). The transient porous network evolves when P-T conditions approach the stability limit of a hydrous phase. Many dehydration reactions do not occur at a specific point in P-T space but develop over a P-T window because the accompanied minerals form solid solutions, where e.g. the Fe-richer minerals react at lower P-T conditions than their Mg-richer equivalents.

Such variations in the mineral assemblage and the mineral compositions are in turn controlled by the local bulk rock composition. Chemical heterogeneities, i.e. spatial variations in the bulk rock composition, therefore have a first-order effect on the local thermodynamic equilibrium. This is especially true on small scales, where temperature and pressure gradients may be small, whereas significant chemical heterogeneities occur on the grain scale and below. Thus, assuming local thermodynamic equilibrium (e.g. Öttinger, 2023; Lebon et al., 2008), the local bulk composition determines when, and if, a dehydration reaction occurs for given P-T conditions. Plümper et al. (2017) showed that millimeter-scale chemical heterogeneities in a serpentinite lead to a heterogeneous vein-like porosity formation already at the onset of dehydration.

As porosity production continues, the liberated fluid will start to flow along fluid pressure gradients as soon as the percolation threshold is overcome (Bloch et al., 2018). The percolation threshold depends on the amount and geometry of the developing porosity (Bloch et al., 2018). A percolation fluid can cause local metasomatism in the porous network, making reactive fluid flow an important process at this stage of the porosity network evolution (Steefel et al., 2005; Seigneur et al., 2019; Zack and John, 2007; Beinlich et al., 2020; Putnis and Putnis, 2007). Eventually, upward-directed buoyancy forces will dominate over local fluid pressure gradients and compaction causes an upward-directed fluid expulsion.

Such fluid expulsion events have been recorded extensively (e.g. Dragovic et al., 2015; Taetz et al., 2018; John et al., 2012; Piccoli et al., 2021) and can serve as an explanation for a temporal heterogeneous behavior of pulse-like fluid release from the dehydrating slab. During fluid expulsion, the transient high-porosity network in the rocks allows fluid fluxes to exceed the pervasive Darcy fluxes in the intrinsic low-porosity rocks. One mechanism for a rapid and drastic increase in permeability is hydraulic fracturing when the fluid pressure exceeds the rock's yield strength and causes brittle deformation (Davies, 1999; Muñoz-Montecinos et al., 2021; Saffer and Tobin, 2011; Meneghini and Moore, 2007; Padrón-Navarta et al., 2010). Another mechanism that has been evoked to explain fluid expulsion from the slab are porosity waves (Connolly and Podladchikov, 1998, 2012; Yarushina and Podladchikov, 2015). Porosity waves describe the upward movement of a high porosity anomaly due to buoyancy forces and viscous, or viscoelastic, deformation of the surrounding rock. The concept of

porosity waves has gained increasing attention in the past years and has been applied to explain vertical fluid flow focusing structures in petroleum reservoirs in Norway (Yarushina et al., 2022), to melt migration in the mantle (Räss et al., 2018; Bessat et al., 2022) and has also been linked to subduction zone seismicity (Skarbek and Rempel, 2016).

The evolution of the vein network and the pulse-like fluid release from the slab pose an interesting problem because of the wide range of time and length scales that the different processes act on. Initial porosity formation occurs on micrometer length scales and is mainly temperature-dependent, thus controlled by heating of the slab on geological timescales (e.g. Taetz et al., 2018). In contrast, reactive fluid flow-induced metasomatism can progress at rates of decimeters/year (Beinlich et al., 2020; Taetz et al., 2018), and the propagation of hydraulic fractures happens almost instantaneously but can facilitate fluid flow over several hundreds of meters or even kilometers (e.g. Davies, 1999; Agard et al., 2018).

The multiscale aspect and chemical heterogeneities pose a challenging problem to bridge the gap between purely numerical studies and static thermodynamic equilibrium models that do not consider dynamic porosity evolution. To solve this problem, numerical models constrained by field observations can be combined with thermodynamic data. Thus, natural examples of dehydration-related fluid path networks in rocks can serve as a starting point for the study of rock dehydration using numerical modeling. Such preserved fluid pathway networks can be directly accessible in exhumed rocks or can be observed indirectly by geophysical methods.

1.1.3 Multiscale Fluid Flow Focusing

On large scales, geophysical imaging can help to reveal the presence of fluids at depth (Araya Vargas et al., 2019; Pommier and Evans, 2017; McGary et al., 2014). A magnetotelluric profile through the Cascadia subduction zone [Figure 1.3, modified from McGary et al. (2014)] shows the slab of the Nazca Plate in blue colors, subducting under the North American plate. Red colors indicate low resistivity caused by the presence of a fluid-filled porosity. After the expulsion of pore water sediments (Figure 1.3D), dehydration reactions in the slab liberate a fluid that is expelled from the slab into the mantle wedge (Figure 1.3A) and migrates further upwards and causes arc volcanism (Figure 1.3B, C). The arrow connecting A and B indicates focusing of the fluids liberated in A into a relatively narrow zone (B, C). Such large-scale fluid flow focusing can be explained by variations in compaction pressures (Wilson et al., 2014) and mantle wedge grain sizes (Cerpa et al., 2017). Focused fluid flow in the mantle wedge has also been indicated by isotope studies (Pirard, 2015) and diffusion modeling (Yoshida et al., 2023).

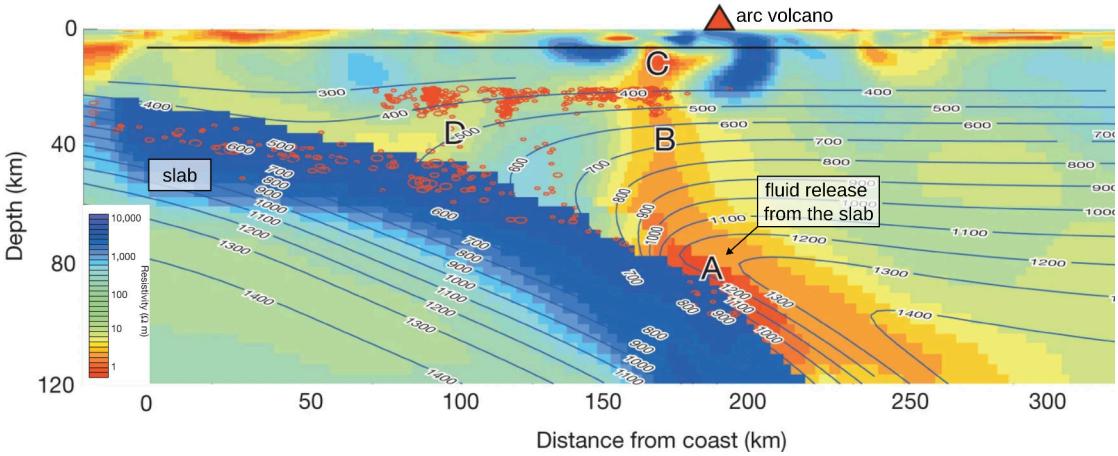

Figure 1.3: Magnetotelluric imaging of the Cascadia subduction zone, modified from McGary et al. (2014). Red colors indicate low resistivity caused by the presence of a free fluid phase. Fluids liberated by dehydration reactions (A) are focused on the slab scale into the mantle wedge (B), eventually causing partial melting of the mantle (C) and feeding arc volcanoes. Red circles represent hypocenters of seismic events.

Figure 1.4 shows a schematic overview of different types of fluid pathways at the subduction zone (plate) interface (Konrad-Schmolke et al., 2011). The figure indicates that fluid flow from the slab (medium grey) into the plate interface is also focused, similar to the large-scale geophysical observations (van der Straaten et al., 2008). The upward-directed flow of material at the plate interface can lead to the exhumation of high-pressure (HP) rocks, which may preserve a developed vein network of subduction zone fluid flow. Such exhumed HP rocks commonly occur in many orogens and allow to directly study the types of vein networks that formed during prograde metamorphism.

1.1.4 The Erro Tobbio Meta-Serpentinites as a Natural Example of an Exhumed Partially Dehydrated Rock

Exhumed ultramafic rocks are common in the Penninic units of the Alpine orogen (Evans, 1977; Piccardo and Guarnieri, 2010; Piccardo et al., 2004). One of the largest of these ultramafic bodies are the the Erro Tobbio (ET) unit in the Ligurian Alps in Northern Italy (Scambelluri et al., 1995; Strating et al., 1990; Rampone et al., 2005; Vissers et al., 1991). The ET unit is part of the Voltri massif and consists of ultramafic rocks from the former Piemonte-Ligurian Ocean (Strating, 1991) that largely preserve the pre-oceanic textures (Piccardo and Vissers, 2007). Pre-Jurassic rifting caused hyperextension of the continental margin, followed by Cretaceous convergence and subduction of the European plate under-

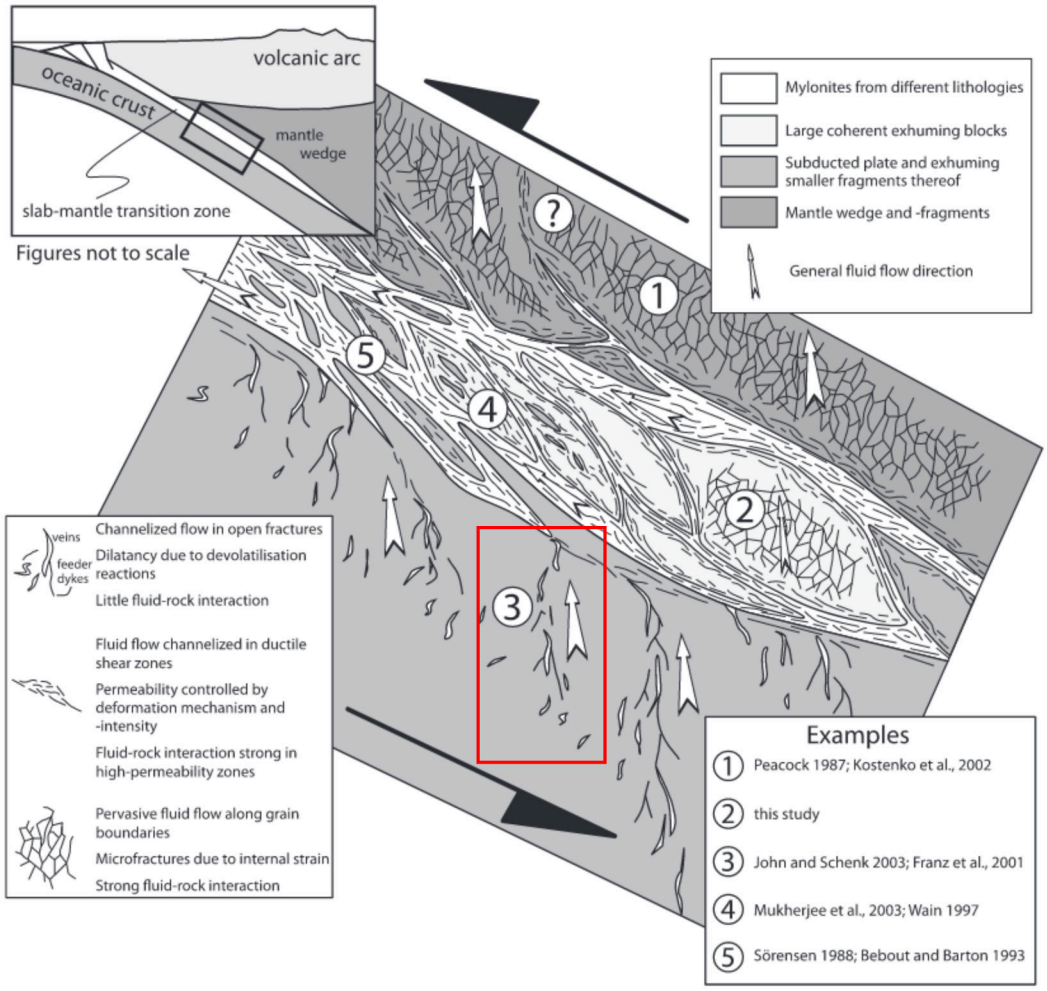

Figure 1.4: Different types of fluid pathways in a subduction zone, from Konrad-Schmolke et al. (2011). Fluid flow from the slab (medium grey) occurs via an interconnected, channelized vein network (type 3, red box). Exhumed and partially dehydrated rocks, such as the HP-meta-serpentinites of the Erro Tobbio unit, have such a vein network preserved.

neath the Adriatic plate prior to exhumation during the Alpine orogeny (Piccardo et al., 1988; Scambelluri et al., 1995; Rampone and Borghini, 2008).

The ET meta-serpentinites record peak P-T conditions of 500-550 °C and 2-2.2 GPa (Messiga et al., 1995) and comprise a prograde metamorphic mineral assemblage of olivine (ol), antigorite (atg), and Ti-clinohumite (Tclh) that indicates eclogite facies conditions (Scambelluri et al., 1991). This assemblage is also found in other Alpine peridotites of the Western Alps (Groppo and Compagnoni, 2007; Gilio et al., 2019) and is usually linked

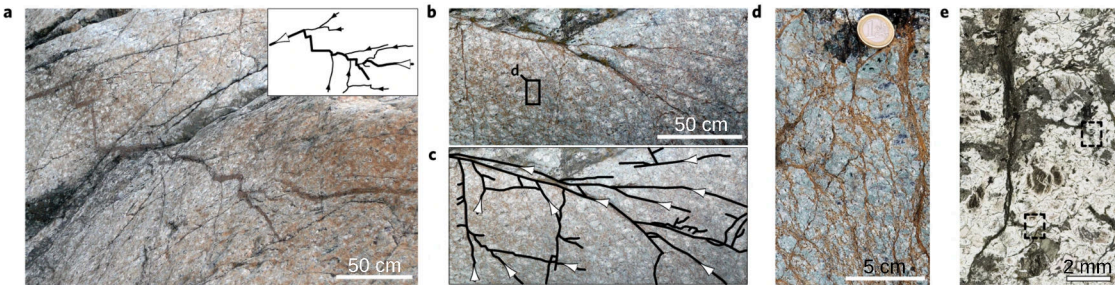

Figure 1.5: The channelized, olivine-rich eclogite facies vein network in the Erro Tobbio meta-serpentinites in the Ligurian Alps, Italy. Figure modified from (Plümper et al., 2017). a–d: field images of olivine-rich patches and veins on different scales. Arrows indicate potential fluid flow direction during dehydration. e: microphotograph of a micrometer scale vein tip (dashed square).

to deformational textures. Interestingly, in the ET unit, the atg-ol-Tclh assemblage also occurs in undeformed parts (Piccardo et al., 1988; Strating et al., 1990) within a distinct channelized vein network. This channelized vein network is indicative of the multiscale evolution of a dehydration-related vein network (Plümper et al., 2017). The formation of this vein network and the associated atg-ol-Tclh assemblage is linked to the olivine-producing dehydration reaction of atg + brucite (br) = ol + fluid, which is one of the main fluid-liberating dehydration reactions due to the high H_2O content of brucite.

Recently, Schmalholz et al. (2023) presented a numerical model that showed how a drop in fluid pressure during the opening of en-echelon can shift the thermodynamic equilibrium of the brucite-consuming dehydration reaction to the product side and thus to higher olivine contents. In the absence of deformation-related fluid pathways, the role of intrinsic chemical heterogeneities for the formation of fluid pathways has been demonstrated by Plümper et al. (2017).

The role of chemical heterogeneities offers a good explanation for the channelization of such a vein network (Plümper et al. (2017), see also Figure 1.4) on small scales. To study the further evolution of such a small-scale vein network and eventually large-scale fluid release, data about chemical heterogeneities on larger scales need to be coupled with numerical models for reactive fluid flow in a deforming porous medium. Such a multiscale model can then be used to study the formation of an olivine-rich vein network over multiple orders of length scales. Field observations from the dehydration-related vein network in the Erro Tobbio meta-serpentinites can be used to further constrain the numerical model.

1.2 Research Questions

Previous results show that fluid flow in subduction zones is channelized from the sub-µm scale up to the slab scale. However, a systematic study of slab dehydration across this range of scales is missing. Serpentinites represent the most important fluid source in descending slabs and are chemically the least complex rock type of those constituting the hydrated oceanic plate, hence a promising target system to study rock dehydration during subduction. Thus, the first aim of this study is to create a multiscale dataset of a serpentinite to provide insights into the occurrence of chemical heterogeneities on multiple scales. Next, this work aims to use the findings from the multiscale dataset with numerical models to investigate the effects of coupled thermal-hydro-mechanical-chemical (THMC) models on dehydration, fluid flow focusing, and the formation of olivine-rich veins such as observed in the Erro Tobbio meta-serpentinites. The CRC 1114 framework further allows to perform a mathematical analysis of the underlying equations with respect to applicability over the range of scales. In particular, the research questions addressed in each chapter are:

- Which chemical heterogeneities occur on the micro, meso, and macro scale? What is the effect of these heterogeneities on fluid production and porosity evolution during dehydration? Intrinsic chemical heterogeneities are reported for the µm scale and have been proven to be important for the development of porosity structure at the onset of dehydration. Do such heterogeneities also exist at larger scales? Do they have the same significance at the larger scales? (Chapter 2)
- How do the chemical heterogeneities of the rock at different scales affect the chemistry of the released fluid, and how can variations in fluid chemistry affect dehydration by reactive fluid flow? (Chapter 3)
- Are the equations used for large scale porous flow also valid on smaller scales, and on which timescales do the solid and the fluid phase reequilibrate? (Chapter 4)
- Can a coupled THMC model with input data from the multiscale dataset reproduce olivine-rich flow focus structures at the slab scale? (Chapter 6)

1.3 Thesis in the Context of the CRC 1114

This thesis is part of the second funding period of the Collaborative Research Center (CRC) 1114 *Scaling Cascades in Complex Systems*, project C09. The CRC 1114 is a multidisciplinary research project that studies natural phenomena occurring over many orders of magnitudes

and aims to understand system properties on various scales. Rock dehydration is a great example of such a process that acts over many orders of magnitudes of scales. Project C09 is a collaboration between mathematicians (Marita Thoma, Dirk Peschka, and Andrea Zafferi) and geoscientists (Timm John, Johannes C. Vrijmoed, and Konstantin Huber). The project goals are to establish a common language between geoscientists and mathematicians and to develop a multiscale model for rock dehydration with a multiscale dataset derived from a natural serpentinite as input. The collaboration further allows advanced mathematical analysis of the underlying equations.

References

P. Agard, A. Plunder, S. Angiboust, G. Bonnet, and J. Ruh. The subduction plate interface: Rock record and mechanical coupling (from long to short timescales). *Lithos*, 320–321:537–566, 2018. ISSN 0024-4937. doi:10.1016/j.lithos.2018.09.029.

J. C. Alt, E. M. Schwarzenbach, G. L. Früh-Green, W. C. Shanks, S. M. Bernasconi, C. J. Garrido, L. Crispini, L. Gaggero, J. A. Padrón-Navarta, and C. Marchesi. The role of serpentinites in cycling of carbon and sulfur: Seafloor serpentinization and subduction metamorphism. *Lithos*, 178:40–54, 2013. ISSN 0024-4937. doi:10.1016/j.lithos.2012.12.006.

J. Araya Vargas, N. M. Meqbel, O. Ritter, H. Brasse, U. Weckmann, G. Yáñez, and B. Godoy. Fluid Distribution in the Central Andes Subduction Zone Imaged With Magnetotellurics. *J. Geophys. Res. Solid Earth*, 124(4):4017–4034, 2019. ISSN 2169-9356. doi:10.1029/2018JB016933.

J. D. Barnes, C. E. Manning, M. Scambelluri, and J. Selverstone. The Behavior of Halogens During Subduction-Zone Processes. In D. E. Harlov and L. Aranovich, editors, *The Role of Halogens in Terrestrial and Extraterrestrial Geochemical Processes: Surface, Crust, and Mantle*, Springer Geochemistry, pages 545–590. Springer International Publishing, Cham, 2018. ISBN 978-3-319-61667-4. doi:10.1007/978-3-319-61667-4_8.

A. Beinlich, T. John, J. C. Vrijmoed, M. Tominaga, T. Magna, and Y. Y. Podladchikov. Instantaneous rock transformations in the deep crust driven by reactive fluid flow. *Nat. Geosci.*, 13(4):307–311, 2020. ISSN 1752-0908. doi:10.1038/s41561-020-0554-9.

A. Bessat, S. Pilet, Y. Y. Podladchikov, and S. M. Schmalholz. Melt Migration and Chemical Differentiation by Reactive Porosity Waves. *Geochem. Geophys. Geosystems*, 23(2), 2022. ISSN 1525-2027, 1525-2027. doi:10.1029/2021GC009963.

W. Bloch, T. John, J. Kummerow, P. Salazar, O. S. Krüger, and S. A. Shapiro. Watching Dehydration: Seismic Indication for Transient Fluid Pathways in the Oceanic Mantle of the Subducting Nazca Slab. *Geochem. Geophys. Geosystems*, 19(9):3189–3207, 2018. ISSN 1525-2027. doi:10.1029/2018GC007703.

A. V. Brovarone, C. J. Butch, A. Ciappa, H. J. Cleaves, A. Elmaleh, M. Faccenda, M. Feineman, J. Hermann, F. Nestola, A. Cordone, and D. Giovannelli. Let there be water: How Hydration/De-

hydration reactions accompany key Earth and life processes. *Am. Mineral.*, 105(8):1152–1160, 2020. ISSN 1945-3027. doi:10.2138/am-2020-7380.

R. L. Carlson and D. J. Miller. Mantle wedge water contents estimated from seismic velocities in partially serpentinized peridotites. *Geophys. Res. Lett.*, 30(5), 2003. ISSN 1944-8007. doi:10.1029/2002GL016600.

N. G. Cerpa, I. Wada, and C. R. Wilson. Fluid migration in the mantle wedge: Influence of mineral grain size and mantle compaction. *JGR Solid Earth*, 122(8):6247–6268, 2017. ISSN 2169-9313, 2169-9356. doi:10.1002/2017JB014046.

S. Chen, R. C. Hin, T. John, R. Brooker, B. Bryan, Y. Niu, and T. Elliott. Molybdenum systematics of subducted crust record reactive fluid flow from underlying slab serpentine dehydration. *Nat. Commun.*, 10(1):4773, 2019. ISSN 2041-1723. doi:10.1038/s41467-019-12696-3.

E. Clarke, J. De Hoog, L. Kirstein, J. Harvey, and B. Debret. Metamorphic olivine records external fluid infiltration during serpentinite dehydration. *Geochem. Persp. Let.*, 16:25–29, 2020. ISSN 24103403. doi:10.7185/geochemlet.2039.

J. A. D. Connolly and Y. Y. Podladchikov. An analytical solution for solitary porosity waves: Dynamic permeability and fluidization of nonlinear viscous and viscoplastic rock. In *Crustal Permeability*, chapter 23, pages 285–306. John Wiley & Sons, Ltd, 2012. ISBN 978-1-119-16657-3. doi:10.1002/9781119166573.ch23.

J. A. D. Connolly and Yu. Yu. Podladchikov. Compaction-driven fluid flow in viscoelastic rock. *Geodinamica Acta*, 11(2-3):55–84, 1998. ISSN 0985-3111, 1778-3593. doi:10.1080/09853111.1998.11105311.

J. H. Davies. The role of hydraulic fractures and intermediate-depth earthquakes in generating subduction-zone magmatism. *Nature*, 398(6723):142–145, 1999. ISSN 1476-4687. doi:10.1038/18202.

S. Demouchy and N. Bolfan-Casanova. Distribution and transport of hydrogen in the lithospheric mantle: A review. *Lithos*, 240–243:402–425, 2016. ISSN 0024-4937. doi:10.1016/j.lithos.2015.11.012.

F. Deschamps, M. Godard, S. Guillot, and K. Hattori. Geochemistry of subduction zone serpentinites: A review. *Lithos*, 178:96–127, 2013. ISSN 0024-4937. doi:10.1016/j.lithos.2013.05.019.

B. Dragovic, E. F. Baxter, and M. J. Caddick. Pulsed dehydration and garnet growth during subduction revealed by zoned garnet geochronology and thermodynamic modeling, Sifnos, Greece. *Earth and Planetary Science Letters*, 413:111–122, 2015. ISSN 0012-821X. doi:10.1016/j.epsl.2014.12.024.

D. Dymkova and T. Gerya. Porous fluid flow enables oceanic subduction initiation on Earth. *Geophys. Res. Lett.*, 40(21):5671–5676, 2013. ISSN 1944-8007. doi:10.1002/2013GL057798.

T. Elliott, T. Plank, A. Zindler, W. White, and B. Bourdon. Element transport from slab to volcanic front at the Mariana arc. *J. Geophys. Res. Solid Earth*, 102(B7):14991–15019, 1997. ISSN 2156-2202. doi:10.1029/97JB00788.

B. W. Evans. Metamorphism of Alpine Peridotite and Serpentinite. *Annu. Rev. Earth Planet. Sci.*, 5 (1):397–447, 1977. doi:10.1146/annurev.ea.05.050177.002145.

B. W. Evans. The Serpentinite Multisystem Revisited: Chrysotile Is Metastable. *International Geology Review*, 46(6):479–506, 2004. ISSN 0020-6814, 1938-2839. doi:10.2747/0020-6814.46.6.479.

B. W. Evans, K. Hattori, and A. Baronnet. Serpentinite: What, Why, Where? *Elements*, 9(2): 99–106, 2013. ISSN 1811-5209, 1811-5217. doi:10.2113/gselements.9.2.99.

M. Faccenda. Water in the slab: A trilogy. *Tectonophysics*, 614:1–30, 2014. ISSN 0040-1951. doi:10.1016/j.tecto.2013.12.020.

T. P. Ferrand. Seismicity and mineral destabilizations in the subducting mantle up to 6 GPa, 200 km depth. *Lithos*, 334–335:205–230, 2019. ISSN 0024-4937. doi:10.1016/j.lithos.2019.03.014.

G. Fujie, S. Kodaira, M. Yamashita, T. Sato, T. Takahashi, and N. Takahashi. Systematic changes in the incoming plate structure at the Kuril trench. *Geophys. Res. Lett.*, 40(1):88–93, 2013. ISSN 1944-8007. doi:10.1029/2012GL054340.

M. N. Georgieva, C. T. S. Little, V. V. Maslennikov, A. G. Glover, N. R. Ayupova, and R. J. Herrington. The history of life at hydrothermal vents. *Earth-Science Reviews*, 217:103602, 2021. ISSN 0012-8252. doi:10.1016/j.earscirev.2021.103602.

M. Gilio, M. Scambelluri, S. Agostini, M. Godard, D. Peters, and T. Pettke. Petrology and Geochemistry of Serpentinites Associated with the Ultra-High Pressure Lago di Cignana Unit (Italian Western Alps). *Journal of Petrology*, 60(6):1229–1262, 2019. ISSN 0022-3530. doi:10.1093/petrology/egz030.

M. Godard, L. Luquot, M. Andreani, and P. Gouze. Incipient hydration of mantle lithosphere at ridges: A reactive-percolation experiment. *Earth and Planetary Science Letters*, 371–372:92–102, 2013. ISSN 0012-821X. doi:10.1016/j.epsl.2013.03.052.

I. Grevemeyer, C. R. Ranero, and M. Ivandic. Structure of oceanic crust and serpentinization at subduction trenches. *Geosphere*, 14(2):395–418, 2018. ISSN 1553-040X. doi:10.1130/GES01537.1.

C. Groppo and R. Compagnoni. Metamorphic veins from the serpentinites of the Piemonte Zone, western Alps, Italy: A review. *Period. Mineral.*, (76.2-3):127–153, 2007. ISSN 0369-8963. doi:10.2451/2007PM0021.

T. L. Grove, N. Chatterjee, S. W. Parman, and E. Médard. The influence of H2O on mantle wedge melting. *Earth and Planetary Science Letters*, 249(1):74–89, 2006. ISSN 0012-821X. doi:10.1016/j.epsl.2006.06.043.

S. Guillot, S. Schwartz, B. Reynard, P. Agard, and C. Prigent. Tectonic significance of serpentinites. *Tectonophysics*, 646:1–19, 2015. ISSN 0040-1951. doi:10.1016/j.tecto.2015.01.020.

B. R. Hacker, G. A. Abers, and S. M. Peacock. Subduction factory 1. Theoretical mineralogy, densities, seismic wave speeds, and H $_2$ O contents. *J. Geophys. Res.*, 108(B1):2001JB001127, 2003a. ISSN 0148-0227. doi:10.1029/2001JB001127.

B. R. Hacker, S. M. Peacock, G. A. Abers, and S. D. Holloway. Subduction factory 2. Are intermediate-depth earthquakes in subducting slabs linked to metamorphic dehydration reactions? *J. Geophys. Res. Solid Earth*, 108(B1), 2003b. ISSN 2156-2202. doi:10.1029/2001JB001129.

M. D. Hannington, C. E. J. De Ronde, and S. Petersen. Sea-Floor Tectonics and Submarine Hydrothermal Systems. In J. W. Hedenquist, J. F. H. Thompson, R. J. Goldfarb, and J. P. Richards,

editors, *One Hundredth Anniversary Volume*, page 0. Society of Economic Geologists, 2005. ISBN 978-1-887483-01-8. doi:10.5382/AV100.06.

K. H. Hattori and S. Guillot. Volcanic fronts form as a consequence of serpentinite dehydration in the forearc mantle wedge. *Geology*, 31(6):525–528, 2003. ISSN 0091-7613. doi:10.1130/0091-7613(2003)031<0525:VFFAAC>2.0.CO;2.

G. Hirth and S. Guillot. Rheology and Tectonic Significance of Serpentinite. *Elements*, 9(2):107–113, 2013. ISSN 1811-5209. doi:10.2113/gselements.9.2.107.

T. John, M. Scambelluri, M. Frische, J. D. Barnes, and W. Bach. Dehydration of subducting serpentinite: Implications for halogen mobility in subduction zones and the deep halogen cycle. *Earth and Planetary Science Letters*, 308(1):65–76, 2011. ISSN 0012-821X. doi:10.1016/j.epsl.2011.05.038.

T. John, N. Gussone, Y. Y. Podladchikov, G. E. Bebout, R. Dohmen, R. Halama, R. Klemd, T. Magna, and H.-M. Seitz. Volcanic arcs fed by rapid pulsed fluid flow through subducting slabs. *Nat. Geosci.*, 5(7):489–492, 2012. ISSN 1752-0908. doi:10.1038/ngeo1482.

J. Kodolányi, T. Pettke, C. Spandler, B. S. Kamber, and K. Gméling. Geochemistry of Ocean Floor and Fore-arc Serpentinites: Constraints on the Ultramafic Input to Subduction Zones. *J. Petrol.*, 53(2):235–270, 2012. ISSN 1460-2415, 0022-3530. doi:10.1093/petrology/egr058.

M. Konrad-Schmolke, P. J. O'Brien, and T. Zack. Fluid Migration above a Subducted Slab—Constraints on Amount, Pathways and Major Element Mobility from Partially Overprinted Eclogite-facies Rocks (Sesia Zone, Western Alps). *Journal of Petrology*, 52(3):457–486, 2011. ISSN 0022-3530. doi:10.1093/petrology/egq087.

G. Lebon, D. Jou, and J. Casas-Vázquez. *Understanding Non-equilibrium Thermodynamics: Foundations, Applications, Frontiers*. Springer, Berlin, Heidelberg, 2008. ISBN 978-3-540-74251-7 978-3-540-74252-4. doi:10.1007/978-3-540-74252-4.

J.-L. Li, E. M. Schwarzenbach, T. John, J. J. Ague, F. Huang, J. Gao, R. Klemd, M. J. Whitehouse, and X.-S. Wang. Uncovering and quantifying the subduction zone sulfur cycle from the slab perspective. *Nat. Commun.*, 11, 514, 2020.

W. Martin, J. Baross, D. Kelley, and M. J. Russell. Hydrothermal vents and the origin of life. *Nat Rev Microbiol*, 6(11):805–814, 2008. ISSN 1740-1534. doi:10.1038/nrmicro1991.

R. S. McGary, R. L. Evans, P. E. Wannamaker, J. Elsenbeck, and S. Rondenay. Pathway from subducting slab to surface for melt and fluids beneath Mount Rainier. *Nature*, 511(7509):338–+, 2014. ISSN 0028-0836. doi:10.1038/nature13493.

D. McKenzie. The Generation and Compaction of Partially Molten Rock. *J. Petrol.*, 25(3):713–765, 1984. ISSN 0022-3530, 1460-2415. doi:10.1093/petrology/25.3.713.

F. Meneghini and J. C. Moore. Deformation and hydrofracture in a subduction thrust at seismogenic depths: The Rodeo Cove thrust zone, Marin Headlands, California. *GSA Bulletin*, 119(1-2):174–183, 2007. ISSN 0016-7606. doi:10.1130/B25807.1.

B. Messiga, M. Scambelluri, and G. B. Piccardo. Chloritoid-bearing assemblages in mafic systems and eclogite-facies hydration of alpine Mg-Al metagabbros (Erro-Tobbio Unit, Ligurian Western Alps). *Eur. J. Mineral.*, pages 1149–1168, 1995. ISSN ,. doi:10.1127/ejm/7/5/1149.

S. A. Miller, W. van der Zee, D. L. Olgaard, and J. A. D. Connolly. A fluid-pressure feedback model of dehydration reactions: Experiments, modelling, and application to subduction zones. *Tectonophysics*, 370(1):241–251, 2003. ISSN 0040-1951. doi:10.1016/S0040-1951(03)00189-6.

M. Morishige and P. E. van Keken. Fluid Migration in a Subducting Viscoelastic Slab. *Geochem. Geophys. Geosystems*, 19(2):337–355, 2018. ISSN 1525-2027. doi:10.1002/2017GC007236.

J. Muñoz-Montecinos, S. Angiboust, A. Garcia-Casco, J. Glodny, and G. Bebout. Episodic hydrofracturing and large-scale flushing along deep subduction interfaces: Implications for fluid transfer and carbon recycling (Zagros Orogen, southeastern Iran). *Chemical Geology*, 571:120173, 2021. ISSN 0009-2541. doi:10.1016/j.chemgeo.2021.120173.

S. Naif, K. Key, S. Constable, and R. L. Evans. Water-rich bending faults at the Middle America Trench. *Geochem. Geophys. Geosystems*, 16(8):2582–2597, 2015. ISSN 1525-2027. doi:10.1002/2015GC005927.

D. S. O'Hanley. *Serpentinites: Records of Tectonic and Petrological History*. Number no. 34 in Oxford Monographs on Geology and Geophysics. Oxford University Press, New York, 1996. ISBN 978-0-19-508254-8.

H. C. Öttinger. On small local equilibrium systems. *J. Non-Equilib. Thermodyn.*, 48(2):149–159, 2023. ISSN 1437-4358. doi:10.1515/jnet-2022-0074.

J. A. Padrón-Navarta, A. Tommasi, C. J. Garrido, V. L. Sánchez-Vizcaíno, M. T. Gómez-Pugnaire, A. Jabaloy, and A. Vauchez. Fluid transfer into the wedge controlled by high-pressure hydrofracturing in the cold top-slab mantle. *Earth Planet. Sci. Lett.*, 297(1):271–286, 2010. ISSN 0012-821X. doi:10.1016/j.epsl.2010.06.029.

L. Pagé and K. Hattori. Abyssal Serpentinites: Transporting Halogens from Earth's Surface to the Deep Mantle. *Minerals*, 9(1):61, 2019. ISSN 2075-163X. doi:10.3390/min9010061.

R. Parai and S. Mukhopadhyay. How large is the subducted water flux? New constraints on mantle regassing rates. *Earth and Planetary Science Letters*, 317–318:396–406, 2012. ISSN 0012-821X. doi:10.1016/j.epsl.2011.11.024.

S. M. Peacock. Are the lower planes of double seismic zones caused by serpentine dehydration in subducting oceanic mantle? *Geology*, 29(4):299–302, 2001. ISSN 0091-7613. doi:10.1130/0091-7613(2001)029<0299:ATLPOD>2.0.CO;2.

G. B. Piccardo and L. Guarnieri. Alpine peridotites from the Ligurian Tethys: An updated critical review. *Int. Geol. Rev.*, 52(10-12):1138–1159, 2010. ISSN 0020-6814. doi:10.1080/00206810903557829.

G. B. Piccardo and R. L. M. Vissers. The pre-oceanic evolution of the Erro-Tobbio peridotite (Voltri Massif, Ligurian Alps, Italy). *Journal of Geodynamics*, 43(4):417–449, 2007. ISSN 0264-3707. doi:10.1016/j.jog.2006.11.001.

G. B. Piccardo, O. Müntener, A. Zanetti, and T. Pettke. Ophiolitic Peridotites of the Alpine-Apennine System: Mantle Processes and Geodynamic Relevance. *Int. Geol. Rev.*, 46(12):1119–1159, 2004. ISSN 0020-6814. doi:10.2747/0020-6814.46.12.1119.

GB. Piccardo, E. Rampone, and M. Scambelluri. The alpine evolution of the Erro-Tobbio peridotites

(Voltri Massif-Ligurian Alps): Some field and petrographic constraints. *Ofioliti*, 13(2/3):169–174, 1988.

F. Piccoli, J. J. Ague, X. Chu, M. Tian, and A. Vitale Brovarone. Field-Based Evidence for Intra-Slab High-Permeability Channel Formation at Eclogite-Facies Conditions During Subduction. *Geochem. Geophys. Geosystems*, 22(3):e2020GC009520, 2021. ISSN 1525-2027. doi:10.1029/2020GC009520.

C. Pirard. Focused fluid transfer through the mantle above subduction zones. *Geology*, 43(10): 915–918, 2015. ISSN 0091-7613. doi:10.1130/G37026.1.

O. Plümper, T. John, Y. Y. Podladchikov, J. C. Vrijmoed, and M. Scambelluri. Fluid escape from subduction zones controlled by channel-forming reactive porosity. *Nature Geosci*, 10(2):150–156, 2017. ISSN 1752-0908. doi:10.1038/ngeo2865.

A. Pommier and R. L. Evans. Constraints on fluids in subduction zones from electromagnetic data. *Geosphere*, 13(4):1026–1041, 2017. ISSN 1553-040X. doi:10.1130/GES01473.1.

C. Prigent, J. M. Warren, A. H. Kohli, and C. Teyssier. Fracture-mediated deep seawater flow and mantle hydration on oceanic transform faults. *Earth and Planetary Science Letters*, 532:115988, 2020. ISSN 0012-821X. doi:10.1016/j.epsl.2019.115988.

A. Putnis and C. V. Putnis. The mechanism of reequilibration of solids in the presence of a fluid phase. *Journal of Solid State Chemistry*, 180(5):1783–1786, 2007. ISSN 00224596. doi:10.1016/j.jssc.2007.03.023.

C. B. Raleigh and M. S. Paterson. Experimental deformation of serpentinite and its tectonic implications. *J. Geophys. Res. 1896-1977*, 70(16):3965–3985, 1965. ISSN 2156-2202. doi:10.1029/JZ070i016p03965.

E. Rampone and G. Borghini. Melt migration and intrusion in the Erro-Tobbio peridotites (Ligurian Alps, Italy): Insights on magmatic processes in extending lithospheric mantle. *ejm*, 20(4):573–585, 2008. ISSN 0935-1221. doi:10.1127/0935-1221/2008/0020-1807.

E. Rampone, A. Romairone, W. Abouchami, G. B. Piccardo, and A. W. Hofmann. Chronology, Petrology and Isotope Geochemistry of the Erro–Tobbio Peridotites (Ligurian Alps, Italy): Records of Late Palaeozoic Lithospheric Extension. *Journal of Petrology*, 46(4):799–827, 2005. ISSN 0022-3530. doi:10.1093/petrology/egi001.

C. R. Ranero, J. Phipps Morgan, K. McIntosh, and C. Reichert. Bending-related faulting and mantle serpentinization at the Middle America trench. *Nature*, 425(6956):367–373, 2003.

L. Räss, N. S. C. Simon, and Y. Y. Podladchikov. Spontaneous formation of fluid escape pipes from subsurface reservoirs. *Sci Rep*, 8(1):11116, 2018. ISSN 2045-2322. doi:10.1038/s41598-018-29485-5.

L. Rüpke, J. Phipps Morgan, and J. Eaby Dixon. Implications of Subduction Rehydration for Earth's Deep Water Cycle. In S. D. Jacobsen and S. Van Der Lee, editors, *Geophysical Monograph Series*, pages 263–276. American Geophysical Union, Washington, D. C., 2006. ISBN 978-1-118-66648-7 978-0-87590-433-7. doi:10.1029/168GM20.

L. H. Rüpke, J. P. Morgan, M. Hort, and J. A. D. Connolly. Serpentine and the subduc-

tion zone water cycle. *Earth Planet. Sci. Lett.*, 223(1):17–34, 2004. ISSN 0012-821X. doi:10.1016/j.epsl.2004.04.018.

D. M. Saffer and H. J. Tobin. Hydrogeology and Mechanics of Subduction Zone Forearcs: Fluid Flow and Pore Pressure. *Annu. Rev. Earth Planet. Sci.*, 39(1):157–186, 2011. doi:10.1146/annurev-earth-040610-133408.

M. Scambelluri, E. H. H. Strating, G. B. Piccardo, R. L. M. Vissers, and E. Rampone. Alpine olivine- and titanian clinohumite-bearing assemblages in the Erro-Tobbio peridotite (Voltri Massif, NW Italy). *J. Metamorph. Geol.*, 9(1):79–91, 1991. ISSN 0263-4929, 1525-1314. doi:10.1111/j.1525-1314.1991.tb00505.x.

M. Scambelluri, O. Müntener, J. Hermann, G. B. Piccardo, and V. Trommsdorff. Subduction of water into the mantle: History of an Alpine peridotite. *Geology*, 23(5):459, 1995. ISSN 0091-7613. doi:10.1130/0091-7613(1995)023<0459:SOWITM>2.3.CO;2.

M. Scambelluri, J. Fiebig, N. Malaspina, O. Müntener, and T. Pettke. Serpentinite Subduction: Implications for Fluid Processes and Trace-Element Recycling. *Int. Geol. Rev.*, 46(7):595–613, 2004a. ISSN 0020-6814, 1938-2839. doi:10.2747/0020-6814.46.7.595.

M. Scambelluri, O. Müntener, L. Ottolini, T. T. Pettke, and R. Vannucci. The fate of B, Cl and Li in the subducted oceanic mantle and in the antigorite breakdown fluids. *Earth and Planetary Science Letters*, 222(1):217–234, 2004b. ISSN 0012-821X. doi:10.1016/j.epsl.2004.02.012.

M. Scambelluri, E. Cannaò, and M. Gilio. The water and fluid-mobile element cycles during serpentinite subduction. A review. *Eur. J. Mineral.*, pages 405–428, 2019. ISSN ,. doi:10.1127/ejm/2019/0031-2842.

S. M. Schmalholz, E. Moulas, L. Räss, and O. Müntener. Serpentinite Dehydration and Olivine Vein Formation During Ductile Shearing: Insights From 2D Numerical Modeling on Porosity Generation, Density Variations, and Transient Weakening. *J. Geophys. Res. Solid Earth*, 128(11): e2023JB026985, 2023. ISSN 2169-9313. doi:10.1029/2023JB026985.

M. Schmidt and S. Poli. Devolatilization During Subduction. In *Treatise on Geochemistry*, pages 669–701. Elsevier, 2014. ISBN 978-0-08-098300-4. doi:10.1016/B978-0-08-095975-7.00321-1.

M. W. Schmidt and S. Poli. Experimentally based water budgets for dehydrating slabs and consequences for arc magma generation. *Earth Planet. Sci. Lett.*, 163(1-4):361–379, 1998. ISSN 0012-821X. doi:10.1016/S0012-821X(98)00142-3.

N. Seigneur, K. U. Mayer, and C. I. Steefel. Reactive Transport in Evolving Porous Media. *Rev. Mineral. Geochem.*, 85(1):197–238, 2019. ISSN 1529-6466. doi:10.2138/rmg.2019.85.7.

R. M. Skarbek and A. W. Rempel. Dehydration-induced porosity waves and episodic tremor and slip. *Geochem. Geophys. Geosystems*, 17(2):442–469, 2016. ISSN 1525-2027, 1525-2027. doi:10.1002/2015GC006155.

C. Spandler and C. Pirard. Element recycling from subducting slabs to arc crust: A review. *Lithos*, 170–171:208–223, 2013. ISSN 0024-4937. doi:10.1016/j.lithos.2013.02.016.

C. I. Steefel, D. J. DePaolo, and P. C. Lichtner. Reactive transport modeling: An essential tool and a new research approach for the Earth sciences. *Earth and Planetary Science Letters*, 240(3):

539–558, 2005. ISSN 0012-821X. doi:10.1016/j.epsl.2005.09.017.

E. H. H. Strating. *The Evolution of the Piemonte-Ligurian Ocean : A Structural Study of Ophiolite Complexes in Liguria (NW Italy)*. PhD thesis, Instituut voor Aardwetenschappen der Rijksuniversiteit Utrecht, 1991.

E. H. H. Strating, G. B. Piccardo, E. Rampone, M. Scambelluri, and R. L. M. Vissers. The structure and petrology of the Erro-Tobbio peridotite, Voltri massif, Ligurian Alps. Guidebook for a two-day -excursion with emphasis on processes in the upper mantle (Voltri Massif, June 26-28, 1989). *Ofioliti*, 15(1):119–184, 1990. ISSN 0391-2612.

E. M. Syracuse, P. E. van Keken, and G. A. Abers. The global range of subduction zone thermal models. *Physics of the Earth and Planetary Interiors*, 183(1):73–90, 2010. ISSN 0031-9201. doi:10.1016/j.pepi.2010.02.004.

S. Taetz, T. John, M. Bröcker, C. Spandler, and A. Stracke. Fast intraslab fluid-flow events linked to pulses of high pore fluid pressure at the subducted plate interface. *Earth and Planetary Science Letters*, 482:33–43, 2018. ISSN 0012-821X. doi:10.1016/j.epsl.2017.10.044.

P. Ulmer. Partial melting in the mantle wedge — the role of H2O in the genesis of mantle-derived 'arc-related' magmas. *Physics of the Earth and Planetary Interiors*, 127(1):215–232, 2001. ISSN 0031-9201. doi:10.1016/S0031-9201(01)00229-1.

P. Ulmer and V. Trommsdorff. Serpentine Stability to Mantle Depths and Subduction-Related Magmatism. *Science*, 268(5212):858–861, 1995. ISSN 0036-8075, 1095-9203. doi:10.1126/science.268.5212.858.

F. van der Straaten, V. Schenk, T. John, and J. Gao. Blueschist-facies rehydration of eclogites (Tian Shan, NW-China): Implications for fluid–rock interaction in the subduction channel. *Chemical Geology*, 255(1):195–219, 2008. ISSN 0009-2541. doi:10.1016/j.chemgeo.2008.06.037.

P. E. van Keken, B. R. Hacker, E. M. Syracuse, and G. A. Abers. Subduction factory: 4. Depth-dependent flux of H2O from subducting slabs worldwide. *J. Geophys. Res. Solid Earth*, 116(B1), 2011. ISSN 2156-2202. doi:10.1029/2010JB007922.

R. Vissers, M. R. Drury, E. H. H. Strating, and D. van der Wal. Shear zones in the upper mantle: A case study in an Alpine Iherzolite massif. *Geology*, 19(10):990–993, 1991. ISSN 0091-7613. doi:10.1130/0091-7613(1991)019<0990:SZITUM>2.3.CO;2.

K. J. Walowski, P. J. Wallace, E. H. Hauri, I. Wada, and M. A. Clynne. Slab melting beneath the Cascade Arc driven by dehydration of altered oceanic peridotite. *Nature Geosci*, 8(5):404–408, 2015. ISSN 1752-0908. doi:10.1038/ngeo2417.

Q. Williams and R. J. Hemley. Hydrogen in the Deep Earth. *Annu. Rev. Earth Planet. Sci.*, 29(1): 365–418, 2001. ISSN 0084-6597, 1545-4495. doi:10.1146/annurev.earth.29.1.365.

C. R. Wilson, M. Spiegelman, P. E. van Keken, and B. R. Hacker. Fluid flow in subduction zones: The role of solid rheology and compaction pressure. *Earth Planet. Sci. Lett.*, 401:261–274, 2014. ISSN 0012-821X. doi:10.1016/j.epsl.2014.05.052.

V. M. Yarushina and Y. Y. Podladchikov. (De)compaction of porous viscoelastoplastic media: Model formulation: (DE)COMPACTION OF POROUS MEDIA. *J. Geophys. Res. Solid Earth*, 120(6):

4146–4170, 2015. ISSN 21699313. doi:10.1002/2014JB011258.

V. M. Yarushina, L. H. Wang, D. Connolly, G. Kocsis, I. Fæstø, S. Polteau, and A. Lakhlifi. Focused fluid-flow structures potentially caused by solitary porosity waves. *Geology*, 50(2):179–183, 2022. ISSN 0091-7613, 1943-2682. doi:10.1130/G49295.1.

T. Yokoyama, E. Nakamura, K. Kobayashi, and T. Kuritani. Timing and trigger of arc volcanism controlled by fluid flushing from subducting slab. *Proc. Jpn. Acad., Ser. B*, 78(7):190–195, 2002. ISSN 0386-2208, 1349-2896. doi:10.2183/pjab.78.190.

K. Yoshida, R. Oyanagi, M. Kimura, O. Plümper, M. Fukuyama, and A. Okamoto. Geological records of transient fluid drainage into the shallow mantle wedge. *Sci. Adv.*, 9(14):eade6674, 2023. doi:10.1126/sciadv.ade6674.

T. Zack and T. John. An evaluation of reactive fluid flow and trace element mobility in subducting slabs. *Chem. Geol.*, 239(3):199–216, 2007. ISSN 0009-2541. doi:10.1016/j.chemgeo.2006.10.020.

Chapter 2

Pulsed Fluid Release from Subducting Slabs Caused by a Scale-Invariant Dehydration Process

Submitted to Earth and Planetary Science Letters (EPSL) as: **Huber, K.**, John, T., Vrimoed J. C., Pleuger, J., Zhong, X. (2023); Pulsed fluid release from subducting slabs caused by a scale-invariant dehydration process

Abstract

The chemical composition of a rock has a first-order effect on the onset and duration of rock dehydration. We present a multiscale dataset of chemical heterogeneities found in a low-temperature serpentinite from the Mirdita ophiolite in Albania, and we explore the effects of such heterogeneities on slab dehydration during subduction. The dataset consists of chemical and geological mappings from the micrometer to the meter scale, spanning five orders of magnitude. At each scale, we investigate the interplay of metamorphic reactions as well as porosity and fluid production through thermodynamic modeling along a slab Moho P-T path typical for subducting plates. Notably, our results show that chemical heterogeneities are preserved, regardless of the observation scale, even in the case of local homogenization by events such as the lizardite-antigorite transition. Consequently, scale-invariant patterns of porosity evolution and fluid production along the P-T path emerge, with characteristic peaks for each dehydration reaction. As such, the dehydration behavior on the slab scale seems to be controlled by the processes on the millimeter scale, whereby resulting peaks correspond to pulsed slab fluid release localized in space and time at each scale, along strike and along dip of the subducting plate.

2.1 Introduction

Subduction zones play a crucial role in the Earth's deep water cycle by transporting large amounts of water stored in the hydrated oceanic lithosphere into the mantle (Brovarone et al., 2020; Schmidt and Poli, 1998; Ulmer and Trommsdorff, 1995; Rüpke et al., 2004). The release of this water during slab dehydration, together with the subsequent fluid flow back to the surface, is a process that affects several geological phenomena, including arc volcanism (John et al., 2012; Elliott et al., 1997; Ague et al., 2022), seismicity (Hacker et al., 2003; Ferrand et al., 2017; Shao et al., 2023), and mantle rheology (Hirth and Guillot, 2013; Reynard, 2013; Nakagawa et al., 2015). In addition, slab dehydration mechanisms and subsequent fluid ascent must keep pace with subduction rates on the order of millimeters per year to avoid significant loss of water from the Earth's surface into the mantle (van Keken et al., 2011; Rüpke et al., 2004, 2006; Plümper et al., 2017).

To understand slab dehydration processes, geochemical (Chen et al., 2019; John et al., 2012), geophysical (Bloch et al., 2018), and field-based observations on partially dehydrated exhumed meta-serpentinites show that fluid release from the slab occurs via an interconnected, channeled vein network that forms dynamically during dehydration at depth (Groppo and Compagnoni, 2007; Plümper et al., 2017; Jabaloy-Sanchez et al., 2022; Kempf et al., 2020; Scambelluri et al., 1991). Vein networks associated with mantle dehydration are reported in several localities (Groppo and Compagnoni, 2007; Jabaloy-Sanchez et al., 2022; López Sánchez-Vizcaíno et al., 2009; Scambelluri et al., 1991; Herms et al., 2012; John et al., 2012; Spandler et al., 2011; Ulrich et al., 2024) and often consist of a mineral assemblage rich in metamorphic olivine contrasting with a matrix that often still contains abundant hydrous minerals. The high olivine content within these veins can provide information about the processes controlling their formation and the composition of the percolating fluid.

The formation of such a vein network is thought to occur in three main steps (e.g. Zack and John, 2007; Taetz et al., 2018; Miller et al., 2003). First, at the microscale, fluid is liberated by mineral dehydration. As dehydration progresses, the previously isolated fluid pockets form an interconnected vein network, eventually allowing the fluid to escape from the rock (Taetz et al., 2018). In the first step, dehydration is controlled by the heterogeneities in the local bulk composition (Plümper et al., 2017). In the second step, reactive transport within the porous network becomes important at larger scales (Huber et al., 2022; Chen et al., 2019; John et al., 2012). Finally, fluid escape from the dehydrating rock is likely facilitated by mechanical processes such as hydraulic fracturing (John et al., 2012; Padrón-Navarta et al., 2010) or porosity waves (Connolly and Podladchikov, 2015; Yarushina and Podladchikov, 2015; Yarushina et al., 2022).

The extent to which chemical heterogeneities influence or even control the overall dehydration process as the system evolves from the microscale to larger scales remains uncertain. Huber et al. (2022) demonstrated the importance of centimeter-scale chemical heterogeneities for reactive fluid flow in a dehydrating serpentinite by showing that fluids liberated from silica-poor parts of the rock also have a low silica concentration. These silica-poor fluids can trigger dehydration in other parts of the rock when fluid flow within the porous network is possible. However, the question remains as to what extent such heterogeneities occur at even larger scales and how these variations affect the overall dehydration process.

We present a multiscale dataset from highly hydrated serpentinites of the Mirdita ophiolite in northern Albania. The microstructures and composition of our samples fit into the range of other oceanic serpentinites worldwide (e.g. Niu, 2004; Evans and Frost, 2021). Therefore, we assume the Mirdita serpentinites can be considered as a reasonable case study of serpentinites entering subduction zones worldwide. Spatial variations in silica and iron content occur from the micro- up to the kilometer scale, and we investigate whether the chemical heterogeneity affects dehydration systematics along a typical slab Moho P-T path.

2.2 Geological Setting - The Mirdita Ophiolite

Ophiolites of Tethyan origin are common in the Alpine-Himalayan orogenic belt. However, many ophiolites experienced at least a low degree of metamorphism due to tectonic burial, such that they lost their original ocean floor textures and mineral assemblage, such as by the formation of antigorite from lizardite and chrysotile. Yet, some sections of oceanic lithosphere have undergone only little orogenic metamorphism, like the Mirdita ophiolite of the Western Vardar Zone in northern Albania (Bortolotti et al., 1996; Morishita et al., 2011; Nicolas et al., 1999).

The Mirdita ophiolites are situated next to the Dinarides in the northernmost Hellenides and belong to the Western Vardar zone of the Dinaric-Hellenic orogenic belt (e.g. Schmid et al., 2020). The Jurassic Western Vardar ophiolites originate from the Neotethys Ocean that separated the Adriatic microcontinent from Europe. They formed in a slow-spreading back-arc basin above the subducting Triassic (Meliata) Neotethyan oceanic lithosphere that was part of the Adriatic plate. Following the complete subduction of the Meliata oceanic lithosphere, the Western Vardar ophiolites were obducted onto the Pelagonian zone of the Adriatic margin in the Late Jurassic to Early Cretaceous (e.g. Bortolotti et al., 2005; Schmid et al., 2008; Tremblay et al., 2015). The Western Vardar ophiolites and their Pelagonian sole were imbricated during Alpine orogeny in a piggyback style and formed a stack of nappe complexes (from bottom to top, the lower Pelagonian, upper Pelagonian, and Jadar-

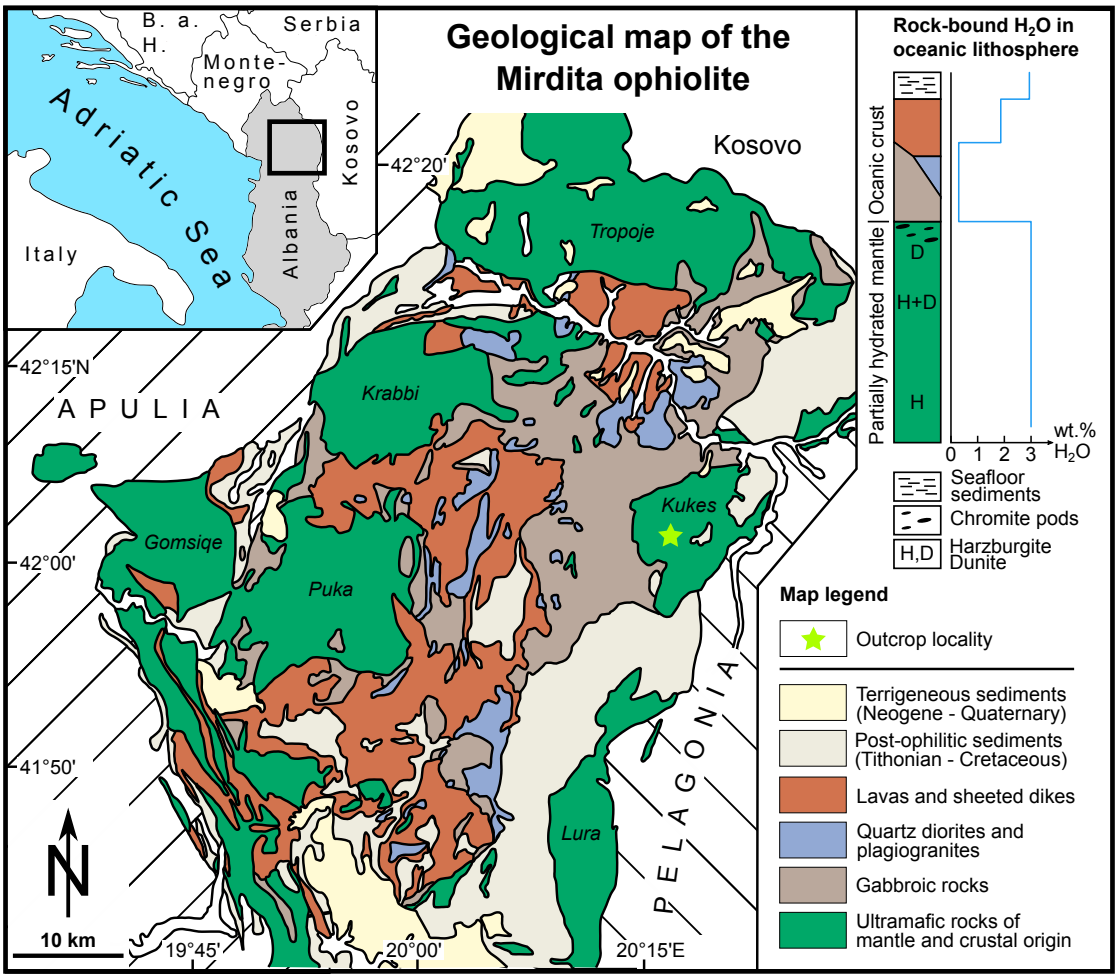

Figure 2.1: Geological map of the Mirdita ophiolite in northern Albania [redrawn from Bortolotti et al. (2005)] with green colors marking the occurrence of ultramafic units. The yellow star in the Kukes massif highlights the outcrop locality. The top right panel shows a simplified lithostratigraphic chart representative of the eastern part of the Mirdita ophiolite. Dunite content and the abundance of chromite pods in the ultramafic section increase with proximity to the Moho. Note that the sketch of the rock column is not to scale. The graph to the right of the column shows estimates of H_2O bound in the solid for the different lithologies [from Rüpke et al. (2004)]. 3 wt.% bulk H_2O in the mantle implies about 20 % hydration of the upper mantle, which contains up to 13 wt.% when fully serpentinized.

Kopaonik units (Schmid et al., 2020, 2008), each consisting of ophiolites on top of Adria-derived rocks. The Mirdita ophiolites lie on top of the upper Pelagonian and were probably never overthrust by the Jadar-Kopaonik unit, whose Alpine thrust front is presently exposed ∼100 km east of the Mirdita ophiolites. Therefore, the Mirdita ophiolites were not buried under higher tectonic units, and the temperature gradient in the ophiolite was probably not significantly raised during Alpine orogeny. This is in line with field observations that Alpine deformation of the ophiolites was localized along rather thin (centimeters- to tens of meters-thick) brittle to semi-ductile shear zones, leaving the largest portion of the ophiolites undeformed during obduction and Alpine orogeny. Geochemical and petrological differences further divide the ultramafic massifs of the Mirdita ophiolite into western and eastern units. The signature of the western units indicates a mid-ocean ridge (MOR) origin, in contrast to the predominantly supra-subduction zone (SSZ) signature of the eastern units (Dilek et al., 2007, 2008). Thickness also increases from 2 to 3 km in the west to 10 to 12 km in the east. The eastern units include all units of the Penrose model of oceanic lithosphere. We conducted the fieldwork and sampling for this study in the ultramafic Kukes massif in the eastern units of the Mirdita zone. We assume that these serpentinites, characterized by mineral assemblages characteristic of low temperatures, represent a typical hydrated oceanic lithosphere entering a subduction zone.

2.3 Methods

2.3.1 Fieldwork and Analytical Methods

Sampling

Based on field observations of the ultramafic section of the Mirdita ophiolite, we chose a representative outcrop for detailed lithological mapping (42°01'27"N 20°17'33"E, Figure 2.2). The outcrop is located at the eastern portal of the Thirrë-Kalimash tunnel, along a small road built during tunnel construction in 2009, thus providing access to relatively fresh rock. The outcrop is a 16 m long, north-south oriented wall, 3 to 5 m high. Within the outcrop, we identified serpentinized harzburgites and dunites as the primary lithologies and sampled them using a portable drill and rock saw. To prepare the multiscale dataset, we took a representative piece of serpentinized harzburgite and cut from it a circular sample with a diameter of ∼10 cm, sample ALB05. From this sample, we collected 6 EDS (energy dispersive spectroscopy) maps of varying sizes, from the decimeter scale down to the microscale.

Analytical Methods

A ZEISS Axio Imager M2m optical microscope at the Freie Universität Berlin was used to map entire thin sections using reflected and plane polarized transmitted light. Subsequently, selected regions on the thin sections were mapped in the ZEISS Automated Mineralogy Lab at the Freie Universität Berlin using a ZEISS Sigma 300 VP field-emission scanning electron microscope, integrating two energy dispersive X-ray silicon drift detectors (Bruker Quantax XFlash 6, 60 mm^2). The measurements were performed with an acceleration voltage of 20 kV, an aperture size of 120 µm, and a dwell time of 100 ms. To obtain the multiscale dataset, we collected 6 maps on a representative region by varying the size of the domain and the pixel resolutions: 76, 36, 20, 10, 5, and 2.5 µm, respectively. Quantitative wavelength dispersive spectroscopy (WDS) point analyses on the harzburgite (sample ALB09-1) and dunite (sample ALB06-1) were carried out using the JEOL JXA 8200 Superprobe at Freie Universität Berlin, using an acceleration potential of 20 kV, a beam current of 20 nA, and a beam size of 1 µm. Table 2.1 shows a summary of representative analyses. Raman mapping was performed to reveal characteristics of the serpentinite and brucite mineral phase distribution within a domain of 40 × 60 µm on a typical mesh texture of the dunite sample ALB06-2. We used a WiTec alpha 300 R spectrometer at Freie Universität Berlin equipped with a Zeiss EC Epiplan 50X/0.75 objective and a polarized solid-state laser with a wavelength of 532.1 nm. Because brucite grains are sensitive to the laser heating, potentially triggering a dehydration reaction, we set the laser power to ∼1 mW, using a pixel dwell time of ∼10 s and step size of 0.5 µm. The obtained Raman spectra were fitted with a MATLAB script to obtain the peak position and peak area. The 230 cm^{-1} and 1100 cm^{-1} peaks were taken to identify the distribution of lizardite and chrysotile (Compagnoni et al., 2021; Groppo et al., 2006), whereas the 440 cm^{-1} peak was used to characterize brucite (Groppo and Compagnoni, 2007).

2.3.2 Upscaling Method

For upscaling, we selected representative areas of 1 × 1 mm for the millimeter scale on the 2.5-µm pixel size map, 1 × 1 cm for the centimeter scale on the 20-µm pixel size map, and 5 × 5 cm for the decimeter scale on the 76-µm pixel size map. We considered an area representative if it contained the prominent textural and chemical heterogeneities found at that scale (Figure 2.2). From the millimeter to the decimeter scale, this includes the difference between bastites and mesh texture; from the meter to outcrop scale, it includes the lithological difference between dunites, harzburgites, and pyroxenites. To create the meter-scale dataset, we rearranged and resized the geological map (Figure 2.2C). We saved

an image of the rearranged outcrop at a resolution of 100×100 pixels so that each pixel represented $1\,dm^2$. We then assigned each pixel a bulk composition based on the lithology that each pixel represented on the geological map. As harzburgite bulk composition, we used 46 wt.% SiO_2, 42 wt.% MgO, and 9 wt.% FeO; as dunite bulk composition, we used 41 wt.% SiO_2, 44 wt.% MgO, and 10 wt.% FeO; for the pyroxenite bulk composition, we used 56 wt.% SiO_2, 35 wt.% MgO and 5 wt.% FeO. To add bulk composition variations within each lithology, we varied each composition by using a Gaussian distribution with the bulk composition as the mean value and a standard deviation of 4 wt.% for both SiO_2 and MgO and 3 wt.% for FeO. The chemical heterogeneities hence bulk composition variations produced by this method are within the natural range found in oceanic peridotites and dunites (Niu, 2004) and reflect observations in partially serpentinized high-pressure units such as Erro Tobbio, see, e.g., Peters et al. (2020). For the final data set, we performed the map coarsening for each of the selected representative areas (mm-, cm-, dm-scales) and the rearranged outcrop (m-scale) by dividing the chemical maps of the respective domains into a coarser grid of 10×10 pixels (Figure 2.2C) and applying a volumetric averaging (e.g. Zhang et al., 2021) within each of these coarse pixels. We considered the area covered by the coarse pixel as the effective thermodynamic domain size, i.e., an area over which the domain behaves as a chemically effective bulk volume for which we explore the mineral assemblage, porosity formation, and fluid production by applying equilibrium thermodynamics. Our approach led to thermodynamic equilibrium domain sizes of $0.01\,mm^2$ for the millimeter scale, $1\,mm^2$ for the centimeter scale, $2.5\,cm^2$ for the decimeter scale, and $1\,m^2$ for the meter scale. A similar approach of varying thermodynamic domain sizes was used by Plümper et al. (2017), who additionally used a diffusion model to obtain a local bulk composition. For the sake of simplicity, we apply this rather simplified concept. We refer to Evans et al. (2013a) for a detailed discussion about exploring length scales of equilibrium for mineral reactions and system and domain sizes of equilibrium in the context of serpentinization/deserpentinization.

2.3.3 Thermodynamic Model and Porosity Calculation

Phase Equilibria Calculations

To study the effect of the chemical variations found in the chemical mappings at each scale (mm-, cm-, dm- and m-scale; Figure 2.2C), we performed Gibbs free energy minimization calculations along a typical slab Moho path in a subduction zone (Figure 2.6A) for every composition (pixel) in the coarse 10×10 pixel maps of each scale. For the thermodynamic calculations, we used Thermolab codes (Vrijmoed and Podladchikov, 2022) with the thermodynamic dataset tc-ds633 from Holland and Powell (2011). Calculations were done in

the FMSH (FeO-MgO-SiO_2-H_2O) chemical subsystem, with values for SiO_2, FeO, and MgO taken from the coarse chemical maps (e.g., those of the mm-scale in Figure 2.5) and H_2O in excess. Additional calculations are done considering Al_2O_3 (FMASH) and with variations of the Fe3+/FeToT (FMSHO). The solid phases considered in our calculations were lizardite, antigorite, brucite, talc, orthopyroxene, and olivine. For chemically more complex calculations (FMASH and FMSHO) also magnetite and chlorite are considered. We accounted for the effects of Fe-Mg partitioning for each solid phase, using the solution models of Evans and Frost (2021) and added an ideal solution model for lizardite. To generate the lizardite iron endmember, we used the reaction Fe-lizardite = Fe-talc + 3 Fe-brucite, assuming $\Delta H_r = 0$, as we are currently unaware of any thermodynamic data on this reaction. In the discussion, we address our choice of solution models and compare our results to those obtained when using the solution models of Holland and Powell (2004).

Slab Moho P-T path

We performed Gibbs free energy minimization for every composition in the 2D serpentinite domains along a distinct slab Moho P-T path from the compilation of Syracuse et al. (2010, P-T paths given in the appendix). We chose the Lesser Antilles P-T path for our calculations because represents an intermediate P-T path and therefore similar to many other subduction zone P-T paths worldwide. The subduction zone data are taken from the Supplementary Material of Syracuse et al. (2010, Figure 13), and pressure is calculated as lithostatic overburden pressure.

Porosity Calculation

To study the effects of chemical heterogeneities on the timing and the amount of porosity production, we used Equation (2.1) to calculate porosity along the P-T path. This equation is based on the conservation of non-hydrous mass (Malvoisin et al., 2015), i.e., mass always bound to the solid, and has been successfully applied in previous studies, such as Plümper et al. (2017); Beinlich et al. (2020), and Huber et al. (2022). In our system, with H_2O being the only fluid mobile component, the non-volatile density was calculated as $\varrho_s(1-X_{H_2O})$, with ϱ_s and X_{H_2O} obtained from the post-processing of the Gibbs free energy minimization results, with ϱ_s and X_{H_2O} being the solid density and the rock-bound water content, respectively. Equation (2.1) accounts for porosity formation by densification of the solid during dehydration without considering mechanical effects, such as compaction, or metasomatic effects, such as reactive fluid flow.

$$\phi = 1 - \frac{\varrho_s^0(1 - X_{H_2O}^0)(1 - \phi^0)}{\varrho_s(1 - X_{H_2O})} \tag{2.1}$$

The superscript 0 refers to the reference point for the background porosity ϕ^0, which we set to zero before the first dehydration reaction occurs.

2.4 Results

2.4.1 Sample Characteristics at Various Scales

The bulk part of the outcrop consists of serpentinized harzburgite including a significant volume of serpentinized dunite. Both lithologies have undergone almost complete serpentinization, but we use the terminology based on the precursor rock because this difference matters for our study. Dunite occurs as lenses within harzburgite, often reaching sizes of several meters or more (Figure 2.2B). For example, near the outcrop, the entire section above the tunnel portal consists of a single dunite lens about 20 m in diameter. Both harzburgites and dunites are cut by pyroxenite dykes with centimeter-sized pyroxene crystals, most of which are altered to bastites. Bortolotti et al. (1996) recognized an increasing dunite content toward the Moho in their geological map of the ophiolite. Such a presence of significant amounts of dunite is considered as being indicative of the proximity to the petrological Moho (e.g. Morishita et al., 2011, and references therein), which in our case lies about 3 km further to the southwest (Figure 2.1). The presence of dunite and harzburgites represents a first-order chemical heterogeneity on the km-scale of the Mirdita ophiolite (Bortolotti et al., 1996) down to the meter scale of our outcrop. A similar pattern emerges on the decimeter scale and is visible in the field photographs (Figure 2.3). The view of a fresh harzburgite surface (Figure 2.3A), taken perpendicular to the mantle layering, shows the abundance of pyroxenes oriented along the primary mantle layering. Such pyroxene-rich layers are absent in the dunite (Figure 2.3B), which appears more homogeneous at the decimeter scale compared to the harzburgite.

Zooming further in reveals that the same principal heterogeneity is also present on the centimeter scale (Figure 2.3C, D). Figure 2.3C and 3D show thin-section photographs of a representative sample of harzburgite and dunite, respectively. On the millimeter scale, some domains in the harzburgite are dominated by bastites, others by mesh texture only, as highlighted by the white boxes in Figure 2.3C. In contrast, all millimeter-scale domains in the dunite are dominated by mesh textures. A direct comparison of the millimeter-scale textures shows the textural similarity between mesh textures in harzburgite and dunite (Figure 2.3E and 3G, respectively). A clear textural difference, however, is visible between mesh textures and bastite (Figure 2.3F).

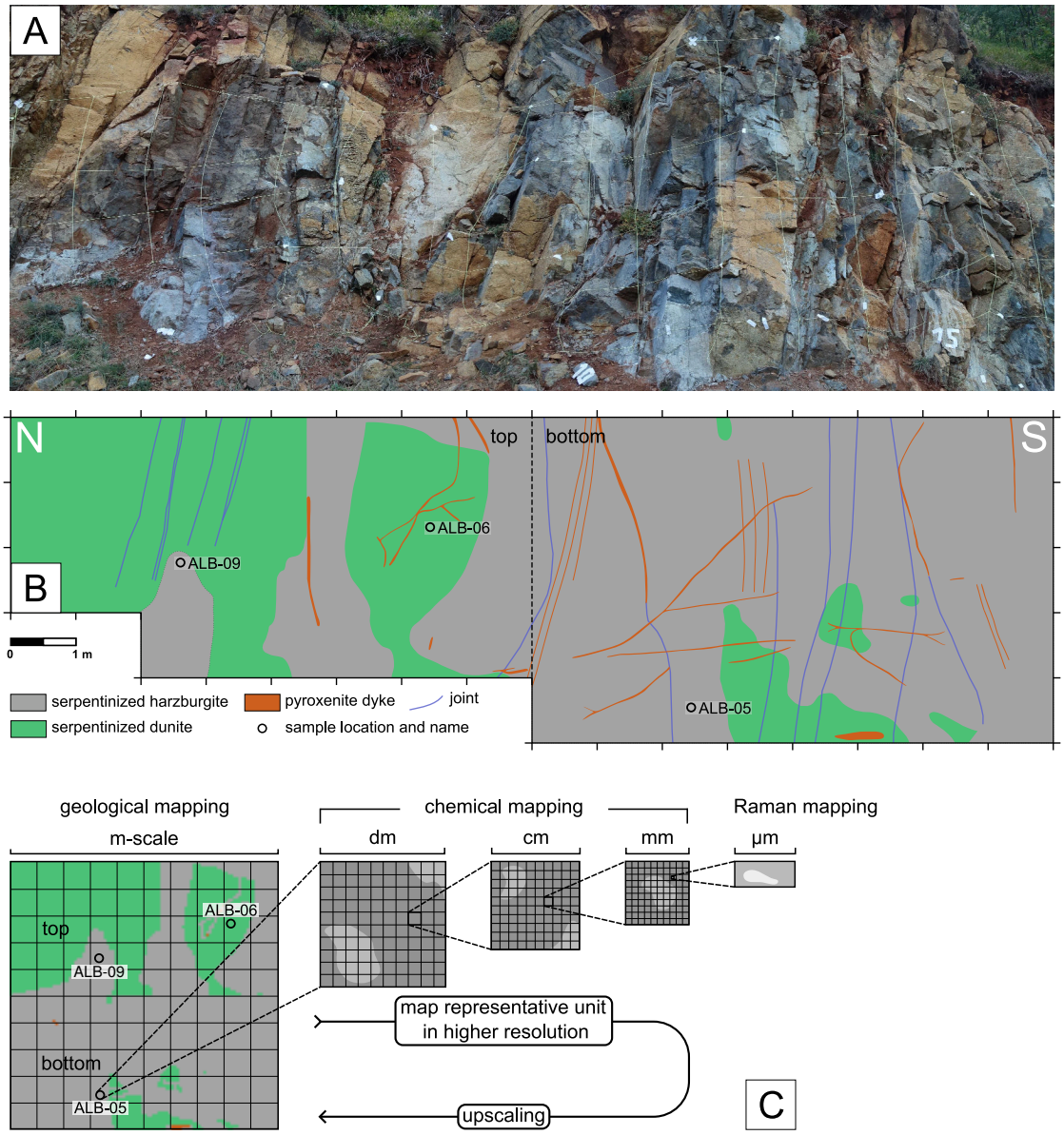

Figure 2.2: A, B: Photograph and geologic map of outcrop. C: Approach to generate a multiscale dataset. Starting with field observations at the tens of meters scale, we identified representative units and examined them in more detail at the next smaller scale until we reached the submillimeter scale. For the meter scale, we rearranged the outcrop by stacking the northern half on top of the southern half (the vertical dashed line in B indicates where we separated the map, see Section 2.3.2). From the decimeter down to the millimeter scale, we performed chemical mapping with increasing resolutions toward smaller scales to capture chemical heterogeneities. For the submillimeter scale, we performed a Raman mapping. At the submillimeter scale, we then upscaled our results by homogenization to finally reach the meter scale again (see Section 2.3.2).

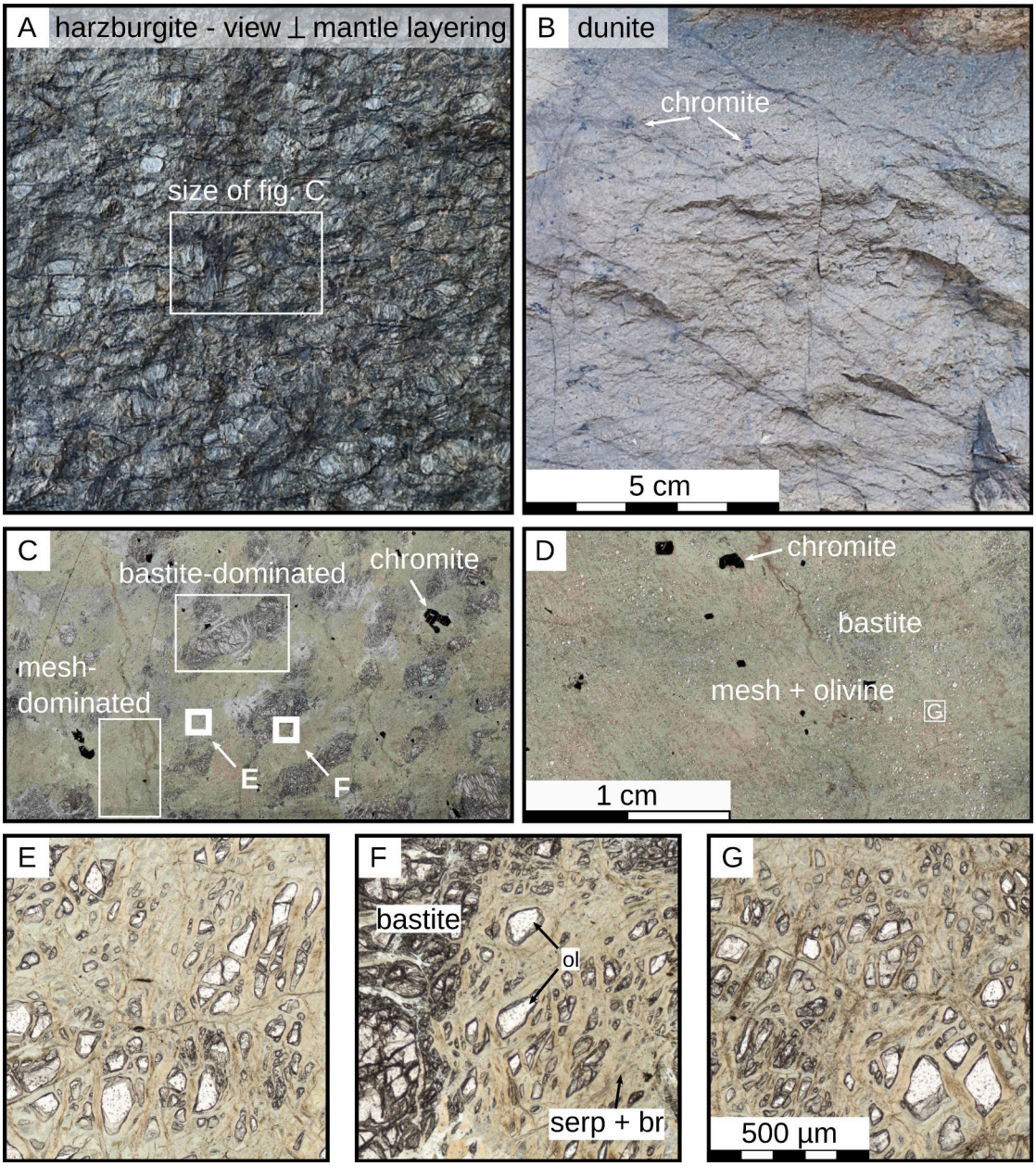

Figure 2.3: Representative field images and textures found in serpentinized harzburgites and dunites in the outcrop. A: Bastite-rich layer, resulting from high-T mantle layering. B: Serpentinized dunite with chromite pods. C, D: Thin sections of serpentinized harzburgite and dunite, respectively. E, G: Mesh texture in serpentinized harzburgite and dunite, respectively, with remnants of mantle olivine. F: Contact between bastite and mesh texture in serpentinized harzburgite.

Table 2.1: Mineral chemical data of mesh texture and main minerals found in our samples. Values are mean values of the single measurements given in the Supplementary Information. H = harzburgite, D = dunite with the number of measurements considered given in braces.

	Mesh (Srp.+Brc.)		**Serpentine**		**Olivine**		**Cpx**		**Opx**
	H (17)	*D (17)*	*H (18)*	*D (10)*	*H (17)*	*D (17)*	*H (15)*	*D (3)*	*H (18)*
SiO_2	32.11	30.28	38.42	38.06	41.00	40.74	54.14	54.03	56.92
MgO	41.23	41.39	35.22	39.23	49.98	49.86	17.84	17.38	34.52
FeO	8.03	8.83	6.18	4.95	8.65	8.85	1.78	1.40	5.64
CaO	0.10	0.10	0.47	0.09	0.03	0.06	24.29	25.39	0.74
Cr_2O_3			0.29			0.01	0.40	0.29	0.42
Al_2O_3			0.49				0.75	0.60	0.89
TiO_2			0.01	0.01			0.01	0.02	0.01
Na_2O	0.04	0.04	0.03	0.02	0.01		0.08	0.08	0.01
K_2O			0.02					0.01	
MnO	0.09	0.11	0.19	0.07	0.12	0.13	0.07	0.02	0.13
Total	*81.6*	*80.75*	*81.32*	*82.43*	*99.79*	*99.65*	*99.36*	*99.22*	*99.28*
atoms per unit formula, normalized to the number of oxygens given in the last row									
Si	2.18	2.10	2.53	2.47	1.00	1.00	1.98	1.98	1.97
Mg	4.17	4.28	3.46	3.79	1.82	1.82	0.97	0.95	1.78
Fe	0.46	0.51	0.34	0.27	0.18	0.18	0.05	0.04	0.16
Ca	0.01	0.01	0.03	0.01	0.00	0.00	0.95	1.00	0.03
Cr	0.00	0.00	0.01	0.00	0.00	0.00	0.01	0.00	0.01
Al	0.00	0.00	0.02	0.00	0.00	0.00	0.02	0.01	0.02
Ti	0.00	0.00	0.00	0.00	0.00	0.00	0.00	0.00	0.00
Na	0.00	0.00	0.00	0.00	0.00	0.00	0.00	0.00	0.00
K	0.00	0.00	0.00	0.00	0.00	0.00	0.00	0.00	0.00
Mn	0.01	0.01	0.01	0.00	0.00	0.00	0.00	0.00	0.00
O	7.00	7.00	7.00	7.00	4.00	4.00	6.00	6.00	6.00

Mineral chemical data

The information we could extract from mesh textures below the millimeter scale using optical microscopy is limited. To obtain further information about chemical heterogeneities and differences in the mineral chemistry between both lithologies, we performed chemical mappings and quantitative point analysis on individual minerals; Table 2.1 shows representative results. We provide a complete list of all microprobe data in the Supplementary Information. The characteristic of the mesh texture is the serpentine mineral with intergrown brucite (Figure 2.4). Our measurements show two main compositional differences between the two lithologies. Mesh textures in dunites contain about 2 wt.% less SiO_2 and are slightly FeO-richer than the textural equivalent mesh textures in harzburgites (Table 2.1). The second

main difference is the MgO content of serpentine. Dunite serpentine is MgO-richer (about 4 wt.%) and FeO-poorer (about 1.2 wt.%) than serpentine minerals in the harzburgite sample. The occurrence of clinopyroxene (Cpx)-bastites near some measurement points can explain the 0.47 wt.% CaO in harzburgite serpentines. The composition of remnant mantle olivines is similar in both lithologies, with FeO contents of about 8-9 wt.%, which is typical for mantle olivines. Orthopyroxenes (Opx) are abundant in harzburgite and are often heavily altered to talc and serpentine (bastites). The contact zone between bastites and mesh textures usually consists of pure serpentine due to the transition from relatively high SiO_2 in bastites to lower SiO_2 contents in the mesh texture. Clinopyroxenes (Cpx) are more common in harzburgites and only occur as small remnants in dunites. The number of Cpx measurements in dunites is limited to only 3; no significant compositional differences exist between Cpx in harzburgites and dunites.

2.4.2 Grain Coarsening During the Lizardite-Antigorite Transition

The minerals' chemical data show that the mesh texture has a significantly lower SiO_2 content than areas consisting of pure serpentine minerals, which are present in bastites (along with talc) or in veins cutting the mesh texture (Figure 2.4B). SiO_2 contents of less than $\sim$42 wt.% are insufficient to form pure serpentine and may result in the formation of fine-grained ($< 1\,\mu m$) intergrown brucite. Brucite also commonly occurs as single crystals in both lithologies and is visible in backscatter electron images due to its typically high iron content (Figure 2.4B). To confirm the presence of brucite within the mesh texture, we performed Raman spectroscopy mapping in the area depicted by the blue box in Figure 2.4B. The results of Raman mapping and two representative Raman spectra are shown in Figure 2.4A. The two circles on the map indicate the location of the two spectra, showing the representative peaks for lizardite and chrysotile (top spectrum), and brucite (bottom). Panels 1-3 in Figure 2.4A show the spatial distribution of the peak intensity for each of these three peaks.

Our Raman mapping results confirm that the mesh texture consists mainly of a mixture of lizardite and brucite along with minor amounts of chrysotile. Accordingly, varying contents of iron-rich brucite lead to the more subtle brightness differences in Figure 2.4B in the mesh texture, with brighter gray tones indicating higher brucite content. Figure 2.4B also shows veins of pure serpentine cutting through the mesh texture. These veins are common in serpentinites and are interpreted as the result of a multistage serpentinization process (e.g. Evans and Frost, 2021). In our samples, fine-grained magnetite is distributed in the mesh texture (Figure 2.4B). This texture is interpreted as the result of serpentinization below $\sim$200 °C, while magnetite concentrated in the center of serpentinization veins indicates

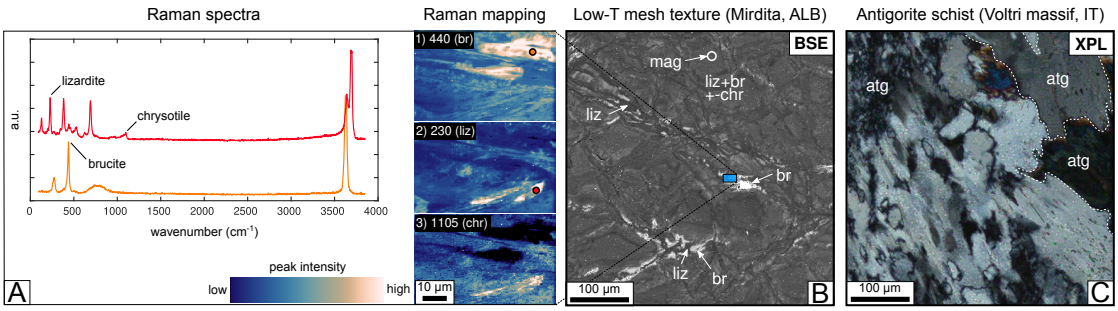

Figure 2.4: Results of (A) Raman mapping and (B-C) mineralogical and textural changes during the lizardite-antigorite transition. A: Two representative spectra whose position on the map is shown by the two circles in the respective color of the spectrum. Panels 1-3 show the peak intensities for brucite (440 cm^{-1}), lizardite (230 cm^{-1}), and chrysotile (1105 cm^{-1}), respectively. Chrysotile occurs only in minor amounts along with lizardite, typically filling up voids during the final stages of serpentinization (Evans, 2004). B: BSE image of a typical low-temperature mesh texture (sample ALB06-2) found in both harzburgites and dunites (Figure 2.3E, G). The blue box highlights the Raman mapping area. The single brucite flakes are typically iron-rich and preferably occur along veins of pure lizardite, commonly interpreted as the result of a multistage serpentinization process. C: Crossed polarizers photomicrograph of an antigorite schist (courtesy of E. Schwarzenbach) with typical interlocking texture, showing the effect of grain coarsening after the lizardite-antigorite transition. BSE = backscatter electron, XPL = crossed polarizers

serpentinization between 200 and 300 °C (Bach et al., 2006). During the onset of subduction and with increasing P-T conditions, lizardite and chrysotile transform into antigorite during the lizardite-antigorite transition, which Schwartz et al. (2013) report to occur at temperatures between 300 and 390 °C. Antigorite overgrows the previous fine-grained texture and forms an interlocking or interpenetrating texture of coarser antigorite blades. Figure 4C shows a crossed polarizer photomicrograph of an antigorite schist from the Voltri Massif in Liguria, Italy. This sample shows a complete lizardite-antigorite transition but has not yet experienced P-T conditions high enough for dehydration to begin. The textural difference between Figure 2.4B and C must be considered when studying the effects of chemical heterogeneities on dehydration dynamics because, at the time of dehydration onset at depth, the coarser antigorite texture will most likely have already replaced the low-temperature mesh texture. Antigorite growth is accompanied not only by textural but also by chemical changes. The growth of antigorite flakes leads to a local homogenization, overprinting the previous submicron- to micron-scaled chemical heterogeneities (see also Evans et al., 2013b). To account for the grain coarsening and the local homogenization, we added coarsening and local homogenization to our millimeter-scale chemical maps (Figure 2.5). Note that each

of the 10×10 pixels of the coarse map (Figure 2.5E-G) will be modeled following the P-T path (Figure 2.6) A second chemical effect during the lizardite-antigorite transition is attributed to the slightly higher SiO_2 content of antigorite compared to lizardite. Antigorite may form by one of the following two reactions. (1) liz/chr + SiO_2(aq) = atg or (2) liz/chr = atg + br (e.g. Evans, 2004). Reaction 1 occurs at least locally in an open system where an external fluid adds SiO_2, whereas reaction 2 occurs in a closed system with additional brucite growth during the transition. As we performed our thermodynamic calculations in a closed system, the results of our calculations show increasing brucite abundance during the lizardite-antigorite transition according to reaction 2 (Figure 2.6).

2.4.3 Chemical Heterogeneities on Millimeter Scales

We started our investigations with representative mapping on the millimeter scale. Figure 2.5 shows the distribution of SiO_2, MgO, and FeO, the main elements of interest for our thermodynamic calculations. The top row of Figure 2.5 (A-C) shows the original maps with size 1×1 mm with a step size of 2.5 µm, i.e., every pixel covers an area of 6.25 µm^2. Two distinct domains are visible in the SiO_2 and MgO distributions. The upper left part of the maps consists of serpentine, characterized by relatively high SiO_2 and low MgO contents. Toward the bottom right corner, the maps consist of mesh texture, visible by lower SiO_2 and higher FeO contents, attributed to brucite. Spots with the highest MgO contents are remnant mantle olivine grains. The bottom row of Figure 2.5 (E-G) shows the coarsened maps with 10×10 pixels, i.e., each pixel now covers an area of 10 000 mm^2. Each pixel in the coarsened maps reflects the average composition of 1600 pixels (40×40) in the original maps. The result is an overall more homogeneous material and a loss of information about the chemical variability, but the coarsened maps still preserve the primary information about the presence of a bastite-dominated part and a mesh texture-dominated part.

2.4.4 Metamorphic Evolution Along the P-T Path

The chemical heterogeneities in the coarse millimeter-scale chemical maps affect the spatial distribution of the initial stable mineral assemblage at the first point of the P-T path and the subsequent metamorphic evolution. Figure 2.6A shows the P-T path used in our calculations, with three boxes highlighting the main events during dehydration. First, the lizardite-antigorite transition at temperatures below ~350 °C; second, the onset of dehydration as defined by the first occurrence of a non-hydrous phase (Ol or Opx); and, third, the subsequent porosity evolution due to dehydration reactions.

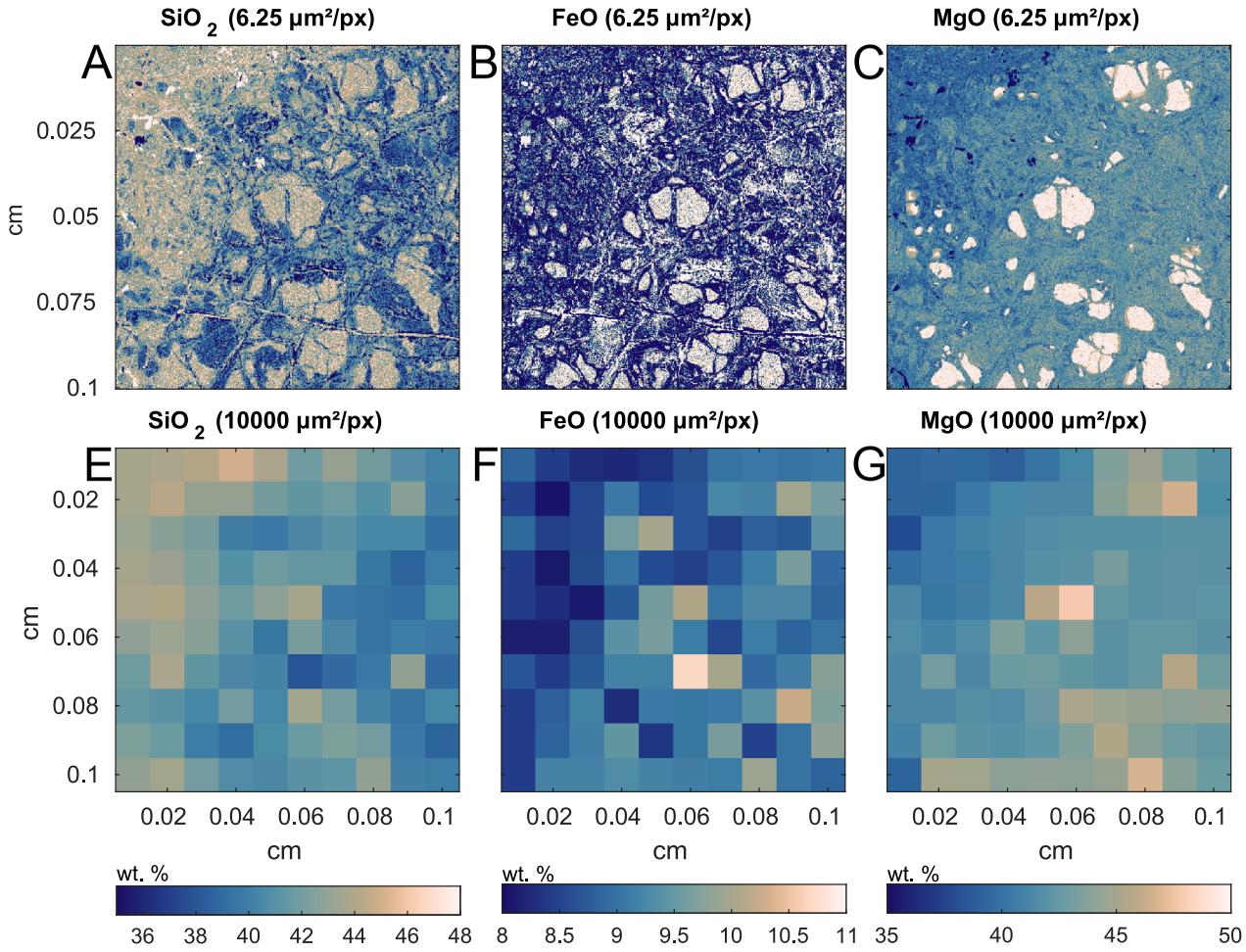

Figure 2.5: Element distribution mappings for an area of 1 mm^2 in sample ALB05 (serpentinized harzburgite). Top (A-C): Original maps with a step size of 2.5 µm (or 6.25 $µm^2$/pixel). Bottom (E-G): Coarsened maps with a step size of 100 µm, which is equivalent to 100 000 $µm^2$/pixel. The map covers a bastite-dominated part (top left) and a mesh texture-dominated part (lower right) with remnant mantle olivines (visible in the high Mg contents). The coarsened maps preserve the primary chemical heterogeneities. All plots in a row and column share the same y- and x-axis, respectively. Each component's original and coarse maps share the same color bar.

In Figure 2.6B and 6C, we show the evolution of the stable mineral assemblage for the coarse-mapped pixel with the lowest and highest temperature of dehydration onset, respectively. The bulk rock composition for the mineral assemblage shown in Figure 2.6B contains more SiO_2 than the bulk composition of Figure 2.6C, which stabilizes antigorite over lizardite and brucite at lower P-T conditions. Because we performed our thermodynamic calculations in a closed system, additional brucite formed in both Figure 2.6B and Figure 2.6C during the lizardite-antigorite transition. The dehydration onset, marked by the occurrence of the first metamorphic olivine, was at 498 °C in the SiO_2-richer composition (Figure 2.6B), compared to 520 °C in the SiO_2-poorer domain (Figure 2.6C). The higher brucite abundance in Figure 2.6C led to more antigorite consumption in the brucite-out reaction and, thus, a larger decrease in solid-bound H_2O. The SiO_2-richer domain retained more antigorite until the antigorite-out reaction started at ~580 °C. Therefore, this second dehydration reaction was more pronounced in the SiO_2-richer domain. Our results show that dehydration starts in parts of the rock with a relatively high SiO_2 and FeO content. However, these domains will retain more solid-bound H_2O in antigorite until the antigorite-out reaction, whereas SiO_2-poorer parts of the rock, with a later dehydration onset, release more H_2O with the brucite-out reaction.

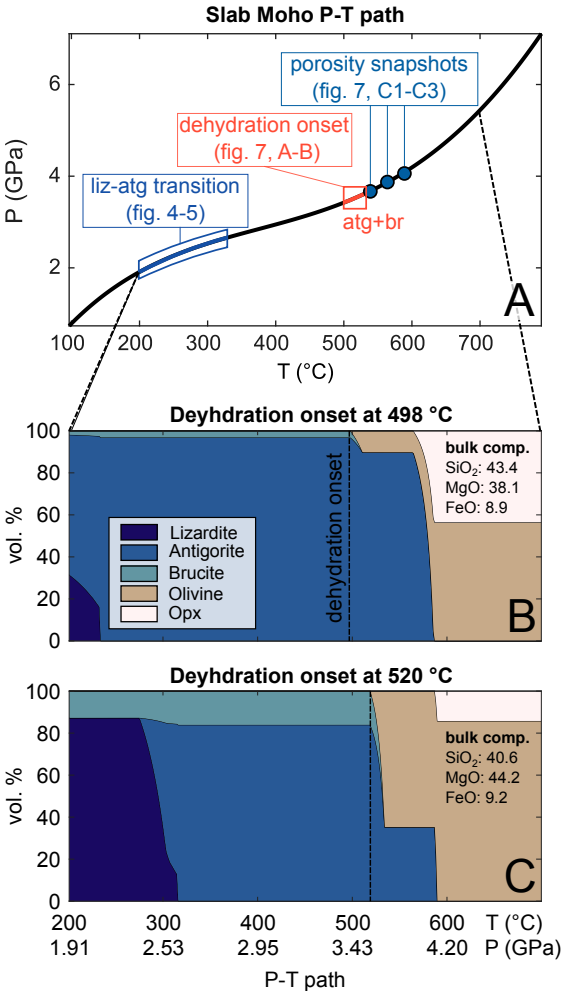

Figure 2.6: A: Slab Moho P-T path with a blue and red box highlighting the P-T range for the lizardite-antigorite transition and the onset of dehydration, respectively. Blue circles indicate the P-T conditions of the porosity snapshots in Figure 2.7C. B-C: Evolution of mineral assemblage along the P-T path for the domain in the coarse map with (A) the lowest and (B) the highest temperature for dehydration onset, as marked by the vertical dashed line. Bulk compositions are given in wt.%.

2.5 Discussion

2.5.1 Effects of Local Variations in FeO and SiO_2 Abundance

Compared to other rock types undergoing dehydration during subduction, serpentinites have a relatively simple chemistry, making them an ideal lithology for studying the effects of chemical variations on dehydration dynamics through single-component exploration. In the FMSH system, the local FeO and SiO_2 contents control both the temperature of the dehydration onset and the extent of each of the two subsequent dehydration reactions (and thus the porosity evolution) while dehydration proceeds. At low P-T conditions, SiO_2 abundance governs brucite stability and, thus, the extent of the brucite-out reaction (Figure 2.6B, C). A higher FeO abundance leads to Fe-richer compositions of ferromagnesian silicates, which react at lower temperatures than their Mg-richer equivalents. Thus, higher FeO contents extend the divariant field of the dehydration reaction toward lower temperatures.

We show the combined effects of SiO_2 and FeO abundance on the dehydration onset in Figure 2.7A, displaying the molar Si ratios of all pixels in the coarse millimeter-scale maps against molar Fe ratios. The colors filling the circles indicate the temperature for the dehydration onset as defined by the first occurrence of a metamorphic non-hydrous phase. The figure shows that the temperatures of dehydration onset decrease upon increasing molar Si/Fe ratios. The spatial distribution of the dehydration onset temperature (Figure 2.7B) and three snapshots of the spatial porosity distribution (Figure 2.7C) also show the correlation between porosity and the spatial distribution of SiO_2 and FeO in the coarse maps (Figure 2.5). The figure demonstrates that domains with a higher SiO_2 and FeO content form the first porosity (Figure 2.7B, C1), whereas the SiO_2-poorer regions produce more porosity during the brucite-out reaction (Figure 2.7C2). At P-T conditions above the terminal antigorite-out reaction (Figure 2.7C3), all pixels have similarly high values for the cumulative porosity of around 0.3.

The choice of solution models has a significant impact on the results. We used the solution models of Evans and Frost (2021), as the results of the calculations are in good agreement with experimental data (e.g. Padrón-Navarta et al., 2011, 2013). In addition, we performed the same calculations using the Holland et al. (2018) solution models and found that olivine is stable at temperatures as low as 200 °C, or already at the beginning of the P-T path. Brucite consumption by the brucite-out reaction starts at around 400 °C, thus about 100 °C lower than in the results presented in Figure 2.7. The reason for olivine stability at such low temperatures is the fayalite-rich olivine compositions with Mg-numbers of around 0.04 using the solution models of Holland et al. (2018). In comparison, the Evans and Frost (2021) solution models result in Mg-numbers for the first stable olivine of ∼0.7, which

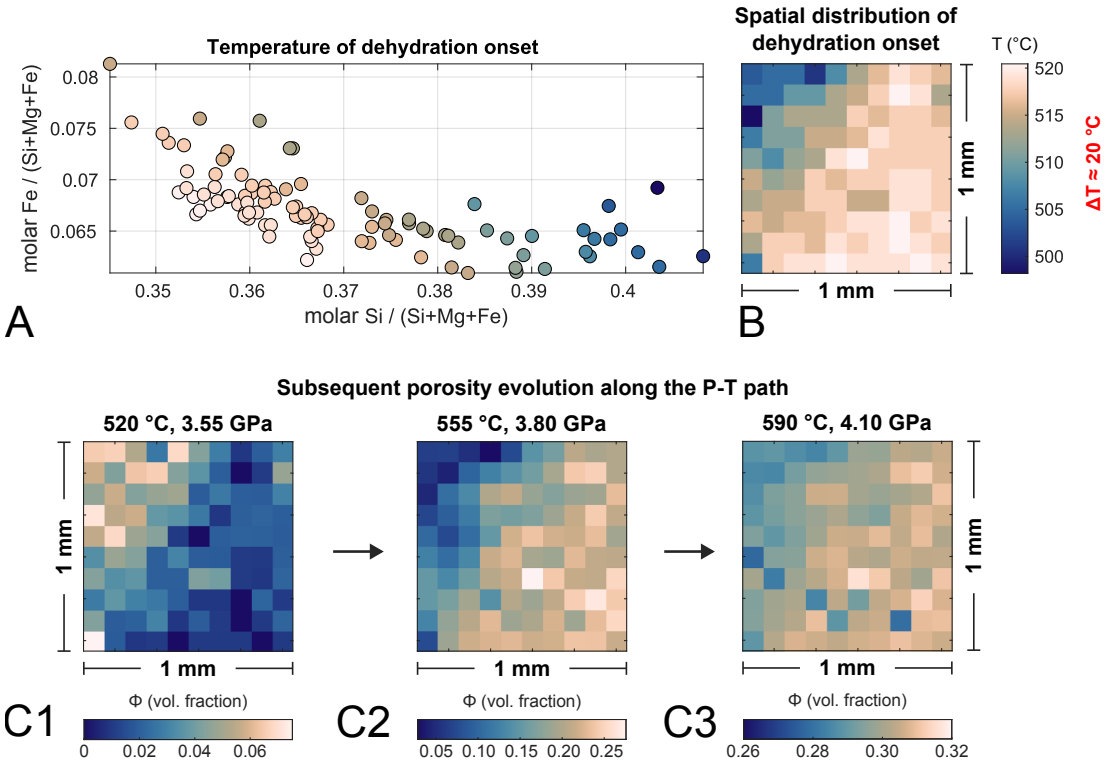

Figure 2.7: Effect of bulk Si and Fe variations (molar ratios) on the temperature of dehydration onset and subsequent porosity evolution. B: Spatial distribution of dehydration onset. The part of the map with the highest molar Si and Fe ratio dehydrates first (top left). C: Spatial porosity snapshots along the P-T path after (C1) the onset of dehydration until (C3) the end of the antigorite-out reaction. P-T conditions of snapshots C1-C3 are shown by blue circles on the P-T path in Figure 2.6A. Note that the range of ϕ varies in each color bar of C1-C3.

is in better agreement with our measured olivine compositions (Table 2.1). The appendix contains a figure that compares the results of both solution models.

2.5.2 Fluid Production Comparison Across All Scales

To investigate a potential scale dependence of the spatial-temporal fluid production during slab dehydration, we calculated the cumulative fluid release and the time-dependent fluid production over five orders of magnitude, from the millimeter scale to the outcrop scale (Figure 2.8). The top row of Figure 2.8 shows the evolution of cumulative fluid release for the domain with the earliest, the mean, and the latest dehydration onset on each scale (blue, red, and yellow graphs, respectively). The figure shows that the later the brucite-out

reaction starts, the more fluid it liberates, while the opposite trend occurs for the antigorite-out reaction. In the middle row of Figure 2.8, we show the fluid production between two steps along the P-T path. The graphs in the middle row represent the first derivative of the curves in the top row with respect to time. Every graph shows two distinct peaks corresponding to the two dehydration reactions. We calculated time intervals by calculating the vertical slab velocity and assuming lithostatic pressure to calculate the time between two points along the P-T path. For the depicted P-T path, we used a convergence rate of 17.9 km/Ma and a subduction angle of 42.4°, as given in Syracuse et al. (2010), and a mantle density of $3300\,\mathrm{kg\,m^{-3}}$. Under these assumptions, the 20 °C difference in the temperature for the dehydration onset corresponds to a time difference of about 0.4 Ma, or 4 km depth. The complete brucite-out reaction within the millimeter-scale domain would occur over 0.6 Ma (or 9 km), compared to about 0.7 Ma for the antigorite-out reaction. The fluid production evolution demonstrates that similar peaks of fluid production occur over five orders of magnitude of length scales. The peak distribution shows that fluid production during subduction occurs in scale-independent pulses, which vary in time and space due to the intrinsic chemical heterogeneities of the slab. The results of our fluid release calculation show that a coherently similar pattern for the production emerges across all scales due to the highly similar patterns in SiO_2 and FeO abundance on every scale. On the millimeter to centimeter scale, these differences in SiO_2 and FeO availability emerge as mesh texture and bastites, i.e., textural differences. On the meter or even kilometer scale, these chemical differences manifest as different lithologies such as dunite, harzburgite, or pyroxenite and their intrinsic chemical heterogeneities (e.g. Bortolotti et al., 1996; Niu, 2004; Peters et al., 2020).

2.5.3 Effects of Extension to FMSHO and FMASH Systems

We performed all our thermodynamic calculations in the FMSH system for simplicity reasons as it allows exploring the effects of the principle dehydration reactions systematically. However, serpentinization is often accompanied by the formation of various amounts of magnetite, which may occur localized along veins or more disseminated in other cases (Bach et al., 2006; Schwarzenbach, 2016; Klein et al., 2014; Evans and Frost, 2021). This suggests that serpentinites are to some extent oxidized, although it is difficult to accurately estimate both the extent of oxidation and the spatial extent of variability especially when departing from the thin section scale (e.g. Evans and Frost, 2021). Extending the chemical system to FMSHO is done for a very oxidized case of approximately 2/3 of the total Fe is ferric (i.e., Evans and Frost (2021)). For our dm-scale, which already considers a larger degree of chemical

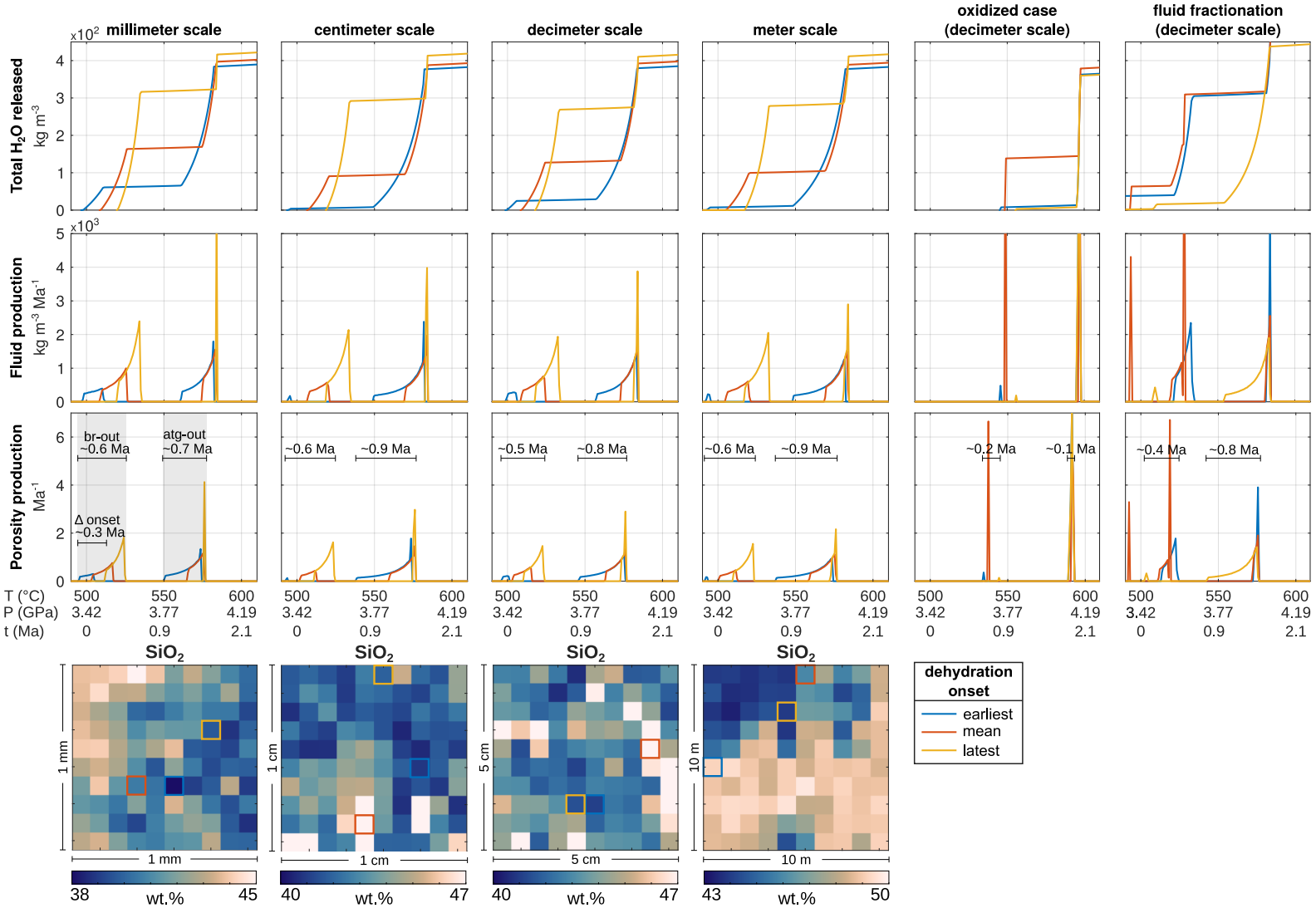

Figure 2.8: Comparison of fluid production evolution along the P-T path across all scales considered in this study, focusing on domains with the lowest, mean, and highest temperatures of dehydration onset in case of a reduced bulk composition without fluid fractionation. Time (t) is calculated for the Antilles subduction zone, assuming lithostatic pressure, a subduction angle of 42.4°, mantle density of 3300 kg m^{-3}, and a subduction rate of 17.9 km/Ma (Syracuse et al., 2010). The effects of an oxidized bulk composition and complete fluid fractionation after each P-T step are shown in columns four and five, respectively. Top row: total H_2O released; center and bottom row: fluid and porosity production per Ma, respectively; lowermost row: heterogeneous SiO_2 distribution at each scale. Colored boxes highlight the domains whose evolution is depicted in the plots above. Note that all chemical maps have a range of 7 wt.% with different minimum and maximum values.

homogenization, such a highly oxidized system leads to an onset of dehydration at a higher temperature, at about 550 °C for the earliest start (Figure 2.8). The related divariant field is very narrow as only about 4.4 vol.% of rather Mg-rich brucite formed because a significant portion Fe is bound in magnetite (approx. 4.6 vol. %), also causing lower Fe/Mg ratios in silicates (see also Trommsdorff and Evans, 1972; Evans and Frost, 2021). A second pulse of fluid release occurs at about 595 °C which reflects the terminal antigorite out reaction, which again is characterized by a narrow divariant field as the antigorite composition is close to the Mg-endmember (Figure 2.8). These findings indicate that for highly oxidized cases the fluid production occurs at minuscule T intervals and thus short pulses (approx. 0.2 Ma for the brucite-out reaction), with almost the entire fluid release being connected to the terminal antigorite out reaction. Consequently, higher oxygen fugacities increase temperatures for the dehydration onset by decreasing the temperature intervals of the divalent fluid-releasing reactions.

Extending the chemical system to an FMASH creates new divariant fields by stabilizing chlorite and, at high P-T conditions, garnet (Padrón-Navarta et al., 2013; Evans and Frost, 2021). Chlorite is an important carrier of solid-bound water to sub-arc depths and is the last hydrous phase to break down during prograde metamorphism. Considering chlorite formation in our calculations would lower the magnitude of the first two peaks for porosity production and result in a third peak at about 770 °C, after the terminus of the antigorite-out reaction. Including Al_2O_3 allows for the incorporation of Al in antigorite, which widens the divariant field of the antigorite-out reaction (Padrón-Navarta et al., 2013). Thus, Al in antigorite has a similar effect to Fe-Mg substitution, which the FMSH system can reflect. Padrón-Navarta et al. (2013) note that the divariant fields in the FMASH system widen compared to in the FMSH system, which would result in less pronounced peaks in our porosity evolution curves (Figure 2.8). As Evans and Frost (2021) note, highly oxidized serpentinites are probably rather rare, the spatial distribution of the different degrees of oxidation of serpentinites is in principle unknown, but certainly heterogeneous. The low aluminum contents in our samples suggest that aluminum is also heterogeneously distributed within the slab mantle (e.g. Niu, 2004; Peters et al., 2020), contributing to the chemical heterogeneity of the mantle. Consequently, the third peak in porosity production will not occur in all parts of the slab. Al-bearing parts will retain water to depths at which Al-free parts have undergone complete dehydration, whereas more oxidized parts will be characterized by shorter and more pronounced pulses of fluid release.

2.5.4 Porosity Formation and Percolation Threshold

Our porosity calculation is based on densification of the solid phase and neglects deformation effects, most importantly compaction. The calculations of porosity production (Figure 2.8, bottom row) have been conducted similarly to those of fluid production (Figure 2.8, middle row). As the dehydration reactions are causing the densification of the bulk solid, porosity formation and fluid production display the same pulse-like pattern during the simulated subduction. The liberated fluid will fill the dynamically forming porosity and eventually flow along fluid pressure gradients within the porous network when the newly formed porosity reaches the percolation threshold. Thermodynamic and petrophysical modeling (Plümper et al., 2017) have shown that vein-like porosity structures are formed even at the onset of serpentinite dehydration, and vein networks related to slab mantle dehydration are reported from several localities (Groppo and Compagnoni, 2007; Jabaloy-Sanchez et al., 2022; López Sánchez-Vizcaíno et al., 2009; Scambelluri et al., 1991; Herms et al., 2012; John et al., 2012; Spandler et al., 2011). For such a vein-like porosity geometry, the percolation threshold is reached even for porosities below 0.1 vol.%, or 0.001 in volume fractions (Bloch et al., 2018). Accordingly, considering the non-spherical porosity shape in our domain (Figure 2.7C), fluid flow within the porous network will likely start soon after the dehydration onset, and compaction will lead to a dynamic closing of the compliant porosity. Such a compaction-related deformation process would be in agreement with a fluid-channeling process such as porosity waves (Connolly and Podladchikov, 2015; Yarushina and Podladchikov, 2015; Yarushina et al., 2022), which would accelerate the spatial-temporal pulse-like behavior of the slab fluid release (Tian et al., 2018; Piccoli et al., 2021; Wilson et al., 2017). Therefore, the peaks in our porosity- and fluid-production calculations suggest that chemical heterogeneities at all scales lead to fluid pulses through high transient porosities localized in both space and time. The vein-like shape of the porosity and the high porosity production rates allow for efficient fluid transport within the porous network throughout slab dehydration.

2.5.5 Effects of H_2O Fractionation

We performed our thermodynamic calculations without removing H_2O in the liberated fluid phase from the bulk composition. However, the elongated porosity shape shown in Figure 2.7C likely facilitates fluid flow even at low porosities, effectively removing part of the H_2O in the liberated fluid phase from the local bulk composition. To evaluate the effects of fluid fractionation, we repeated the thermodynamic calculations for the dm-scale with complete H_2O fractionation (Figure 2.8). The comparison shows the system's scale-independent behavior with two main peaks for the brucite-out and antigorite-out reaction. With frac-

tionation, the peak amplitudes increase, and the peaks narrow, corresponding to a shorter reaction timespan. The duration for the brucite-out decreases from approximately 0.5 Ma without fractionation to approximately 0.4 Ma with fractionation. H_2O fractionation also affects the metamorphic evolution and significantly expands the P-T window for the onset of dehydration. SiO_2-richer domains form olivine at temperatures as low as 250 °C. In contrast, the highest temperature for the onset dehydration occurs in a relatively SiO_2-poor domain at 520 °C, i.e., at conditions similar to the non-fractionated case.

2.6 Conclusions and Implications for Slab Fluid Release

Self-similar silica and iron distribution patterns occur in serpentinites derived from harzburgitic or dunitic precursors over at least five spatial orders of magnitude. These intrinsic chemical heterogeneities manifest as differences between mesh texture and bastites on the millimeter and centimeter scale and as lithological contrasts between dunites, harzburgites, and pyroxenites on the outcrop and crustal scale. Our results show that fluid production within the slab occurs by spatially localized pulses rather than due to continuous pervasive dehydration fluid flow. Fluid pulses occur on the order of several 0.5-0.9 Ma for reduced and as short as 0.1 Ma for oxidized serpentinite bulk compositions (see colored lines in the grey areas of Figure 2.8) and fluid production peaks when P-T conditions approach the stability limit of hydrous phases. Fluid pulse timespans are also significantly shortened by 0.2-0.4 Ma in the case of continuous fluid fractionation (Figures 2.8 and 2.9), resembling high fluid fluxes, for example by hydrofracturing, once the percolation threshold is reached. Our finding on fluid pulses aligns with other studies revealing that fluid release from subduction slab is episodic at various scales with durations on the order of thousands of years to months, using chronometric approaches such as bulk- or garnet-diffusion modeling of dehydrating rocks or related vein-network systems (John et al., 2012; Yokoyama et al., 2002; Dragovic et al., 2015; Taetz et al., 2018; Yoshida et al., 2023).

The porosity structure evolves during subduction by feeding new fluid-filled porosity structures from different domains of their fluid source regions (Figure 2.9). The scale-independent chemical heterogeneities in turn cause variations in the chemical composition of the released fluid which is in thermodynamic equilibrium with the composition of the host rock (Huber et al., 2022). Reactive fluid flow in such transient high-porosity structures (e.g. John et al., 2012; Piccoli et al., 2021; Tian et al., 2018; Taetz et al., 2018) can locally lower the temperature for dehydration reactions by changing the local bulk composition in the rock (e.g. Huber et al., 2022). Zooming out from the millimeter to the outcrop scale, fluid production occurs always heterogeneously distributed (Figure 2.9). This likely holds

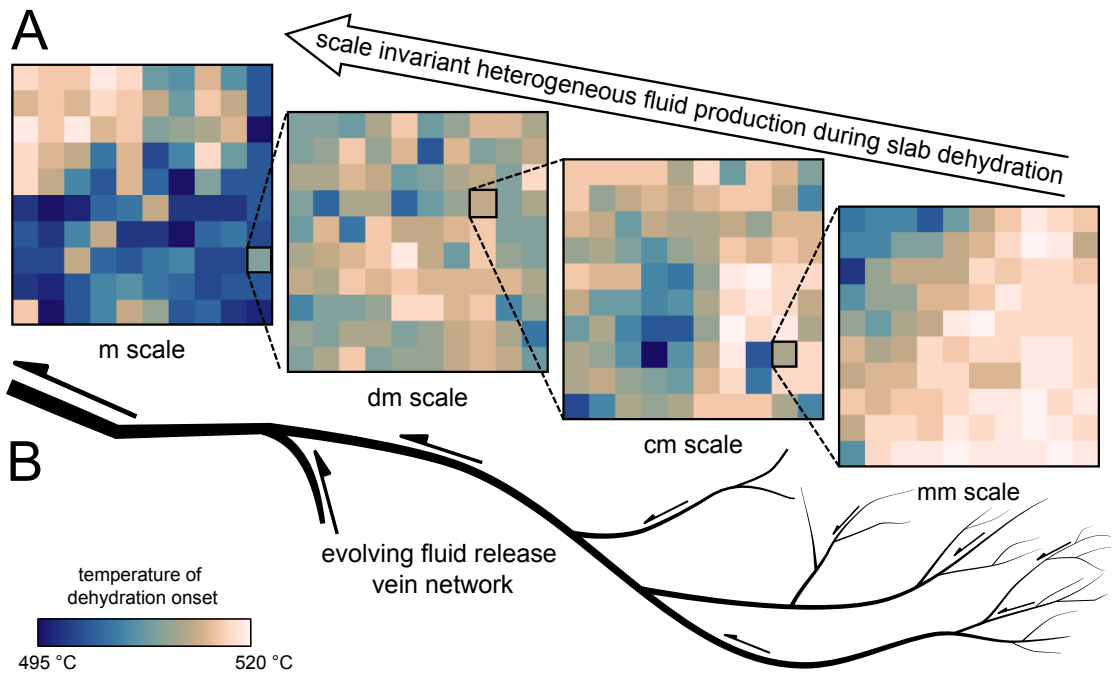

Figure 2.9: Similar chemical heterogeneities from the millimeter up to the meter scale and beyond lead to scale-invariant fluid production. A: Temperature of dehydration onset on all scales investigated in this study. Note that the plots do share the same color bar. The appendix contains the same diagrams for all other scales for comparison. B: Conceptual sketch of a dehydration vein network where dehydration starts at the millimeter scale and channelizes when going to larger scales. Arrows indicate the direction of fluid flow. Interpretation according to John et al. (2012); Plümper et al. (2017); John et al. (2008).

true for the entire slab mantle, considering the regional distribution of the lithologies within the ophiolite (Bortolotti et al., 2005). Thus, a heterogeneous, spatio-temporal distribution of fluid production should occur at every scale, both along the strike and along the dip of the subducting plate.

Data availability

The Supplementary Information, the mineral chemical data, the Raman mapping data, the multiscale dataset, and the MATLAB codes used to compile it are available on Zenodo (doi: 10.5281/zenodo.10368961).

Acknowledgements

This research was funded by the Deutsche Forschungsgemeinschaft (DFG) through grant CRC 1114 Scaling Cascades in Complex Systems, Project Number 235221301, Project C09 and PI 534/3-1. The authors thank M. Scambelluri and E. Schwarzenbach for helpful discussions and for providing us with an antigorite schist sample. The authors would also like to thank the two anonymous reviewers for their constructive criticism and Laurence Coogan for the good editorial handling, which together improved the quality of the study.

References

J. J. Ague, S. Tassara, M. E. Holycross, J.-L. Li, E. Cottrell, E. M. Schwarzenbach, C. Fassoulas, and T. John. Slab-derived devolatilization fluids oxidized by subducted metasedimentary rocks. *Nat. Geosci.*, 15(4):320–326, 2022. ISSN 1752-0908. doi:10.1038/s41561-022-00904-7.

W. Bach, H. Paulick, C. J. Garrido, B. Ildefonse, W. P. Meurer, and S. E. Humphris. Unraveling the sequence of serpentinization reactions: Petrography, mineral chemistry, and petrophysics of serpentinites from MAR 15°N (ODP Leg 209, Site 1274). *Geophysical Research Letters*, 33(13): 2006GL025681, 2006. ISSN 0094-8276, 1944-8007. doi:10.1029/2006GL025681.

A. Beinlich, T. John, J. C. Vrijmoed, M. Tominaga, T. Magna, and Y. Y. Podladchikov. Instantaneous rock transformations in the deep crust driven by reactive fluid flow. *Nat. Geosci.*, 13(4):307–311, 2020. ISSN 1752-0908. doi:10.1038/s41561-020-0554-9.

W. Bloch, T. John, J. Kummerow, P. Salazar, O. S. Krüger, and S. A. Shapiro. Watching Dehydration: Seismic Indication for Transient Fluid Pathways in the Oceanic Mantle of the Subducting Nazca Slab. *Geochem. Geophys. Geosystems*, 19(9):3189–3207, 2018. ISSN 1525-2027. doi:10.1029/2018GC007703.

V. Bortolotti, A. Korda, M. Marroni, L. Pandolfi, M. Faruk, P. Gianfranco, and E. Saccani. Geology and petrology of ophiolitic sequences in Mirdita region (northern Albania). 1996.

V. Bortolotti, M. Marroni, L. Pandolfi, and G. Principi. Mesozoic to Tertiary tectonic history of the Mirdita ophiolites, northern Albania. *Isl Arc*, 14(4):471–493, 2005. ISSN 1038-4871, 1440-1738. doi:10.1111/j.1440-1738.2005.00479.x.

A. V. Brovarone, C. J. Butch, A. Ciappa, H. J. Cleaves, A. Elmaleh, M. Faccenda, M. Feineman, J. Hermann, F. Nestola, A. Cordone, and D. Giovannelli. Let there be water: How Hydration/Dehydration reactions accompany key Earth and life processes. *Am. Mineral.*, 105(8):1152–1160, 2020. ISSN 1945-3027. doi:10.2138/am-2020-7380.

S. Chen, R. C. Hin, T. John, R. Brooker, B. Bryan, Y. Niu, and T. Elliott. Molybdenum systematics of subducted crust record reactive fluid flow from underlying slab serpentine dehydration. *Nat. Commun.*, 10(1):4773, 2019. ISSN 2041-1723. doi:10.1038/s41467-019-12696-3.

R. Compagnoni, R. Cossio, and M. Mellini. Raman anisotropy in serpentine minerals, with a *caveat*

on identification. *J Raman Spectroscopy*, 52(7):1334–1345, 2021. ISSN 0377-0486, 1097-4555. doi:10.1002/jrs.6128.

J. A. D. Connolly and Y. Y. Podladchikov. An analytical solution for solitary porosity waves: Dynamic permeability and fluidization of nonlinear viscous and viscoplastic rock. *Geofluids*, 15(1-2):269–292, 2015. ISSN 14688115. doi:10.1111/gfl.12110.

Y. Dilek, H. Furnes, and M. Shallo. Suprasubduction zone ophiolite formation along the periphery of Mesozoic Gondwana. *Gondwana Research*, 11(4):453–475, 2007. ISSN 1342937X. doi:10.1016/j.gr.2007.01.005.

Y. Dilek, H. Furnes, and M. Shallo. Geochemistry of the Jurassic Mirdita Ophiolite (Albania) and the MORB to SSZ evolution of a marginal basin oceanic crust. *Lithos*, 100(1-4):174–209, 2008. ISSN 00244937. doi:10.1016/j.lithos.2007.06.026.

B. Dragovic, E. F. Baxter, and M. J. Caddick. Pulsed dehydration and garnet growth during subduction revealed by zoned garnet geochronology and thermodynamic modeling, Sifnos, Greece. *Earth and Planetary Science Letters*, 413:111–122, 2015. ISSN 0012-821X. doi:10.1016/j.epsl.2014.12.024.

T. Elliott, T. Plank, A. Zindler, W. White, and B. Bourdon. Element transport from slab to volcanic front at the Mariana arc. *J. Geophys. Res. Solid Earth*, 102(B7):14991–15019, 1997. ISSN 2156-2202. doi:10.1029/97JB00788.

B. W. Evans. The Serpentinite Multisystem Revisited: Chrysotile Is Metastable. *International Geology Review*, 46(6):479–506, 2004. ISSN 0020-6814, 1938-2839. doi:10.2747/0020-6814.46.6.479.

B. W. Evans, K. Hattori, and A. Baronnet. Serpentinite: What, Why, Where? *Elements*, 9(2): 99–106, 2013a. ISSN 1811-5209, 1811-5217. doi:10.2113/gselements.9.2.99.

K. A. Evans and B. R. Frost. Deserpentinization in Subduction Zones as a Source of Oxidation in Arcs: A Reality Check. *J. Petrol.*, 62(3):egab016, 2021. ISSN 0022-3530, 1460-2415. doi:10.1093/petrology/egab016.

K. A. Evans, R. Powell, and B. R. Frost. Using equilibrium thermodynamics in the study of metasomatic alteration, illustrated by an application to serpentinites. *Lithos*, 168–169:67–84, 2013b. ISSN 0024-4937. doi:10.1016/j.lithos.2013.01.016.

T. P. Ferrand, N. Hilairet, S. Incel, D. Deldicque, L. Labrousse, J. Gasc, J. Renner, Y. Wang, H. W. Green II, and A. Schubnel. Dehydration-driven stress transfer triggers intermediate-depth earthquakes. *Nat. Commun.*, 8(1):15247, 2017. ISSN 2041-1723. doi:10.1038/ncomms15247.

C. Groppo and R. Compagnoni. Metamorphic veins from the serpentinites of the Piemonte Zone, western Alps, Italy: A review. *Period. Mineral.*, (76.2-3):127–153, 2007. ISSN 0369-8963. doi:10.2451/2007PM0021.

C. Groppo, C. Rinaudo, S. Cairo, D. Gastaldi, and R. Compagnoni. Micro-Raman spectroscopy for a quick and reliable identification of serpentine minerals from ultramafics. *ejm*, 18(3):319–329, 2006. ISSN 0935-1221. doi:10.1127/0935-1221/2006/0018-0319.

B. R. Hacker, S. M. Peacock, G. A. Abers, and S. D. Holloway. Subduction factory 2. Are intermediate-depth earthquakes in subducting slabs linked to metamorphic dehydration reactions? *J. Geophys.*

Res. Solid Earth, 108(B1), 2003. ISSN 2156-2202. doi:10.1029/2001JB001129.

P. Herms, T. John, R. J. Bakker, and V. Schenk. Evidence for channelized external fluid flow and element transfer in subducting slabs (Raspas Complex, Ecuador). *Chemical Geology*, 310–311: 79–96, 2012. ISSN 0009-2541. doi:10.1016/j.chemgeo.2012.03.023.

G. Hirth and S. Guillot. Rheology and Tectonic Significance of Serpentinite. *Elements*, 9(2):107–113, 2013. ISSN 1811-5209. doi:10.2113/gselements.9.2.107.

T. J. B. Holland and R. Powell. An internally consistent thermodynamic data set for phases of petrological interest: An internally consistent thermodynamic data set. *J. Metamorph. Geol.*, 16 (3):309–343, 2004. ISSN 02634929, 15251314. doi:10.1111/j.1525-1314.1998.00140.x.

T. J. B. Holland and R. Powell. An improved and extended internally consistent thermodynamic dataset for phases of petrological interest, involving a new equation of state for solids. *J. Metamorph. Geol.*, 29(3):333–383, 2011. ISSN 1525-1314. doi:10.1111/j.1525-1314.2010.00923.x.

T. J. B. Holland, E. C. R. Green, and R. Powell. Melting of Peridotites through to Granites: A Simple Thermodynamic Model in the System KNCFMASHTOCr. *Journal of Petrology*, 59(5):881–900, 2018. ISSN 0022-3530. doi:10.1093/petrology/egy048.

K. Huber, J. C. Vrijmoed, and T. John. Formation of Olivine Veins by Reactive Fluid Flow in a Dehydrating Serpentinite. *Geochem Geophys Geosyst*, 23(6):e2021GC010267, 2022. ISSN 1525-2027, 1525-2027. doi:10.1029/2021GC010267.

A. Jabaloy-Sanchez, V. L. Sanchez-Vizcaino, J. A. Padron-Navarta, K. Hidas, M. T. Gomez-Pugnaire, and C. J. Garrido. Olivine-rich veins in high-pressure serpentinites: A far-field paleo-stress snapshot during subduction. *J. Struct. Geol.*, 163:104721, 2022. ISSN 0191-8141. doi:10.1016/j.jsg.2022.104721.

T. John, R. Klemd, J. Gao, and C.-D. Garbe-Schönberg. Trace-element mobilization in slabs due to non steady-state fluid–rock interaction: Constraints from an eclogite-facies transport vein in blueschist (Tianshan, China). *Lithos*, 103(1):1–24, 2008. ISSN 0024-4937. doi:10.1016/j.lithos.2007.09.005.

T. John, N. Gussone, Y. Y. Podladchikov, G. E. Bebout, R. Dohmen, R. Halama, R. Klemd, T. Magna, and H.-M. Seitz. Volcanic arcs fed by rapid pulsed fluid flow through subducting slabs. *Nat. Geosci.*, 5(7):489–492, 2012. ISSN 1752-0908. doi:10.1038/ngeo1482.

E. D. Kempf, J. Hermann, E. Reusser, L. P. Baumgartner, and P. Lanari. The role of the antigorite + brucite to olivine reaction in subducted serpentinites (Zermatt, Switzerland). *Swiss J. Geosci.*, 113(1):16, 2020. ISSN 1661-8726, 1661-8734. doi:10.1186/s00015-020-00368-0.

F. Klein, W. Bach, S. E. Humphris, W.-A. Kahl, N. Jons, B. Moskowitz, and T. S. Berquo. Magnetite in seafloor serpentinite–Some like it hot. *Geology*, 42(2):135–138, 2014. ISSN 0091-7613, 1943-2682. doi:10.1130/G35068.1.

V. López Sánchez-Vizcaíno, M. T. Gómez-Pugnaire, C. J. Garrido, J. A. Padrón-Navarta, and M. Mellini. Breakdown mechanisms of titanclinohumite in antigorite serpentinite (Cerro del Almirez massif, S. Spain): A petrological and TEM study. *Lithos*, 107(3-4):216–226, 2009. ISSN 00244937. doi:10.1016/j.lithos.2008.10.008.

B. Malvoisin, Y. Y. Podladchikov, and J. C. Vrijmoed. Coupling changes in densities and porosity to fluid pressure variations in reactive porous fluid flow: Local thermodynamic equilibrium. *Geochem. Geophys. Geosyst.*, 16(12):4362–4387, 2015. ISSN 1525-2027, 1525-2027. doi:10.1002/2015GC006019.

S. A. Miller, W. van der Zee, D. L. Olgaard, and J. A. D. Connolly. A fluid-pressure feedback model of dehydration reactions: Experiments, modelling, and application to subduction zones. *Tectonophysics*, 370(1):241–251, 2003. ISSN 0040-1951. doi:10.1016/S0040-1951(03)00189-6.

T. Morishita, Y. Dilek, M. Shallo, A. Tamura, and S. Arai. Insight into the uppermost mantle section of a maturing arc: The Eastern Mirdita ophiolite, Albania. *Lithos*, 124(3-4):215–226, 2011. ISSN 00244937. doi:10.1016/j.lithos.2010.10.003.

T. Nakagawa, T. Nakakuki, and H. Iwamori. Water circulation and global mantle dynamics: Insight from numerical modeling. *Geochem. Geophys. Geosystems*, 16(5):1449–1464, 2015. ISSN 1525-2027. doi:10.1002/2014GC005701.

A. Nicolas, F. Boudier, and A. Meshi. Slow spreading accretion and mantle denudation in the Mirdita ophiolite (Albania). *J. Geophys. Res.*, 104(B7):15155–15167, 1999. ISSN 01480227. doi:10.1029/1999JB900126.

Y. Niu. Bulk-rock Major and Trace Element Compositions of Abyssal Peridotites: Implications for Mantle Melting, Melt Extraction and Post-melting Processes Beneath Mid-Ocean Ridges. *J. Petrol.*, 45(12):2423–2458, 2004. ISSN 1460-2415, 0022-3530. doi:10.1093/petrology/egh068.

J. A. Padrón-Navarta, A. Tommasi, C. J. Garrido, V. L. Sánchez-Vizcaíno, M. T. Gómez-Pugnaire, A. Jabaloy, and A. Vauchez. Fluid transfer into the wedge controlled by high-pressure hydrofracturing in the cold top-slab mantle. *Earth Planet. Sci. Lett.*, 297(1):271–286, 2010. ISSN 0012-821X. doi:10.1016/j.epsl.2010.06.029.

J. A. Padrón-Navarta, V. López Sánchez-Vizcaíno, C. J. Garrido, and M. T. Gómez-Pugnaire. Metamorphic Record of High-pressure Dehydration of Antigorite Serpentinite to Chlorite Harzburgite in a Subduction Setting (Cerro del Almirez, Nevado–Filábride Complex, Southern Spain). *Journal of Petrology*, 52(10):2047–2078, 2011. ISSN 0022-3530. doi:10.1093/petrology/egr039.

J. A. Padrón-Navarta, V. L. Sánchez-Vizcaíno, J. Hermann, J. A. Connolly, C. J. Garrido, M. T. Gómez-Pugnaire, and C. Marchesi. Tschermak's substitution in antigorite and consequences for phase relations and water liberation in high-grade serpentinites. *Lithos*, 178:186–196, 2013. ISSN 00244937. doi:10.1016/j.lithos.2013.02.001.

D. Peters, T. Pettke, T. John, and M. Scambelluri. The role of brucite in water and element cycling during serpentinite subduction – Insights from Erro Tobbio (Liguria, Italy). *Lithos*, 360–361: 105431, 2020. ISSN 00244937. doi:10.1016/j.lithos.2020.105431.

F. Piccoli, J. J. Ague, X. Chu, M. Tian, and A. Vitale Brovarone. Field-Based Evidence for Intra-Slab High-Permeability Channel Formation at Eclogite-Facies Conditions During Subduction. *Geochem. Geophys. Geosystems*, 22(3):e2020GC009520, 2021. ISSN 1525-2027. doi:10.1029/2020GC009520.

O. Plümper, T. John, Y. Y. Podladchikov, J. C. Vrijmoed, and M. Scambelluri. Fluid escape from

subduction zones controlled by channel-forming reactive porosity. *Nature Geosci*, 10(2):150–156, 2017. ISSN 1752-0908. doi:10.1038/ngeo2865.

B. Reynard. Serpentine in active subduction zones. *Lithos*, 178:171–185, 2013. ISSN 0024-4937. doi:10.1016/j.lithos.2012.10.012.

L. Rüpke, J. Phipps Morgan, and J. Eaby Dixon. Implications of Subduction Rehydration for Earth's Deep Water Cycle. In S. D. Jacobsen and S. Van Der Lee, editors, *Geophysical Monograph Series*, pages 263–276. American Geophysical Union, Washington, D. C., 2006. ISBN 978-1-118-66648-7 978-0-87590-433-7. doi:10.1029/168GM20.

L. H. Rüpke, J. P. Morgan, M. Hort, and J. A. D. Connolly. Serpentine and the subduction zone water cycle. *Earth Planet. Sci. Lett.*, 223(1):17–34, 2004. ISSN 0012-821X. doi:10.1016/j.epsl.2004.04.018.

M. Scambelluri, E. H. H. Strating, G. B. Piccardo, R. L. M. Vissers, and E. Rampone. Alpine olivine- and titanian clinohumite-bearing assemblages in the Erro-Tobbio peridotite (Voltri Massif, NW Italy). *J. Metamorph. Geol.*, 9(1):79–91, 1991. ISSN 0263-4929, 1525-1314. doi:10.1111/j.1525-1314.1991.tb00505.x.

S. M. Schmid, D. Bernoulli, B. Fügenschuh, L. Matenco, S. Schefer, R. Schuster, M. Tischler, and K. Ustaszewski. The Alpine-Carpathian-Dinaridic orogenic system: Correlation and evolution of tectonic units. *Swiss J. Geosci.*, 101(1):139–183, 2008. ISSN 1661-8734. doi:10.1007/s00015-008-1247-3.

S. M. Schmid, B. Fügenschuh, A. Kounov, L. Maţenco, P. Nievergelt, R. Oberhänsli, J. Pleuger, S. Schefer, R. Schuster, B. Tomljenović, K. Ustaszewski, and D. J. J. van Hinsbergen. Tectonic units of the Alpine collision zone between Eastern Alps and western Turkey. *Gondwana Res.*, 78: 308–374, 2020. ISSN 1342-937X. doi:10.1016/j.gr.2019.07.005.

M. W. Schmidt and S. Poli. Experimentally based water budgets for dehydrating slabs and consequences for arc magma generation. *Earth Planet. Sci. Lett.*, 163(1-4):361–379, 1998. ISSN 0012-821X. doi:10.1016/S0012-821X(98)00142-3.

S. Schwartz, S. Guillot, B. Reynard, R. Lafay, B. Debret, C. Nicollet, P. Lanari, and A. L. Auzende. Pressure–Temperature estimates of the Lizardite/Antigorite transition in high pressure serpentinites. *Lithos*, 178:197–210, 2013. ISSN 00244937. doi:10.1016/j.lithos.2012.11.023.

E. M. Schwarzenbach. Serpentinization, element transfer, and the progressive development of zoning in veins: Evidence from a partially serpentinized harzburgite. *Contrib Miner. Pet.*, page 22, 2016.

T. Shao, M. Song, X. Ma, X. Ding, S. Liu, Y. Zhou, J. Wu, X. Wang, and J. Li. Potential link between antigorite dehydration and shallow intermediate-depth earthquakes in hot subduction zones. *Am. Mineral.*, 108(1):127–139, 2023. ISSN 0003-004X. doi:10.2138/am-2022-8271.

C. Spandler, T. Pettke, and D. Rubatto. Internal and External Fluid Sources for Eclogite-facies Veins in the Monviso Meta-ophiolite, Western Alps: Implications for Fluid Flow in Subduction Zones. *Journal of Petrology*, 52(6):1207–1236, 2011. ISSN 0022-3530. doi:10.1093/petrology/egr025.

E. M. Syracuse, P. E. van Keken, and G. A. Abers. The global range of subduction zone thermal models. *Physics of the Earth and Planetary Interiors*, 183(1):73–90, 2010. ISSN 0031-9201.

doi:10.1016/j.pepi.2010.02.004.

S. Taetz, T. John, M. Bröcker, C. Spandler, and A. Stracke. Fast intraslab fluid-flow events linked to pulses of high pore fluid pressure at the subducted plate interface. *Earth and Planetary Science Letters*, 482:33–43, 2018. ISSN 0012-821X. doi:10.1016/j.epsl.2017.10.044.

M. Tian, J. J. Ague, X. Chu, E. F. Baxter, N. Dragovic, C. P. Chamberlain, and D. Rumble. The Potential for Metamorphic Thermal Pulses to Develop During Compaction-Driven Fluid Flow. *Geochem. Geophys. Geosystems*, 19(1):232–256, 2018. ISSN 1525-2027, 1525-2027. doi:10.1002/2017GC007269.

A. Tremblay, A. Meshi, T. Deschamps, F. Goulet, and N. Goulet. The Vardar zone as a suture for the Mirdita ophiolites, Albania: Constraints from the structural analysis of the Korabi-Pelagonia zone. *Tectonics*, 34(2):352–375, 2015. ISSN 1944-9194. doi:10.1002/2014TC003807.

V. Trommsdorff and B. W. Evans. Progressive metamorphism of antigorite schist in the Bergell tonalite aureole (Italy). *American Journal of Science*, 272(5):423–437, 1972. ISSN 0002-9599. doi:10.2475/ajs.272.5.423.

P. Ulmer and V. Trommsdorff. Serpentine Stability to Mantle Depths and Subduction-Related Magmatism. *Science*, 268(5212):858–861, 1995. ISSN 0036-8075, 1095-9203. doi:10.1126/science.268.5212.858.

M. Ulrich, D. Rubatto, J. Hermann, T. A. Markmann, A.-S. Bouvier, and E. Deloule. Olivine formation processes and fluid pathways in subducted serpentinites revealed by in-situ oxygen isotope analysis (Zermatt-Saas, Switzerland). *Chemical Geology*, 649:121978, 2024. ISSN 0009-2541. doi:10.1016/j.chemgeo.2024.121978.

P. E. van Keken, B. R. Hacker, E. M. Syracuse, and G. A. Abers. Subduction factory: 4. Depth-dependent flux of H2O from subducting slabs worldwide. *J. Geophys. Res. Solid Earth*, 116(B1), 2011. ISSN 2156-2202. doi:10.1029/2010JB007922.

J. C. Vrijmoed and Y. Y. Podladchikov. Thermolab: A Thermodynamics Laboratory for Nonlinear Transport Processes in Open Systems. *Geochem. Geophys. Geosystems*, 23(4):e2021GC010303, 2022. ISSN 1525-2027. doi:10.1029/2021GC010303.

C. R. Wilson, M. Spiegelman, and P. E. van Keken. Terra FERMA : The T ransparent F inite E lement R apid M odel A ssembler for multiphysics problems in E arth sciences. *Geochem. Geophys. Geosyst.*, 18(2):769–810, 2017. ISSN 1525-2027, 1525-2027. doi:10.1002/2016GC006702.

V. M. Yarushina and Y. Y. Podladchikov. (De)compaction of porous viscoelastoplastic media: Model formulation: (DE)COMPACTION OF POROUS MEDIA. *J. Geophys. Res. Solid Earth*, 120(6): 4146–4170, 2015. ISSN 21699313. doi:10.1002/2014JB011258.

V. M. Yarushina, L. H. Wang, D. Connolly, G. Kocsis, I. Fæstø, S. Polteau, and A. Lakhlifi. Focused fluid-flow structures potentially caused by solitary porosity waves. *Geology*, 50(2):179–183, 2022. ISSN 0091-7613, 1943-2682. doi:10.1130/G49295.1.

T. Yokoyama, E. Nakamura, K. Kobayashi, and T. Kuritani. Timing and trigger of arc volcanism controlled by fluid flushing from subducting slab. *Proc. Jpn. Acad., Ser. B*, 78(7):190–195, 2002. ISSN 0386-2208, 1349-2896. doi:10.2183/pjab.78.190.

K. Yoshida, R. Oyanagi, M. Kimura, O. Plümper, M. Fukuyama, and A. Okamoto. Geological records of transient fluid drainage into the shallow mantle wedge. *Sci. Adv.*, 9(14):eade6674, 2023. doi:10.1126/sciadv.ade6674.

T. Zack and T. John. An evaluation of reactive fluid flow and trace element mobility in subducting slabs. *Chem. Geol.*, 239(3):199–216, 2007. ISSN 0009-2541. doi:10.1016/j.chemgeo.2006.10.020.

X. Zhang, F. Ma, S. Yin, C. D. Wallace, M. R. Soltanian, Z. Dai, R. W. Ritzi, Z. Ma, C. Zhan, and X. Lü. Application of upscaling methods for fluid flow and mass transport in multi-scale heterogeneous media: A critical review. *Appl. Energy*, 303:117603, 2021. ISSN 0306-2619. doi:10.1016/j.apenergy.2021.117603.

Chapter 3

Formation of Olivine Veins by Reactive Fluid Flow in a Dehydrating Serpentinite

Published as: **Huber, K.**, Vrijmoed, J. C., & John, T. (2022); Formation of olivine veins by reactive fluid flow in a dehydrating serpentinite. Geochemistry, Geophysics, Geosystems, 23, e2021GC010267 (https://doi.org/10.1029/2021GC010267) under the Creative Commons License (https://creativecommons.org/licenses/by/4.0/)

Abstract

Many exposed high-pressure meta-serpentinites comprise a channelized network of olivine-rich veins that formed during dehydration at depth and allowed the fluid to escape from the dehydrating rock. While previous studies have shown that chemical heterogeneities in rocks can control the formation of olivine-enriched vein-like interconnected porosity networks on the sub-millimeter scale, it is still unclear how these networks evolve toward larger scales and develop nearly pure olivine veins. To explore this, we study the effect of reactive fluid flow on a dehydrating serpentinite. We use thermodynamic equilibrium calculations to investigate the effect of variations in the bulk silica content in serpentinites on the dehydration reaction of antigorite + brucite = olivine + fluid and the silica content of this fluid phase. Further, we develop a numerical model that combines the effects of intrinsic chemical heterogeneities with reactive transport with dissolved silica as metasomatic agent. Our model shows how reactive transport can lead to vein widening and olivine enrichment within a vein in an antigorite-rich matrix, such as observed in the veins of the Erro Tobbio meta-serpentinites. This is a critical step in the evolution toward larger-scale vein systems and in the evolution of dynamic

porosity, as this step helps account for the chemical feedback between the dehydrating rock and the liberated fluid.

3.1 Introduction

Serpentinites represent the major fluid source within subducting oceanic plates and carry large amounts of water, stored in hydrous minerals, into subduction zones worldwide (e.g. Scambelluri et al., 1995; van Keken et al., 2011; Rüpke et al., 2004). Fully hydrated oceanic mantle can store up to 13 wt. % water, which is released in a series of dehydration reactions (e.g. Ulmer and Trommsdorff, 1995; Rüpke et al., 2004; Plümper et al., 2017). In turn, these released fluids have large effects on important geodynamic processes such as earthquakes (Moreno et al., 2014; Jung et al., 2004; Hacker et al., 2003) and arc magmatism (Mazza et al., 2020; John et al., 2012; Schmidt and Poli, 1998).

In more detail, dehydration reactions lead to densification of the solid slab, which, in turn, gives rise to the formation of fluid-filled porosity. Initially, this porosity forms on the sub-millimeter scale and is heterogeneously distributed in the rock (Figure 3.1a), as defined by the local bulk composition (Plümper et al., 2017). As dehydration continues, these first vein-like porosity structures connect and form a vein network (Figure 3.1b). Within these centimeter-scale veins, metamorphic olivine and porosity form by the breakdown of antigorite via an intermediate phyllosilicate phase (IPP, Plümper et al. (2017), Figure 3.1d) which leads to widening of the veins and increasing draining efficiency. Finally, the fluid escapes (Figure 3.1c) by the formation of either fracture-like (e.g. Padrón-Navarta et al., 2010; Herms et al., 2012; Spandler et al., 2011; John et al., 2008) or porosity wave-like fluid pathways (Connolly and Podladchikov, 2007; Miller et al., 2003; Skarbek and Rempel, 2016; Chen et al., 2019; Piccoli et al., 2021).

One of the key dehydration reactions occurring in hydrated slab mantle is the breakdown of brucite and antigorite to form olivine and an aqueous fluid phase (Ulmer and Trommsdorff, 1995). In partially dehydrated serpentinites, the emergence of metamorphic olivine after serpentine is used as an indicator that these domains underwent dehydration. Such olivine-rich dehydration structures are commonly observed in previously subducted high-pressure ophiolites, e.g., the Cerro del Almirez massif in Spain (López Sánchez-Vizcaíno et al., 2005, 2009), in the Sanbagwa metamorphic belt in Japan (Fukumura et al., 2019) or in various locations in the Western Alps (Groppo and Compagnoni, 2007; Scambelluri et al., 1991; Clément et al., 2020; Kempf et al., 2020). In many cases, olivine enrichment in these rocks is associated with deformation structures such as mylonitic shear zones (Hermann et al., 2000) or pseudotachylites (Magott et al., 2020), but occasionally these rocks also contain

an olivine-rich vein network in parts with only very little deformation. A key locality to study these olivine-rich veins is in the meta-serpentinites of the Erro Tobbio unit in the Ligurian Alps in Italy (Scambelluri et al., 1991; Plümper et al., 2017). These rocks show both olivine-rich mylonites and the olivine-rich vein network in an undeformed body of antigorite-rich country rock (Figure 3.1b and c).

As shown by Plümper et al. (2017), the formation of sub-millimeter vein-like porosity structures that are enriched in olivine (compared to the antigorite-rich surrounding matrix) are caused by intrinsic local variations in the bulk rock chemistry (Figure 3.1a), suggesting that dehydration leads to fluid channeling directly at the onset of the dehydration process. Such a dynamic vein network formation that eventually results in fluid release from the dehydrating rock volume has also been suggested, on the basis of measured variations in Vp/Vs ratios, in a seismological study of the slab mantle of the descending Nazca plate beneath Chile (Bloch et al., 2018). Further, magnetotelluric data derived from the Cascadia subduction zone imply that fluid flow from slabs is highly focused and directly feeds arc volcanoes (McGary et al., 2014). Along these lines, recent numerical studies (e.g. Wilson et al., 2014; Cerpa et al., 2017) have shown that on similarly large scales, compaction of mantle wedge rocks can also lead to fluid flow focusing. This type of fluid focusing also appears in geodynamic models: Models developed by Connolly (1997), Spiegelman et al. (2001) and Hesse et al. (2011) couple mineral reactions and solid deformation to show how melt flux in an uprising mantle section underneath a mid-ocean ridge localizes into meso-scale channels that feed the submarine volcanic systems. However, while these large-scale models offer important insights, they do not conceptually describe how the fluid flow mechanisms operate on the small scale, namely the scale at which dehydration reactions occur, nor do they indicate which mechanisms control and define the transition toward larger scales, such as the outcrop or plate scales. Accordingly, a key question remains: How do small-scale dehydrating systems, such as those described by Plümper et al. (2017), then further develop into near-pure olivine vein networks that occur on the outcrop scale (Figure 3.1, Scambelluri et al., 1995) and, thus, likely on even larger scales? This step is needed to derive a mechanistic understanding of how small-scale veins organize themselves on the larger scale to eventually form efficient fluid escape pathways that can drain the descending slab.

To understand this transition from the sub-millimeter scale studied by Plümper et al. (2017) to larger scales, one must consider the effects of reactive transport and, eventually, deformation. In the model by Plümper et al. (2017), the liberated fluid was treated as pure H_2O, and the chemistry of the liberated fluid and its interaction with the wall rock system was not included in the dynamic modelling. However, changes in the fluid chemistry certainly feed back into the chemistry of the affected rock volume and, thus, may drive

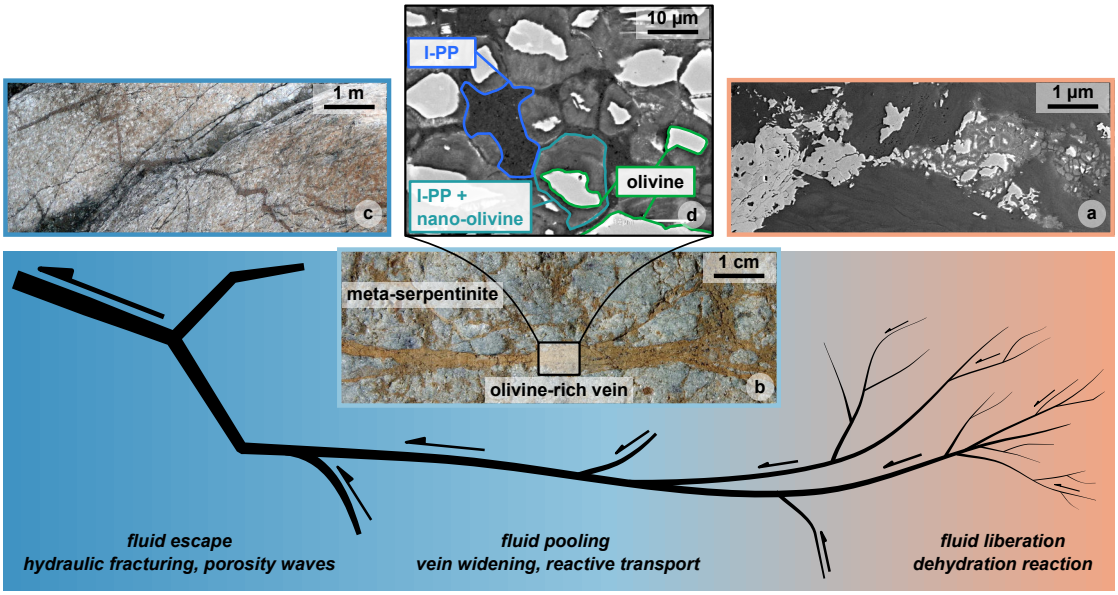

Figure 3.1: Channelized network of dehydration-related olivine-rich veins as observed in the Erro-Tobbio meta-serpentinites. Colors indicate the three main stages of rock dehydration on different length scales. The dominant processes acting on each scale are listed at the bottom. Arrows indicate the direction and magnitude of fluid flow in the veins. Figures a)-c) show the natural occurrence of olivine-rich veins on the µm-, the cm- and the m-scale, respectively. d) shows the mineral assemblage in an olivine-rich vein, displaying the reaction of intermediate phyllosilicate-phase [I-PP, Plümper et al. (2017)] to metamorphic olivine.

mineral reactions that consequently result in dehydration and, accordingly, a change in the mineral assemblage.

Therefore, in this work we extend the model of Plümper et al. (2017) by also considering silica dissolution and precipitation as well as transport of dissolved silica in the fluid phase. Here, we study the effects of reactive fluid flow on the development of the dehydration vein network in an undeformed serpentinite during dehydration of a subducting slab. In our model, we neglect compaction effects and gravity because the model deals with the local scale (millimeter to centimeter). Although compaction effects do become important at larger scales (decimeter to meter), where gravity plays an important role due to buoyancy effects, on this small scale compaction effects are assumed to have little influence on channelization. Our model shows how changes in the silica content of the fluid can lead to enhanced dehydration, vein widening, and olivine purification within the vein on the millimeter to centimeter scale. Starting from a non-porous rock, all porosity in our model is generated by dehydration mineral reactions first due to increasing temperature and then dynamically by subsequent reactive fluid flow.

3.2 Model Concept

3.2.1 Equations and Solution Strategy

The model is described by three balance laws for (1) total mass, (2) total silica mass and (3) non-volatile mass, i.e., a chemical component that is present in the solid phase only and is not dissolved in the fluid phase. By substituting Darcy's law to describe fluid flow in the porous medium, assuming zero solid velocity ($v_s = 0$) and integrating over the non-volatile mass balance, these balance laws can be expressed in the form of equations 1-3. The formulation of the reactive transport model follows the approach also used by Beinlich et al. (2020), here neglecting gravity due to the arguments outlined above. We consider SiO_2 to be dissolved in H_2O and also include transient fluid pressure evolution and its effect on mineral reactions as done in Plümper et al. (2017):

$$\frac{\partial\left(\varrho_s\left(1-\phi\right)+\varrho_f\phi\right)}{\partial t} = \nabla\cdot\left(\varrho_f\frac{k_0\phi^3}{\mu}\nabla P_f\right) \tag{3.1}$$

$$\frac{\partial\left(\varrho_s c_s\left(1-\phi\right)+\varrho_f c_f\phi\right)}{\partial t} = \nabla\cdot\left(\varrho_f c_f\frac{k_0\phi^3}{\mu}\nabla P_f + \varrho_f c_f\phi D_c\nabla c_f\right) \tag{3.2}$$

$$\phi = 1-\frac{\varrho_s^0\left(1-c_s^0-X_h^0\right)\left(1-\phi^0\right)}{\varrho_s\left(1-c_s-X_h\right)} \tag{3.3}$$

In total, these three equations contain seven unknowns: The fluid pressure (P_f), the SiO_2 content of the solid and the fluid (c_s and c_f, respectively), the H_2O content of the solid (X_h), porosity (ϕ) and the density of the solid and the fluid phase (ϱ_s and ϱ_f, respectively). D_c, k_0 and μ are the diffusivity of aqueous silica, the intrinsic solid permeability and the fluid viscosity, respectively, and are treated as constants. A superscript 0 denotes the initial value of that variable at time zero; the full list of variables and their units used in our model is also given in Table 3.1. Three of these variables (P_f, c_s and ϕ) can be obtained by solving equations 1-3, and the remaining four unknowns (ϱ_s, ϱ_f, X_h and c_f) have been pre-computed and stored as functions of P_f and c_s in lookup tables from where they can be interpolated using the assumption of local equilibrium (Malvoisin et al., 2015; Plümper et al., 2017). Equations (3.1)-(3.3) were solved on a Cartesian grid using an explicit finite difference code with pseudo-transient iterations (e.g. Räss et al., 2019). The codes for the 1D and a 2D models as well as the lookup tables and the codes used to calculate them are available on Zenodo.

Table 3.1: Notation used in our model

Symbol	Meaning	Unit
ϱ_s	solid density	$\mathrm{kg\,m^{-3}}$
ϱ_s^0	initial solid density at T_0	$\mathrm{kg\,m^{-3}}$
ϱ_f	fluid density	$\mathrm{kg\,m^{-3}}$
ϕ	porosity	dimensionless (volume fraction)
ϕ^0	initial porosity at T_0	dimensionless (volume fraction)
c_f	SiO_2 content of fluid	dimensionless (weight fraction)
c_s	SiO_2 content of solid	dimensionless (weight fraction)
c_s^0	initial SiO_2 content of solid at T_0	weight fraction
X_h	H_2O content of solid	dimensionless (weight fraction)
X_h^0	initial H_2O content of solid at T_0	weight fraction
P_f	fluid pressure	GPa
P_f^0	initial fluid pressure	GPa
D_c	diffusion constant	$\mathrm{m^2\,s^{-1}}$
k_0	permeability	$\mathrm{m^2}$
μ	kinematic viscosity	Pa s
T	temperature	°C
t	time	s
L	length	m
*	non-dimensional variable	dimensionless

3.2.2 Scaling and Non-Dimensionalization

To reduce the number of independent physical parameters in our model, we used non-dimensional parameters. As independent parameters, we chose the diffusion constant D_c ($\mathrm{m\,s^{-2}}$), length L (m), the fluid pressure P_f (Pa) and density ϱ ($\mathrm{kg\,m^{-3}}$). This choice allows one to express the time t and the permeability constant k_0/μ in dimensionless forms as $t^* = tD_c/L^2$ and $(k_0/\mu)^* = \frac{k_0 P_f}{\mu D_c}$, where * denotes the dimensionless parameter (Table 3.2).

Table 3.2: Scaling used in the model. D_c, L and P_f are chosen as independent variables to scale the dimensionless time t^* and the permeability constant $(k_0/\mu)^*$. All simulations shown in the results section are presented at $t^* = 2.2e7$ and $k_0/\mu = 1$.

Parameter	D_c	L	t	$\frac{k_0}{\mu}$	P_f	ϱ
Unit	$\mathrm{m\,s^{-2}}$	m	s	$\mathrm{m^2\,Pa^{-1}\,s^{-1}}$	Pa	$\mathrm{kg\,m^{-3}}$
Dimensionless parameter	1	1	$\frac{tD_c}{L^2}$	$\frac{k_0 P_f}{\mu D_c}$	1	1

3.2.3 Equilibrium Thermodynamics

To calculate the lookup tables to close our set of equations, we used the Thermolab package of Vrijmoed and Podladchikov (2022). Gibbs energy minimization was used to calculate phase diagrams and postprocess thermodynamic variables. We calculated phase diagrams for 75 different bulk compositions with varying bulk silica and bulk iron contents in the range of 0.1- 2.0 GPa and 100-550 °C. From these phase diagrams, we postprocessed the values for the thermodynamic closure relationships (ϱ_s, ϱ_f, c_f, X_h) and expressed them as functions of fluid pressure (P_f), solid composition (c_s) and iron content for a fixed temperature (T). Once the values for P_f and c_s are obtained from Equation (3.1) and (3.2), respectively, the closure relationships can be interpolated from the pre-computed equilibrium data. All thermodynamic calculations were performed in the FeO-MgO-SiO_2-H_2O (FMSH) system. The bulk compositions consist of Fe-poor and Fe-rich antigorite to which silica is added to cover a full range of compositions spanning a suitable range of fluid compositions. The initial bulk compositions used in each of the three domains of our model are given in Table 3.4. In our model, we considered as solid phases antigorite, brucite, olivine, orthopyroxene, talc and quartz, and we consider SiO_2-H_2O a fluid phase. To account for the formation of Fe-Mg solid solutions in minerals and for SiO_2-H_2O mixing in the fluid, we used the solution models given in Table 3.3.

Table 3.3: Solution Models Used for Phase Diagram Calculations

Phase	Solution model used
Antigorite	Padrón-Navarta et al. (2013)
Olivine	Holland and Powell (2004)
Orthopyroxene	Powell and Holland (1999)
Talc	Holland and Powell (2004)
Brucite	Ideal
Fluid	Ideal mixing with a combination of CORK EOS for H_2O (Holland and Powell, 1991) with aqueous silica neutral species from (Holland and Powell, 2004)

3.2.4 The Simplified FMSH System

In our model, we used a more simplified chemical system than that in the model by Plümper et al. (2017) by excluding calcium and aluminum. In serpentinites, calcium would be stored in either diopside (at higher pressures) or tremolite (at lower pressures), but serpentinites have very limited abundances of these phases because they usually have low calcium contents

(e.g. bulk compositions of Li et al., 2004), thus supporting our choice to exclude calcium from the model. Regarding aluminum, incorporating aluminum (Tschermak's substitution) in antigorite lowers the temperature of the first antigorite breakdown, as does iron (Padrón-Navarta et al., 2013), and including aluminum also allows one to account for the formation of chlorite, which can retain H_2O in the solid for temperatures up to ∼750 °C (e.g. Scambelluri et al., 2014). However, because both aluminum and iron have similar effects on the onset of dehydration, and because the goal of this work is to study the effects of silica metasomatism and its first-order effects on serpentinite dehydration after an initial fluid pathway forms due to variations in bulk rock chemistry, we chose to exclude aluminum and only include iron. This allowed us to use the simplest chemical system necessary to describe a heterogeneously dehydrating serpentinite while still being able to examine the effects of a solid solution. Also, including iron only, which has a well-known effect on the onset of dehydration, allowed us to better differentiate between the porosity increase due to the increase in temperature and the porosity increase due to the reactive fluid flow. Furthermore, this simplified chemical system enabled us to use high-resolution lookup tables, as only solid solutions between the magnesium and the iron endmembers needed to be considered.

3.3 Model Setup

In order to investigate the dynamic effects of reactive fluid flow in a dehydrating serpentinite, we developed a numerical model that combines the findings of Plümper et al. (2017) with the effects of reactive transport by fluids carrying aqueous silica. The model can be used to show how reactive fluid flow on the millimeter to centimeter scale can lead to the formation of almost pure olivine in a matrix that still contains significant amounts of antigorite, as observed in the field (Figure 3.1).

3.3.1 Geometry of Model

Observations from the Erro Tobbio meta-serpentinites show that the fluid is heterogeneously distributed in the rock and then pooled into larger veins (Figure 3.1). To simplify the problem, we set up three chemically distinct domains with varying bulk silica and bulk iron contents, as shown in Figure 3.6. The three domains represent (1) a matrix with (2) a vein placed in its center and (3) a fluid source region from where fluid flows into the vein. Because we assume that fluid from multiple fluid source regions flows into the vein, the composition of the fluid source region is assigned to one end of the vein in order to simulate a constant fluid influx from a region external but adjacent to our initial vein-wall rock assemblage. We first

Table 3.4: Initial Bulk Compositions in wt. % for the Three Domains used in the Numerical Model. Note: The vein and the fluid source region have the same FeO content in moles

	SiO_2	MgO	FeO	H_2O
Matrix	42.07	39.78	2.95	15.19
Vein	39.39	37.59	8.38	14.35
Source region	34.68	40.71	9.07	15.54

use 1D setups to separately demonstrate the effects of fluid influx into the vein (Figure 3.7a-c) and the fluid-rock interaction between the vein and the wall rock (Figure 3.7d-e) before combining these findings in a 2D model (Figure 3.8) with a setup as shown in Figure 3.6.

3.3.2 Initial Conditions

Initially, both the matrix and the vein have a higher bulk silica content than the fluid source region, but the vein has a higher bulk iron content than the matrix (see Table 3.4 for exact compositions). This is based on the findings of Plümper et al. (2017), where iron was the main driver of the intrinsic chemical heterogeneities that resulted in a vein network formation. In the fluid source region at one end of the vein, the silica content is lower than in the vein, resulting in a high iron and a low silica content in this domain (see Figure 3.6). All three domains have initially zero background porosity ($\phi^0 = 0$) and a homogeneous fluid pressure ($P_f^0 = 1.0\,\text{GPa}$, equal to ambient pressure) at an initial temperature (T_0) of 440 °C. To simulate dehydration during subduction, the temperature is instantaneously increased to 480 °C (T_1) to cross the 450 °C boundary at which the fluid composition of high- and low-silica systems start to vary significantly (Figure 3.3). The temperature increase leads to dehydration in all domains, but the extent of dehydration and the composition of the liberated fluid is different in every domain because both depend on the bulk composition, as in Plümper et al. (2017). Starting from a homogeneous zero background porosity and homogeneous fluid pressure, the temperature increase leads to the formation of porosity and to changes in the fluid pressure to different extents in every domain, depending on each domain's initial bulk composition. All simulations were run for a total dimensionless time of $t^* = 2.2e7$ and used a dimensional permeability constant $k_0/\mu = 1$.

3.3.3 Boundary Conditions

In our model, we use Neumann (zero flux) boundary conditions at all boundaries, which allows the boundary nodes to be updated after the temperature increase. In the 2D model

(Figure 3.8), the composition of the fluid source region is kept constant at the lower end of the vein after the temperature increase; thus, this end of the vein acts as a constant fluid source, assuming that the fluid is pooled from a larger reservoir (the fluid source region) that is connected to one end of the vein (Figure 3.6).

3.4 Results

3.4.1 Effects of Chemical Heterogeneities on the Onset of Dehydration

The local bulk composition controls the stability and abundance of hydrous minerals and, thus, the onset of dehydration (e.g. Plümper et al., 2017). Iron is one of the components with a strong influence on the temperature at which the first dehydration reaction occurs (e.g. Merkulova et al., 2016; Spear, 1993); a high iron content decreases the temperature of the first dehydration reaction by stabilizing brucite and iron-rich antigorite at lower temperatures. This effect can be seen in Figure 3.2, which shows isochemical phase diagram P-T sections for two serpentinite bulk compositions that are varied only in their iron content. In the iron-rich system (Figure 3.2a) the onset of dehydration, shown by the reaction line labeled 'free fluid in', is 100 °C lower than the iron-poor system (Figure 3.2b).

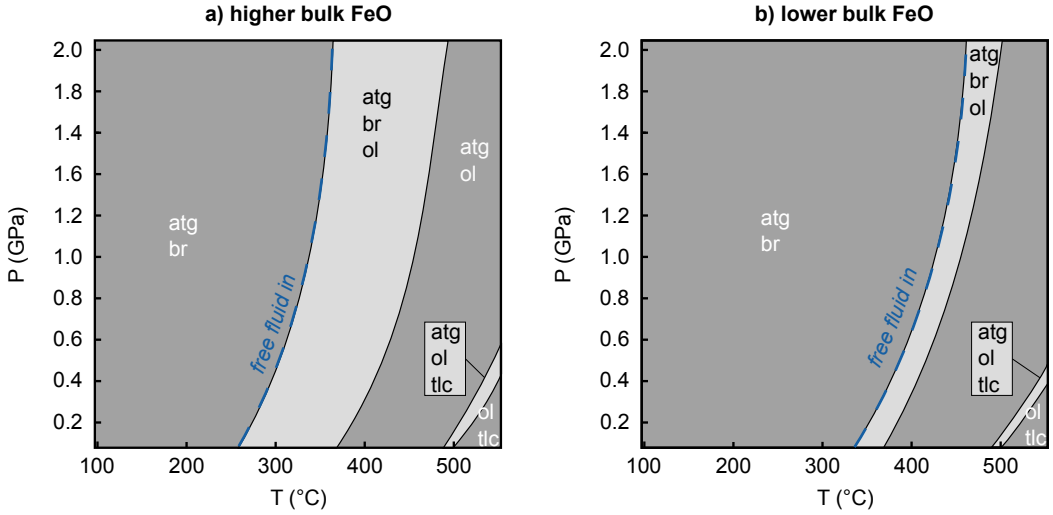

Figure 3.2: P-T diagrams for two typical serpentinite bulk compositions with identical silica and varying iron contents. A higher iron content (a) lowers the temperature for the onset of dehydration (marked by the blue dashed 'free fluid in' reaction line) by ca. 100 °C compared to the iron-poor composition (b). atg = antigorite, br = brucite, ol = olivine, tlc = talc. Different grey shadings represent varying degrees of freedom with respect to the Gibbs phase rule.

However, because of its very low solubility at deep subduction zone conditions, iron has only a minor effect on the composition of the liberated fluid (Manning, 2004; Charlou et al., 2002; Ding and Seyfried, 1992). Silica, on the other hand, is abundant in serpentinites and has a significantly higher solubility (Manning, 2004). Therefore, to study first-order mechanisms of reactive transport in serpentinites, we investigated the effect of silica as the metasomatic agent in our model.

If silica can either be stored in the solid or dissolved in the fluid phase, the equilibrium composition of both phases depends on the bulk composition of the entire system and especially on the total silica abundance. To study how varying the bulk silica contents affects a dehydrating serpentinite, we calculated isochemical phase diagram P-T sections for two serpentinite bulk compositions with identical bulk iron but varying bulk silica contents. Figure 3.3 shows the effect of bulk silica variations on dehydration with increasing P-T conditions. The left and right columns show the results for the low-silica and the high-silica systems, respectively. The range of P-T conditions captures the dehydration reaction of antigorite and brucite to form olivine and a free fluid. In the low-silica system, dehydration starts at lower temperatures than in the high-silica system (Figure 3.3a and b). Consequently, nearly 90 vol. % olivine forms in the system with lower bulk SiO_2, whereas in the system with higher bulk SiO_2, the olivine abundance increases only slightly (Figure 3.3c and d). The reason for this is that a low silica content stabilizes more brucite, which is only stable up to temperatures of 450 °C and 475 °C in the low- and high- silica systems, respectively. As brucite contains large amounts of H_2O, the strong decrease in the brucite content also leads to a stronger decrease in the overall H_2O content of the solid (Figure 3.3e and f) and, thus, to the liberation of more fluid in the silica-poor system. The composition of the liberated fluid (Figure 3.3g and h) is very similar with respect to silica up to temperatures of around 450 °C. For higher temperatures, the fluid released from the low-silica system also contains less dissolved silica than the fluid from the high-silica system. Thus, a lower bulk silica content leads to (1) a larger amount of liberated fluid during dehydration and (2) the generation of a low-silica fluid at temperatures above ∼450 °C.

These calculations show that a low silica content stabilizes higher brucite abundances at temperatures below ∼475 °C. For higher temperatures, brucite breaks down, and a fluid forms that is poorer in silica compared to the fluid released from more antigorite-rich domains, i.e., the silica-poorer domains dehydrate more strongly than the silica-richer domains in this temperature range. The resulting local fluid overpressure then drives fluid flow of the silica-poor fluid into other areas of the porous network.

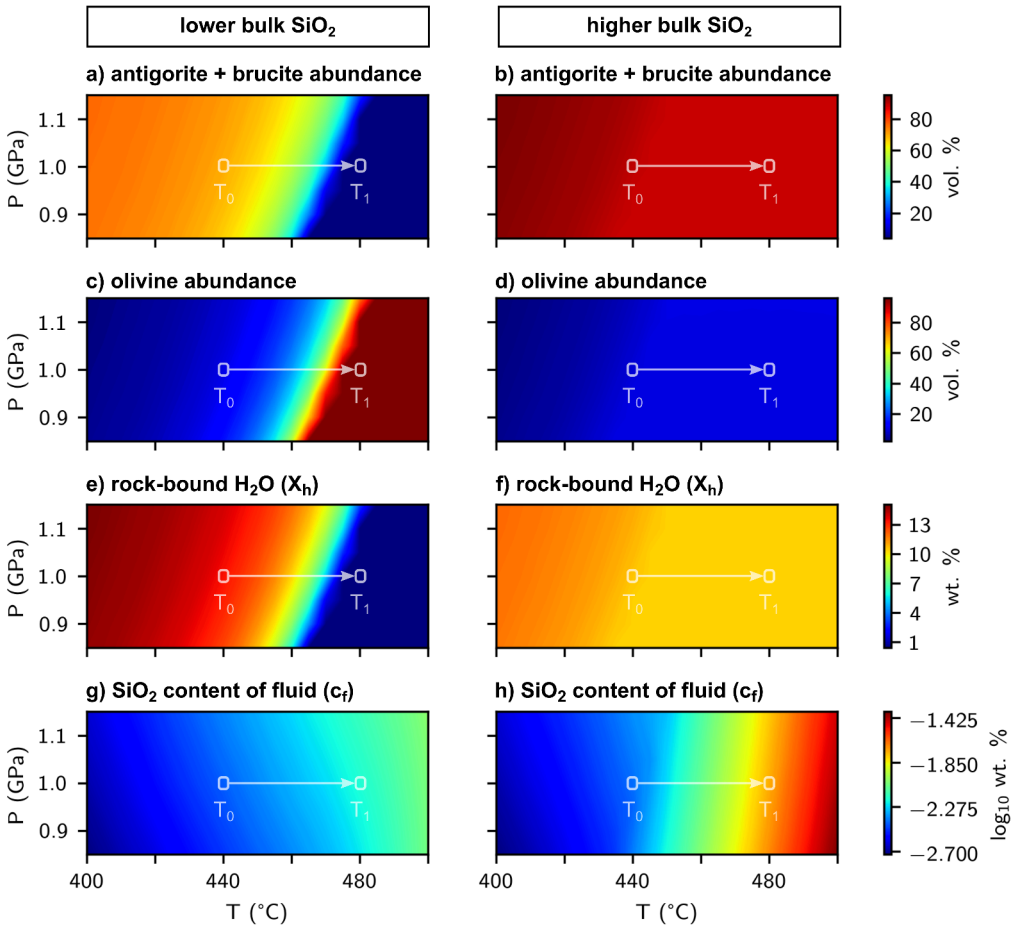

Figure 3.3: Effects of varying bulk silica contents in a system with a high bulk iron content. A low bulk silica content stabilizes more brucite which is only stable up to around 470 °C (a, b) and reacts with antigorite to form olivine (c, d). The sharp decrease in the brucite content in the low silica system between 450 °C and 475 °C leads to a stronger overall decrease in the amount of solid-bound H_2O in the low silica system (e, f) and thus to the liberation of more fluid. The fluid released from the low-silica system has a lower silica content compared to the fluid liberated from the high-silica system (g, h). The bulk composition of the low-silica system is used as source region in the numerical model (see Figure 3.6). The arrow connecting the white circles shows the temperature step in the numerical model from 440 °C (T_0) to 480 °C (T_1) at 1 GPa.

3.4.2 Shifting Thermodynamic Equilibrium Towards Olivine Enrichment

Therefore, silica gets transported along with the fluid, and the resulting changes in the fluid composition affect the bulk silica content of the surrounding solid because the bulk silica content re-equilibrates with the changing fluid composition. This means that the bulk silica content of a system, as in Figure 3.3, can take on higher or lower values due to transport of aqueous silica in the fluid. The effects of such a shift in the bulk silica content are illustrated in Figure 3.4: This figure shows the equilibrium relationships between the silica content of the fluid (c_f) and the solid (c_s) and the resulting stable mineral assemblage in the rock for a system with a higher bulk iron content (Figure 3.4a) and for a system with a lower bulk iron content (Figure 3.4b). In both systems, lowering the fluid silica content leads to a decrease in the bulk silica content. This decrease in the bulk silica content causes dehydration by antigorite breakdown and olivine formation.

The results in Figure 3.4 are shown for a constant pressure, but in our model we also consider effects of changes in the fluid pressure, as both c_s and P_f are used for interpolation in the lookup tables. The equilibrium relationships between c_s, c_f, P_f and the olivine abundance in the rock are shown in Figure 3.5. Figure 3.5a and 3.5c show the fluid composition as a function of fluid pressure and the bulk silica content of the solid. The abundance of olivine in the associated mineral assemblage is shown in Figure 3.5b and 3.5d. In both the low and the high bulk iron systems, there is a sharp, nearly pressure-independent drop in the equilibrium fluid composition at a c_s value of around 44 wt. % SiO_2 in the low-iron system and 43 wt. % SiO_2 in the high-iron system. The olivine abundance plots show that for pressures below $\sim$ 1.0 GPa (Figure 3.5b) and 1.5 GPa (Figure 3.5d), this change in the fluid composition is accompanied by the onset of olivine occurrence in the solid. For c_s values of 41.5 wt. % SiO_2 (Figure 3.5b) and 40.5 wt. % SiO_2 (Figure 3.5d), the olivine abundance reaches almost 100 vol. %, as shown by the black boxes. For even lower c_s values the olivine abundance decreases again due to the formation of brucite, and for pressures above $\sim$1 GPa olivine reacts to form antigorite.

Figure 3.5 shows how changes in fluid pressure and the fluid composition can shift the thermodynamic equilibrium toward olivine formation and even "olivine purification" of the system due to an increase of olivine abundance at constant temperature. The shift occurs along a c_s-P-path that is controlled by the solutions of the equations (3.1)-(3.3), i.e., by local thermodynamic equilibrium. The figure also demonstrates that to reach 'olivine purification' of the vein, the silica content of the fluid must be low ($<$0.01 wt. % SiO_2) and the fluid pressure must be below $\sim$1 GPa.

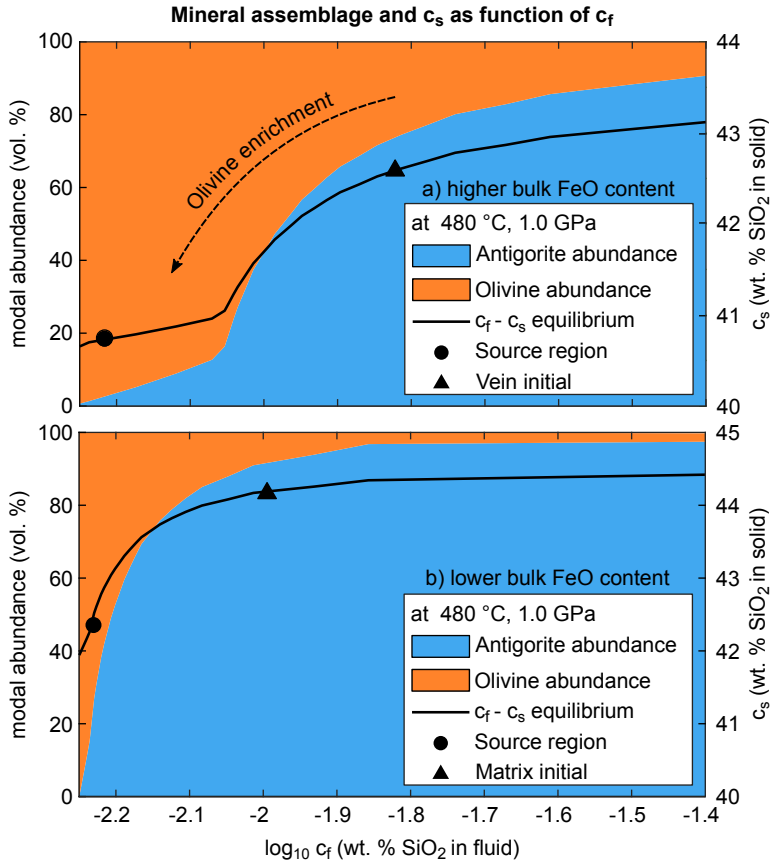

Figure 3.4: Equilibrium silica contents of fluid (c_f) and solid (c_s) in a system with a higher (a) and a lower (b) bulk iron content at a fixed temperature of 480 °C (T_1) and a pressure of 1.0 GPa (P_f^0). The solid black line represents the thermodynamic equilibrium between fluid and solid for varying bulk silica contents. The colored areas show the stable mineral assemblage in the rock for every value of c_s (blue = antigorite, orange = olivine). The filled circles are plotted at the bulk composition of the fluid source region, the triangles at the initial bulk composition of the vein (a) and the matrix (b). Lowering the fluid composition in the vein and matrix shifts the solid composition along the black curve towards the left, resulting in dehydration by antigorite breakdown and olivine enrichment, reaching an almost pure olivine assemblage in the system with a higher bulk iron content (a).

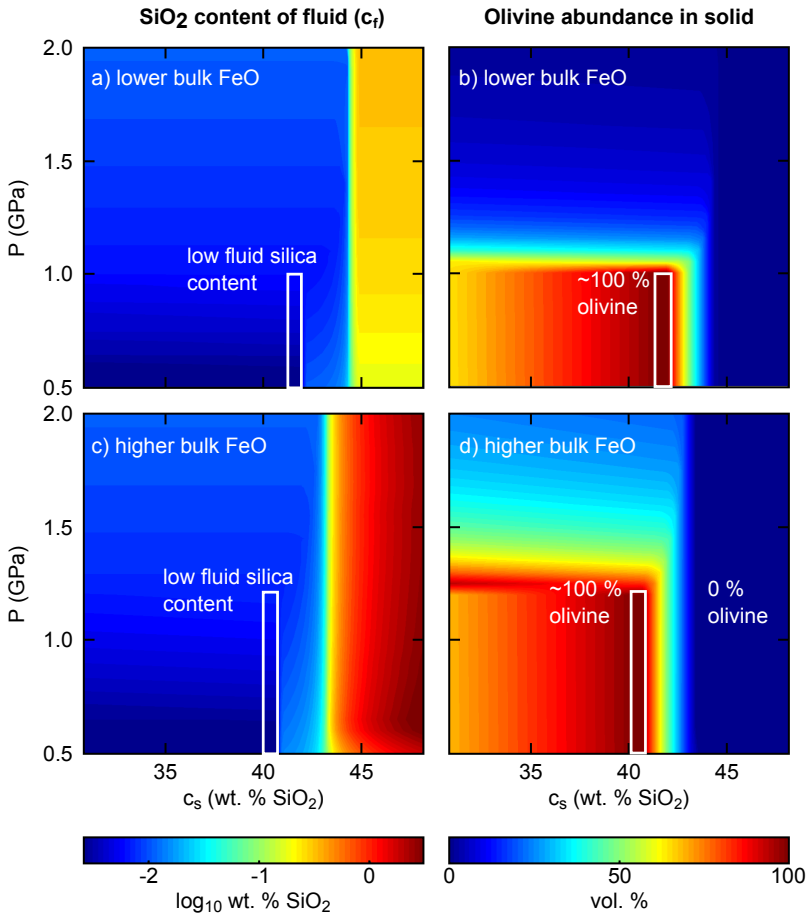

Figure 3.5: Composition and olivine abundance in the solid as functions of bulk silica content (c_s) and pressure (P) at a constant temperature of 480 °C for two systems with varying bulk iron contents. a) and b) show fluid silica content and olivine abundance in the solid in a system with lower bulk iron content, respectively. c) and d) show fluid silica content and olivine abundance in the solid in a system with higher bulk iron content. Black boxes higlight a range of c_s-P values where the solid consists of almost pure olivine. Changes in fluid pressure and fluid composition can shift the equilibrium towards values within the black boxes and thus to olivine purification at constant temperature.

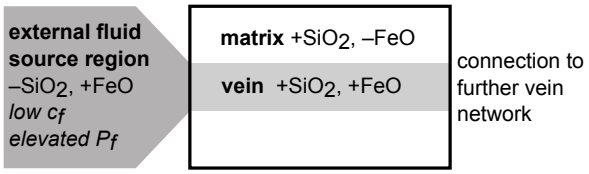

Figure 3.6: Conceptual sketch of the 2D model setup. A high silica domain with iron heterogeneities (black rectangle) is connected to a fluid source region (dark grey), where enhanced dehydration results in fluid pressure increase and the liberation of a low-silica fluid which flows into the vein. The composition of the fluid source region (Table 3.4) is assigned at one end of the vein and kept constant after the temperature increase, thus acting as constant source of a low-silica fluid. Both fluid pressure and fluid composition are defined by thermodynamic equilibrium with the surrounding solid and depend on the local bulk composition. The bulk composition of each domain in the model is listed in Table 3.4. Zero flux (Neumann) boundary conditions are used at all boundaries in the model. The 1D setups (Figure 3.7) represent profiles parallel (Figure 3.7a-c) and perpendicular (Figure 3.7d-e) to the vein.

3.4.3 Porosity and Fluid Pressure

The temperature increase leads to changes in fluid pressure and to the formation of porosity via dehydration-causing mineral reactions in the initially non-porous rock ($\phi^0 = 0$). Figure 3.7a and Figure 3.7d show the fluid pressure (blue lines) and porosity (orange lines) after a non-dimensional time of $t^* = 2.2e7$ for the case where fluid flows from the fluid source region into the vein and perpendicular to the vein, i.e., the fluid-rock interaction between fluid and the vein and the matrix. Dehydration and, thus, porosity increase after the temperature increase is highest in the fluid source region ($\phi \sim 0.25$), followed by the vein ($\phi \sim 0.05$) and the matrix ($\phi \sim 0.03$). The fluid pressure increases in parts of the domain that show stronger dehydration and drives fluid flow from the fluid source region into the vein and from the vein into the matrix. Subsequent to the temperature increase, porosity then increases further by dehydration-related mineral reactions that are induced by the reactive fluid flow (orange areas in Figure 3.7a and d). These calculated porosities reflect realistic values for subducted oceanic lithosphere at comparable P-T conditions (Katayama et al., 2012; Taetz et al., 2016).

3.4.4 Olivine Enrichment and Antigorite Breakdown

Olivine enrichment by reactive fluid flow-induced antigorite breakdown can be seen in Figure 3.7c and Figure 3.7f. In the fluid source region, the olivine content after the temperature increase reaches almost 100 vol. % compared to ∼42 vol. % in the vein and ∼10 vol. %

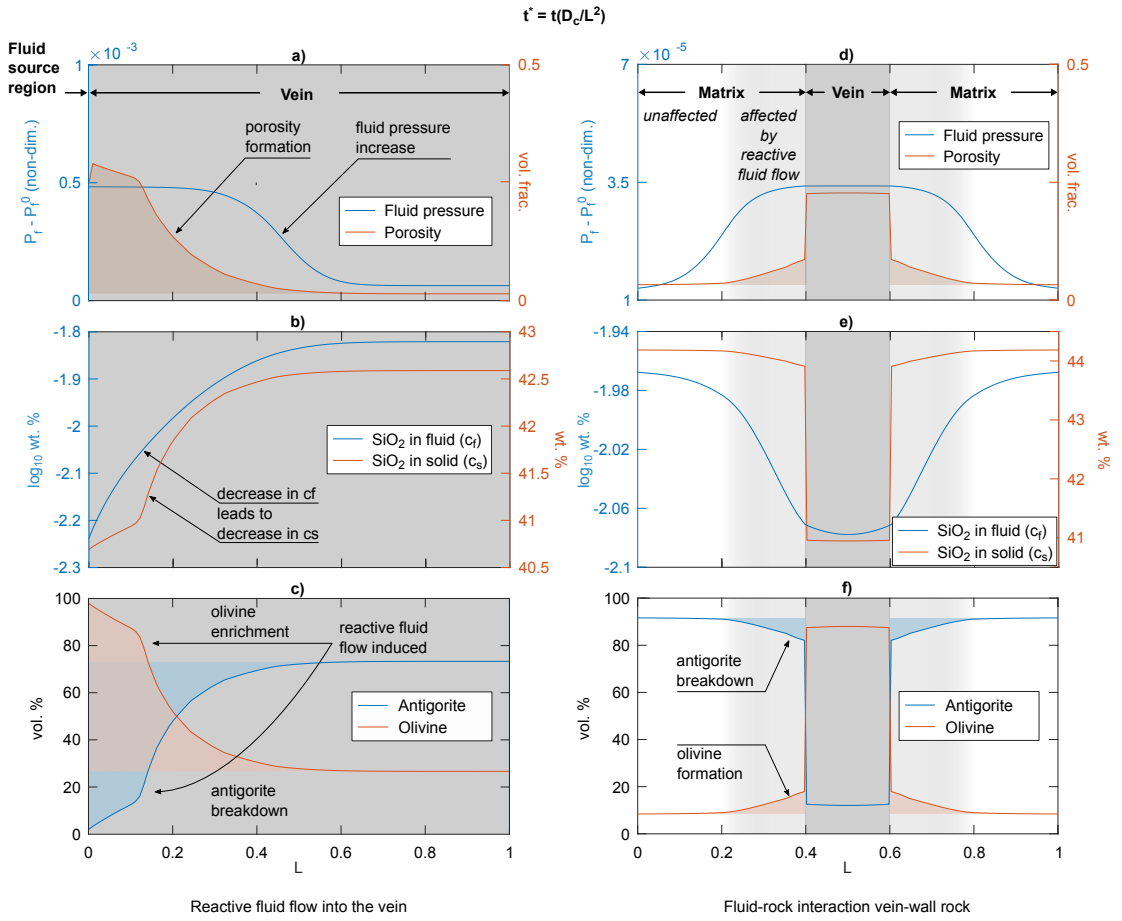

Figure 3.7: Results of the numerical model in a 1D domain with non-dimensional length L. a–c: reactive fluid flow from the source region into the vein; d–f: fluid-rock interaction between the vein and the wall rock. a) fluid flow from the source region (left boundary) into the vein (gray) leads to fluid pressure increase (blue graph) and porosity increase (orange graph). b) the decrease in the silica content of the fluid (blue graph) and changes in the fluid pressure cause a decrease in the bulk silica content of the solid (orange graph). c) modal abundances of olivine and antigorite show olivine enrichment in the vein. d) porosity also forms in the wall rock at the vein boundary (orange graph). e) Diffusion of aqueous silica from the matrix into the vein leads to dehydration at the vein wall (f). Olivine formation in the matrix however is limited because the low iron content of the matrix stabilizes antigorite (Figure 3.4b). The non-dimensional time for these results is $t^* = 2.2e7$. If L = 1 cm, the diffusion length (width of the matrix affected by reactive fluid flow) would be 0.4 cm. Using the equation of Watson and Wark (1997) to calculate the diffusivity of aqueous silica at 1 GPa and 480 °C gives a real time of t $\sim$ 1600 years.

in the matrix. The almost olivine-pure mineral assemblage in the fluid source region is in equilibrium with a fluid that contains the lowest amount of silica of all three domains. The influx of this low-silica fluid into the vein (Figure 3.7b) leads to antigorite breakdown and olivine enrichment in the vein. Within the vein, the equilibrium is shifted toward the almost olivine-pure mineral assemblage (Figure 3.7c) because the fluid source region and the vein only vary in their initial bulk silica content but have the same bulk iron content. Fluid flow between an olivine-rich vein and the surrounding host rock (matrix) leads to dehydration at the vein margins and to re-hydration within the vein if no constant influx of a low-silica fluid occurs (Figure 3.7e and f). In the matrix, the lower bulk iron content stabilizes antigorite and limits olivine formation to max. ∼20 vol. % even though c_s in the matrix is also lowered by reactive fluid flow.

3.4.5 2D Model

The 2D model includes the vein, the matrix and the fluid source region arranged in one domain as shown in Figure 3.6. As in the 1D model, the initial porosity is zero everywhere at a homogeneous fluid pressure of 1.0 GPa and a temperature of 440 °C. After the temperature increase, the elevated fluid pressure in the source region (Figure 3.8a) drives fluid flow into the vein and the vein-surrounding matrix. The increased porosity in the vein (Figure 3.8b) channelizes the fluid flow into the vein. As demonstrated in the 1D model, minor dehydration and olivine formation at the expense of antigorite also occurs at the slightly widening vein margins (Figure 3.8e and Figure 3.8f). After the temperature increase, c_f is higher within the vein than in the matrix (Figure 3.8c). Diffusion of silica from the vein into the matrix also lowers the silica content of the fluid in the vein prior to the influx of the low-silica fluid from the fluid source region. This interaction between the vein and the matrix increases porosity in the vein from $\phi \sim 0.05$ after the temperature increase to $\phi \sim 0.1$ when the low-silica fluid from the source region affects the vein. The higher porosity in the vein after the temperature increase and the strong porosity increase due to reactive fluid flow channelize the fluid flow into the vein.

3.5 Discussion

3.5.1 The Fluid Source Regions

In the numerical model, the composition of the fluid source region has been assigned at one end of the vein, which leads to a constant fluid influx into the vein. This source region does not necessarily represent a single spot in the rock but rather multiple volumes of rock

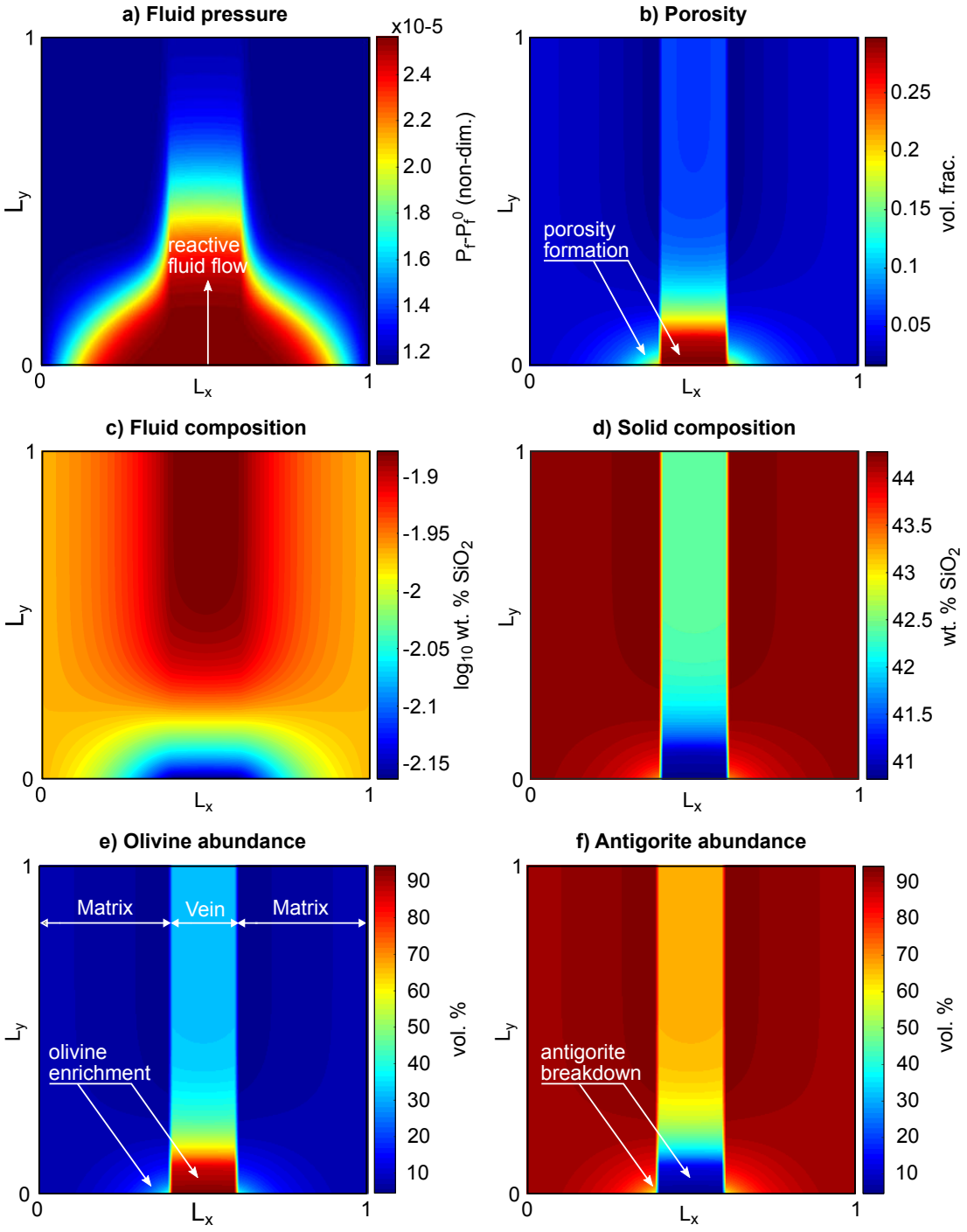

Figure 3.8: Results of the numerical model in a 2D domain with a setup as shown in Figure 3.6. a) non-dimensional fluid overpressure, b) porosity (ϕ), c) fluid composition (c_f), d) solid composition (c_s), e) olivine abundance and f) antigorite abundance after $t^* \sim 2.1e7$. Fluid influx from the fluid source region results in olivine formation by antigorite breakdown in the vein and the adjacent wall rock at constant temperature. The initial bulk compositions of the vein, the matrix and the source regions are identical to the ones used for the 1D model (Figure 3.7 and Table 3.4). The composition of the fluid source region is set as boundary condition at the lower end of the vein.

that dehydrate and release a low-silica fluid. We hypothesize that when the porosity and, hence, permeability in the porous media-like rock system is high enough, i.e., the percolation threshold is reached (e.g. Bloch et al., 2018), the fluid from these domains will continue channelizing (e.g. Plümper et al., 2017) into larger veins, such as the one in our model. The low silica content and high iron content of the source regions stabilize a significant amount of brucite at lower temperatures. In a natural serpentinite, the source regions would therefore be brucite-rich domains that are distributed in the mantle section of interest. In fact, Klein et al. (2020) and (Kempf et al., 2020) used the distribution of olivine-rich patches in the Zermatt ophiolite to infer to former brucite-rich spots. They also related the olivine-rich shear zones in the ophiolite to the pathways of the fluid released from the brucite-rich spots. Therefore, the initial composition chosen for the fluid source region in our model reflects those brucite-rich and silica-poor domains in natural systems (Li et al., 2004).

3.5.2 The Instantaneous Increase in Temperature

As no large temperature gradients are expected on the micro scale, we applied a spatially homogeneous temperature throughout all domains. The instantaneous temperature increase in our model simulates the effect of subduction deeper down into the subduction zone, namely the descent into the hot mantle. In nature, this temperature increase certainly happens continuously. Smaller temperature steps would lead to a more continuous approximation of the dehydration process and a competition between the relaxation of the fluid pressure and the fluid chemistry gradients. Here, our focus was on the process of fluid pressure relaxation and fluid composition evolution after a single step of heating, which allowed us to study only the transient effects of reactive fluid flow in more detail. In order to simulate a more complete subduction zone dehydration process, a more complex approach involving heat transport is needed. We chose the temperature range from 440 °C to 480 °C at which the reactive fluid flow most likely becomes important. Our calculations (Figure 3.3g and h) show that until a temperature of about 460 °C, the silica content of fluids derived from the high- and the low-silica domains are quite similar; only at higher temperatures is more silica dissolved in the fluid of the high-silica system than in the low-silica system, and reactive fluid flow will be more effective.

3.5.3 Fe Dissolution in the Fluid

Although the dissolution of ferrous iron in aqueous fluids is very low (e.g. Charlou et al., 2002; Ding and Seyfried, 1992), Debret et al. (2016) showed isotopic evidence for long-distance iron transport via subduction zone fluids. In a reduced serpentinite as used in our

model, ferrous iron is mostly transported by forming sulfur and chlorine complexes (Chen et al., 2019). The amount of dissolved iron, therefore, also depends on the abundance of these elements in the serpentinite (Alt et al., 2013). A high concentration of iron in solution would also lead to iron exchange between the solid and the fluid and, thus, affect the iron content of the solid. Because the iron content has a large effect on dehydration reactions, the transport of iron in the fluid could amplify the effects of reactive fluid flow beyond the effects due to transport of aqueous silica.

3.5.4 Implications for Fluid Release in Subduction Zones

Various studies have shown that intra-slab fluid flow and fluid escape from the slab is channelized and reactive, both to various degrees (e.g. Chen et al., 2019; Angiboust et al., 2014; Herms et al., 2012; John et al., 2012; Taetz et al., 2016). Our findings indicate that reactive fluid flow is able to transform an initially fine and small-scale, high-porosity structure into a wider and larger vein system that could also develop reaction halos. Thus, our findings reflect a first step toward a mechanistic understanding of how dehydration leads from the first stage of chemistry-controlled local dehydration to the development of intra-slab flow structures that are either highly channelized with only limited interaction with the wall rock (e.g. Breeding and Ague, 2002; Spandler et al., 2011) or highly channelized with significant reaction halos surrounding the vein (e.g. Herms et al., 2012; Taetz et al., 2016; John et al., 2012); further, some structures might even be porosity wave-like high-permeability structures that affect rock volumes on the scale of centimeters to tens of meters without necessarily having fracture-like vein structures (e.g. Piccoli et al., 2021; Chen et al., 2019).

3.6 Conclusions

Here, we have presented a reactive fluid flow model for the transport of aqueous silica in a dehydrating serpentinite. In our model, porosity is generated dynamically with dehydration, demonstrating how an initial non-porous rock can evolve into a channelized fluid flow system. We show how changes in the bulk silica and the bulk iron content affect the dehydration reaction of antigorite + brucite = olivine + fluid and affect the composition of this fluid with respect to silica. Domains with higher bulk iron and lower bulk silica contents dehydrate more strongly and earlier than domains with higher bulk silica and lower bulk iron contents. The fluid released from these early dehydrating domains contains low amounts of aqueous silica, and the elevated fluid pressure in the more strongly dehydrated domains will drive fluid flow of this low-silica fluid into domains with higher silica contents, where changes in

the fluid composition cause dehydration and widening of existing veins by induced antigorite breakdown and olivine formation. In iron-richer domains, the mineral assemblage can be shifted toward olivine purification, whereas in iron-poorer areas substantial amounts of antigorite remain stable. This is in accordance with observations of olivine-rich veins in an antigorite-rich country rock, such as in the Erro-Tobbio meta-serpentinites.

3.7 Open Research

A 1D and a 2D version of the reactive transport code as well as the codes used to create the thermodynamic lookup tables used in this study are available at Zenodo via 10.5281/zenodo.6569809 with CC-BY 4.0.

3.8 Acknowledgments

The Deutsche Forschungsgemeinschaft (DFG) financially supported this research through grant CRC 1114 'Scaling Cascades in Complex Systems', Project Number 235221301, Project (C09) – 'Dynamics of rock dehydration on multiple scales'. We also thank the members of the C09 project from the Weierstraß Institut (WIAS) in Berlin, M. Thomas, D. Peschka and A. Zafferi for their collaboration in this project and the fruitful discussions. The authors also thank M. Scambelluri for his collaboration and for helping us in the field and two anonymous reviewers who considerably helped to improve this paper.

References

J. C. Alt, E. M. Schwarzenbach, G. L. Früh-Green, W. C. Shanks, S. M. Bernasconi, C. J. Garrido, L. Crispini, L. Gaggero, J. A. Padrón-Navarta, and C. Marchesi. The role of serpentinites in cycling of carbon and sulfur: Seafloor serpentinization and subduction metamorphism. *Lithos*, 178:40–54, 2013. ISSN 0024-4937. doi:10.1016/j.lithos.2012.12.006.

S. Angiboust, T. Pettke, J. C. M. De Hoog, B. Caron, and O. Oncken. Channelized Fluid Flow and Eclogite-facies Metasomatism along the Subduction Shear Zone. *J. Petrol.*, 55(5):883–916, 2014. ISSN 0022-3530. doi:10.1093/petrology/egu010.

A. Beinlich, T. John, J. C. Vrijmoed, M. Tominaga, T. Magna, and Y. Y. Podladchikov. Instantaneous rock transformations in the deep crust driven by reactive fluid flow. *Nat. Geosci.*, 13(4):307–311, 2020. ISSN 1752-0908. doi:10.1038/s41561-020-0554-9.

W. Bloch, T. John, J. Kummerow, P. Salazar, O. S. Krüger, and S. A. Shapiro. Watching Dehydration: Seismic Indication for Transient Fluid Pathways in the Oceanic Mantle of the Sub-

ducting Nazca Slab. *Geochem. Geophys. Geosystems*, 19(9):3189–3207, 2018. ISSN 1525-2027. doi:10.1029/2018GC007703.

C. M. Breeding and J. J. Ague. Slab-derived fluids and quartz-vein formation in an accretionary prism, Otago Schist, New Zealand. *Geology*, 30(6):499–502, 2002. ISSN 0091-7613. doi:10.1130/0091-7613(2002)030<0499:SDFAQV>2.0.CO;2.

N. G. Cerpa, I. Wada, and C. R. Wilson. Fluid migration in the mantle wedge: Influence of mineral grain size and mantle compaction. *JGR Solid Earth*, 122(8):6247–6268, 2017. ISSN 2169-9313, 2169-9356. doi:10.1002/2017JB014046.

J. L. Charlou, J. P. Donval, Y. Fouquet, P. Jean-Baptiste, and N. Holm. Geochemistry of high H2 and CH4 vent fluids issuing from ultramafic rocks at the Rainbow hydrothermal field (36°14'N, MAR). *Chem. Geol.*, 191(4):345–359, 2002. ISSN 0009-2541. doi:10.1016/S0009-2541(02)00134-1.

S. Chen, R. C. Hin, T. John, R. Brooker, B. Bryan, Y. Niu, and T. Elliott. Molybdenum systematics of subducted crust record reactive fluid flow from underlying slab serpentine dehydration. *Nat. Commun.*, 10(1):4773, 2019. ISSN 2041-1723. doi:10.1038/s41467-019-12696-3.

M. Clément, J. A. Padrón-Navarta, and A. Tommasi. Interplay between fluid extraction mechanisms and antigorite dehydration reactions (val malenco, italian alps). *J. Petrol.*, 60(10):1935–1962, 2020. ISSN 0022-3530. doi:10.1093/petrology/egz058.

J. A. D. Connolly. Devolatilization-generated fluid pressure and deformation-propagated fluid flow during prograde regional metamorphism. *J. Geophys. Res. Solid Earth*, 102(B8):18149–18173, 1997. doi:10.1029/97jb00731.

J. A. D. Connolly and Y. Y. Podladchikov. Decompaction weakening and channeling instability in ductile porous media: Implications for asthenospheric melt segregation. *J. Geophys. Res.*, 112 (B10):B10205, 2007. ISSN 0148-0227. doi:10.1029/2005JB004213.

B. Debret, M.-A. Millet, M.-L. Pons, P. Bouilhol, E. Inglis, and H. Williams. Isotopic evidence for iron mobility during subduction. *Geology*, 44(3):215–218, 2016. ISSN 0091-7613. doi:10.1130/G37565.1.

K. Ding and W. E. Seyfried. Determination of Fe-Cl complexing in the low pressure supercritical region (NaCl fluid): Iron solubility constraints on pH of subseafloor hydrothermal fluids. *Geochim. Cosmochim. Acta*, 56(10):3681–3692, 1992. ISSN 0016-7037. doi:10.1016/0016-7037(92)90161-B.

S. Fukumura, K. Okamoto, and M. Terabayashi. Metamorphic olivine after dehydration embrittlement in Serpentinite: Case study from the Shiraga Serpentinite mass in the Sanbagawa high P/T metamorphic belt, central Shikoku, Japan. *Isl. Arc*, 28(2):e12293, 2019. ISSN 1440-1738. doi:10.1111/iar.12293.

C. Groppo and R. Compagnoni. Metamorphic veins from the serpentinites of the Piemonte Zone, western Alps, Italy: A review. *Period. Mineral.*, (76.2-3):127–153, 2007. ISSN 0369-8963. doi:10.2451/2007PM0021.

B. R. Hacker, S. M. Peacock, G. A. Abers, and S. D. Holloway. Subduction factory 2. Are intermediate-depth earthquakes in subducting slabs linked to metamorphic dehydration reactions? *J. Geophys.*

Res. Solid Earth, 108(B1), 2003. ISSN 2156-2202. doi:10.1029/2001JB001129.

J. Hermann, O. Müntener, and M. Scambelluri. The importance of serpentinite mylonites for subduction and exhumation of oceanic crust. *Tectonophysics*, 327(3):225–238, 2000. ISSN 0040-1951. doi:10.1016/S0040-1951(00)00171-2.

P. Herms, T. John, R. J. Bakker, and V. Schenk. Evidence for channelized external fluid flow and element transfer in subducting slabs (Raspas Complex, Ecuador). *Chemical Geology*, 310–311: 79–96, 2012. ISSN 0009-2541. doi:10.1016/j.chemgeo.2012.03.023.

M. A. Hesse, A. R. Schiemenz, Y. Liang, and E. M. Parmentier. Compaction-dissolution waves in an upwelling mantle column. *Geophys. J. Int.*, 187(3):1057–1075, 2011. doi:10.1111/j.1365-246x.2011.05177.x.

T. Holland and R. Powell. A Compensated-Redlich-Kwong (CORK) equation for volumes and fugacities of CO2 and H2O in the range 1 bar to 50 kbar and 100–1600°C. *Contr. Mineral. and Petrol.*, 109(2):265–273, 1991. ISSN 1432-0967. doi:10.1007/BF00306484.

T. J. B. Holland and R. Powell. An internally consistent thermodynamic data set for phases of petrological interest: An internally consistent thermodynamic data set. *J. Metamorph. Geol.*, 16 (3):309–343, 2004. ISSN 02634929, 15251314. doi:10.1111/j.1525-1314.1998.00140.x.

T. John, R. Klemd, J. Gao, and C.-D. Garbe-Schönberg. Trace-element mobilization in slabs due to non steady-state fluid–rock interaction: Constraints from an eclogite-facies transport vein in blueschist (Tianshan, China). *Lithos*, 103(1):1–24, 2008. ISSN 0024-4937. doi:10.1016/j.lithos.2007.09.005.

T. John, N. Gussone, Y. Y. Podladchikov, G. E. Bebout, R. Dohmen, R. Halama, R. Klemd, T. Magna, and H.-M. Seitz. Volcanic arcs fed by rapid pulsed fluid flow through subducting slabs. *Nat. Geosci.*, 5(7):489–492, 2012. ISSN 1752-0908. doi:10.1038/ngeo1482.

H. Jung, H. W. Green II, and L. F. Dobrzhinetskaya. Intermediate-depth earthquake faulting by dehydration embrittlement with negative volume change. *Nature*, 428(6982):545–549, 2004. ISSN 1476-4687. doi:10.1038/nature02412.

I. Katayama, T. Terada, K. Okazaki, and W. Tanikawa. Episodic tremor and slow slip potentially linked to permeability contrasts at the Moho. *Nat. Geosci.*, 5(10):731–734, 2012. doi:10.1038/ngeo1559.

E. D. Kempf, J. Hermann, E. Reusser, L. P. Baumgartner, and P. Lanari. The role of the antigorite + brucite to olivine reaction in subducted serpentinites (Zermatt, Switzerland). *Swiss J. Geosci.*, 113(1):16, 2020. ISSN 1661-8726, 1661-8734. doi:10.1186/s00015-020-00368-0.

F. Klein, S. Humphris, and W. Bach. Brucite formation and dissolution in oceanic serpentinite. *Geochem. Persp. Let.*, pages 1–5, 2020. ISSN 24103403. doi:10.7185/geochemlet.2035.

X.-P. Li, M. Rahn, and K. Bucher. Serpentinites of the Zermatt-Saas ophiolite complex and their texture evolution. *J. Metamorph. Geol.*, 22(3):159–177, 2004. ISSN 1525-1314. doi:10.1111/j.1525-1314.2004.00503.x.

V. López Sánchez-Vizcaíno, V. Trommsdorff, M. T. Gómez-Pugnaire, C. J. Garrido, O. Müntener, and J. A. D. Connolly. Petrology of titanian clinohumite and olivine at the high-pressure breakdown of antigorite serpentinite to chlorite harzburgite (Almirez Massif, S. Spain). *Contrib. Mineral. Petrol.*,

149(6):627–646, 2005. ISSN 1432-0967. doi:10.1007/s00410-005-0678-3.

V. López Sánchez-Vizcaíno, M. T. Gómez-Pugnaire, C. J. Garrido, J. A. Padrón-Navarta, and M. Mellini. Breakdown mechanisms of titanclinohumite in antigorite serpentinite (Cerro del Almirez massif, S. Spain): A petrological and TEM study. *Lithos*, 107(3-4):216–226, 2009. ISSN 00244937. doi:10.1016/j.lithos.2008.10.008.

R. Magott, O. Fabbri, and M. Fournier. Seismically-induced serpentine dehydration as a possible mechanism of water release in subduction zones. Insights from the Alpine Corsica pseudotachylyte-bearing Monte Maggiore ophiolitic unit. *Lithos*, 362–363:105474, 2020. ISSN 0024-4937. doi:10.1016/j.lithos.2020.105474.

B. Malvoisin, Y. Y. Podladchikov, and J. C. Vrijmoed. Coupling changes in densities and porosity to fluid pressure variations in reactive porous fluid flow: Local thermodynamic equilibrium. *Geochem. Geophys. Geosyst.*, 16(12):4362–4387, 2015. ISSN 1525-2027, 1525-2027. doi:10.1002/2015GC006019.

C. E. Manning. The chemistry of subduction-zone fluids. *Earth Planet. Sci. Lett.*, 223(1):1–16, 2004. ISSN 0012-821X. doi:10.1016/j.epsl.2004.04.030.

S. E. Mazza, A. Stracke, J. B. Gill, J.-I. Kimura, and T. Kleine. Tracing dehydration and melting of the subducted slab with tungsten isotopes in arc lavas. *Earth Planet. Sci. Lett.*, 530:115942, 2020. ISSN 0012-821X. doi:10.1016/j.epsl.2019.115942.

R. S. McGary, R. L. Evans, P. E. Wannamaker, J. Elsenbeck, and S. Rondenay. Pathway from subducting slab to surface for melt and fluids beneath Mount Rainier. *Nature*, 511(7509):338–+, 2014. ISSN 0028-0836. doi:10.1038/nature13493.

M. Merkulova, M. Muñoz, O. Vidal, and F. Brunet. Role of iron content on serpentinite dehydration depth in subduction zones: Experiments and thermodynamic modeling. *Lithos*, 264:441–452, 2016. ISSN 0024-4937. doi:10.1016/j.lithos.2016.09.007.

S. A. Miller, W. van der Zee, D. L. Olgaard, and J. A. D. Connolly. A fluid-pressure feedback model of dehydration reactions: Experiments, modelling, and application to subduction zones. *Tectonophysics*, 370(1):241–251, 2003. ISSN 0040-1951. doi:10.1016/S0040-1951(03)00189-6.

M. Moreno, C. Haberland, O. Oncken, A. Rietbrock, S. Angiboust, and O. Heidbach. Locking of the Chile subduction zone controlled by fluid pressure before the 2010 earthquake. *Nat. Geosci.*, 7(4): 292–296, 2014. ISSN 1752-0908. doi:10.1038/ngeo2102.

J. A. Padrón-Navarta, A. Tommasi, C. J. Garrido, V. L. Sánchez-Vizcaíno, M. T. Gómez-Pugnaire, A. Jabaloy, and A. Vauchez. Fluid transfer into the wedge controlled by high-pressure hydrofracturing in the cold top-slab mantle. *Earth Planet. Sci. Lett.*, 297(1):271–286, 2010. ISSN 0012-821X. doi:10.1016/j.epsl.2010.06.029.

J. A. Padrón-Navarta, V. L. Sánchez-Vizcaíno, J. Hermann, J. A. Connolly, C. J. Garrido, M. T. Gómez-Pugnaire, and C. Marchesi. Tschermak's substitution in antigorite and consequences for phase relations and water liberation in high-grade serpentinites. *Lithos*, 178:186–196, 2013. ISSN 00244937. doi:10.1016/j.lithos.2013.02.001.

F. Piccoli, J. J. Ague, X. Chu, M. Tian, and A. Vitale Brovarone. Field-Based Evidence

for Intra-Slab High-Permeability Channel Formation at Eclogite-Facies Conditions During Subduction. *Geochem. Geophys. Geosystems*, 22(3):e2020GC009520, 2021. ISSN 1525-2027. doi:10.1029/2020GC009520.

O. Plümper, T. John, Y. Y. Podladchikov, J. C. Vrijmoed, and M. Scambelluri. Fluid escape from subduction zones controlled by channel-forming reactive porosity. *Nature Geosci*, 10(2):150–156, 2017. ISSN 1752-0908. doi:10.1038/ngeo2865.

R. Powell and T. Holland. Relating formulations of the thermodynamics of mineral solid solutions; activity modeling of pyroxenes, amphiboles, and micas. *Am. Mineral.*, 84(1-2):1–14, 1999. ISSN 0003-004X. doi:10.2138/am-1999-1-201.

L. Räss, A. Licul, F. Herman, Y. Y. Podladchikov, and J. Suckale. Modelling thermomechanical ice deformation using a GPU-based implicit pseudo-transient method (FastICE v1.0). Preprint, Cryosphere, 2019.

L. H. Rüpke, J. P. Morgan, M. Hort, and J. A. D. Connolly. Serpentine and the subduction zone water cycle. *Earth Planet. Sci. Lett.*, 223(1):17–34, 2004. ISSN 0012-821X. doi:10.1016/j.epsl.2004.04.018.

M. Scambelluri, E. H. H. Strating, G. B. Piccardo, R. L. M. Vissers, and E. Rampone. Alpine olivine- and titanian clinohumite-bearing assemblages in the Erro-Tobbio peridotite (Voltri Massif, NW Italy). *J. Metamorph. Geol.*, 9(1):79–91, 1991. ISSN 0263-4929, 1525-1314. doi:10.1111/j.1525-1314.1991.tb00505.x.

M. Scambelluri, O. Müntener, J. Hermann, G. B. Piccardo, and V. Trommsdorff. Subduction of water into the mantle: History of an Alpine peridotite. *Geology*, 23(5):459, 1995. ISSN 0091-7613. doi:10.1130/0091-7613(1995)023<0459:SOWITM>2.3.CO;2.

M. Scambelluri, T. Pettke, E. Rampone, M. Godard, and E. Reusser. Petrology and Trace Element Budgets of High-pressure Peridotites Indicate Subduction Dehydration of Serpentinized Mantle (Cima di Gagnone, Central Alps, Switzerland). *J. Petrol.*, 55(3):459–498, 2014. ISSN 1460-2415. doi:10.1093/petrology/egt068.

M. W. Schmidt and S. Poli. Experimentally based water budgets for dehydrating slabs and consequences for arc magma generation. *Earth Planet. Sci. Lett.*, 163(1-4):361–379, 1998. ISSN 0012-821X. doi:10.1016/S0012-821X(98)00142-3.

R. M. Skarbek and A. W. Rempel. Dehydration-induced porosity waves and episodic tremor and slip. *Geochem. Geophys. Geosystems*, 17(2):442–469, 2016. ISSN 1525-2027, 1525-2027. doi:10.1002/2015GC006155.

C. Spandler, T. Pettke, and D. Rubatto. Internal and External Fluid Sources for Eclogite-facies Veins in the Monviso Meta-ophiolite, Western Alps: Implications for Fluid Flow in Subduction Zones. *Journal of Petrology*, 52(6):1207–1236, 2011. ISSN 0022-3530. doi:10.1093/petrology/egr025.

F. S. Spear. *Metamorphic Phase Equilibria and Pressure-Temperature-Time Paths*. Mineralogical Society of America, 1993.

M. Spiegelman, P. B. Kelemen, and E. Aharonov. Causes and consequences of flow organization during melt transport: The reaction infiltration instability in compactible media. *J. Geophys. Res.*

Solid Earth, 106(B2):2061–2077, 2001. doi:10.1029/2000jb900240.

S. Taetz, T. John, M. Bröcker, and C. Spandler. Fluid-rock interaction and evolution of a high-pressure/low-temperature vein system in eclogite from New Caledonia: Insights into intraslab fluid flow processes. *Contrib. Mineral. Petrol.*, 171(11):90, 2016. ISSN 1432-0967. doi:10.1007/s00410-016-1295-z.

P. Ulmer and V. Trommsdorff. Serpentine Stability to Mantle Depths and Subduction-Related Magmatism. *Science*, 268(5212):858–861, 1995. ISSN 0036-8075, 1095-9203. doi:10.1126/science.268.5212.858.

P. E. van Keken, B. R. Hacker, E. M. Syracuse, and G. A. Abers. Subduction factory: 4. Depth-dependent flux of H2O from subducting slabs worldwide. *J. Geophys. Res. Solid Earth*, 116(B1), 2011. ISSN 2156-2202. doi:10.1029/2010JB007922.

J. C. Vrijmoed and Y. Y. Podladchikov. Thermolab: A Thermodynamics Laboratory for Nonlinear Transport Processes in Open Systems. *Geochem. Geophys. Geosystems*, 23(4):e2021GC010303, 2022. ISSN 1525-2027. doi:10.1029/2021GC010303.

E. B. Watson and D. A. Wark. Diffusion of dissolved SiO_2 in H_2O at 1 GPa, with implications for mass transport in the crust and upper mantle. *Contrib. Mineral. Petrol.*, 130(1):66–80, 1997. doi:10.1007/s004100050350.

C. R. Wilson, M. Spiegelman, P. E. van Keken, and B. R. Hacker. Fluid flow in subduction zones: The role of solid rheology and compaction pressure. *Earth Planet. Sci. Lett.*, 401:261–274, 2014. ISSN 0012-821X. doi:10.1016/j.epsl.2014.05.052.

Chapter 4

A Porous-Media Model for Reactive Fluid-Rock Interaction in a Dehydrating Rock

Published as: Zafferi, A., **Huber, K.**, Peschka, D., Vrijmoed, J., John, T., & Thomas, M. (2023); A porous-media model for reactive fluid-rock interaction in a dehydrating rock. Journal of Mathematical Physics; 64 (9): 091504 (https://doi.org/10.1063/5.0148243)

Abstract

We study the GENERIC structure of models for reactive two-phase flows and their connection to a porous-media model for reactive fluid-rock interaction used in Geosciences. For this, we discuss the equilibration of fast dissipative processes in the GENERIC framework. Mathematical properties of the porous-media model and first results on its mathematical analysis are provided. The mathematical assumptions imposed for the analysis are critically validated with the thermodynamical rock data sets.

4.1 Introduction

During its journey towards the subduction zone, the oceanic lithosphere cools and becomes hydrated, so that the fluid is chemically bound in solid phases. During subduction into the earth mantle, in turn, the plates heat up and the hydrous minerals become unstable. The resulting dehydration reactions are strongly temperature-dependent, and due to the solid solutions of the minerals involved, this dehydration is a continuously evolving process driven

by the steady, slow heat flow into the plate, Figure 4.1 right. Evidence from the global volatile

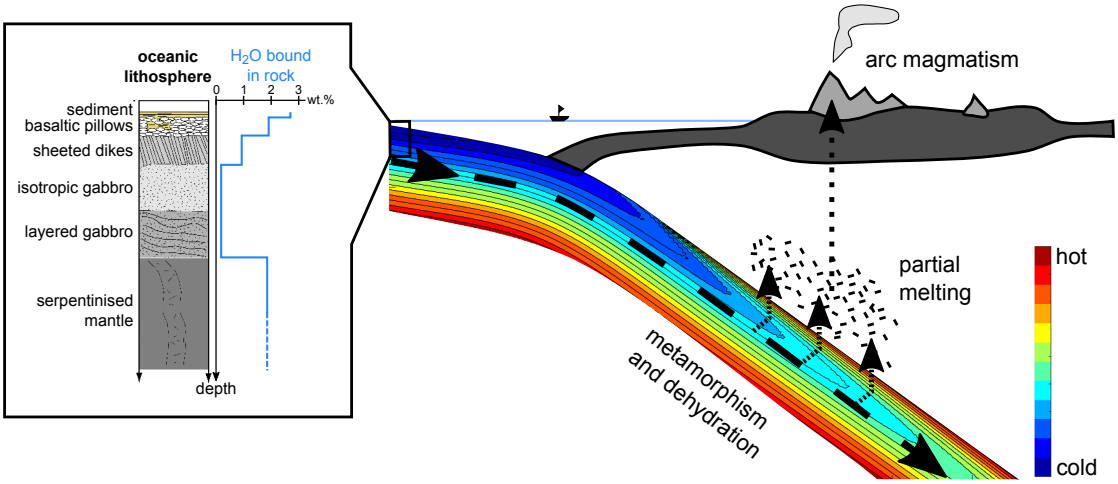

Figure 4.1: Schematic view of a subducting slab that heats up from top and below and therefore dehydrates on its way into the hot earth mantle. Colors within the slab indicate temperature. The left box shows a typical profile through the uppermost part of the slab as it enters the subduction zone. Different lithologies contain various amounts of H_2O that is bound in hydrous minerals. On its decent into the mantle the slab is heated up by heat conduction from the surrounding mantle. Increasing temperatures lead to dehydration, i.e. the release of the rock-bound H_2O in a free fluid phase (small dashed arrows). These fluids cause partial melting of the mantle which gives rise to arc magmatism at the surface. Dimensions are not to scale. Rock-bound H_2O contents are taken from Rüpke et al. (2004).

budget indicates (van Keken et al., 2011) that there must be a fluid escape mechanism that can keep pace with the slab descent velocity (cm/year) to avoid the fluid being lost to the earth interior.

This dynamic fluid escape mechanism leads fluid flow to organize itself into large-scale and high-flux transport systems through which fluids can escape from the subducting plate, (cf., e.g. van Keken et al., 2011; Plümper et al., 2017). In fact, it has been shown in various field-based studies that intra-slab fluid flow and fluid escape from the slab are channelized and reactive, (cf. e.g. Chen et al., 2019; John et al., 2012; Angiboust et al., 2014; Herms et al., 2012; Taetz et al., 2018; Padrón-Navarta et al., 2010).

Dehydration reactions often lead to a densification of the solid phases of the plate and thus to the formation of a fluid-filled porosity. The initial porosity forms at the sub-mm scale and is heterogeneously distributed across the rock as defined by the local bulk composition (Plümper et al., 2017). As dehydration progresses, these initial vein-like porosity structures merge and form a vein network that allows fluid flow in the rock (John et al., 2008; Taetz et al., 2018; Plümper et al., 2017; Bloch et al., 2018; Clément et al., 2020). Hereby, reactive

fluid flow is able to trigger further rcock dehydration and to transform an initially fine and small-scale high-porosity structure into wider and larger vein systems that may also develop reaction halos (Huber et al., 2022) by chemical interaction with the wall rock, cf. also (Taetz et al., 2018; John et al., 2012).

The works Plümper et al. (2017); Beinlich et al. (2020); Huber et al. (2022) develop thermodynamically consistent porous-media models which explain the generation of porosity and veining due to dehydration reactions. They provide a first step towards a mechanistic understanding on how dehydration leads from the first stage of chemistry-controlled local dehydration to the development of intra-slab flow structures that are highly channelized. These channels may show only limited interaction with the wall rock, (cf. e.g. Breeding and Ague, 2002; Spandler et al., 2011; Herms et al., 2012), but they may also have well-developed reaction halos, (cf. e.g. Taetz et al., 2018; John et al., 2012; Huber et al., 2022).

In this work we discuss the porous-media models developed in Plümper et al. (2017); Beinlich et al. (2020); Huber et al. (2022) in more detail from a mathematical point of view. In particular, the porous-media model deduced in Plümper et al. (2017) takes the following form

$$\partial_t\big(\hat{\varrho}_\mathrm{s}(1-X_\mathrm{h})(1-\phi)\big) = 0 \tag{4.1a}$$

$$\partial_t\big(\hat{\varrho}_\mathrm{s}(1-\phi)+\hat{\varrho}_\mathrm{f}\phi\big) = \nabla\cdot\Big(\hat{\varrho}_\mathrm{f}K(\phi)\nabla\pi\Big), \tag{4.1b}$$

Here, ϕ denotes the porosity, π the fluid pressure, and X_h the H_2O-content of the solid phase. Moreover, with index $i \in \{\mathrm{f},\mathrm{s}\}$ for fluid and solid $\hat{\varrho}_\mathrm{i}$ denotes the "pure" mass density of the respective phase and the expression $K(\phi)$ is a Kozeny–Carman-type permeability of the form $K(\phi) = \frac{\kappa}{\mu}\phi^3$ with positive constants $\kappa, \mu > 0$. In this way, (4.1a) expresses the conservation of mass for the immobile solid and (4.1b) provides the conservation of total mass. Given suitable initial data, one observes that (4.1a) may be explicitly solved for the porosity

$$\phi = 1 - \frac{\hat{\varrho}_\mathrm{s}^0(1-X_\mathrm{h}^0)(1-\phi^0)}{\hat{\varrho}_\mathrm{s}(1-X_\mathrm{h})},$$

where quantities with superscript 0 denote given initial data. Additionally, the models studied in Huber et al. (2022); Beinlich et al. (2020) also take into account the influence of further chemical species transported with the fluid on the dehydration process. This chemical species is CO_2 in Beinlich et al. (2020) and SiO_2 in Huber et al. (2022). It is assumed to undergo

a diffusion process in the fluid phase, so that the model in Huber et al. (2022) reads:

$$\partial_t\big(\hat{\varrho}_\mathsf{s}(1-\phi)+\hat{\varrho}_\mathsf{f}\phi\big) = \nabla\cdot\Big(\hat{\varrho}_\mathsf{f}K(\phi)\nabla\pi\Big), \tag{4.2a}$$

$$\partial_t\big(\hat{\varrho}_\mathsf{s}c_\mathsf{s}(1-\phi)+\hat{\varrho}_\mathsf{f}c_\mathsf{f}\phi\big) = \nabla\cdot\Big(\hat{\varrho}_\mathsf{f}c_\mathsf{f}K(\phi)\nabla\pi+\hat{\varrho}_\mathsf{f}c_\mathsf{f}\phi D_c\nabla c_\mathsf{f}\Big), \tag{4.2b}$$

$$\phi = 1-\tfrac{\hat{\varrho}_\mathsf{s}^0(1-c_\mathsf{s}^0-X_\mathsf{h}^0)(1-\phi^0)}{\hat{\varrho}_\mathsf{s}(1-c_\mathsf{s}-X_\mathsf{h})} \tag{4.2c}$$

where ϕ, π, X_h, $\hat{\varrho}_\mathsf{f}$, $\hat{\varrho}_\mathsf{s}$, and $K(\phi)$ have the same meaning as in (4.1). In addition, with index $i\in\{\mathsf{f},\mathsf{s}\}$ for fluid and solid c_i is the SiO_2-content of the respective phase and D_c in (4.2) is a diffusion coefficient. Again, quantities with superscript 0 denote given initial data. In Plümper et al. (2017), resp. Huber et al. (2022), systems are numerically solved for the unknowns ϕ,π, and c_s by a finite difference method, whereas the remaining quantities $c_\mathsf{f}=\tilde{c}_\mathsf{f}(\pi,c_\mathsf{s},\theta), X_\mathsf{h}=\tilde{X}_\mathsf{h}(\pi,c_\mathsf{s},\theta), \hat{\varrho}_i=\tilde{\hat{\varrho}}_i(\pi,c_\mathsf{s},\theta), i\in\{\mathsf{s},\mathsf{f}\}$, implicitly depend on the unknowns and on the (given) temperature θ. Their values are obtained from equilibrium thermodynamical closing relations. In this present work we further discuss models (4.1) and (4.2) from a mathematical point of view.

First, based on our findings in Zafferi and Thomas (2023), we investigate the thermodynamical structure of models (4.1) and (4.2) in the framework GENERIC (the acronym for General Equations of Non-Equilibrium Reversible Irreversible Coupling).

For this, we briefly review the modeling concept of GENERIC in Section 4.2 and use it to develop a model for reactive two-phase Darcy flows, cf. Section 4.2.3 Many porous-media models in literature also consider chemical reactions in a thermodynamically consistent way, (Orava et al., 2015; Ehlers, 2009).

Yet, many treat reactions only within a phase or the exchange of mass between the different phases is incorporated by rather heuristic exchange terms (Coussy, 2004; Aregba-Driollet et al., 2004; Krause, 2014).

The reactive two-phase Darcy-flow model, that we obtain with the aid of the GENERIC framework, allows for the exchange of mass between the different phases by chemical reactions, where the corresponding reaction terms are directly inferred from the thermodynamical functionals and dissipative operators related to the chemical reactions. In this way the exchange process is incorporated in a thermodynamically consistent way and the structure of the process including the reaction kinetics is highlighted very well.

As mentioned above, in the works Plümper et al. (2017); Beinlich et al. (2020); Huber et al. (2022) the determination of the quantities c_f, X_h, $\hat{\varrho}_\mathsf{s}$, and $\hat{\varrho}_\mathsf{f}$ stems from equilibrium thermodynamical closing relations deduced by Gibbs minimization. This approach rests on the assumption that chemical reactions take place on much faster time scales than flow and

transport so that they can be assumed to be in local equilibrium.

In Section 4.3 we therefore discuss the local equilibrium of fast dissipative processes in the GENERIC framework and deduce equations for the effective system. For this, we follow the ideas of Mielke et al. (2021). We apply this approach to the equilibration of temperature in the two-phase system and to the equilibration of chemical reactions.

These considerations put us in the position to show in Section 4.4 that the models (4.1) and (4.2) originate from the reactive two-phase Darcy flow model deduced in Section 4.2.3 by equilibration of the fast reactions. Finally, Section 4.5 provides first analytical results on the existence of weak solutions for the models. Here we take into account the discretization scheme used in Huber et al. (2022) for the numerical simulations and we critically discuss the mathematical assumptions with respect to the evidence of the thermodynamical properties given by the chemical composition of the rock samples considered in Plümper et al. (2017); Huber et al. (2022)

4.2 GENERIC Structure of Reactive Two-Phase Systems

Short introduction to the GENERIC framework The thermodynamical modeling framework of GENERIC (General Equations of Non-Equilibrium Reversible Irreversible Coupling) was introduced by Öttinger and Grmela in Grmela and Öttinger (1997); Öttinger and Grmela (1997). It characterizes the evolution of a thermodynamical system in terms of a state space $\mathcal{Q}$ with dual $\mathcal{Q}^*$, thermodynamical potentials such as energy $\mathcal{E}$ and entropy $\mathcal{S}$, and geometric structures $\mathbb{J}$ and $\mathbb{K}$, which encode the reversible (Hamiltonian) or irreversible (Onsager) nature of the process. Characteristically for this, the Poisson structure $\mathbb{J}(\mathbf{q}) : \mathcal{Q}^* \to \mathcal{Q}$ is antisymmetric $\mathbb{J}^* = -\mathbb{J}$ and satisfies Jacobi's identity, whereas the Onsager operator $\mathbb{K}(\mathbf{q}) : \mathcal{Q}^* \to \mathcal{Q}$ is positively semidefinite $\langle \xi, \mathbb{K}(\mathbf{q})\xi \rangle \geq 0$ for all $\xi \in \mathcal{Q}^*$ and symmetric $\mathbb{K}^* = \mathbb{K}$. The triple $(\mathcal{Q}, \mathcal{E}, \mathbb{J})$ forms a Hamiltonian system for reversible dynamics and the triple $(\mathcal{Q}, \mathcal{S}, \mathbb{K})$ forms an Onsager, resp. gradient system for dissipative dynamics. A GENERIC system $(\mathcal{Q}, \mathcal{E}, \mathcal{S}, \mathbb{J}, \mathbb{K})$ couples the two via the non-interaction conditions (NIC)

$$\mathbb{J}(\mathbf{q})\mathrm{D}\mathcal{S}(\mathbf{q}) = 0 = \mathbb{K}(\mathbf{q})\mathrm{D}\mathcal{E}(\mathbf{q}), \tag{4.3}$$

and the mass conservation condition

$$\mathbb{J}(\mathbf{q})\mathrm{D}\mathcal{M}(\mathbf{q}) = 0 = \mathbb{K}(\mathbf{q})\mathrm{D}\mathcal{M}(\mathbf{q}) \tag{4.4}$$

Table 4.1: List of most recurring symbols in this chapter with references to definitions, sections and relevant examples.

Symbol(s)	Unit	Definition	Reference
Ω		Spatial domain in $\mathbb{R}^d$	(4.6)
$\mathbf{v}_i$	$\mathrm{m\,s^{-1}}$	Velocity of solid-s and fluid-f	(4.7)
$\mathbf{P}_i$		Momentum density of solid-s and fluid-f	(4.11)
$\mathbf{C}_i$		Concentration density vector of solid-s and fluid-f	(4.11),(4.12), Ex. 4.2.2
U_i	$\mathrm{J\,m^{-3}}$	Internal energy density of solid-s and fluid-f	(4.11)
S_i	$\mathrm{J\,K^{-1}\,m^{-3}}$	Entropy density of solid-s and fluid-f	(4.3),(4.13),(4.24)
E_i	$\mathrm{J\,m^{-3}}$	Total energy density of solid-s and fluid-f	(4.3),(4.13)
$\mathbf{M}_i$	$\mathrm{kg\,mol^{-1}}$	Vector of molar masses of solid-s and fluid-f	(4.12),Ex. 4.2.2
ϱ_i	$\mathrm{kg\,m^{-3}}$	Mass density of solid-s and fluid-f	(4.12)
π_i	Pa	Pressure of solid-s and fluid-f	(4.14)
θ_i	K	Temperature of solid-s and fluid-f	(4.14)
μ_i	$\mathrm{J\,mol^{-1}}$	Chemical potential of solid-s and fluid-f	(4.14)
ϕ	vol. fr.	Porosity	(4.1), (4.2), Sec. 4.4.2
$\hat{\varrho}_\mathrm{i}$	$\mathrm{kg\,m^{-3}}$	"pure" mass density of solid-s and fluid-f	(4.1), (4.2), (4.66)
$c_\mathrm{f}, c_\mathrm{s}$	wt. fr.	SiO_2 content of solid-s and fluid-f	Sec. 4.4.3
X_h	wt. fr.	H_2O in solid	(4.2), Sec. 4.4.2
$\mathbf{q}$		State vector	Sec. 4.2, (4.11)
$\dot{\mathbf{q}} = \partial_t \mathbf{q}$		Partial time derivative of $\mathbf{q}$	(4.1),(4.2),(4.5)
$\mathcal{Q}, \mathcal{Q}^*$		State space and its dual	Sec. 4.2
$\boldsymbol{\eta}, \boldsymbol{\xi}$		Element of $\mathcal{Q}^*$	(4.21a)
$\mathcal{E}$	J	Total energy functional	Sec. 4.2, (4.13)
$\mathcal{S}$	$\mathrm{J\,K^{-1}}$	Total entropy functional	Sec. 4.2, (4.13), (4.24)
$\mathbb{J}$		Poisson operator	Sec. 4.2, (4.16)
$\mathbb{K}$		Onsager operator	Sec. 4.2, (4.17),(4.26)
$\mathrm{D}\mathcal{A}$		Functional derivative	Sec. 4.2, (4.15)
T		Transformation between state spaces	
$\mathbb{L}, \mathbb{L}^*$		Fréchet derivative of T, $\mathbb{L} := \mathrm{DT}$ and its adjoint $\mathbb{L}^*$	

for the total mass $\mathcal{M}$ of the system. We call conditions (4.3) and (4.4) degeneracy conditions. Above, D denotes the Fréchet derivative of the driving functional with respect to $\mathbf{q}$. The properties of $\mathbb{J}$ and $\mathbb{K}$ together with the NIC (4.3) ensure the compatibility of the system with the laws of thermodynamics and (4.4) ensures the conservation of the total mass of the system. The evolution of a state vector $\mathbf{q} : [0, \mathrm{T}] \to \mathcal{Q}$ describing the mechanical and thermodynamical properties of the system is then given by

$$\partial_t \mathbf{q} = \mathbb{J}(\mathbf{q})\mathrm{D}\mathcal{E}(\mathbf{q}) + \mathbb{K}(\mathbf{q})\mathrm{D}\mathcal{S}(\mathbf{q})\,. \tag{4.5}$$

For more details on the GENERIC framework we refer to Grmela and Öttinger (1997); Öttinger and Grmela (1997) and with regard to transformation properties of GENERIC systems, we refer the reader to Zafferi et al. (2022).

In Zafferi et al. (2022) we discussed the GENERIC framework for reactive fluid flows. In this section we extend these results to multiphase systems. For this, we will introduce a two-phase Darcy model in Section 4.2.1 and study a multiphase system with diffusion and chemical reactions between the two phases in Section 4.2.2. Subsequently, we will combine these results in Section 4.2.3 to obtain the GENERIC structure of reactive two-phase Darcy flows.

Kinematics of two-phase flows We follow here the approach to the theory of porous media as outlined e.g. in Ehlers (2009) and describe the two-phase system, consisting of a fluid (f) and a solid (s) phase, in the Eulerian frame, where $\Omega(t) \subset \mathbb{R}^d$ denotes the domain in Eulerian coordinates at time $t \in [0, \mathrm{T}]$. To each phase $i \in \{\mathrm{f}, \mathrm{s}\}$ there is an associated reference domain $\bar{\Omega}_i \subset \mathbb{R}^d$ and a sufficiently smooth flow map $\bar{\boldsymbol{\chi}}_i : [0, \mathrm{T}] \times \bar{\Omega}_i \to \mathbb{R}^d$, $(t, \bar{\mathbf{x}}) \in [0, \mathrm{T}] \times \bar{\Omega}_i \mapsto \mathbf{x} = \bar{\boldsymbol{\chi}}_i(t, \bar{\mathbf{x}}) \in \Omega(t)$, so that

$$\Omega(t) := \{\mathbf{x} \in \mathbb{R}^d,\, \mathbf{x} = \bar{\boldsymbol{\chi}}_i(t, \bar{\mathbf{x}}_i) \text{ for some } \bar{\mathbf{x}}_i \in \bar{\Omega}_i\} \quad \text{for } i \in \{\mathrm{s}, \mathrm{f}\}\,. \tag{4.6}$$

When there is no chance for misunderstanding, we omit indicating the time dependence of the current configuration, i.e., we write Ω for $\Omega(t)$. The motion of phase i is characterized by the following ODE Cauchy problem

$$\partial_t \bar{\boldsymbol{\chi}}_i(t, \bar{x}) = \mathbf{v}_i(t, \bar{\boldsymbol{\chi}}_i(t, \bar{x})) \qquad \text{for all } \bar{x} \in \bar{\Omega}_i,\ t \in [0, \mathrm{T}]\,, \tag{4.7a}$$

$$\bar{\boldsymbol{\chi}}_i(0, \bar{x}) = \bar{x} \qquad \text{for all } \bar{x} \in \bar{\Omega}_i\,, \tag{4.7b}$$

where $\mathbf{v}_i : [0, \mathrm{T}] \times \Omega(t) \to \mathbb{R}^d$ denotes the Eulerian velocity field of phase i and we ask that

$$\mathbf{v}_\mathrm{s}(t, \cdot) = \mathbf{v}_\mathrm{f}(t, \cdot) \ \text{ on } \ \partial\Omega(t)\,. \tag{4.8}$$

In order to ensure that the flow map is orientation-preserving, we claim that its Jacobi determinant is positive, i.e.,

$$\bar{V}_i := \det \bar{\nabla} \bar{\boldsymbol{\chi}}_i > 0\,, \tag{4.9}$$

and we denote the Jacobi matrix by

$$F_i := \bar{\nabla} \bar{\boldsymbol{\chi}}_i\,, \quad \text{where } (F_i)_{kI} = (\bar{\nabla} \bar{\boldsymbol{\chi}}_i)_{kI} = (\partial_{\bar{x}_I} (\bar{\boldsymbol{\chi}}_i)_k) \tag{4.10}$$

where $\bar{\mathbf{x}} = (\bar{x}_1, \dots, \bar{x}_d)^\top$ are the coordinates of the Lagrangian domain $\bar{\Omega}_i$ of phase i.

4.2.1 Two-Phase Darcy Flow

We now deduce the GENERIC structure for a two-phase Darcy model without reactions but with an interphase friction term. For this we extend our findings from Zafferi et al. (2022, Sec. 6) to the two-phase setting. To keep the presentation concise, we directly start the considerations in Eulerian coordinates. As described above, the state $\mathbf{q} \in \mathcal{Q}$ of the multiphase flow is defined by a vector of fluid (f) and solid (s) quantities

$$\mathbf{q} = \begin{pmatrix} \mathbf{q}_\mathsf{s} \\ \mathbf{q}_\mathsf{f} \end{pmatrix} = \begin{pmatrix} \mathbf{P}_\mathsf{s} : \Omega \to \mathbb{R}^d \\ \mathbf{C}_\mathsf{s} : \Omega \to \mathbb{R}^{N_\mathsf{s}} \\ U_\mathsf{s} : \Omega \to \mathbb{R} \\ \mathbf{P}_\mathsf{f} : \Omega \to \mathbb{R}^d \\ \mathbf{C}_\mathsf{f} : \Omega \to \mathbb{R}^{N_\mathsf{f}} \\ U_\mathsf{f} : \Omega \to \mathbb{R} \end{pmatrix} . \tag{4.11}$$

In each phase $i \in \{\mathsf{s}, \mathsf{f}\}$ there are N_i components with a vector of concentrations $\mathbf{C}_i = (C_{i,k})_{k=1}^{N_i} \in \mathbb{R}^{N_i}$ and a corresponding vector of molar masses $\mathbf{M}_i = (M_{i,k})_{k=1}^{N_i} \in \mathbb{R}^{N_i}$, such that each phase has the mass density ϱ_i and the total mass density is ϱ_tot defined by

$$\varrho_i = \sum_{k=1}^{N_i} M_{i,k} C_{i,k} = \mathbf{M}_i \cdot \mathbf{C}_i \quad \text{and} \quad \varrho_\mathsf{tot} = \varrho_\mathsf{s} + \varrho_\mathsf{f}. \tag{4.12}$$

Additionally, each phase has a separate momentum $\mathbf{P}_i$ and internal energy U_i. At this point we observe that the quantities here defined account already for the volume fraction of the respective phase. Definitions of "pure" and "partial" quantities and their relation to volume fractions are treated in Sec. 4.4.2.

Above notation allows us to define the functionals for total energy $\mathcal{E}$ and entropy $\mathcal{S}$ as

$$\mathcal{E}(\mathbf{q}) := \int_\Omega E_\mathsf{s}(\mathbf{q}_\mathsf{s}) + E_\mathsf{f}(\mathbf{q}_\mathsf{f}) \,\mathrm{d}\mathbf{x} \quad \text{with} \quad E_i(\mathbf{q}_i) = \frac{|\mathbf{P}_i|^2}{2\varrho_i} + U_i \,, \tag{4.13a}$$

$$\mathcal{S}(\mathbf{q}) := \int_\Omega S_\mathsf{s}(\mathbf{C}_\mathsf{s}, U_\mathsf{s}) + S_\mathsf{f}(\mathbf{C}_\mathsf{f}, U_\mathsf{f}) \,\mathrm{d}\mathbf{x} \,, \tag{4.13b}$$

where the total energy and entropy densities are $E = E_\mathsf{s} + E_\mathsf{f}$ and $S = S_\mathsf{s} + S_\mathsf{f}$. The entropies satisfy the Gibbs relations

$$\frac{\pi_i}{\theta_i} := S_i - \mathbf{C}_i \partial_{\mathbf{C}_i} S_i - U_i \partial_{U_i} S_i, \qquad \frac{1}{\theta_i} := \partial_{U_i} S_i, \qquad \frac{\mu_i}{\theta_i} := \partial_{\mathbf{C}_i} S_i \tag{4.14}$$

separately for each phase $i \in \{\mathsf{s},\mathsf{f}\}$ with pressure π_i, temperature θ_i, and chemical potential μ_i. This gives the driving forces for the GENERIC evolution as

$$\mathrm{D}\mathcal{E}(\mathbf{q}) = \boldsymbol{\eta} = \begin{pmatrix} \mathbf{P}_\mathsf{s}/\varrho_\mathsf{s} \\ 0 \\ 1 \\ \mathbf{P}_\mathsf{f}/\varrho_\mathsf{f} \\ 0 \\ 1 \end{pmatrix}, \qquad \mathrm{D}\mathcal{S}(\mathbf{q}) = \boldsymbol{\xi} = \begin{pmatrix} 0 \\ \mu_\mathsf{s}/\theta_\mathsf{s} \\ 1/\theta_\mathsf{s} \\ 0 \\ \mu_\mathsf{f}/\theta_\mathsf{f} \\ 1/\theta_\mathsf{f} \end{pmatrix}, \tag{4.15}$$

where we will denote with the subscript $\mathrm{D}_a\mathcal{A}, \xi_a$ and η_a the a-component of the vectors $\mathrm{D}\mathcal{A}, \boldsymbol{\xi}, \boldsymbol{\eta}$. The reversible dynamics of the system follows the evolution given by the Poisson structure

$$\mathbb{J}(\mathbf{q}) = \begin{pmatrix} \mathbb{J}_{\mathbf{P}_\mathsf{s}\mathbf{P}_\mathsf{s}} & \mathbb{J}_{\mathbf{P}_\mathsf{s}\mathbf{C}_\mathsf{s}} & \mathbb{J}_{\mathbf{P}_\mathsf{s}U_\mathsf{s}} & 0 & 0 & 0 \\ \mathbb{J}_{\mathbf{C}_\mathsf{s}\mathbf{P}_\mathsf{s}} & 0 & 0 & 0 & 0 & 0 \\ \mathbb{J}_{U_\mathsf{s}\mathbf{P}_\mathsf{s}} & 0 & 0 & 0 & 0 & 0 \\ 0 & 0 & 0 & \mathbb{J}_{\mathbf{P}_\mathsf{f}\mathbf{P}_\mathsf{f}} & \mathbb{J}_{\mathbf{P}_\mathsf{f}\mathbf{C}_\mathsf{f}} & \mathbb{J}_{\mathbf{P}_\mathsf{f}U_\mathsf{f}} \\ 0 & 0 & 0 & \mathbb{J}_{\mathbf{C}_\mathsf{f}\mathbf{P}_\mathsf{f}} & 0 & 0 \\ 0 & 0 & 0 & \mathbb{J}_{U_\mathsf{f}\mathbf{P}_\mathsf{f}} & 0 & 0 \end{pmatrix} \quad \text{with} \quad \begin{aligned} \mathbb{J}_{\mathbf{P}_i\mathbf{P}_i}\square &:= -(\nabla\square)^\top\mathbf{P}_i - \nabla\cdot(\mathbf{P}_i\otimes\square)\,, \\ \mathbb{J}_{\mathbf{P}_i\mathbf{C}_i}\square &:= -(\nabla\square)^\top\mathbf{C}_i\,, \\ \mathbb{J}_{\mathbf{C}_i\mathbf{P}_i}\square &:= -\nabla\cdot(\mathbf{C}_i\otimes\square)\,, \\ \mathbb{J}_{\mathbf{P}_iU_i}\square &:= -U_i\nabla\square + \nabla(\square\pi_i)\,, \\ \mathbb{J}_{U_i\mathbf{P}_i}\square &:= -\nabla\cdot(U_i\square) + \pi_i\nabla\cdot\square\,. \end{aligned} \tag{4.16}$$

The irreversible processes are encoded in an Onsager operator

$$\mathbb{K}(\mathbf{q}) = \begin{pmatrix} \mathbb{K}_{\mathsf{ss}}(\mathbf{q}) & \mathbb{K}_{\mathsf{sf}}(\mathbf{q}) \\ \mathbb{K}_{\mathsf{fs}}(\mathbf{q}) & \mathbb{K}_{\mathsf{ff}}(\mathbf{q}) \end{pmatrix} = \begin{pmatrix} \mathbb{K}^\mathsf{s}_\mathsf{visc} + \mathbb{K}^\mathsf{s}_\mathsf{ht} & 0 \\ 0 & \mathbb{K}^\mathsf{f}_\mathsf{visc} + \mathbb{K}^\mathsf{f}_\mathsf{ht} \end{pmatrix} + \begin{pmatrix} \mathbb{K}^\mathsf{ss}_\mathsf{he} + \mathbb{K}^\mathsf{ss}_\mathsf{fric} & \mathbb{K}^\mathsf{sf}_\mathsf{he} + \mathbb{K}^\mathsf{sf}_\mathsf{fric} \\ \mathbb{K}^\mathsf{fs}_\mathsf{he} + \mathbb{K}^\mathsf{fs}_\mathsf{fric} & \mathbb{K}^\mathsf{ff}_\mathsf{he} + \mathbb{K}^\mathsf{ff}_\mathsf{fric} \end{pmatrix}, \tag{4.17}$$

where each of the blocks $\mathbb{K}_{ji}$ for $i,j \in \{\mathsf{s},\mathsf{f}\}$ is a 3×3 block acting on the derivatives of $\mathcal{S}$ with respect to $\mathbf{q}_i = (\mathbf{P}_i, \mathbf{C}_i, U_i)^\top$. Single-phase effects are solely encoded in the diagonal operators $\mathbb{K}_{\mathsf{ss}}, \mathbb{K}_{\mathsf{ff}}$ and interaction terms are encoded in all the components of $\mathbb{K}$. We consider irreversible processes due to single-phase Stokesian viscous dissipation $\mathbb{K}^i_\mathsf{visc}$ and heat transport $\mathbb{K}^i_\mathsf{ht}$. Phase interaction is due to interfacial friction $\mathbb{K}^{ij}_\mathsf{fric}$ and due to heat exchange $\mathbb{K}^{ij}_\mathsf{he}$. First we consider the single-phase effect of viscous dissipation

$$\mathbb{K}^i_{\text{visc}} = \begin{pmatrix} \mathbb{K}^{\text{visc},i}_{\mathbf{PP}} & 0 & \mathbb{K}^{\text{visc},i}_{\mathbf{P}U} \\ 0 & 0 & 0 \\ \mathbb{K}^{\text{visc},i}_{U\mathbf{P}} & 0 & \mathbb{K}^{\text{visc},i}_{UU} \end{pmatrix} \quad \text{with} \quad \begin{aligned} \mathbb{K}^{\text{visc},i}_{\mathbf{PP}}\Box &:= -\nabla\cdot\left(2\theta_i\lambda_i\nabla_{\text{s}}\Box + \theta_i\zeta_i\text{tr}(\nabla_{\text{s}}\Box)\mathbb{I}_d\right), \\ \mathbb{K}^{\text{visc},i}_{UU}\Box &:= \left(2\theta_i\lambda_i|\nabla_{\text{s}}\mathbf{v}_i|^2 + \theta_i\zeta_i\,\text{tr}(\nabla_{\text{s}}\mathbf{v}_i)^2\right)\Box, \\ \mathbb{K}^{\text{visc},i}_{U\mathbf{P}}\Box &:= -\left(2\theta_i\lambda_i\nabla_{\text{s}}\Box + \theta_i\zeta_i\text{tr}(\nabla_{\text{s}}\Box)\mathbb{I}_d\right):\nabla\mathbf{v}_i, \\ \mathbb{K}^{\text{visc},i}_{\mathbf{P}U}\Box &:= \nabla\cdot\left((2\theta_i\lambda_i\nabla_{\text{s}}\mathbf{v}_i + \theta_i\zeta_i\text{tr}(\nabla_{\text{s}}\mathbf{v}_i)\mathbb{I}_d)\Box\right), \end{aligned} \tag{4.18}$$

where λ_i, ζ_i are the viscous parameter of the solid and fluid Stokes dissipation and $\mathbf{v}_i = \mathbf{P}_i/\varrho_i$ the single-phase velocity. Furthermore we have the symmetric gradient $\nabla_{\text{s}}\Box = \frac{1}{2}(\nabla\Box + \nabla\Box^\top)$. The heat conduction is given by the operator

$$\mathbb{K}^i_{\text{ht}} = \begin{pmatrix} 0 & 0 & 0 \\ 0 & 0 & 0 \\ 0 & 0 & \mathbb{K}^{\text{ht},i}_{UU} \end{pmatrix} \quad \text{with} \quad \mathbb{K}^{\text{ht},i}_{UU}\Box := -\nabla\cdot\left(\theta_i^2 k_i\nabla\Box\right), \tag{4.19}$$

where k_i is the heat conduction of each phase. The heat exchange is of the 6×6 block form

$$\begin{pmatrix} \mathbb{K}^{\text{ss}}_{\text{he}} & \mathbb{K}^{\text{sf}}_{\text{he}} \\ \mathbb{K}^{\text{fs}}_{\text{he}} & \mathbb{K}^{\text{ff}}_{\text{he}} \end{pmatrix} = k_{\text{he}}(\mathbf{q}) \begin{pmatrix} 0 & 0 & 0 & 0 & 0 & 0 \\ 0 & 0 & 0 & 0 & 0 & 0 \\ 0 & 0 & +1 & 0 & 0 & -1 \\ 0 & 0 & 0 & 0 & 0 & 0 \\ 0 & 0 & 0 & 0 & 0 & 0 \\ 0 & 0 & -1 & 0 & 0 & +1 \end{pmatrix} \tag{4.20}$$

for some given heat exchange coefficient function $k_{\text{he}}(\mathbf{q}) \geq 0$. The isotropic Darcy interaction between the two phases is generated by the dual dissipation potential

$$\Psi^*_{\text{fric}}(\mathbf{q}, \boldsymbol{\xi}) = \int_\Omega \frac{K_{\text{D}}}{2}\frac{\theta_{\text{s}}\theta_{\text{f}}}{\theta_{\text{s}}+\theta_{\text{f}}}|\mathbf{w}|^2\,\text{d}\mathbf{x}, \tag{4.21a}$$

where $\mathbf{w} = \xi_{\mathbf{P}_{\text{s}}} - \xi_{\mathbf{P}_{\text{f}}} - (\alpha\xi_{U_{\text{s}}} + (1-\alpha)\xi_{U_{\text{f}}})\gamma$. Here $\gamma = (\mathbf{v}_{\text{s}} - \mathbf{v}_{\text{f}})$ and $\alpha(\mathbf{q}) \in (0,1)$ is arbitrary and controls how much of the generated entropy is converted into heat of the solid

and fluid phase, respectively. The Onsager operator corresponding to this dual dissipation is

$$\mathbb{K}_{\text{fric}} = K_{\text{D}}(\mathbf{q})\frac{\theta_{\text{s}}\theta_{\text{f}}}{\theta_{\text{s}}+\theta_{\text{f}}}\begin{pmatrix} +1 & 0 & -\gamma\alpha & -1 & 0 & -\gamma(1-\alpha) \\ 0 & 0 & 0 & 0 & 0 & 0 \\ -\gamma\alpha & 0 & \gamma^2\alpha^2 & \gamma\alpha & 0 & |\gamma|^2\alpha(1-\alpha) \\ -1 & 0 & \gamma\alpha & +1 & 0 & \gamma(1-\alpha) \\ 0 & 0 & 0 & 0 & 0 & 0 \\ -\gamma(1-\alpha) & 0 & |\gamma|^2\alpha(1-\alpha) & \gamma(1-\alpha) & 0 & |\gamma|^2(1-\alpha)^2 \end{pmatrix}. \tag{4.21b}$$

Based on these definitions, the GENERIC evolution of the compressible two-phase flow reads

$$\dot{\mathbf{P}}_{\text{s}} + \nabla\cdot(\mathbf{P}_{\text{s}}\otimes\mathbf{v}_{\text{s}}) = -\nabla\pi_{\text{s}} - K_{\text{D}}\gamma + \nabla\cdot\boldsymbol{\sigma}_{\text{s}}\,, \tag{4.22a}$$

$$\dot{\mathbf{P}}_{\text{f}} + \nabla\cdot(\mathbf{P}_{\text{f}}\otimes\mathbf{v}_{\text{f}}) = -\nabla\pi_{\text{f}} + K_{\text{D}}\gamma + \nabla\cdot\boldsymbol{\sigma}_{\text{f}}\,, \tag{4.22b}$$

$$\dot{\mathbf{C}}_{\text{s}} + \nabla\cdot(\mathbf{C}_{\text{s}}\otimes\mathbf{v}_{\text{s}}) = 0\,, \tag{4.22c}$$

$$\dot{\mathbf{C}}_{\text{f}} + \nabla\cdot(\mathbf{C}_{\text{f}}\otimes\mathbf{v}_{\text{f}}) = 0\,, \tag{4.22d}$$

$$\dot{U}_{\text{s}} + \nabla\cdot(U_{\text{s}}\mathbf{v}_{\text{s}}) = -\pi_{\text{s}}\nabla\cdot\mathbf{v}_{\text{s}} + \alpha K_{\text{D}}|\gamma|^2 + k_{\text{he}}(\theta_{\text{s}}^{-1}-\theta_{\text{f}}^{-1}) + \nabla\cdot(k_{\text{s}}\nabla\theta_{\text{s}})\,, \tag{4.22e}$$

$$\dot{U}_{\text{f}} + \nabla\cdot(U_{\text{f}}\mathbf{v}_{\text{f}}) = -\pi_{\text{f}}\nabla\cdot\mathbf{v}_{\text{f}} + (1-\alpha)K_{\text{D}}|\gamma|^2 - k_{\text{he}}(\theta_{\text{s}}^{-1}-\theta_{\text{f}}^{-1}) + \nabla\cdot(k_{\text{f}}\nabla\theta_{\text{f}})\,, \tag{4.22f}$$

with the Cauchy stress tensor $\boldsymbol{\sigma}_i = 2\lambda_i(\nabla_{\text{s}}\mathbf{v}_i) + \zeta_i(\nabla\cdot\mathbf{v}_i)\mathbb{I}_d$ for each phase. Using the fundamental Gibbs relation (4.14) one can verify that $\mathbb{J}(\mathbf{q})\mathrm{D}\mathcal{S}(\mathbf{q}) = 0$ and $\mathbb{K}(\mathbf{q})\mathrm{D}\mathcal{E}(\mathbf{q}) = 0$ hold even true on the level of each individual dissipative process, i.e., heat transport, heat exchange, Stokes dissipation, Darcy dissipation. The Darcy friction is objective and conserves the total momentum. The total mass density of the system evolves according to

$$\partial_t\varrho_{\text{tot}} + \nabla\cdot\varrho_{\text{tot}}\mathbf{v} = 0\,, \quad \text{where} \quad \varrho_{\text{tot}}\mathbf{v} = \varrho_{\text{s}}\mathbf{v}_{\text{s}} + \varrho_{\text{f}}\mathbf{v}_{\text{f}}. \tag{4.23}$$

4.2.2 Two-Phase Reaction-Diffusion System

We now discuss the gradient/Onsager structure of a two-phase system that allows for the diffusion of species and intra-phase as well as inter-phase chemical reactions among the species. For this, we suitably adapt the results of Zafferi et al. (2022, Sec. 5 & 6.1) to the two-phase setting. For this two-phase system of solid (s) and fluid (f) phase in Eulerian coordinates we consider the state vector $\mathbf{q} = (\mathbf{q}_{\text{f}}, \mathbf{q}_{\text{s}})$ from (4.11). In particular, we assume that the two-phase system is composed of $N = N_{\text{s}} + N_{\text{f}}$ chemical species

$Z_1, \dots, Z_N$. Hereby, the first N_s species $Z_1, \dots, Z_{N_\mathrm{s}}$ belong to the solid phase and the N_f species $Z_{N_{\mathrm{s}+1}}, \dots, Z_N$ belong to the fluid phase and we denote by C_k the particle density of species Z_k, $k \in \{1, \dots, N\}$. Accordingly, we set $\mathbf{C}_\mathrm{s} := (C_1, \dots, C_{N_\mathrm{s}})^\top = (C_1^\mathrm{s}, \dots, C_{N_\mathrm{s}}^\mathrm{s})^\top$, $\mathbf{C}_\mathrm{f} := (C_{N_{\mathrm{s}+1}}, \dots, C_N)^\top = (C_1^\mathrm{f}, \dots, C_{N_\mathrm{f}}^\mathrm{f})^\top$, and $\mathbf{C} = (C_1, \dots, C_N)^\top$. The total energy and entropy of the system are of the form (4.13), with the chemical part of the entropy of logarithmic type, i.e., S_i in (4.13b) is of the form

$$S_i(\mathbf{C}_i, U_i) := S_i^\mathrm{th}(U_i) + \sum_{k=1}^{N_i} C_k^i(\ln C_k^i - 1) \tag{4.24}$$

with $S_i^\mathrm{th}(U_i)$ a thermal contribution. This leads to the driving force

$$\mathrm{D}_{\mathbf{C}_i} S_i(\mathbf{C}_i, U_i) = (\ln C_k^i)_{k=1}^{N_i}\,. \tag{4.25}$$

We further assume that the conservative contribution to dynamics is represented by the operator $\mathbb{J}$ from (4.16). In analogy to (4.17) we introduce the general structure of the Onsager operator for the two-phase reaction-diffusion system as follows

$$\mathbb{K}_\mathrm{rd} := \begin{pmatrix} \mathbb{K}_\mathrm{rd}^\mathrm{ss} & \mathbb{K}_\mathrm{rd}^\mathrm{sf} \\ \mathbb{K}_\mathrm{rd}^\mathrm{fs} & \mathbb{K}_\mathrm{rd}^\mathrm{ff} \end{pmatrix} \quad \text{with } \mathbb{K}_\mathrm{rd}^{ij} := \begin{pmatrix} 0 & 0 & 0 \\ 0 & \mathbb{K}_{\mathbf{C}_i\mathbf{C}_j} & 0 \\ 0 & 0 & 0 \end{pmatrix} \quad \text{and } \mathbb{K}_{\mathbf{C}_i\mathbf{C}_j} := \mathbb{K}_{\mathbf{C}_i\mathbf{C}_j}^\mathrm{reac} + \mathbb{K}_{\mathbf{C}_i\mathbf{C}_j}^\mathrm{diff} \tag{4.26}$$

for $i, j \in \{\mathrm{s}, \mathrm{f}\}$. In this way the operators $\mathbb{K}_\mathrm{rd}^{ij}$ only account for dissipative interactions of the vectors of concentrations in terms of chemical reactions $\mathbb{K}_{\mathbf{C}_i\mathbf{C}_j}^\mathrm{reac}$ and diffusion $\mathbb{K}_{\mathbf{C}_i\mathbf{C}_j}^\mathrm{diff}$, whereas dissipation due to changes in momentum $\mathbf{P}_i$ and internal energy U_i is not considered for $i \in \{\mathrm{s}, \mathrm{f}\}$. We note that $\mathbb{K}_{\mathbf{C}_i\mathbf{C}_j}^\mathrm{reac}$ describes intra-phase chemical reactions for $i = j$ and inter-phase chemical reactions for $i \neq j$. Following Zafferi et al. (2022, Eq. 6.9) we now introduce the Onsager operators $\mathbb{K}_{\mathbf{C}_i\mathbf{C}_j}^\mathrm{reac}$ and $\mathbb{K}_{\mathbf{C}_i\mathbf{C}_j}^\mathrm{diff}$.

Onsager operator for diffusion. Following Zafferi et al. (2022, Sec. 5 & 6.1) we introduce the Eulerian dual dissipation potential for diffusion

$$\Psi_\mathrm{diff}^*(\mathbf{q}; \boldsymbol{\eta}) := \int_\Omega \tfrac{1}{2}\mathbb{M}_{\mathbf{CC}} \nabla\boldsymbol{\eta} : \nabla\boldsymbol{\eta}\, \mathrm{d}\mathbf{x} \tag{4.27}$$

for any $\boldsymbol{\eta} = (\boldsymbol{\eta}_\mathsf{s}, \boldsymbol{\eta}_\mathsf{f}) = (\boldsymbol{\eta}_{\mathbf{C}_\mathsf{s}}, \boldsymbol{\eta}_{\mathbf{C}_\mathsf{f}})$. Differentiation with respect to $\boldsymbol{\eta}$ and integration by parts under the assumption of homogeneous boundary conditions gives the Onsager operator

$$\mathbb{K}^{\mathsf{diff}}\boldsymbol{\eta} = -\nabla\cdot(\mathbb{M}_{\mathbf{CC}}\nabla\boldsymbol{\eta}) \;\text{ with }\; \mathbb{M}_{\mathbf{CC}} = \begin{pmatrix} \mathbb{M}_{\mathbf{C}_\mathsf{s}\mathbf{C}_\mathsf{s}} & \mathbb{M}_{\mathbf{C}_\mathsf{s}\mathbf{C}_\mathsf{f}} \\ \mathbb{M}_{\mathbf{C}_\mathsf{f}\mathbf{C}_\mathsf{s}} & \mathbb{M}_{\mathbf{C}_\mathsf{f}\mathbf{C}_\mathsf{f}} \end{pmatrix} \in \mathbb{R}^{N\times N} \tag{4.28}$$

a positively semidefinite matrix of diffusion coefficients, which may depend on the state vector $\mathbf{q}$. Comparing (4.28) with (4.26) shows that

$$\mathbb{K}^{\mathsf{diff}}_{\mathbf{C}_i\mathbf{C}_j}\square = \nabla\cdot(\mathbb{M}_{\mathbf{C}_i\mathbf{C}_j}\nabla\square) \;\text{ with }\; \mathbb{M}_{\mathbf{C}_i\mathbf{C}_j} \in \mathbb{R}^{N_i\times N_j} \tag{4.29}$$

and $\square$ indicates where the argument has to be placed.

Onsager operator for chemical reactions. Assume that above N chemical species react with each other in R chemical reactions according to

$$\alpha_1^r Z_1 + \ldots + \alpha_{N^\mathsf{s}}^r Z_{N^\mathsf{s}} + \alpha_{N^\mathsf{s}+1}^r Z_{N^\mathsf{s}+1} + \ldots + \alpha_N^r Z_N \underset{\mathsf{k}_-^r}{\overset{\mathsf{k}_+^r}{\rightleftharpoons}} \beta_1^r Z_1 + \ldots + \beta_{N^\mathsf{s}}^r Z_N + \beta_{N^\mathsf{s}+1}^r Z_1 + \ldots + \beta_N^r Z_N\,, \tag{4.30}$$

for $r = 1, \ldots, R$. For each reaction r there are the vectors of stoichiometric coefficients $\boldsymbol{\alpha}^r = (\boldsymbol{\alpha}_\mathsf{s}^r, \boldsymbol{\alpha}_\mathsf{f}^r) = (\alpha_1^r, \ldots, \alpha_N^r)$ and $\boldsymbol{\beta}^r = (\boldsymbol{\beta}_\mathsf{s}^r, \boldsymbol{\beta}_\mathsf{f}^r) = (\beta_1^r, \ldots, \beta_N^r) \in \mathbb{N}_0^N$, as well as the forward and backward reaction rates $k_+^r, k_-^r > 0$, which may depend on the state $\mathbf{q}$. The equations governing the reaction kinetics are given by an ODE system of the form

$$\mathrm{d}_t^i\mathbf{C}_i = \sum_{r=1}^{R}\left(k_-^r(\mathbf{q})\mathbf{C}^{\beta^r} - k_+^r(\mathbf{q})\mathbf{C}^{\alpha^r}\right)(\boldsymbol{\alpha}_i^r - \boldsymbol{\beta}_i^r) \quad \text{for } i \in \{\mathsf{s},\mathsf{f}\}\,, \tag{4.31}$$

where we use the notation $\mathbf{C}^\alpha := C_1^{\alpha_1}\cdots C_N^{\alpha_N}$ and where d_t^i denotes the material time derivative with respect to the velocity of phase i. The material time derivative is generated by $\mathbb{J}$, see (4.22c) & (4.22d). Furthermore, we assume a detailed balance condition, i.e., there exists a steady state $\mathbf{C}_\mathsf{ref}$, such that

$$k^r(\mathbf{q}) = k_+^r(\mathbf{q})\mathbf{C}_\mathsf{ref}^{\alpha^r} = k_-^r(\mathbf{q})\mathbf{C}_\mathsf{ref}^{\beta^r} \;\text{ for all }\; r = 1, \ldots, R\,. \tag{4.32}$$

Under this condition, system (4.31) can be written as an Onsager system; (cf., e.g., Mielke, 2011). Based on Zafferi et al. (2022, Sec. 5) we introduce the dual dissipation

potential for chemical reactions

$$\Psi^*_{\text{reac}}(\mathbf{q};\boldsymbol{\eta}) := \int_\Omega \tfrac{1}{2} \begin{pmatrix} \boldsymbol{\eta}_\mathsf{s} \\ \boldsymbol{\eta}_\mathsf{f} \end{pmatrix} \cdot \mathbb{H}_{\mathbf{CC}}(\mathbf{q}) \begin{pmatrix} \boldsymbol{\eta}_\mathsf{s} \\ \boldsymbol{\eta}_\mathsf{f} \end{pmatrix} \mathrm{d}\mathbf{x}\,, \tag{4.33a}$$

with the Onsager operator $\mathbb{H}_{\mathbf{CC}}$. Due to (4.25) it follows that the Onsager operator has the following expression

$$\mathbb{H}_{\mathbf{CC}}(\mathbf{q}) := \sum_{r=1}^{R} \frac{k^r(\mathbf{q})}{k_\mathsf{B}} \ell\left(\left(\frac{\mathbf{C}}{\mathbf{C}_{\text{ref}}} \right)^{\alpha^r}, \left(\frac{\mathbf{C}}{\mathbf{C}_{\text{ref}}} \right)^{\beta^r} \right) \bar{\mathbb{S}}^r\,, \tag{4.33b}$$

$$\bar{\mathbb{S}}^r := (\boldsymbol{\alpha}^r - \boldsymbol{\beta}^r) \otimes (\boldsymbol{\alpha}^r - \boldsymbol{\beta}^r)\,, \tag{4.33c}$$

$$\ell(u,v) := \begin{cases} \frac{u-v}{\log u - \log v} & \text{for } u \neq v\,, \\ v & \text{for } u = v\,. \end{cases} \tag{4.33d}$$

$$\mathbb{H}_{\mathbf{CC}}(\mathbf{q}) \;=\; \begin{pmatrix} \mathbb{K}^{\text{reac}}_{\mathbf{C}_\mathsf{s}\mathbf{C}_\mathsf{s}} & \mathbb{K}^{\text{reac}}_{\mathbf{C}_\mathsf{s}\mathbf{C}_\mathsf{f}} \\ \mathbb{K}^{\text{reac}}_{\mathbf{C}_\mathsf{f}\mathbf{C}_\mathsf{s}} & \mathbb{K}^{\text{reac}}_{\mathbf{C}_\mathsf{f}\mathbf{C}_\mathsf{f}} \end{pmatrix} \quad \text{and} \tag{4.34a}$$

$$\mathbb{K}^{\text{reac}}_{\mathbf{C}_i\mathbf{C}_j} \;:=\; \sum_{r=1}^{R} \frac{k^r(\mathbf{q})}{k_\mathsf{B}} \ell\left(\left(\frac{\mathbf{C}}{\mathbf{C}_{\text{ref}}} \right)^{\alpha^r}, \left(\frac{\mathbf{C}}{\mathbf{C}_{\text{ref}}} \right)^{\beta^r} \right) (\boldsymbol{\alpha}^r_i - \boldsymbol{\beta}^r_i) \otimes (\boldsymbol{\alpha}^r_j - \boldsymbol{\beta}^r_j) \;\text{ for } i,j \in \{\mathsf{s},\mathsf{f}\}\,. \tag{4.34b}$$

Example: Rock Dehydration Consider the process of dehydration of serpentinite

$$(\mathrm{Mg},\mathrm{Fe})_3\mathrm{Si}_2\mathrm{O}_5(\mathrm{OH})_4 + (\mathrm{Mg},\mathrm{Fe})(\mathrm{OH})_2 \longleftrightarrow 2\,(\mathrm{Mg},\mathrm{Fe})_2\mathrm{SiO}_4 + 3\,\mathrm{H}_2\mathrm{O}$$

as an example for a single reaction in a two phase system with four species corresponding to antigorite $Z_1 = (\mathrm{Mg},\mathrm{Fe})_3\mathrm{Si}_2\mathrm{O}_5(\mathrm{OH})_4$, brucite $Z_2 = (\mathrm{Mg},\mathrm{Fe})(\mathrm{OH})_2$), olivine $Z_3 = (\mathrm{Mg},\mathrm{Fe})_2\mathrm{SiO}_4$ and water $Z_4 = \mathrm{H}_2\mathrm{O}$. Therefore we have the liquid phase composed only by water and the remaining minerals forming the solid part. If we consider purely Mg-minerals then the vector of molecular masses is $\mathbf{M} = (277.11, 58.32, 140.69, 18.01)$ expressed in g/mol with stoichiometric coefficients

$$\boldsymbol{\alpha}_\mathsf{s} = (1,1,0)\,, \qquad \boldsymbol{\alpha}_\mathsf{f} = (0)\,,$$
$$\boldsymbol{\beta}_\mathsf{s} = (0,0,2)\,, \qquad \boldsymbol{\beta}_\mathsf{f} = (3)\,.$$

Note that conservation of mass is ensured by $\mathbf{M}_\mathsf{s} \cdot (\boldsymbol{\alpha}_\mathsf{s} - \boldsymbol{\beta}_\mathsf{s}) + \mathbf{M}_\mathsf{f} \cdot (\boldsymbol{\alpha}_\mathsf{f} - \boldsymbol{\beta}_\mathsf{f}) = 0$. Finally, the system of ODEs reads

$$\partial_t \begin{pmatrix} \mathbf{C}_1 \\ \mathbf{C}_2 \\ \mathbf{C}_3 \\ \mathbf{C}_4 \end{pmatrix} = k(\mathbf{q}) \left(\frac{(\mathbf{C}_3)^2 (\mathbf{C}_4)^3}{(\mathbf{C}_{3,\mathsf{ref}})^2 (\mathbf{C}_{4,\mathsf{ref}})^3} - \frac{\mathbf{C}_1 \mathbf{C}_2}{\mathbf{C}_{1,\mathsf{ref}} \mathbf{C}_{2,\mathsf{ref}}} \right) \begin{pmatrix} 1 \\ 1 \\ -2 \\ -3 \end{pmatrix}$$

4.2.3 Two-Phase Reactive Darcy Flow

Here we combine our findings from Sections 4.2.1 and 4.2.2 to obtain the GENERIC structure for a two-phase Darcy flow with reactions and diffusion of chemical species. We thus again consider the state vector $\mathbf{q}$ from (4.11), the driving functionals $\mathcal{E}$ and $\mathcal{S}$ from (4.13) with the properties of the chemical part of the entropy as in (4.24) and the properties of the chemical species as discussed in Section 4.2.2. The Poisson operator $\mathbb{J}$ for reversible dynamics is again given by (4.16), while the Onsager operator for the coupled dissipative processes results by the sum of $\mathbb{K}_{\mathsf{SDH}}$ from (4.17) and $\mathbb{K}_{\mathsf{rd}}$ from (4.26), i.e.,

$$\mathbb{K}_{\mathsf{rdSDH}} = \mathbb{K}_{\mathsf{rd}} + \mathbb{K}_{\mathsf{SDH}} \,. \tag{4.35}$$

Following the lines of Zafferi et al. (2022, Sec. 6.1) it can be checked that this choice of driving functionals and operators complies with the degeneracy conditions (4.3) and (4.4). Moreover, the evolution equations of the GENERIC system for the reactive two-phase Darcy flow read

$$\dot{\mathbf{P}}_\mathsf{s} + \nabla \cdot (\mathbf{P}_\mathsf{s} \otimes \mathbf{v}_\mathsf{s}) = -\nabla \pi_\mathsf{s} - K_\mathsf{D} \boldsymbol{\gamma} + \nabla \cdot \boldsymbol{\sigma}_\mathsf{s} \,, \tag{4.36a}$$

$$\dot{\mathbf{P}}_\mathsf{f} + \nabla \cdot (\mathbf{P}_\mathsf{f} \otimes \mathbf{v}_\mathsf{f}) = -\nabla \pi_\mathsf{f} + K_\mathsf{D} \boldsymbol{\gamma} + \nabla \cdot \boldsymbol{\sigma}_\mathsf{f} \,, \tag{4.36b}$$

$$\dot{\mathbf{C}}_\mathsf{s} + \nabla \cdot (\mathbf{C}_\mathsf{s} \otimes \mathbf{v}_\mathsf{s}) = \sum_{r=1}^{R} k^r(\mathbf{q}) \left(\mathbf{C}^{\beta^r} - \mathbf{C}^{\alpha^r} \right) (\boldsymbol{\alpha}_\mathsf{s}^r - \boldsymbol{\beta}_\mathsf{s}^r) \,, \tag{4.36c}$$

$$\dot{\mathbf{C}}_\mathsf{f} + \nabla \cdot (\mathbf{C}_\mathsf{f} \otimes \mathbf{v}_\mathsf{f}) = \sum_{r=1}^{R} k^r(\mathbf{q}) \left(\mathbf{C}^{\beta^r} - \mathbf{C}^{\alpha^r} \right) (\boldsymbol{\alpha}_\mathsf{f}^r - \boldsymbol{\beta}_\mathsf{f}^r) \,, \tag{4.36d}$$

$$\dot{U}_\mathsf{s} + \nabla \cdot (U_\mathsf{s} \mathbf{v}_\mathsf{s}) = -\pi_\mathsf{s} \nabla \cdot \mathbf{v}_\mathsf{s} + \alpha K_\mathsf{D} |\boldsymbol{\gamma}|^2 + k_\mathsf{he} (\theta_\mathsf{s}^{-1} - \theta_\mathsf{f}^{-1}) + \nabla \cdot (k_\mathsf{s} \nabla \theta_\mathsf{s}) \,, \tag{4.36e}$$

$$\dot{U}_\mathsf{f} + \nabla \cdot (U_\mathsf{f} \mathbf{v}_\mathsf{f}) = -\pi_\mathsf{f} \nabla \cdot \mathbf{v}_\mathsf{f} + (1 - \alpha) K_\mathsf{D} |\boldsymbol{\gamma}|^2 - k_\mathsf{he} (\theta_\mathsf{s}^{-1} - \theta_\mathsf{f}^{-1}) + \nabla \cdot (k_\mathsf{f} \nabla \theta_\mathsf{f}) \,. \tag{4.36f}$$

Our deduction shows that the two-phase system (4.36) has a GENERIC structure. This in particular brings about that each phase has its own individual internal energy, entropy, and

temperature. It is our goal to show that the porous-media models (4.1) and (4.2) result from system (4.36) and its GENERIC structure. For this we shall investigate the limit to a joint system's temperature by assuming that heat can be equilibrated infinitely fast throughout the phases. In addition we will assume that the chemical reactions take place on much faster time scales than diffusion and Darcy flow. To this end we subsequently study on a formal level the equilibration of fast dissipative processes within the GENERIC framework.

4.3 Equilibration of Fast Dissipative Processes

We consider GENERIC systems of the form

$$\dot{\mathbf{q}} = \mathbb{J}(\mathbf{q})\mathrm{D}\mathcal{E}(\mathbf{q}) + \mathbb{K}(\mathbf{q})\mathrm{D}\mathcal{S}(\mathbf{q}) \tag{4.37a}$$

where the irreversible processes encoded in $\mathbb{K}$ are of the form

$$\mathbb{K}(\mathbf{q}) = \mathbb{K}_{\mathsf{slow}}(\mathbf{q}) + \varepsilon^{-1}\mathbb{K}_{\mathsf{fast}}(\mathbf{q}), \tag{4.37b}$$

and where $\mathbb{J}, \mathbb{K}$ satisfy the usual conditions of a GENERIC system. The NIC for $\mathbb{K}$ is satisfied for slow and fast processes separately, i.e., $\mathbb{K}_{\mathsf{slow}}(\mathbf{q})\mathrm{D}\mathcal{E}(\mathbf{q}) = 0$ and $\mathbb{K}_{\mathsf{fast}}(\mathbf{q})\mathrm{D}\mathcal{E}(\mathbf{q}) = 0$. We are interested in deriving the effective dynamics for solutions $\mathbf{q} : [0, \mathrm{T}] \to \mathcal{Q}$ of (4.37) as $\varepsilon \to 0$. Based on the considerations in previous sections, we are interested in two particular cases, i.e., the limit of fast exchange of thermal energy and the limit of fast reactions. In the following we present two possible approaches based on considerations in Mielke (2011); Zafferi et al. (2022) that are closely linked to the Gibbs-minimization formalism described in Baker et al. (1982).

4.3.1 Fast Exchange of Thermal Energy

We consider a GENERIC system where energy and entropy are of the form

$$\mathcal{E}(\mathbf{q}) = \int_\Omega \frac{|\mathbf{P}_\mathsf{s}|^2}{2\varrho_\mathsf{s}} + \frac{|\mathbf{P}_\mathsf{f}|^2}{2\varrho_\mathsf{f}} + U_\mathsf{s} + U_\mathsf{f}\,\mathrm{d}\mathbf{x} \tag{4.38a}$$

$$\mathcal{S}(\mathbf{q}) = \int_\Omega S_\mathsf{s}(\hat{q}, U_\mathsf{s}) + S_\mathsf{f}(\hat{q}, U_\mathsf{f})\,\mathrm{d}\mathbf{x} \tag{4.38b}$$

and we write $\mathbf{q} = (\mathbf{P}_\mathsf{s}, \mathbf{P}_\mathsf{f}, \dots, U_\mathsf{s}, U_\mathsf{f}) \equiv (\hat{q}, U_\mathsf{s}, U_\mathsf{f})$. To simplify the notation for the next consideration we introduced $\hat{q}$, which contains all state variables except for the internal energies.

Remark 4.3.1 *Note that S_i for $i \in \{\mathsf{s}, \mathsf{f}\}$ does not depend on the momentum and that the entropy of one phase does not depend on any variables of the other phase. While this structural assumption might be quite restrictive and prevent entropies that feature interaction between phases such as in the Flory-Huggins theory (Flory, 1942; Huggins, 1941), this is necessary in order to guarantee the non-interaction condition $\mathbb{J}(\mathbf{q})\mathrm{D}\mathcal{S}(\mathbf{q}) = 0$ for $\mathbb{J}$ in the current form. In general, Flory-Huggins theory features phase-separation via a non-concave entropy, which we also exclude here.*

Corresponding to this 3-component representation of the state variable $\mathbf{q} = (\hat{q}, U_\mathsf{s}, U_\mathsf{f})$, we consider fast processes of the form

$$\mathbb{K}_{\mathsf{fast}} = \begin{pmatrix} 0 & 0 & 0 \\ 0 & +1 & -1 \\ 0 & -1 & +1 \end{pmatrix}, \tag{4.39}$$

without any dependence on $\mathbf{q}$. Due to $\mathrm{D}\mathcal{E}(\mathbf{q}) = (\mathrm{D}_{\hat{q}}\mathcal{E}(\mathbf{q}), 1, 1)^\top$ we satisfy the NIC for the fast processes, i.e., $\mathbb{K}_{\mathsf{fast}}\mathrm{D}\mathcal{E}(\mathbf{q}) = 0$. Then fast exchange of thermal energy is equivalent to the requirement

$$\xi_{U_\mathsf{s}} = \mathrm{D}_{U_\mathsf{s}}\mathcal{S}(\mathbf{q}) \stackrel{!}{=} \mathrm{D}_{U_\mathsf{f}}\mathcal{S}(\mathbf{q}) = \xi_{U_\mathsf{f}}\,, \tag{4.40}$$

which correspondingly gives us the linear system with Lagrange multipliers

$$\dot{\mathbf{q}} = \begin{pmatrix} \dot{\hat{q}} \\ \dot{U}_\mathsf{s} \\ \dot{U}_\mathsf{f} \end{pmatrix} = \mathbb{J}(\mathbf{q})\mathrm{D}\mathcal{E}(\mathbf{q}) + \mathbb{K}_{\mathsf{slow}}(\mathbf{q})\mathrm{D}\mathcal{S}(\mathbf{q}) + \underbrace{\begin{pmatrix} \hat{0} \\ +\lambda \\ -\lambda \end{pmatrix}}_{=:\Lambda}, \tag{4.41a}$$

$$0 = \mathrm{D}_{U_\mathsf{s}}\mathcal{S}(\mathbf{q}) - \mathrm{D}_{U_\mathsf{f}}\mathcal{S}(\mathbf{q}) \equiv \theta_\mathsf{s}^{-1} - \theta_\mathsf{f}^{-1}. \tag{4.41b}$$

The advantage of the formulation *with Lagrange multipliers* is that it is directly accessible from the full model, but it has the disadvantage of increasing the number of unknowns.

Remark 4.3.2 (NIC for effective dynamics) Using the chain rule we have

$$\begin{aligned} \frac{\mathrm{d}}{\mathrm{d}t}\mathcal{E}(\mathbf{q}(t)) &= \langle \mathrm{D}\mathcal{E}(\mathbf{q}), \Lambda \rangle \equiv 0, \\ \frac{\mathrm{d}}{\mathrm{d}t}\mathcal{S}(\mathbf{q}(t)) &= \underbrace{\langle \mathrm{D}\mathcal{S}(\mathbf{q}), \mathbb{K}_{\mathsf{slow}}(\mathbf{q})\mathrm{D}\mathcal{S}(\mathbf{q}) \rangle}_{\geq 0} + \underbrace{\langle \mathrm{D}\mathcal{S}(\mathbf{q}), \Lambda \rangle}_{=0} \geq 0\,. \end{aligned}$$

This shows that the effective dynamics complies with thermodynamic consistency.

The system (4.41) with Lagrange multipliers presents one possibility to write the fast thermal equilibration limit of the general evolution. Alternatively, we can define the simple transformation

$$\mathsf{T}_U(\mathbf{q}) \equiv (\hat{q}, U = U_\mathsf{s} + U_\mathsf{f}) = \tilde{\mathbf{q}}, \tag{4.42}$$

which, using (4.40), is invertible on the set that also satisfies (4.40). If we define

$$\tilde{\mathcal{S}}(\tilde{\mathbf{q}}) := \mathcal{S}(\mathsf{T}_U^{-1}(\tilde{\mathbf{q}})), \qquad \tilde{\mathcal{E}}(\tilde{\mathbf{q}}) := \mathcal{E}(\mathsf{T}_U^{-1}(\tilde{\mathbf{q}})),$$

and using $\mathbb{L}_U = \mathsf{D}\mathsf{T}_U(\mathbf{q})$ gives the transformed evolution

$$\begin{aligned}\tilde{\mathbb{J}}(\tilde{\mathbf{q}}) &= \mathbb{L}_U\, \mathbb{J}(\mathsf{T}_U^{-1}(\tilde{\mathbf{q}}))\, \mathbb{L}_U^*,\\ \tilde{\mathbb{K}}_\mathsf{slow}(\tilde{\mathbf{q}}) &= \mathbb{L}_U\, \mathbb{K}_\mathsf{slow}(\mathsf{T}_U^{-1}(\tilde{\mathbf{q}}))\, \mathbb{L}_U^*,\end{aligned}$$

governing the reduced dynamics for $\theta_\mathsf{s} = \theta_\mathsf{f} = \theta$ via

$$\dot{\tilde{\mathbf{q}}} = \tilde{\mathbb{J}}(\tilde{\mathbf{q}})\mathsf{D}\tilde{\mathcal{E}}(\tilde{\mathbf{q}}) + \tilde{\mathbb{K}}_\mathsf{slow}(\tilde{\mathbf{q}})\mathsf{D}\tilde{\mathcal{S}}(\tilde{\mathbf{q}}). \tag{4.43}$$

We give a simple ODE example, which shows how this reduction can be performed in more detail.

Example 4.3.3 (Fast thermal equilibration ODE) Consider $\mathbf{q} = (x_1, x_2, p_1, p_2, u_1, u_2) \in \mathbb{R}^6$ as state variable, where x_i denotes position, p_i the momentum, and u_i the internal energy of the components/phases $i \in \{1, 2\}$. The total energy E and entropy S of the system are

$$E(\mathbf{q}) = \sum_i \frac{p_i^2}{2m_i} + u_i, \qquad S(\mathbf{q}) = \sum_i S_i(x_i, u_i),$$

using the entropy $S_i(x_i, u_i)$ for each separate phase and with the Gibbs relations $\partial_{u_i} S_i = 1/\theta_i$ and $\partial_{x_i} S_i = \pi_i/\theta_i$ defining temperature θ_i and pressure π_i. Consider the GENERIC system

$$\dot{\mathbf{q}} = \mathbb{J}(\mathbf{q})\mathsf{D}E(\mathbf{q}) + \mathbb{K}(\mathbf{q})\mathsf{D}S(\mathbf{q}), \tag{4.44a}$$

where the GENERIC structure is defined and NIC $\mathbb{J}(\mathbf{q})\mathrm{D}\mathcal{S}(\mathbf{q}) = 0$ satisfied by using

$$\mathbb{J}(\mathbf{q}) = \begin{pmatrix} 0 & 0 & 1 & 0 & 0 & 0 \\ 0 & 0 & 0 & 1 & 0 & 0 \\ -1 & 0 & 0 & 0 & \pi_1 & 0 \\ 0 & -1 & 0 & 0 & 0 & \pi_2 \\ 0 & 0 & -\pi_1 & 0 & 0 & 0 \\ 0 & 0 & 0 & -\pi_2 & 0 & 0 \end{pmatrix}, \quad \mathrm{D}E(\mathbf{q}) = \begin{pmatrix} 0 \\ 0 \\ \frac{p_1}{m_1} \\ \frac{p_2}{m_2} \\ 1 \\ 1 \end{pmatrix}, \quad \mathrm{D}S(\mathbf{q}) = \begin{pmatrix} \pi_1/\theta_1 \\ \pi_2/\theta_2 \\ 0 \\ 0 \\ 1/\theta_1 \\ 1/\theta_2 \end{pmatrix}. \tag{4.44b}$$

For the dissipation $\mathbb{K}(\mathbf{q}) = \mathbb{K}_{\mathsf{slow}}(\mathbf{q}) + \varepsilon^{-1}\mathbb{K}_{\mathsf{fast}}(\mathbf{q})$ and with $m_i v_i = p_i$ we use

$$\mathbb{K}_{\mathsf{slow}}(\mathbf{q}) = \theta_1 k_1 \begin{pmatrix} 0 & 0 & 0 & 0 & 0 & 0 \\ 0 & 0 & 0 & 0 & 0 & 0 \\ 0 & 0 & 1 & 0 & -v_1 & 0 \\ 0 & 0 & 0 & 0 & 0 & 0 \\ 0 & 0 & -v_1 & 0 & +v_1^2 & 0 \\ 0 & 0 & 0 & 0 & 0 & 0 \end{pmatrix} + \theta_2 k_2 \begin{pmatrix} 0 & 0 & 0 & 0 & 0 & 0 \\ 0 & 0 & 0 & 0 & 0 & 0 \\ 0 & 0 & 0 & 0 & 0 & 0 \\ 0 & 0 & 0 & 1 & 0 & -v_2 \\ 0 & 0 & 0 & 0 & 0 & 0 \\ 0 & 0 & 0 & -v_2 & 0 & +v_2^2 \end{pmatrix}, \qquad \mathbb{K}_{\mathsf{fast}} = \begin{pmatrix} 0 & 0 & 0 & 0 & 0 & 0 \\ 0 & 0 & 0 & 0 & 0 & 0 \\ 0 & 0 & 0 & 0 & 0 & 0 \\ 0 & 0 & 0 & 0 & 0 & 0 \\ 0 & 0 & 0 & 0 & +1 & -1 \\ 0 & 0 & 0 & 0 & -1 & +1 \end{pmatrix}, \tag{4.44c}$$

and observe that it satisfies the other NIC $\mathbb{K}(\mathbf{q})\mathrm{D}E(\mathbf{q}) = 0$. We obtain the following evolution equations

$$\dot{x}_i = v_i = \frac{p_i}{m_i}, \qquad \dot{p}_i = \pi_i - k_i v_i, \tag{4.45a}$$

$$\dot{u}_1 = -\pi_1 v_1 + k_1 v_1^2 + \varepsilon^{-1}(\theta_1^{-1} - \theta_2^{-1}), \tag{4.45b}$$

$$\dot{u}_2 = -\pi_2 v_2 + k_2 v_2^2 + \varepsilon^{-1}(\theta_2^{-1} - \theta_1^{-1}), \tag{4.45c}$$

for $i \in \{1, 2\}$. We introduce an oscillator with $\omega_i \in \mathbb{R}_+$ and heat capacities $c_i \in \mathbb{R}_+$ such that

$$S_i(x_i, u_i) = c_i \log\Big(\tfrac{u_i - V_i(x_i)}{c_i}\Big) = c_i \log\theta_i, \qquad V_i(x_i) = \tfrac{1}{2}\omega_i x_i^2,$$

so that $c_i\theta_i = u_i - V_i(x)$ and $\pi_i = -\partial_x V_i$. Using $\theta_1 = \theta_2 \equiv \theta$, for the total internal energy we get $u = u_1 + u_2 = (c_1 + c_2)\theta + V_1(x_1) + V_2(x_2)$. Correspondingly, the energy $\tilde{E}$ and entropy $\tilde{S} = S_1 + S_2$ can be expressed in $\tilde{\mathbf{q}} = (x_1, x_2, p_1, p_2, u) \in \mathbb{R}^5$ with

$$\tilde{E}(\tilde{\mathbf{q}}) = \tfrac{p_1^2}{2m_1} + \tfrac{p_2^2}{2m_2} + u, \qquad \tilde{S}(x_1, x_2, u) = (c_1 + c_2)\log\Big(\tfrac{u - V_1(x_1) - V_2(x_2)}{(c_1 + c_2)}\Big). \tag{4.46a}$$

Note that $\tilde{S}$ is not a sum of contributions from both components. Using the operators

$$\tilde{\mathbb{J}} = \begin{pmatrix} 0 & 0 & 1 & 0 & 0 \\ 0 & 0 & 0 & 1 & 0 \\ -1 & 0 & 0 & 0 & \pi_1 \\ 0 & -1 & 0 & 0 & \pi_2 \\ 0 & 0 & -\pi_1 & -\pi_2 & 0 \end{pmatrix}, \qquad \tilde{\mathbb{K}}_{\mathsf{slow}} = \theta k_1 \begin{pmatrix} 0 & 0 & 0 & 0 & 0 \\ 0 & 0 & 0 & 0 & 0 \\ 0 & 0 & 1 & 0 & -v_1 \\ 0 & 0 & 0 & 0 & 0 \\ 0 & 0 & -v_1 & 0 & +v_1^2 \end{pmatrix} + \theta k_2 \begin{pmatrix} 0 & 0 & 0 & 0 & 0 \\ 0 & 0 & 0 & 0 & 0 \\ 0 & 0 & 0 & 0 & 0 \\ 0 & 0 & 0 & 1 & -v_2 \\ 0 & 0 & 0 & -v_2 & +v_2^2 \end{pmatrix}, \tag{4.46b}$$

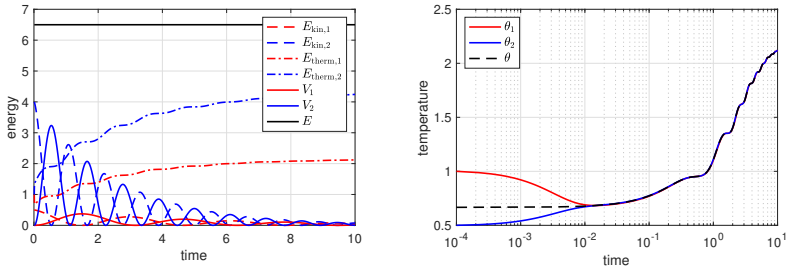

Figure 4.2: Solution of GENERIC system (4.45) with $\varepsilon = 10^{-2}$ and $k_1 = k_2 = 1/5$, $m_1 = 1$, $m_2 = 1/2$, $c_1 = 1$, $c_2 = 2$, $\omega_1 = 1$, $\omega_2 = 4$ with $\mathbf{q}(t=0) = (0,0,1,-2,1,1)^\top$ and $\tilde{\mathbf{q}}(t=0) = (0,0,1,-2,2)^\top$. Numerical solution showing (left) kinetic energy $E_{\mathrm{kin},i} = p_i^2/2m_i$, thermal energy $E_{\mathrm{therm},i} = c_i\theta_i = u_i - V_i$, potential energy V_i and total energy E and (right) temperatures of full model θ_i and effective model θ.

the effective dynamics is $\dot{\tilde{\mathbf{q}}} = \tilde{\mathbb{J}}(\tilde{\mathbf{q}})\mathrm{D}\tilde{E}(\tilde{\mathbf{q}}) + \tilde{\mathbb{K}}_{\mathrm{slow}}(\tilde{\mathbf{q}})\mathrm{D}\tilde{S}(\tilde{\mathbf{q}})$. An exemplary solution is shown in Figure 4.2, where the left panel shows the energetics of the full solution $\mathbf{q}(t)$, and the right panel shows the convergence of the temperatures θ_i to the temperature θ of the effective solution $\tilde{\mathbf{q}}(t)$.

$\star$

4.3.2 Fast Reactions Equilibrium

Similar to what is presented in Mielke (2011) , we apply now the aforementioned method to systems where fast chemical reactions happen on a very short time scale compared to the other involved slow processes. In this case, however, it is not necessary to distinguish between a solid and a liquid phase, but rather between the species involved. Consider a system where R possible reactions with stoichiometric coefficients $\boldsymbol{\alpha}^r, \boldsymbol{\beta}^r \in \mathbb{N}_0^N$ between N species occur. The particle density is denoted by the N-tuple $\mathbf{C} = (\mathbf{C}_i)_{i=1}^N$. We assume that the total energy and total entropy of the system can be expressed in the following way

$$\mathcal{E}(\mathbf{q}) = \int_\Omega \frac{|\mathbf{P}|^2}{2\varrho} + U \,\mathrm{d}\mathbf{x} \tag{4.47a}$$

$$\mathcal{S}(\mathbf{q}) = \int_\Omega S(\hat{q}, \mathbf{C}) \,\mathrm{d}\mathbf{x}\,, \tag{4.47b}$$

where $\mathbf{q} = (\mathbf{P}, U, \mathbf{C}) \equiv (\hat{q}, \mathbf{C})$ with U being the internal energy of the system and $\mathbf{P}$ the momentum density. We consider fast processes of the form

$$\mathbb{K}_{\mathrm{fast}} = \begin{pmatrix} 0 & 0 \\ 0 & \mathbb{H} \end{pmatrix}, \tag{4.48}$$

where $\mathbb{H} = \sum_r (\boldsymbol{\alpha}^r - \boldsymbol{\beta}^r) \otimes (\boldsymbol{\alpha}^r - \boldsymbol{\beta}^r)$ is the reactive operator. In order to have mass conservation and to satisfy the NIC, we require that the vector of particle masses $\mathbf{M}$ lies in the kernel of the matrix $\mathbb{H}$, i.e., $\mathbf{M} \cdot (\boldsymbol{\alpha}^r - \boldsymbol{\beta}^r) = 0$ for all reactions $r = 1, \dots, R$.

Then a fast reactions limit is equivalent to the equilibrium condition

$$(\boldsymbol{\alpha}^r - \boldsymbol{\beta}^r) \cdot \mathrm{D}_{\mathbf{C}} \mathcal{S}(\mathbf{q}) \stackrel{!}{=} 0\,, \qquad \text{for all } r \in \{1, \dots, R\}\,, \tag{4.49}$$

Introducing the constrained dynamics by using Lagrange multipliers λ_r, the effective dynamics can be written as

$$\dot{\mathbf{q}} = \begin{pmatrix} \dot{\hat{q}} \\ \dot{\mathbf{C}} \end{pmatrix} = \mathbb{J}(\mathbf{q}) \mathrm{D}\mathcal{E}(\mathbf{q}) + \mathbb{K}_{\text{slow}}(\mathbf{q}) \mathrm{D}\mathcal{S}(\mathbf{q}) + \underbrace{\begin{pmatrix} 0 \\ \sum_r (\boldsymbol{\alpha}^r - \boldsymbol{\beta}^r) \lambda_r \end{pmatrix}}_{:=\Lambda}, \tag{4.50a}$$

$$0 = (\boldsymbol{\alpha}^r - \boldsymbol{\beta}^r) \mathrm{D}_{\mathbf{C}} \mathcal{S}(\mathbf{q}) \qquad \text{for all } r \in \{1, \dots, R\}\,. \tag{4.50b}$$

Remark 4.3.4 (NIC for effective dynamics) Similarly as in Remark 4.3.2, one confirms that the total energy is conserved and entropy is non-decreasing:

$$\frac{\mathrm{d}}{\mathrm{d}t} \mathcal{E}(\mathbf{q}(t)) = \langle \mathrm{D}\mathcal{E}(\mathbf{q}), \Lambda \rangle \equiv 0\,, \tag{4.51}$$

$$\frac{\mathrm{d}}{\mathrm{d}t} \mathcal{S}(\mathbf{q}(t)) = \underbrace{\langle \mathrm{D}\mathcal{S}(\mathbf{q}), \mathbb{K}_{\text{slow}}(\mathbf{q}) \mathrm{D}\mathcal{S}(\mathbf{q}) \rangle}_{\geq 0} + \underbrace{\langle \mathrm{D}\mathcal{S}(\mathbf{q}), \Lambda \rangle}_{=0} \geq 0\,, \tag{4.52}$$

where we have used $\mathbf{M} \cdot (\boldsymbol{\alpha}^r - \boldsymbol{\beta}^r) = 0$.

The constrained system (4.50a) presents one way to write the fast reactions limit. Another possibility is to define a transformation T_C that reduces the number of variables based on the condition (4.49). In order to build this transformation we use the method presented in Mielke (2011), similar to the reduction presented Zafferi et al. (2022). We start by considering the space

$$\Gamma := \operatorname{span} \{ \boldsymbol{\alpha}^r - \boldsymbol{\beta}^r | r = 1, \dots, R \} \subset \mathbb{R}^N, \tag{4.53}$$

and its orthogonal complement $\Gamma^\perp$. After finding a basis $\{v_1, \dots, v_m\}$ of $\Gamma^\perp$, we construct the adjoint of the transformation Q as $Q^\top = (v_1, \dots, v_m) \in \mathbb{R}^{N \times m}$. Finally the transformation can be defined as

$$\mathsf{T}_{\mathbf{C}}(\mathbf{q}) \equiv (\hat{q}, \mathbf{C}^\perp = Q\mathbf{C}) = \tilde{\mathbf{q}}, \tag{4.54}$$

which is invertible on the set defined by (4.49).

We define

$$\tilde{\mathcal{E}}(\tilde{\mathbf{q}}) := \mathcal{E}(\mathsf{T}_{\mathbf{C}}^{-1}(\tilde{\mathbf{q}}))\,, \qquad \tilde{\mathcal{S}}(\tilde{\mathbf{q}}) := \mathcal{S}(\mathsf{T}_{\mathbf{C}}^{-1}(\tilde{\mathbf{q}}))\,, \tag{4.55}$$

and set $\mathbb{L}_{\mathbf{C}} = \mathrm{D}\mathsf{T}_{\mathbf{C}}(\mathbf{q})$. This gives the transformed operators

$$\tilde{\mathbb{J}}(\tilde{\mathbf{q}}) = \mathbb{L}_{\mathbf{C}}\,\mathbb{J}(\mathsf{T}_{\mathbf{C}}^{-1}(\tilde{\mathbf{q}}))\,\mathbb{L}_{\mathbf{C}}^{*}, \tag{4.56a}$$

$$\tilde{\mathbb{K}}_{\mathsf{slow}}(\tilde{\mathbf{q}}) = \mathbb{L}_{\mathbf{C}}\,\mathbb{K}_{\mathsf{slow}}(\mathsf{T}_{\mathbf{C}}^{-1}(\tilde{\mathbf{q}}))\,\mathbb{L}_{\mathbf{C}}^{*}, \tag{4.56b}$$

governing the reduced dynamics for $(\boldsymbol{\alpha}^r - \boldsymbol{\beta}^r)\cdot\boldsymbol{\mu} = 0$ for every $r \in \{1, \dots, R\}$ via

$$\dot{\tilde{\mathbf{q}}} = \tilde{\mathbb{J}}(\tilde{\mathbf{q}})\mathrm{D}\tilde{\mathcal{E}}(\tilde{\mathbf{q}}) + \tilde{\mathbb{K}}_{\mathsf{slow}}(\tilde{\mathbf{q}})\mathrm{D}\tilde{\mathcal{S}}(\tilde{\mathbf{q}}).$$

Note that the determination of effective equations of state $\tilde{E}(\tilde{\mathbf{q}})$, $\tilde{S}(\tilde{\mathbf{q}})$ and derived quantities is similar to that in the Gibbs minimization process , e.g. cf. Baker et al. (1982), which in general is performed for non-convex potentials with the goal to determine the possible phases a mixture attains under the constraint of a prescribed composition of materials.

We now give an explicit example on how the reduction approach can be applied to rock dehydration processes.

Example 4.3.5 (Fast reactions equilibration for rock dehydration processes.) Consider the following process where water chemically bound to a rock is released

$$\text{hydrous solid} \;\rightleftharpoons\; \text{non-hydrous solid} + \mathsf{H}_2\mathsf{O}\,,$$

and the state $\mathbf{q} = (U, \mathbf{C})^\top = (U, C_{\mathsf{s,h}}, C_{\mathsf{s,nh}}, C_{f,\mathsf{H_2O}})^\top \equiv (u, C_1, C_2, C_{\mathsf{f}})^\top$ with $C_{\mathsf{s,h}}$ and $C_{\mathsf{s,nh}}$ being the concentrations of the hydrous and non-hydrous solid respectively, and u the internal energy. The stoichiometric coefficients for forward and backward reactions are $\boldsymbol{\alpha} = (1,0,0)^\top$ and $\boldsymbol{\beta} = (0,1,1)^\top$ and the vector of particle masses $\mathbf{M} = (M_1, M_2, M_{\mathsf{f}})^\top$, with $M_2 = M_1 - M_{\mathsf{f}}$. One can see immediately that $(\boldsymbol{\alpha} - \boldsymbol{\beta})\cdot\mathbf{M} = 0$ and thus the condition for conservation of mass is satisfied. For this example we focus only on dissipative processes but the transformation we are going to show applies in the same way to the reversible contributions. Consider then the following Onsager system

$$\partial_t \mathbf{q} = \left(\mathbb{K}_{\mathsf{slow}}(\mathbf{q}) + \tfrac{1}{\varepsilon}\mathbb{K}_{\mathsf{fast}}(\mathbf{q})\right)\mathrm{D}\mathcal{S}(\mathbf{q})\,,$$

where

$$\mathbb{K}_{\text{slow}} = \begin{pmatrix} \mathbb{K}_{uu} & \mathbb{K}_{u1} & \mathbb{K}_{u2} & \mathbb{K}_{uf} \\ \mathbb{K}_{1u} & \mathbb{K}_{11} & \mathbb{K}_{12} & \mathbb{K}_{1f} \\ \mathbb{K}_{2u} & \mathbb{K}_{21} & \mathbb{K}_{22} & \mathbb{K}_{2f} \\ \mathbb{K}_{fu} & \mathbb{K}_{f1} & \mathbb{K}_{f2} & \mathbb{K}_{ff} \end{pmatrix}, \qquad \mathbb{K}_{\text{fast}} = \begin{pmatrix} 0 & 0_{1\times 3} \\ 0_{3\times 1} & \mathbb{H} \end{pmatrix}.$$

The total entropy is of Boltzmann type and has the typical "log" structure

$$\mathcal{S}(\mathbf{q}) = \int_\Omega \sum_i C_i^*(u^s)\lambda_B\left(\frac{C_i}{C_i^*}\right) d\mathbf{x} \qquad \text{where } \lambda_B(y) := y\log y - y + 1,$$

and where $\mathbf{C}^*(u) = (C_1^*(u), C_2^*(u), C_f^*(u))^\top$ is the vector of positive concentrations related to the detailed-balance condition. We can directly compute the driving force

$$D_u\mathcal{S} = \frac{1}{\theta}, \qquad (D_{\mathbf{C}}\mathcal{S})_i = \left(\frac{\mu}{\theta}\right)_i = \log C_i/C_i^*.$$

The reduction Q is built from a basis of the orthogonal space of span $\{\boldsymbol{\alpha} - \boldsymbol{\beta}\}$

$$Q = \begin{pmatrix} M_1 & M_2 & M_f \\ M_2 & M_2 & 0 \end{pmatrix}.$$

Combining Q with the identity for u we define the nonlinear mapping

$$\tilde{\mathbf{q}} := T_{\mathbf{C}}(\mathbf{q}) = (u, Q\mathbf{C}) = (u, \varrho_{\text{tot}}, \varrho_{\text{nv}})^\top,$$

where ϱ_{nv} is the mass density of the non-volatile solid, meaning the mass density of the solid that has no chemically bound water. In order to find out the transformed Onsager operator we need to linearize $T_{\mathbf{C}}$ and compute its adjoint:

$$\mathbb{L}_{\mathbf{C}} := DT_{\mathbf{C}} = \begin{pmatrix} 1 & 0 & 0 & 0 \\ 0 & M_1 & M_2 & M_f \\ 0 & M_2 & M_2 & 0 \end{pmatrix}, \qquad \mathbb{L}_{\mathbf{C}}^* = \begin{pmatrix} 1 & 0 & 0 \\ 0 & M_1 & M_2 \\ 0 & M_2 & M_2 \\ 0 & M_f & 0 \end{pmatrix}.$$

The transformed Onsager operator is then given by (4.56b)

$$\mathbb{L}\mathbb{K}(\mathbf{q})\mathbb{L}^* = \begin{pmatrix} \mathbb{K}_{uu} & \sum_{\mathsf{i}\in\{1,2,\mathsf{f}\}} \mathbb{K}_{u\mathsf{i}} M_{\mathsf{i}} & \mathbb{K}_{u1} M_1 + \mathbb{K}_{u2} M_2 \\ \sum_{\mathsf{i}\in\{1,2,\mathsf{f}\}} M_{\mathsf{i}} \mathbb{K}_{\mathsf{i}u} & \sum_{i,j\in\{1,2,\mathsf{f}\}} M_i \mathbb{K}_{ij} M_j & \sum_{\mathsf{i}\in\{1,2,\mathsf{f}\}} M_i(\mathbb{K}_{\mathsf{i}1} + \mathbb{K}_{\mathsf{i}2}) M_2 \\ M_2\mathbb{K}_{1u} + M_2\mathbb{K}_{2u} & \sum_{\mathsf{i}\in\{1,2,\mathsf{f}\}} M_2(\mathbb{K}_{1\mathsf{i}} + \mathbb{K}_{2\mathsf{i}}) M_{\mathsf{i}} & \sum_{\mathsf{i},\mathsf{j}\in\{1,2\}} M_2 \mathbb{K}_{\mathsf{ij}} M_2 \end{pmatrix}.$$

This transformed operator and the entropy functional have to satisfy the conditions (4.56) and (4.55), respectively. One can see that it is verified by using $\mathsf{T}_{\mathbf{C}}^{-1}$. On the set where the equilibrium condition, i.e., $\mu_1 = \mu_2 + \mu_{\mathsf{f}}$, is satisfied the transformation $\mathsf{T}_{\mathbf{C}}$ is invertible and we can reconstruct the vector of concentrations via $\mathbf{C} = \mathsf{T}_{\mathbf{C}}^{-1}(\tilde{\mathbf{q}})$

$$\begin{aligned} C_1 &= \frac{1}{2}\left[K^* + \frac{\varrho_{\mathsf{nv}}}{M_{\mathsf{nv}}} + \frac{\varrho_{\mathsf{tot}} - \varrho_{\mathsf{nv}}}{M_{\mathsf{H_2O}}} - \sqrt{f(u, \varrho_{\mathsf{tot}}, \varrho_{\mathsf{nv}})}\right], \qquad \text{with } K^* := \frac{C^*_{\mathsf{nh}} C^*_{\mathsf{H_2O}}}{C^*_h}, \\ C_2 &= \frac{\varrho_{\mathsf{nv}}}{M_{\mathsf{nh}}} - \frac{1}{2}\left[K^* + \frac{\varrho_{\mathsf{nv}}}{M_{\mathsf{nv}}} + \frac{\varrho_{\mathsf{tot}} - \varrho_{\mathsf{nv}}}{M_{\mathsf{H_2O}}} - \sqrt{f(u, \varrho_{\mathsf{tot}}, \varrho_{\mathsf{nv}})}\right], \\ C_{\mathsf{f}} &= \frac{\varrho_{\mathsf{tot}} - \varrho_{\mathsf{nv}}}{M_{\mathsf{H_2O}}} - \frac{1}{2}\left[K^* + \frac{\varrho_{\mathsf{nv}}}{M_{\mathsf{nv}}} + \frac{\varrho_{\mathsf{tot}} - \varrho_{\mathsf{nv}}}{M_{\mathsf{H_2O}}} - \sqrt{f(u, \varrho_{\mathsf{tot}}, \varrho_{\mathsf{nv}})}\right], \\ \text{with } f(u, \varrho_{\mathsf{tot}}, \varrho_{\mathsf{nv}}) &= \left(\frac{\varrho_{\mathsf{nv}}}{M_{\mathsf{nv}}} - \frac{\varrho_{\mathsf{tot}} - \varrho_{\mathsf{nv}}}{M_{\mathsf{H_2O}}}\right)^2 + \left(K^{*^2} + \frac{2K^*\varrho_{\mathsf{nv}}}{M_{\mathsf{nh}}} + \frac{2K^*(\varrho_{\mathsf{tot}} - \varrho_{\mathsf{nv}})}{M_{\mathsf{H_2O}}}\right). \end{aligned}$$

⋆

Remark 4.3.6 (Equations of state for concentrations and thermodynamic quantities) *In Example 4.3.5 we examplarily showed the reduction of the GENERIC structure under fast processes, which is based on the assumption that $\mathsf{T}_{\mathbf{C}}$ is invertible. Therefore, we can write the original concentrations $\mathbf{C}_i$ using an equation of state in terms of the new variable. Similarly, we can express all other derived thermodynamic quantities in terms of the new variables, e.g., chemical potential, temperature and pressure by*

$$\tilde{\theta}(\tilde{\mathbf{q}}) = \theta(\mathsf{T}_{\mathbf{C}}^{-1}(\tilde{\mathbf{q}})), \quad \tilde{\boldsymbol{\mu}}(\tilde{\mathbf{q}}) = \boldsymbol{\mu}(\mathsf{T}_{\mathbf{C}}^{-1}(\tilde{\mathbf{q}})), \quad \tilde{\pi}_i(\tilde{\mathbf{q}}) = \pi_i(\mathsf{T}_{\mathbf{C}}^{-1}(\tilde{\mathbf{q}})), \quad \tilde{\mathbf{C}}_i(\tilde{\mathbf{q}}) = (\mathsf{T}_{\mathbf{C}}^{-1}(\tilde{\mathbf{q}}))_{\mathbf{C}_i}. \tag{4.57}$$

Remark 4.3.7 (The Gibbs energy minimization method) *The Gibbs energy minimization method is used for a wide variety of applications to multiphase/multicomponent systems (Koukkari and Pajarre, 2006), especially in geosciences where the size and heterogeneity of the system makes it disadvantageous to apply the direct approach described in Section 4.2.2. The main idea behind this method is to find the system composition for which its Gibbs energy is minimized, eventually subject to mass constraints. It can be shown by standard laws of thermodynamics (Connolly, 2017) that a stable configuration corresponds*

to a minimum of the Gibbs energy. Although this idea could be applied to other free energies, the energy dependence on pressure π and temperature θ makes it particularly suited for geological applications. We focus here on the application of Gibbs energy minimization to chemical reactions and show that the equilibrium conditions met by this approach are (4.49)*. We consider the Gibbs energy related to a reactive system where reactions are described through a stoichiometric expression like* (4.30) *with N different components:*

$$G^{\text{sys}} := G^{\text{sys}}(\pi, \theta, \mathbf{C}) \,, \qquad \textit{with } \mathbf{C} = (\mathbf{C}_i)_{i=1}^{N} \,. \tag{4.58}$$

We recall also that the Gibbs energy of a system can be obtained by means of a Legendre transform applied to the internal energy or Helmholtz free energy. Let us assume for the moment that only one reaction occurs. We define a new variable called extent of reaction *$\xi : \Omega \to [0, 1]$ and write*

$$\mathbf{C} = \mathbf{C}^0 + (\boldsymbol{\beta} - \boldsymbol{\alpha})\xi \,,$$

where $\mathbf{C}^0 = \mathbf{C}(t = 0)$. We can rewrite (4.58) *as a function of ξ:*

$$G^{\text{sys}} := G^{\text{sys}}(\pi, \theta, \xi) \,, \tag{4.59}$$

then, by keeping pressure and temperature fixed and recalling that $\partial_{\mathbf{C}} G = \boldsymbol{\mu}$, the necessary condition for a minimum implies

$$\mathrm{D}_{\xi} G^{\text{sys}}(\xi) = (\boldsymbol{\beta} - \boldsymbol{\alpha}) \cdot \boldsymbol{\mu} = 0 \,, \tag{4.60}$$

which is again (4.49) *for a single reaction.*

4.4 Damped-Hamiltonian Structure

4.4.1 Limit of Fast Irreversible Processes

In this section we reproduce the results from Plümper et al. (2017) in GENERIC form. The two-phase system introduced therein aims to model rock dehydration processes at their primal stage, that is when bounded water is released via chemical reactions and starts flowing through the newborn pore system. Although for the moment we will consider only one single reaction, other reactions are possibly involved in rock dehydration processes. Our example is the following dehydration reaction

$$(\mathrm{Mg, Fe})_{48}\mathrm{Si}_{34}\mathrm{O}_{85}(\mathrm{OH})_{62} + 20\,(\mathrm{Mg, Fe})(\mathrm{OH})_2 \longleftrightarrow 34\,(\mathrm{Mg, Fe})_2\mathrm{SiO}_4 + 51\,\mathrm{H}_2\mathrm{O}$$

where antigorite $(Mg, Fe)_{48}Si_{34}O_{85}(OH)_{62}$ together with brucite $(Mg, Fe)(OH)_2$ are transformed into olivine $(Mg, Fe)_2SiO_4$ and a fluid phase. Antigorite is an abundant mineral in rocks that undergo subduction and is relevant in subduction zone dynamics because of its high water content. The reaction of antigorite and brucite to olivine and fluid is further discussed in Example 4.2.2 in a simplified version. We start from the full two-phase GENERIC system of the form

$$\dot{\mathbf{P}}_\mathsf{s} + \nabla \cdot (\mathbf{P}_\mathsf{s} \otimes \mathbf{v}_\mathsf{s}) = -\nabla \pi_\mathsf{s} - K_\mathsf{D}\boldsymbol{\gamma} + \nabla \cdot \boldsymbol{\sigma}_\mathsf{s}\,, \tag{4.61a}$$

$$\dot{\mathbf{P}}_\mathsf{f} + \nabla \cdot (\mathbf{P}_\mathsf{f} \otimes \mathbf{v}_\mathsf{f}) = -\nabla \pi_\mathsf{f} + K_\mathsf{D}\boldsymbol{\gamma} + \nabla \cdot \boldsymbol{\sigma}_\mathsf{f}\,, \tag{4.61b}$$

$$\dot{\mathbf{C}}_\mathsf{s} + \nabla \cdot (\mathbf{C}_\mathsf{s} \otimes \mathbf{v}_\mathsf{s}) = \sum_r k^r(\mathbf{q}) \left(\mathbf{C}^{\beta^r} - \mathbf{C}^{\alpha^r}\right) (\boldsymbol{\alpha}_\mathsf{s}^r - \boldsymbol{\beta}_\mathsf{s}^r)\,, \tag{4.61c}$$

$$\dot{\mathbf{C}}_\mathsf{f} + \nabla \cdot (\mathbf{C}_\mathsf{f} \otimes \mathbf{v}_\mathsf{f}) = \sum_r k^r(\mathbf{q}) \left(\mathbf{C}^{\beta^r} - \mathbf{C}^{\alpha^r}\right) (\boldsymbol{\alpha}_\mathsf{f}^r - \boldsymbol{\beta}_\mathsf{f}^r)\,, \tag{4.61d}$$

$$\dot{U}_\mathsf{s} + \nabla \cdot (U_\mathsf{s}\mathbf{v}_\mathsf{s}) = -\pi_\mathsf{s} \nabla \cdot \mathbf{v}_\mathsf{s} + \alpha K_\mathsf{D} |\boldsymbol{\gamma}|^2 + k_\mathsf{he}(\theta_\mathsf{s}^{-1} - \theta_\mathsf{f}^{-1}) + \nabla \cdot (k_\mathsf{s} \nabla \theta_\mathsf{s})\,, \tag{4.61e}$$

$$\dot{U}_\mathsf{f} + \nabla \cdot (U_\mathsf{f}\mathbf{v}_\mathsf{f}) = -\pi_\mathsf{f} \nabla \cdot \mathbf{v}_\mathsf{f} + (1-\alpha) K_\mathsf{D} |\boldsymbol{\gamma}|^2 - k_\mathsf{he}(\theta_\mathsf{s}^{-1} - \theta_\mathsf{f}^{-1}) + \nabla \cdot (k_\mathsf{f} \nabla \theta_\mathsf{f})\,, \tag{4.61f}$$

and assume that both heat-exchange and reactions are fast, i.e., $k_\mathsf{he}, k^r \to \infty$.

Fast thermal exchange Using fast heat-exchange we find new state variables with a combined internal energy $U = U_\mathsf{s} + U_\mathsf{f}$, following the evolution equation

$$\dot{U} + \nabla \cdot (U_\mathsf{s}\mathbf{v}_\mathsf{s} + U_\mathsf{f}\mathbf{v}_\mathsf{f}) = -\pi_\mathsf{s} \nabla \cdot \mathbf{v}_\mathsf{s} - \pi_\mathsf{f} \nabla \cdot \mathbf{v}_\mathsf{f} + K_\mathsf{D} |\boldsymbol{\gamma}|^2 + \nabla \cdot (k \nabla \theta) \tag{4.62}$$

where $k = k_\mathsf{s} + k_\mathsf{f}$. We can express $U_i = U_i(\mathbf{C}_\mathsf{s}, \mathbf{C}_\mathsf{f}, U)$ and all resulting thermodynamic quantities using the new state variable $\tilde{\mathbf{q}} = (\mathbf{P}_\mathsf{s}, \mathbf{C}_\mathsf{s}, \mathbf{P}_\mathsf{f}, \mathbf{C}_\mathsf{f}, U)$ under the assumption of $\theta_\mathsf{s} = \theta_\mathsf{f}$. As outlined in the previous section, this also produces an energy and entropy

$$\tilde{\mathcal{E}}(\tilde{\mathbf{q}}) = \int_\Omega \frac{\mathbf{P}_\mathsf{s}^2}{2\varrho_\mathsf{s}} + \frac{\mathbf{P}_\mathsf{f}^2}{2\varrho_\mathsf{f}} + U \,\mathrm{d}\mathbf{x}, \tag{4.63}$$

$$\tilde{\mathcal{S}}(\tilde{\mathbf{q}}) = \int_\Omega \tilde{S}(\mathbf{C}_\mathsf{s}, \mathbf{C}_\mathsf{f}, U) \,\mathrm{d}\mathbf{x}, \tag{4.64}$$

such that $\tilde{\mathcal{E}}(\tilde{\mathbf{q}}) = \mathcal{E}(\mathbf{q})$ and $\tilde{\mathcal{S}}(\tilde{\mathbf{q}}) = \mathcal{S}(\mathbf{q})$. This results in the new evolution $\dot{\tilde{\mathbf{q}}} = \tilde{\mathbb{J}}(\tilde{\mathbf{q}})\mathrm{D}\tilde{\mathcal{E}}(\tilde{\mathbf{q}}) + \tilde{\mathbb{K}}(\tilde{\mathbf{q}})\mathrm{D}\tilde{\mathcal{S}}(\tilde{\mathbf{q}})$. The previous Example 4.3.3 provides a practical recipe how the effective GENERIC dynamics is constructed.

Fast reactions In a similar spirit, we assume fast reactions and transform the fast reactions via $(\mathbf{C}_\mathsf{s}, \mathbf{C}_\mathsf{f})^\top \to Q(\mathbf{C}_\mathsf{s}, \mathbf{C}_\mathsf{f})^\top$, where the column vectors of $Q^\top$ span the space $\Gamma^\perp$ orthogonal to the stoichiometric space Γ defined in (4.53). Since $\mathbf{M} \in \Lambda^\perp$ we will always use the conservation of total mass (4.23) as one evolution equation. As suggested in Plümper et al. (2017), we also assume that the dehydration processes can be formulated in terms of the mass density of non-volatile solids $\varrho_\mathsf{nv} = \varrho_\mathsf{s}(1 - X_h)$, which can be obtained through the transformation Q. Here, $0 \leq X_h \leq 1$ is the relative hydrous content of the solid (rock) phase, that can potentially converted into the fluid phase. The precise definition of X_h depends on the interpretation of the components in $\mathbf{M} = (\mathbf{M}_\mathsf{s}, \mathbf{M}_\mathsf{f})^\top$. Having the invertibility of the corresponding equilibrium constraints from the Gibbs minimization we can write $\mathbf{C}_i = \mathbf{C}_i(\tilde{\mathbf{q}})$ and all remaining thermodynamic quantities with the help of the reduced concentration-like variables $\mathbf{C}^\perp = (\varrho, \varrho_\mathsf{nv}, ...) = Q\mathbf{C}$ assuming that the reactions are in equilibrium. As before, we can define the driving energy $\tilde{\mathcal{E}}(\tilde{\mathbf{q}})$ and entropy $\tilde{\mathcal{S}}(\tilde{\mathbf{q}})$ for this evolution in terms of the new state variable $\tilde{\mathbf{q}} = (\mathbf{P}_\mathsf{s}, \mathbf{P}_\mathsf{f}, U, \mathbf{C}^\perp)$. While details of this construction depend on the stoichiometry and the original entropy density, the final result maintains the GENERIC structure with modified operators and driving functionals. A concrete example relating to fast dehydration reactions as in (4.61) was provided in Example 4.3.5.

4.4.2 Discussion of Model (4.1)

We assume that by the limit of fast irreversible processes for heat exchange and reactions we have obtained a GENERIC formulation for $\mathbf{q} = (\mathbf{P}_\mathsf{s}, \mathbf{P}_\mathsf{f}, U, \mathbf{C}^\perp)^\top$ with driving energy $\tilde{\mathcal{E}}(\tilde{\mathbf{q}})$ and entropy $\tilde{\mathcal{S}}(\tilde{\mathbf{q}})$ as they were constructed before. In geoscientific applications, however, evolution equations are usually formulated in certain compositional variables (Plümper et al., 2017; Beinlich et al., 2020; Huber et al., 2022), which we address below. For simplicity, we assume that the reduced concentrations are $\mathbf{C}^\perp = (\varrho_\mathsf{tot}, \varrho_\mathsf{nv})$, i.e., the total mass density and the mass density of non-volatile solids. For more complex systems and other slow processes one might have to include further state variables into $\mathbf{C}^\perp$.

For each phase $i \in \{\mathsf{s}, \mathsf{f}\}$ we assume the existence of *volume fractions* $\phi_i : \Omega \to [0, 1]$, such that

$$0 \leq \phi_i(\mathbf{x}) \leq 1 \qquad \text{for all } \mathbf{x} \in \Omega \text{ and} \tag{4.65a}$$

$$\phi_\mathsf{s}(\mathbf{x}) + \phi_\mathsf{f}(\mathbf{x}) = 1 \qquad \text{for all } \mathbf{x} \in \Omega\,. \tag{4.65b}$$

Based on these variables it is now possible to define "pure" mass densities, i.e., the value

of ϱ_i if only phase i would be present in the system,

$$\hat{\varrho}_\mathsf{i} := \frac{\varrho_i}{\phi_i}\,, \qquad \text{for } i \in \{\mathsf{s},\mathsf{f}\}\,. \tag{4.66}$$

Similarly, it is possible to generalize the previous relation for any extensive variable A^i and distinguish it between "pure" and "partial" where the former will be denoted by $\hat{A}^i$ and related via

$$A^i(\mathbf{x}) = \hat{A}^i(\mathbf{x})\phi_i(\mathbf{x})\,, \qquad \text{for } i \in \{\mathsf{s},\mathsf{f}\}\,.$$

Remark 1 (Weight fractions) *Another commonly used variable is the weight fraction X_h of a given chemical compound h, where h could be a species C_i itself or just part of it. Here we are interested in the weight fraction of bound water within the solid phase. We will denote it by $X_{b\mathsf{H_2O}}$ and introduce*

$$\varrho_\mathsf{s}(1 - X_{b\mathsf{H_2O}}) = \varrho_\mathsf{nv} \quad \Leftrightarrow \quad \hat{\varrho}_\mathsf{s}(1 - X_{b\mathsf{H_2O}}) = \hat{\varrho}_\mathsf{nv} \tag{4.67}$$

for the system described above.

In total this gives the following evolution equations for the two-phase system

$$\partial_t \mathbf{P}_\mathsf{s} = -\nabla\cdot(\mathbf{P}_\mathsf{s}\otimes\mathbf{v}_\mathsf{s}) - \nabla\pi_\mathsf{s} + K_\mathsf{D}\left(\mathbf{v}_\mathsf{f} - \mathbf{v}_\mathsf{s}\right)\,, \tag{4.68a}$$

$$\partial_t \mathbf{P}_\mathsf{f} = -\nabla\cdot(\mathbf{P}_\mathsf{f}\otimes\mathbf{v}_\mathsf{f}) - \nabla\pi_\mathsf{f} - K_\mathsf{D}\left(\mathbf{v}_\mathsf{f} - \mathbf{v}_\mathsf{s}\right)\,, \tag{4.68b}$$

$$\dot{U} + \nabla\cdot(U_\mathsf{s}\mathbf{v}_\mathsf{s} + U_\mathsf{f}\mathbf{v}_\mathsf{f}) = -\pi_\mathsf{s}\nabla\cdot\mathbf{v}_\mathsf{s} - \pi_\mathsf{f}\nabla\cdot\mathbf{v}_\mathsf{f} + K_\mathsf{D}\left|\mathbf{v}_\mathsf{f} - \mathbf{v}_\mathsf{s}\right|^2 + \nabla\cdot(k\nabla\theta)\,, \tag{4.68c}$$

$$\partial_t \varrho_\mathsf{tot} \equiv \partial_t((1-\phi_\mathsf{f})\hat{\varrho}_\mathsf{s} + \phi_\mathsf{f}\hat{\varrho}_\mathsf{f}) = -\nabla\cdot((1-\phi_\mathsf{f})\hat{\varrho}_\mathsf{s}\mathbf{v}_\mathsf{s} + \phi_\mathsf{f}\hat{\varrho}_\mathsf{f}\mathbf{v}_\mathsf{f})\,, \tag{4.68d}$$

$$\partial_t \varrho_\mathsf{nv} \equiv \partial_t((1-\phi_\mathsf{f})\hat{\varrho}_\mathsf{nv}) = -\nabla\cdot((1-\phi_\mathsf{s})\hat{\varrho}_\mathsf{nv}\mathbf{v}_\mathsf{s} + Q_{\mathsf{nv},k}\,\mathbf{j}_k)\,, \tag{4.68e}$$

where at this point the evolution for the volume fraction ϕ is not yet determined. For a discussion of this evolution we refer to Mielke and Rohan (2013); Ehlers (2009). However, we will assume that the solid is immobile, i.e., $\mathbf{v}_\mathsf{s} = 0$ such that

$$\phi_\mathsf{f}(t) = 1 - \frac{(1-\phi_\mathsf{f}(t=0))\hat{\varrho}_\mathsf{nv}(t=0)}{\hat{\varrho}_\mathsf{nv}(t)}, \tag{4.69}$$

e.g. see Plümper et al. (2017, Eq. 11). In this equation, as discussed in Example 4.3.5, $\hat{\varrho}_\mathsf{s}$, $\hat{\varrho}_\mathsf{f}$ are given by an equation of state as in (4.57) and the weight fraction for water is given by (4.67).

Neglecting the diffusion flux in the non-volatile solid and making the identification of

the Darcy flux $\mathbf{v}_\mathrm{f} = -K_\mathrm{D}^{-1}\nabla\pi_\mathrm{f}$, setting the temperature to a given constant, the evolution equations for the mass densities become

$$\partial_t\left(\hat{\varrho}_\mathrm{s}(1-X_{b\mathrm{H_2O}})(1-\phi_\mathrm{f})\right) = 0\,, \tag{4.70a}$$

$$\partial_t\left(\hat{\varrho}_\mathrm{s}(1-\phi_\mathrm{f}) + \hat{\varrho}_\mathrm{l}\phi_\mathrm{f}\right) = \nabla\cdot\left(\frac{\phi_\mathrm{f}\hat{\varrho}_\mathrm{f}}{K_\mathrm{D}}\nabla\pi_\mathrm{f}\right)\,. \tag{4.70b}$$

This is, in fact, an evolution system for the unknowns ϱ_nv and ϱ_tot. However, the construction in Plümper et al. (2017) suggests that a change of variables in the sense of Zafferi et al. (2022) should be applied, where the equations of state are determined as functions of temperature θ and fluid pressure π_f. This is the model (4.1) from (Plümper et al., 2017).

4.4.3 Discussion of Model (4.2)

Analogously to what is described in Sec. 4.4.2 we can obtain system (4.2) as a GENERIC system in the limit of fast irreversible processes for temperature and reactions equilibration. In this case we will also account for reactions in which other species are released along with the fluid and are subject to diffusion. An example for this type of reaction is: $(\mathrm{Mg,Fe})_{48}\mathrm{Si}_{34}\mathrm{O}_{85}(\mathrm{OH})_{62} \longleftrightarrow 34\,(\mathrm{Mg,Fe})_2\mathrm{SiO}_4 + 31\,\mathrm{H_2O} + 10\,{\mathrm{SiO_2}}^{\mathrm{aq}}$ where ${\mathrm{SiO_2}}^{\mathrm{aq}}$ on the product-side (right) diffuses within the fluid. Therefore we extend the GENERIC system (4.61) by adding the diffusive Onsager operator (4.28). Herein, since no solid-state diffusion is assumed here, we set all diffusion coefficients except for that of $C_{\mathrm{f},\mathrm{SiO_2}}$ to zero. System (4.2) is then recovered taking the limits of fast heat exchange and of fast reactions, for which we assume the reduced concentration vector to be $\mathbf{C}^\perp = (\varrho_\mathrm{tot}, \varrho_\mathrm{nv}, \varrho_{\mathrm{SiO_2}})$. By assuming zero solid velocity, i.e., $\mathbf{v}_\mathrm{s} = \mathbf{0}$ and conservation of the non-volatile mass density ϱ_nv, the evolution equations of $\mathbf{C}^\perp$ give exactly (4.2a)-(4.2c). Furthermore, it should be noted that in applications a variable is often used to denoted the total amount of a particular chemical element or constituent in a compound/phase. In this way, the content of k-th component in the i-th phase can be defined as follows

$$c_\mathrm{i}^k := \frac{M_{\mathrm{i},k}\,C_{\mathrm{i},k}}{\varrho_\mathrm{i}}\,.$$

In equations (4.2) we omit the superscript $\mathrm{SiO_2}$ since no misunderstanding is possible. In fact, (4.2b) is the evolution equation for $\varrho_{\mathrm{SiO_2}} = \varrho_\mathrm{s}c_\mathrm{s}(1-\phi) + \varrho_\mathrm{f}c_\mathrm{f}\phi$.

4.4.4 Geological Interpretation of the Models

The model defined by the set of equations (4.70), resp. (4.1), describes the general case of fluid flow through a porous rock where mass is exchanged between the fluid and the solid phase by mineral dissolution and precipitation. The assumption of an immobile solid, i.e., of zero solid velocity, is valid for small length scales (sub-µm to mm) where gravitational effects can be neglected because the density contrast is small compared to the variations in fluid pressure controlled by the local thermodynamic equilibrium.

On such small length scales the large-scale temperature gradients, see Figure 4.1, can be neglected and thus, for a given pressure and temperature, the local bulk composition controls when the dehydration reaction occurs. Therefore, chemical heterogeneities, i.e., local bulk composition variations in the domain, and chemical processes such as reactive fluid flow dominate rock dehydration on small length scales. Such variations in the composition are taken into account in model (4.2) in terms of the silicon dioxide SiO_2 content c_s and its diffusion and transport.

The focus of this study on the dehydration reaction of antigorite and brucite sets certain limits to the range of variables of models (4.1) and (4.2), especially the values for temperature, pressure and c_s. Pressure and temperature are confined to values that occur during ongoing subduction and c_s is limited to values where the minerals of interest are stable.

As antigorite and brucite form solid solutions between magnesium (Mg)- and iron (Fe)-endmembers, the reaction occurs not at a single point in π-θ space but rather in a divariant π-θ field. The onset of the reaction typically occurs at around 350 °C with the reaction of Fe-rich antigorite and brucite and is limited to higher temperatures by the stability limit of Mg-rich brucite at around 550 °C. Pressures depend on the depth at which the slab reaches those temperatures and on the fluid pressure that is controlled by the local thermodynamic equilibrium of the reaction. Typical lithostatic pressures, i.e. the pressure exerted on the solid by the overlying rock column, are in the range of 1-2.5 GPa [for a compilation of π-θ paths during subduction see e.g. Syracuse et al. (2010)].

The third variable controlling the stable mineral assemblage is the rock composition. A serpentinite that consists entirely of antigorite has a bulk Si content of $c_s \approx 0.205$. However, Si is distributed heterogeneously in the rock and c_s can therefore vary on smaller local domains within the rock. At low temperatures, c_s values below 0.205 lead to an increase of brucite abundance. A domain with a Si content of $c_s \approx 0.17$ contains significant amounts of brucite and antigorite at lower temperatures. At higher temperatures, this domain will form an almost pure olivine mineral assemblage. We therefore limit the range of c_s values to $0.17 - 0.205$ because in this range the mineral assemblage consists of various proportions

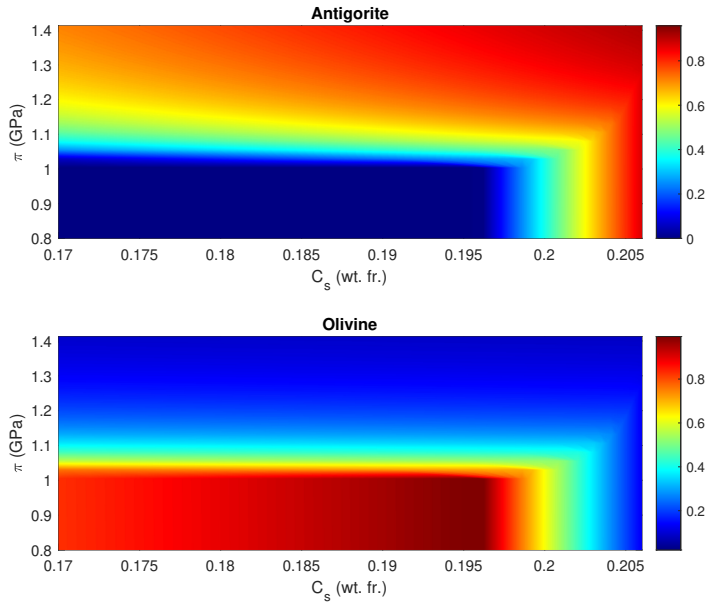

Figure 4.3: Abundances (volume fraction) of antigorite (hydrated mineral) and olivine (dehydrated mineral) as a function of silica content in the solid (c_s) and pressure (π) for a fixed temperature $\theta = 480\,°\text{C}$. An almost olivine-pure mineral assemblage forms at $c_s \approx 0.19$ for pressures below 1 GPa while for higher values antigorite becomes the dominant phase. Again, we underline that these plots are for a given composition at a given temperature, however the qualitative behaviour does not change for composition and temperature within the range of values discussed in Section 4.4.4.

of antigorite, olivine and brucite. For values $c_s > 0.205$ talc, another hydrous mineral that dehydrates to the dry mineral orthopyroxene, becomes stable. This dehydration reaction however is not within the scope of this study.

4.5 Towards the Analysis of a Reactive Diffusive Porous Media Model

In this section we discuss first steps and results on the mathematical analysis of models (4.1) and (4.2). Our approach combines a Galerkin approximation in space with an implicit Euler scheme in time as to provide a convergence result for a discretization scheme close to that already used in Plümper et al. (2017); Huber et al. (2022) for their numerical implementation. As a first step, we revisit the two models and reformulate them as a system of parabolic equations by means of a suitable transformation of variables. Based on this we state first existence results, which are deduced in detail in Zafferi and Thomas (2023). Our mathe-

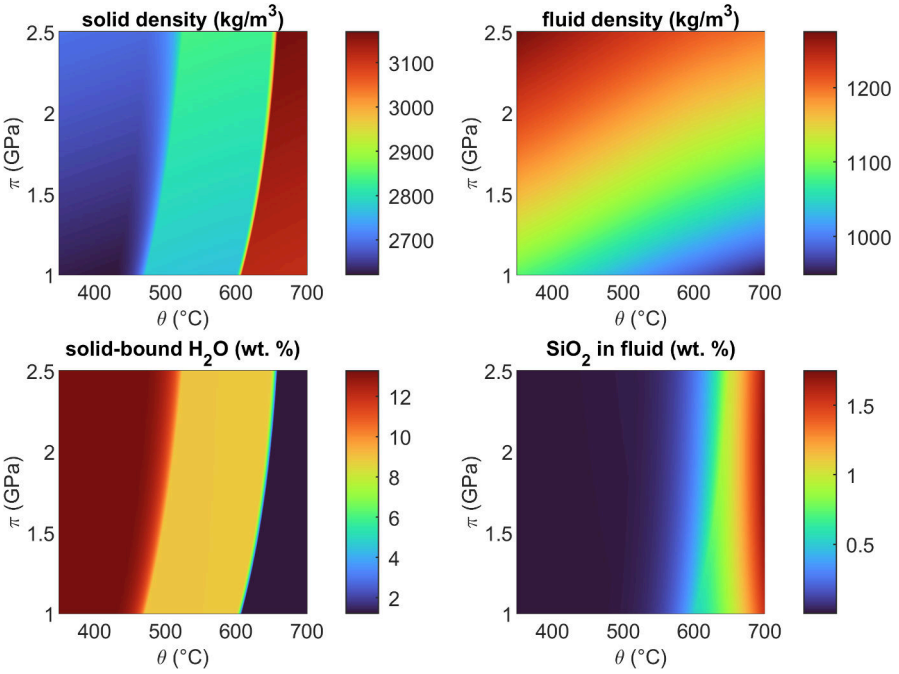

Figure 4.4: Pressure-temperature dependence of solid density, fluid density, solid-bound H_2O content and fluid composition wrt. SiO_2 for a typical serpentinite bulk rock composition as also used in the model of (Huber et al., 2022). Their model uses these pre-computed values as lookup tables to close the system of equations. One can see the qualitative changes of these functions for different values of (π, θ). More specifically, the rapid change in color for the solid mass density in the top left corner at fixed θ with varying π corresponds to a kink w.r.t. π of the type shown in Figure 4.5.

matical results require certain smoothness assumptions for the transformation maps and the resulting coefficient functions. We validate them in detail for specific thermodynamical rock data in Sections 4.5.1 and 4.5.2. This perusal will show that the mathematical assumptions are met in a certain ´´good" range of the thermodynamical data set but violated in another regime of the data set. We prove that a well-prepared initial datum keeps a solution within the good range for all times.

In this section we will denote the "pure" mass densities by ϱ_s and ϱ_f in contrast to $\hat{\varrho}_s$ and $\hat{\varrho}_f$ in model (4.1) and (4.2).

4.5.1 Results and Challenges of Model (4.1)

Parabolic Form of System (4.1)

Model (4.1) consists of the conservation of the mass of non-volatile species (4.1a) and of the conservation of total mass (4.1b). As a direct consequence of relation (4.1a) the porosity ϕ can be explicitly determined as follows

$$\phi = 1 - \frac{\varrho_s^0(1-X_h^0)(1-\phi^0)}{\varrho_s(1-X_h)}\,. \tag{4.71}$$

It is further assumed in Plümper et al. (2017) for the mass densities ϱ_s and ϱ_f of the solid and the fluid, and for the fraction X_h of fluid stored in the solid that

$$\begin{aligned} &\varrho_s = \tilde{\varrho}_s(\pi,\theta), \quad \varrho_f = \tilde{\varrho}_f(\pi,\theta), \quad \text{and } X_h = \tilde{X}_h(\pi,\theta) \\ &\text{are functions of pressure } \pi \text{ and temperature } \theta. \end{aligned} \tag{4.72}$$

Although the closed mathematical expression for these functions is not known, the values of $\varrho_s, \varrho_f, X_h$ in dependence of π and θ can be recovered from thermodynamical data tables. An example of data so produced is shown in Figure 4.4. Due to this, also the porosity can be seen as a function of π and θ, while also dependent on the initial data ϱ_s^0, X_h^0 as well , i.e. (4.71) gives

$$\phi = 1 - \frac{\varrho_s^0(1-X_h^0)(1-\phi^0)}{\tilde{\varrho}_s(\pi,\theta)(1-\tilde{X}_h(\pi,\theta))} =: \tilde{\phi}(\pi,\theta)\,. \tag{4.73}$$

Similarly, the terms appearing in (4.1b) can be rewritten as functions of π and θ, i.e., we introduce

$$\tilde{\varrho}(\pi,\theta) := (\tilde{\varrho}_f(\pi,\theta)\tilde{\phi}(\pi,\theta) + \tilde{\varrho}_s(\pi,\theta)(1-\tilde{\phi}(\pi,\theta))) \quad \text{and} \tag{4.74}$$

$$\widetilde{K}(\pi,\theta) := \tilde{\varrho}_f(\pi,\theta)K_\phi(\tilde{\phi}(\pi,\theta)) = \tilde{\varrho}_f(\pi,\theta)\frac{\kappa}{\mu}\tilde{\phi}(\pi,\theta)^3 \text{ with constants } \kappa,\mu > 0 \tag{4.75}$$

for the total mass and for the permeability. Then (4.1b) takes the form

$$\partial_t \tilde{\varrho}(\pi,\theta) = \nabla\cdot\widetilde{K}(\pi,\theta)\nabla\pi\,. \tag{4.76}$$

Now we set

$$\varrho := \tilde{\varrho}(\pi,\theta) \tag{4.77}$$

and we assume that

$$\text{for all } \theta > 0 \text{ fixed the function } \tilde{\varrho}(\cdot,\theta) \text{ is invertible in } \pi, \tag{4.78a}$$

$$\text{the inverse function } \tilde{\varrho}^{-1}(\cdot,\theta) \text{ is continuously differentiable, and} \tag{4.78b}$$

$$\text{there are constants } 0 < c_* < c^* \text{ such that } \tfrac{1}{c^*} < \partial_\varrho \tilde{\varrho}^{-1}(\varrho,\theta) = \frac{1}{\partial_\pi \tilde{\varrho}(\tilde{\varrho}^{-1}(\tilde{\varrho}(\pi,\theta),\theta),\theta)} < \tfrac{1}{c_*}. \tag{4.78c}$$

Thus, for any $\theta > 0$ fixed we find

$$\pi = \tilde{\pi}(\varrho,\theta) := \tilde{\varrho}^{-1}(\varrho,\theta)\,. \tag{4.79}$$

Due to the fast equilibration of temperature discussed for the model (4.1) in Sec. 4.4, we can assume that θ is constant in space. Thus, in view of (4.78) together with the chain rule and the rule for differentiating the inverse we calculate

$$\nabla\pi = \nabla\tilde{\pi}(\varrho,\theta) = \partial_\varrho\tilde{\pi}(\varrho,\theta)\nabla\varrho = \frac{1}{\partial_\pi\tilde{\varrho}(\tilde{\pi}(\varrho,\theta),\theta)}\nabla\varrho \tag{4.80}$$

This gives the relation

$$\widetilde{\mathsf{K}}(\pi,\theta)\nabla\pi = \widehat{\mathsf{K}}(\varrho,\theta)\nabla\varrho \;\text{ with }\; \widehat{\mathsf{K}}(\varrho,\theta) = \frac{\widetilde{\mathsf{K}}(\tilde{\pi}(\varrho,\theta),\theta)}{\partial_\pi\tilde{\varrho}(\tilde{\pi}(\varrho,\theta),\theta)}\,. \tag{4.81}$$

Hence, (4.76) can be rewritten as a parabolic equation for the total mass density ϱ

$$\partial_t\varrho = \nabla\cdot\widehat{\mathsf{K}}(\varrho,\theta)\nabla\varrho\,. \tag{4.82}$$

Furthermore, for $\widehat{\mathsf{K}}$ we make the assumptions

$$\text{for all } \theta > 0 \text{ fixed the function } \widehat{\mathsf{K}}(\varrho,\theta) \text{ is continuous and} \tag{4.83a}$$

$$\text{there are constants } 0 < \hat{k}_* < \hat{k}^* \text{ such that } \hat{k}_* \le \widehat{\mathsf{K}}(\varrho,\theta) \le \hat{k}^* \text{ for all } \varrho \in \mathbb{R}. \tag{4.83b}$$

We point out that above assumptions (4.83) are satisfied if $\widetilde{\mathsf{K}}$ is continuous and uniformly bounded, and if properties (4.78) hold true. This, in turn, is closely linked to the properties of the given functions $\tilde{\phi}(\cdot,\theta)$, $\tilde{\varrho}_{\mathsf{s}}(\cdot,\theta)$, $\tilde{\varrho}_{\mathsf{f}}(\cdot,\theta)$, and $\tilde{X}_{\mathsf{h}}$.

Existence of a Weak Solution

Thanks to the above assumptions (4.83) one can deduce the existence of a weak solution $\varrho : [0,\mathsf{T}]\times\Omega \to (0,\infty)$ for the transformed system (4.82). Since the assumptions (4.78)

guarantee the bijectivity of the transformation map one can also infer the existence of a weak solution $\pi : [0, \mathsf{T}] \times \Omega \to (0, \infty)$ for the original system (4.1). Our existence result reads as follows:

Theorem 4.5.1 (Existence of a weak solution for system (4.82)) *Let $\mathsf{T} > 0$ and let $\Omega \subset \mathbb{R}^d$ be a bounded Lipschitz domain. Let $\partial_{\mathsf{N}}\Omega = \partial\Omega \backslash \partial_{\mathsf{D}}\Omega$ its Neumann part. Let $Q_{\mathsf{T}} := (0, \mathsf{T}) \times \Omega$ denote the space-time cylinder and set*

$$V := H^1(\Omega)\,. \tag{4.84}$$

Then the following statements hold true:

1. *Let $\varrho_0 \in V$ be a given initial datum and assume that $\widehat{\mathsf{K}}(\cdot, \theta)$ satisfies (4.83). Then there exists a function*

$$\varrho \in H^1(0, \mathsf{T}; V^*) \cap L^2(0, \mathsf{T}; V) \cap L^\infty(0, \mathsf{T}; L^2(\Omega)) \cap C^0([0, \mathsf{T}]; L^2(\Omega))\,, \tag{4.85a}$$

   which satisfies

$$\int_{Q_{\mathsf{T}}} \Big(\partial_t \varrho v + \widehat{\mathsf{K}}(\varrho, \theta) \nabla \varrho \cdot \nabla v \Big) \,\mathrm{d}x \,\mathrm{d}t = 0 \quad \text{for all } v \in L^2(0, \mathsf{T}; V) \tag{4.85b}$$

   and $\varrho(0) = \varrho_0$.
2. *Further assume that there are constants $0 < r_* < r^*$ such that $r_* \le \varrho_0(x) \le r^*$ holds true for a.e. $x \in \Omega$ for the initial datum ϱ_0. Then for all $t \in [0, \mathsf{T}]$ also a solution ϱ satisfies $r_* \le \varrho(t, x) \le r^*$ for a.e. $x \in \Omega$.*

Comments on the proof: We refer the reader to Zafferi and Thomas (2023, Sec. 3, 4) for the details of the proof. Here we give a short outline of the main steps.

To 1. In order to prove the existence of a weak solution satisfying (4.85) we introduce a discretization in time $\mathbb{T}_\tau := \{t_\tau^0 = 0,\ t_\tau^k = k\tau \text{ for } \tau = \mathsf{T}\mathbb{N},\ k = 1, \dots N \in \mathbb{N}\}$ and a Galerkin approximation in space by finite-dimensional subspaces $V^n = \operatorname{span}\{e_1, \dots, e_n\} \subset V$, $n \in \mathbb{N}$ such that $\bigcup_{n\in\mathbb{N}} V^n \subset V$ densely, with e_i, $i = 1, \dots, n$ denoting a basis of V^n. By invoking Zeidler (1985, Prop. 2.8, p. 53) we obtain for every time-step $k \le N$, all $N \in \mathbb{N}$, and all $n \in \mathbb{N}$ the existence of a vector of coefficients $\boldsymbol{\varrho}_n^{\tau k} = (\varrho_{n1}^{\tau k}, \dots, \varrho_{nn}^{\tau k})$ providing an element $\varrho_n^{\tau k} = \sum_{i=1}^n \varrho_{ni}^{\tau k} e_i \in V^n$ that solves the system of n nonlinear equations

$$\sum_{i=1}^n \int_\Omega \Big(\frac{\varrho_{ni}^{\tau k} - \varrho_{ni}^{\tau k-1}}{\tau} e_i e_j + \widehat{\mathsf{K}}(\varrho_n^{\tau k}, \theta) \varrho_{ni}^{\tau k} \nabla e_i \cdot \nabla e_j \Big) \,\mathrm{d}x = 0 \quad \text{for all } j = 1, \dots, n. \tag{4.86}$$

By testing (4.86) with $\varrho_n^{\tau k} \in V^n$ and summing up over $k \leq l \in \{1, \dots, N\}$ one obtains the following a priori estimates uniformly for all $n \in \mathbb{N}$ and $\tau = \mathsf{T}/N$, $N \in \mathbb{N}$:

$$\tfrac{1}{2}\|\varrho_n^{\tau l}\|^2_{L^2(\Omega)} + \sum_{k=1}^{l} \tau \hat{k}_* \|\nabla \varrho_n^{\tau k}\|^2_{L^2(\Omega,\mathbb{R}^d)} \leq \tfrac{1}{2}\|\varrho_n^{\tau 0}\|^2_{L^2(\Omega)} = \|\mathbb{P}_n \varrho_0\|^2_{L^2(\Omega)}\,, \qquad \text{hence:}$$

$$\tfrac{1}{2}\|\varrho_n^{\tau l}\|^2_{L^2(\Omega)} + \sum_{k=1}^{l} \tau \hat{k}_* \|\varrho_n^{\tau k}\|^2_{V} \leq (\tfrac{1}{2} + \mathsf{T}\hat{k}_*)\|\mathbb{P}_n \varrho_0\|^2_{L^2(\Omega)}\,, \tag{4.87}$$

where $\mathbb{P}_n \varrho_0$ is the projection of the initial datum $\varrho_0 \in V$ into V^n and where we have also used (4.83). For each $k \in \{1, \dots, N\}$, with $N \in \mathbb{N}$ fixed, as $n \to \infty$, this provides the existence of a (not relabelled) subsequence $(\varrho_n^{\tau k})_{n\in\mathbb{N}}$ and of an element $\varrho^{\tau k} \in V$ such that

$$\varrho_n^{\tau k} \rightharpoonup \varrho^{\tau k} \quad \text{ in } V \quad \text{as } n \to \infty\,. \tag{4.88}$$

By the compact embedding $V \Subset L^2(\Omega)$ and the boundedness of $\widehat{\mathsf{K}}$ we conclude by the dominated convergence theorem that $\widehat{\mathsf{K}}(\varrho_n^{\tau k})\nabla \mathbb{P}_n v \to \widehat{\mathsf{K}}(\varrho_n^{\tau k})\nabla v$ for every test function $v \in V$ and for all $k \in \{1, \dots, N\}$, and $\tau = \mathsf{T}/N$, $N \in \mathbb{N}$. Therefore we deduce by weak-strong convergence arguments that

$$0 \;=\; \sum_{k=1}^{N} \tau \int_\Omega \Big(\frac{\varrho_n^{\tau k} - \varrho_n^{\tau k-1}}{\tau} \mathbb{P}_n v^{\tau k} + \widehat{\mathsf{K}}(\varrho_n^{\tau k}, \theta)\nabla \varrho_n^{\tau k} \cdot \nabla \mathbb{P}_n v^{\tau k} \Big)\, \mathrm{d}x \tag{4.89a}$$

$$\downarrow\ n \to \infty$$

$$0 \;=\; \sum_{k=1}^{N} \tau \int_\Omega \Big(\frac{\varrho^{\tau k} - \varrho^{\tau k-1}}{\tau} v^{\tau k} + \widehat{\mathsf{K}}(\varrho^{\tau k}, \theta)\nabla \varrho^{\tau k} \cdot \nabla v^{\tau k} \Big)\, \mathrm{d}x \quad \text{for all } v^{\tau k} \in V \tag{4.89b}$$

We introduce the piecewise constant $\overline{\varrho}_\tau$, $\underline{\varrho}_\tau$, and affine ϱ_τ interpolants in time, i.e., for any $t \in (t_\tau^{k-1}, t_\tau^k]$, $k = 1, \dots, N$ we set

$$\overline{\varrho}_\tau(t) := \varrho^{\tau k},\ \underline{\varrho}_\tau(t) := \varrho^{\tau k-1},\ \varrho_\tau(t) := \frac{t - t_\tau^{k-1}}{\tau}\varrho^{\tau k} + \frac{t_\tau^k - t}{\tau}\varrho^{\tau k-1} \quad \text{as well as } \overline{t}_\tau(t) := t_\tau^k\,, \tag{4.90}$$

and we write $\dot{\varrho}_\tau(t) = (\varrho^{\tau k} - \varrho^{\tau k-1})/\tau$, $k \in \{1, \dots, N\}$, for the time-derivative of the affine interpolant ϱ_τ. We approximate any test function $v \in L^2(0, \mathsf{T}; V)$ by

$$v^{\tau k} := \frac{1}{\tau} \int_{t_\tau^{k-1}}^{t_\tau^k} v(s)\, \mathrm{d}s$$

and use these values to introduce the interpolants $\overline{v}_\tau$, $\underline{v}_\tau$, and v_τ as in (4.90). This ensures strong convergence of the interpolants, i.e., $\overline{v}_\tau, \underline{v}_\tau, v_\tau \to v$ strongly in $L^2(0, \mathsf{T}; V)$. Moreover,

for the interpolants $(\overline{\varrho}_\tau, \underline{\varrho}_\tau, \varrho_\tau)$ the estimate (4.87) together with

(4.89) provides the following bounds uniformly in $\tau = \mathsf{T}/N$, $N \in \mathbb{N}$:

$$\|\overline{\varrho}_\tau\|_{\mathrm{B}(0,\mathsf{T};L^2(\Omega))} + \|\underline{\varrho}_\tau\|_{\mathrm{B}(0,\mathsf{T};L^2(\Omega))} + \|\varrho_\tau\|_{\mathrm{B}(0,\mathsf{T};L^2(\Omega))} \leq C\,, \tag{4.91a}$$

$$\|\overline{\varrho}_\tau\|_{L^2(0,\mathsf{T};V)} \leq C\,, \tag{4.91b}$$

$$\|\dot{\varrho}_\tau\|_{L^2(0,\mathsf{T};V^*)} \leq C\,, \tag{4.91c}$$

with a constant $C > 0$ independent of $\tau = \mathsf{T}/N$ and $N \in \mathbb{N}$. Accordingly, one concludes the existence of a (not relabelled) subsequence and of a limit ϱ of regularity (4.85a) such that the following convergence properties hold true:

$$\overline{\varrho}_\tau, \underline{\varrho}_\tau, \varrho_\tau \overset{*}{\rightharpoonup} \varrho \quad \text{weakly-}* \text{ in } L^\infty(0,\mathsf{T};L^2(\Omega))\,, \tag{4.92a}$$

$$\overline{\varrho}_\tau, \varrho_\tau \rightharpoonup \varrho \quad \text{weakly in } L^2(0,\mathsf{T};V)\,, \tag{4.92b}$$

$$\dot{\varrho}_\tau \rightharpoonup \dot{\varrho} \quad \text{weakly in } L^2(0,\mathsf{T};V^*)\,, \tag{4.92c}$$

$$\overline{\varrho}_\tau, \varrho_\tau \to \varrho \quad \text{strongly in } L^2(0,\mathsf{T};L^2(\Omega))\,, \tag{4.92d}$$

$$\overline{\varrho}_\tau(t), \underline{\varrho}_\tau(t), \varrho_\tau(t) \overset{*}{\rightharpoonup} \varrho(t) \quad \text{weakly-}* \text{ in } V^* \text{ for all } t \in [0,\mathsf{T}]\,. \tag{4.92e}$$

Here, convergences (4.92a)-(4.92c) follow from standard compactness arguments. Moreover, convergence (4.92d) is deduced from estimates (4.91b) and (4.91c) by means of a time-discrete version of the Aubin-Lions lemma, cf. Dreher and Jüngel (2012, Thm. 1). We further observe that estimates (4.91a) and (4.91c) result in a uniform bound for the interpolants in $BV(0,\mathsf{T};V^*)$. From this, the pointwise convergence in time (4.92e) ensues by means of Helly's selection principle (Mielke and Roubíček, 2015, Thm. B.5.10, p. 610). Convergence results (4.92) then enable us to pass to the limit in $\tau = \mathsf{T}/N \to 0$ as $N \to \infty$ in (4.89b) and to conclude the validity of the weak formulation (4.85b). In addition, convergence result (4.92e) allows it to deduce that the initial datum is attained, i.e. that $\varrho(0) = \varrho_0$ in V. Let us also note that the regularity $\varrho \in H^1(0,\mathsf{T};V^*) \cap L^2(0,\mathsf{T};V) \cap L^\infty(0,\mathsf{T};L^2(\Omega))$ in (4.85a) ensues from convergence results (4.92), while $\varrho \in C^0([0,\mathsf{T}];L^2(\Omega))$ is a consequence of the regularity in Bochner spaces for the Gelfand triple $V \Subset L^2(\Omega) \subset V^*$.

To 2. Assume that the initial datum satisfies $r_* \leq \varrho_0 \leq r^*$ a.e. in Ω. We observe that the functions $\max\{\varrho - r^*, 0\}|_{[0,t]}$ and $\min\{\varrho - r_*, 0\}|_{[0,t]}$ for all $t \in [0,\mathsf{T}]$ are admissible test functions for (4.85b) since they are compositions of Lipschitz-continuous functions with Sobolev functions, cf. Marcus and Mizel (1979). Subsequent integration by parts in time

results in the relations

$$0 = \|\max\{\varrho(t)-r^*,0\}\|^2_{L^2(\Omega)} - \|\max\{\varrho_0-r^*,0\}\|^2_{L^2(\Omega)} + \int_{Q_t\cap[\varrho\geq r^*]} \widehat{\mathsf{K}}(\varrho,\theta)\nabla\varrho\cdot\nabla\varrho\,\mathrm{d}x\,\mathrm{d}s\,,$$

$$0 = \|\min\{\varrho(t)-r_*,0\}\|^2_{L^2(\Omega)} - \|\min\{\varrho_0-r_*,0\}\|^2_{L^2(\Omega)} + \int_{Q_t\cap[\varrho\leq r_*]} \widehat{\mathsf{K}}(\varrho,\theta)\nabla\varrho\cdot\nabla\varrho\,\mathrm{d}x\,\mathrm{d}s$$

for any $t\in(0,\mathsf{T}]$. In both expressions, the second term is zero due to the boundedness of the initial datum. Moreover, in both expressions the third term is non-negative thanks to (4.83). Thus, necessarily $\max\{\varrho(t)-r^*,0\}=\min\{\varrho(t)-r_*,0\}=0$ a.e. in Ω, which concludes the proof of statement 2. □

Remark 4.5.2 (Boundary conditions) *For simplicity we have formulated Thm. 4.5.1 with homogeneous Neumann boundary conditions* $\widehat{\mathsf{K}}(\varrho(t),\theta)\nabla\varrho(t)\cdot\mathbf{n}=0$ *on* $\partial\Omega$ *for all* $t\in[0,\mathsf{T}]$ *with* $\mathbf{n}$ *the outer unit normal vector to* $\partial\Omega$*. This can be extended to inhomogeneous Neumann boundary conditions for a prescribed datum* $h\in H^{-1/2}(\partial\Omega,\mathbb{R}^d)$*, so that* (4.85b) *additionally features the term* $\int_0^{\mathsf{T}}\int_{\partial\Omega} hv\,\mathrm{d}S\,\mathrm{d}t$*. Introducing* $\emptyset\neq\partial_{\mathsf{D}}\Omega\subset\partial\Omega$ *as the Dirichlet boundary and* $\partial_{\mathsf{N}}\Omega=\partial\Omega\backslash\partial_{\mathsf{D}}\Omega$*, Thm. 4.5.1 can also be adapted to inhomogeneous Dirichlet boundary conditions on* $\partial_{\mathsf{D}}\Omega$*. For this, consider* $g\in H^1(\Omega)$ *an extension of the given Dirichlet datum into the domain* Ω *and replace* ϱ *in* (4.85b) *by the shifted function* $\varrho+g$*, where both* ϱ *and the test functions* v *are now chosen in* $V_0:=\{u\in H^1(\Omega)\,|\,u=0\text{ on }\partial_{\mathsf{D}}\Omega\}$ *in space. This setting even provides a unique weak solution. We note that also statement 2. can be adapted to the case of inhomogeneous Dirichlet conditions: Given* $g_{\mathsf{D}}\in H^{1/2}(\partial_{\mathsf{D}}\Omega)$ *such that* $g_{\mathsf{D}}\in[r_*,r^*]$ *a.e. on* $\partial_{\mathsf{D}}\Omega$ *and* $g\in H^1(\Omega)$ *an extension of* g_{D} *into* Ω *one observes that* $\max\{\varrho+g-r^*,0\}\in V_0$ *and* $\min\{\varrho+g-r_*,0\}\in V_0$ *are admissible test functions, so that the proof of 2. can be reproduced.*

Perusal of Assumptions (4.78) & (4.83) for Thermodynamical Rock Data

In the following we validate the mathematical assumptions (4.78) and (4.83) with the thermodynamical rock data used in Plümper et al. (2017). Figure 4.5 shows the total mass density $\varrho=\tilde{\varrho}(\pi)$ as a function of pressure π in its geologically relevant range of 0.8-2 GPa, see also Sec. 4.4.4. Figure 4.5 confirms that $\tilde{\varrho}$ is a continuous and strictly monotone function of pressure π, hence bijective. Yet, it also turns out that the map suffers from a kink at $\pi=1.2$ GPa, which hampers the assumption of continuous differentiability of $\tilde{\varrho}$ and its inverse $\tilde{\varrho}^{-1}$, cf. (4.78b). Indeed, this kink coincides with a phase transformation between antigorite and olivine as shown is Figure 4.3 and in Figure 4.4. It therefore also 1.2 GPa, see Figure 4.6. As expected this translates into a discontinuity of the coefficient function $\widehat{\mathsf{K}}(\cdot,\theta)$

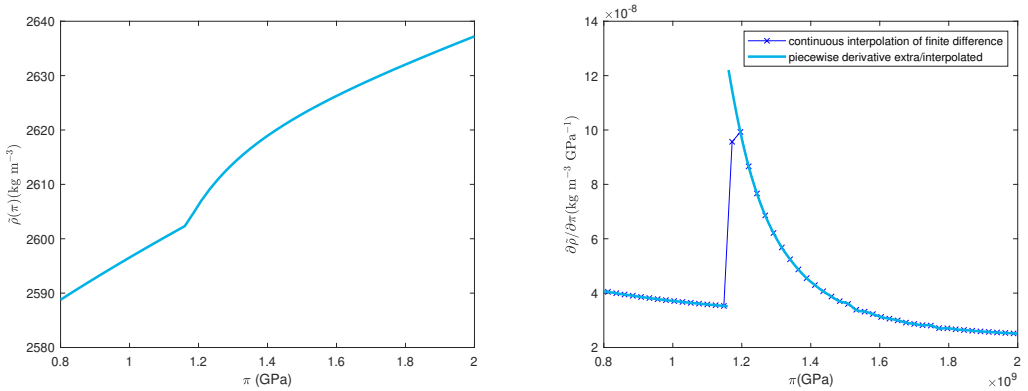

Figure 4.5: on the left: Example of $\tilde{\varrho} = \tilde{\varrho}(\pi, \theta)$ for a given composition and at fixed temperature of 480 °C. One can see the continuity and strict monotonicity of $\tilde{\varrho}$ which in return guarantee the existence of a continuous inverse $\tilde{\varrho}^{-1}$. On the right: plot of the derivative $\partial\tilde{\varrho}/\partial\pi$ for two possible discretizations. It can bee seen that it is discontinuous at $\pi = 1.2\,\text{GPa}$ and that is bounded from below and above satisfying assumption (4.78c).

at $\varrho \approx 2600\,\text{kg}\,\text{m}^{-3}$. We further point out that the porosity shown in Fig.4.6 is strictly positive and bounded from below by the value $\tilde{\phi}(2\,\text{GPa}, 480\,^\circ\text{C}) = 0.035 > 0$. In turn, we find the coefficient function $\widehat{\mathsf{K}}(\cdot, \theta)$ to be uniformly bounded from above and from below by a value strictly larger than zero, so that assumption (4.83b) is satisfied.

As the violation of the continuity assumptions (4.83a) for $\widehat{\mathsf{K}}(\cdot, \theta)$ and (4.78b) are concerned, we point out that the analytical results given in Thm. 4.5.1, 2. predict that the weak solution $\varrho(t, \cdot)$ for all $t \in [0, \mathrm{T}]$ stays confined between values $0 < r_* < r^*$ a.e. in Ω, if the initial datum ϱ_0 is chosen with this property. In other words, if the initial datum is chosen with values strictly below or strictly above the critical value of $\varrho = 2600\,\text{kg}\,\text{m}^{-3}$ (corresponding to the critical pressure of 1.2 GPa), then also the solution will not exceed this value apart from a set of zero measure at any later time $t \in (0, \mathrm{T}]$. Thus, under this additional assumption on the initial datum, all the assumptions (4.78) and (4.83) are met and therefore existence of a unique weak solution is guaranteed by Thm. 4.5.1, 1. However, this also means that in this setting the phase transition, with ϱ exceeding the critical value on sets of positive measure, cannot be described by Thm. 4.5.1 using the original thermodynamical data set. Instead, in order to cover also this case, one would have to mollify $\tilde{\varrho}(\cdot, \theta)$ and $\widehat{\mathsf{K}}(\cdot, \theta)$ in a small neighbourhood of the non-smoothness. From a geological perspective, even though the interesting pressure range is between 0.8-2 GPa, it is very difficult for a geological system to experience this complete range. Usually, pressure variations are very small and π is confined to a neighborhood of a certain value. Therefore it is usually sufficient to study one of either areas below or above 1.2 GPa. Additionally let us point out that the

phase stability, hence the position of the kink, varies with temperature and rock composition: If the system has a high iron content, one would find this kink in the mass density for higher values of pressure, cf. Huber et al. (2022). As explained in Figure 4.3 for the composition and temperature of this specific example, antigorite, the hydrated rock, is stable for pressure values above 1.2 GPa and olivine, the dehydrated rock, is stable at pressure values below 1.2 GPa. In conclusion, since the interest lies in the investigation of the dehydration process, we can confine the analysis to the regime below 1.2 GPa.

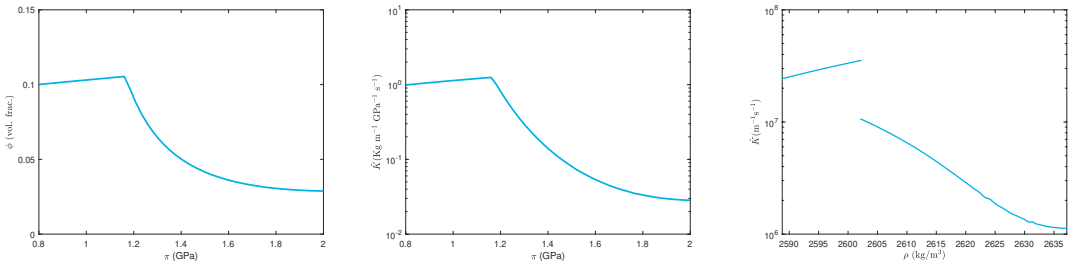

Figure 4.6: Example of $\phi = \phi(\pi, \theta)$, $\hat{K}(\pi, \theta)$ and $\tilde{K}(\pi, \theta)$ for a given composition and at fixed temperature of 480 °C. For these simulations we have set ratio between permeability of the medium and viscosity of the fluid $\hat{K}/\mu = 1$. Thus, positivity and continuity of $\hat{K}$ relies on ϕ, which never reaches zero.

4.5.2 Results and Challenges of Model (4.2)

Although the application of a similar approach as the one used in Section 4.5.1 might seem straightforward, the thermodynamical data behind the model (4.2) hide a series of challenges that require a special treatment. We dedicate this section to their description.

Parabolic Form of System (4.2)

Also in model (4.2) it is assumed that the quantities

$$\begin{aligned} &\varrho_s = \tilde{\varrho}_s(\pi, c_s, \theta), \quad \varrho_f = \tilde{\varrho}_f(\pi, c_s, \theta), \quad c_f = \tilde{c}_f(\pi, c_s, \theta) \text{ are given functions} \\ &\text{of pressure } \pi, \text{ concentration } c_s, \text{ and temperature } \theta\,. \end{aligned} \tag{4.93}$$

Again, their analytical form is unknown, but their values can be determined from thermodynamical data tables. Combining (4.93) and (4.2c) also the porosity ϕ can be understood as a function of the variables (π, c_s, θ) as follows

$$\phi = 1 - \frac{\varrho_s^0(1-c_s^0-X_h^0)(1-\phi^0)}{\tilde{\varrho}_s(\pi,c_s,\theta)(1-\tilde{c}_s-\tilde{X}_h(\pi,c_s,\theta))} =: \tilde{\phi}(\pi, c_s, \theta)\,. \tag{4.94}$$

Based on this we introduce the notation

$$\tilde{\varrho}_1(\pi, c_s, \theta) := \tilde{\varrho}_f(\pi, c_s, \theta)\tilde{\phi}(\pi, c_s, \theta) + \tilde{\varrho}_s(\pi, c_s, \theta)(1 - \tilde{\phi}(\pi, c_s, \theta)), \tag{4.95a}$$

$$\tilde{\varrho}_2(\pi, c_s, \theta) := \tilde{\varrho}_f(\pi, c_s, \theta)\tilde{\phi}(\pi, c_s, \theta)\tilde{c}_f(\pi, c_s, \theta) + \tilde{\varrho}_s(\pi, c_s, \theta)(1 - \tilde{\phi}(\pi, c_s, \theta))c_s, \tag{4.95b}$$

$$\widetilde{K}_1(\pi, c_s, \theta) := \tilde{\varrho}_f(\pi, c_s, \theta)K_\phi(\tilde{\phi}(\pi, c_s, \theta)), \tag{4.95c}$$

$$\widetilde{K}_2(\pi, c_s, \theta) := \tilde{\varrho}_f(\pi, c_s, \theta)\tilde{c}_f(\pi, c_s, \theta)K_\phi(\tilde{\phi}(\pi, c_s, \theta)), \tag{4.95d}$$

$$K_\phi(\tilde{\phi}(\pi, c_s, \theta)) := \frac{\kappa}{\mu}\tilde{\phi}(\pi, c_s, \theta)^3, \tag{4.95e}$$

$$\widetilde{\mathbb{D}}(\pi, c_s, \theta) := \tilde{\varrho}_f(\pi, c_s, \theta)\tilde{\phi}(\pi, c_s, \theta)D_c, \tag{4.95f}$$

with constants $\kappa, \mu, D_c > 0$. Thus, equations (4.2a) and (4.2b) can be rewritten as follows

$$\partial_t \tilde{\varrho}_1(\pi, c_s, \theta) = \nabla \cdot \left(\widetilde{K}_1(\pi, c_s, \theta)\nabla\pi\right), \tag{4.96a}$$

$$\partial_t \tilde{\varrho}_2(\pi, c_s, \theta) = \nabla \cdot \left(\widetilde{K}_2(\pi, c_s, \theta)\nabla\pi + \widetilde{\mathbb{D}}(\pi, c_s, \theta)\nabla\tilde{c}_f(\pi, c_s, \theta)\right). \tag{4.96b}$$

This is a PDE system of the form

$$\partial_t \tilde{\boldsymbol{\varrho}}(\mathbf{q}, \theta) - \nabla \cdot \left(\widetilde{K}_D(\mathbf{q}, \theta)\nabla\mathbf{q}\right) = 0 \quad \text{with} \tag{4.97a}$$

$$\mathbf{q} := \begin{pmatrix} \pi \\ c_s \end{pmatrix}, \quad \tilde{\boldsymbol{\varrho}} := \begin{pmatrix} \tilde{\varrho}_1 \\ \tilde{\varrho}_2 \end{pmatrix}, \quad \widetilde{K}_D := \begin{pmatrix} \widetilde{K}_1 & 0 \\ \widetilde{K}_2 + \partial_\pi \tilde{c}_f \widetilde{\mathbb{D}} & \partial_{c_s} \tilde{c}_f \widetilde{\mathbb{D}} \end{pmatrix}, \tag{4.97b}$$

where we have used the chain rule $\nabla\tilde{c}_f = \partial_\pi \tilde{c}_f \nabla\pi + \partial_{c_s}\tilde{c}_f \nabla c_s$.

Now we set

$$\boldsymbol{\varrho} := \tilde{\boldsymbol{\varrho}}(\mathbf{q}, \theta) \tag{4.98}$$

and make the following assumptions on the map $\tilde{\boldsymbol{\varrho}}$ and its inverse

$$\begin{aligned} &\text{for every } \theta > 0 \text{ fixed the function } \tilde{\boldsymbol{\varrho}}(\cdot, \theta) \text{ is continuously differentiable in } \mathbf{q} \\ &\text{and invertible in } \mathbf{q} \text{ and the inverse} \\ &\tilde{\boldsymbol{\varrho}}^{-1}(\cdot, \theta) \text{ is continuously differentiable.} \end{aligned} \tag{4.99a}$$

We note that assumptions (4.99) amount to the following conditions

$$\text{For all } \theta > 0 \text{ the Jacobian } \mathrm{D}_{\mathbf{q}}\tilde{\boldsymbol{\varrho}}(\cdot, \theta) = \begin{pmatrix} \partial_\pi \tilde{\varrho}_1(\cdot, \theta) & \partial_{c_s}\tilde{\varrho}_1(\cdot, \theta) \\ \partial_\pi \tilde{\varrho}_2(\cdot, \theta) & \partial_{c_s}\tilde{\varrho}_2(\cdot, \theta) \end{pmatrix} \text{ is continuous with} \tag{4.100a}$$

$$\det \mathrm{D}_{\mathbf{q}}\tilde{\boldsymbol{\varrho}}(\mathbf{q}, \theta) > 0 \text{ for all admissible } \mathbf{q} \in \mathbb{R}^2, \text{ and also} \tag{4.100b}$$

$$\mathrm{D}_{\boldsymbol{\varrho}}\tilde{\boldsymbol{\varrho}}^{-1}(\cdot, \theta) = \mathrm{D}_{\mathbf{q}}\tilde{\boldsymbol{\varrho}}(\tilde{\boldsymbol{\varrho}}^{-1}(\cdot, \theta), \theta)^{-1} \text{ is a continuous function in } \boldsymbol{\varrho}. \tag{4.100c}$$

Then we have

$$\mathbf{q} = \tilde{\boldsymbol{\varrho}}^{-1}(\boldsymbol{\varrho}, \theta) =: \tilde{\mathbf{q}}(\boldsymbol{\varrho}, \theta) \tag{4.101}$$

and system (4.97) can be rewritten as a parabolic PDE system of the form

$$\partial_t \boldsymbol{\varrho} - \nabla \cdot \left(\widehat{\mathsf{K}}_{\mathrm{D}}(\boldsymbol{\varrho}, \theta) \nabla \boldsymbol{\varrho} \right) = 0 \,, \tag{4.102a}$$

where we used the relations

$$\nabla \mathbf{q} = \partial_{\boldsymbol{\varrho}} \tilde{\mathbf{q}}(\boldsymbol{\varrho}, \theta) \nabla \boldsymbol{\varrho} \quad \text{and} \quad \widehat{\mathsf{K}}_{\mathrm{D}}(\boldsymbol{\varrho}, \theta) := \widetilde{\mathsf{K}}_{\mathrm{D}}(\tilde{\mathbf{q}}(\boldsymbol{\varrho}, \theta), \theta) \partial_{\boldsymbol{\varrho}} \tilde{\mathbf{q}}(\boldsymbol{\varrho}, \theta) \,. \tag{4.102b}$$

We now state the following assumptions on $\widehat{\mathsf{K}}_{\mathrm{D}}$:

For all $\theta > 0$ the matrix $\widehat{\mathsf{K}}_{\mathrm{D}}(\cdot, \theta)$ has the following properties:

- $\widehat{\mathsf{K}}_{\mathrm{D}}(\cdot, \theta) : \mathbb{R}^2 \to \mathbb{R}^{2\times 2}$ is continuous, (4.103a)
- $\widehat{\mathsf{K}}_{\mathrm{D}}(\mathbf{q}, \theta) : \mathbb{R}^{2\times 2} \to \mathbb{R}^{2\times 2}$ is bounded and positively definite uniformly wrt. $(\mathbf{q}, \theta)$, (4.103b)

  i.e., there are constants $0 < K_* < K^*$ s.th. for all $(\mathbf{q}, \theta)$ and all $\mathbf{v} \in \mathbb{R}^2$ there holds :

  $$K_* |\mathbf{v}|^2 \leq \mathbf{v} \cdot \widehat{\mathsf{K}}_{\mathrm{D}}(\mathbf{q}, \theta) \mathbf{v} \leq K^* |\mathbf{v}|^2 \,.$$

Existence of Weak Solutions

We observe that assumptions (4.100) and (4.103) are the immediate translation of the assumptions from the scalar-valued to the vector-valued setting. Accordingly, we here state the following existence result. Its proof closely follows the outline given in Section 4.5.1 and we refer the reader to Zafferi and Thomas (2023, Sec. 3, 4) for further details.

Theorem 4.5.3 (Existence of a weak solution for system (4.102)) *Let the prerequisites of Theorem 4.5.1 be satisfied and denote $\mathbf{V} := V \times V$. Then the following statements hold true:*

1. *Let $\boldsymbol{\varrho}_0 \in \mathbf{V}$ be a given initial datum and assume that $\widehat{\mathsf{K}}_{\mathrm{D}}(\cdot, \theta)$ satisfies (4.103). Then there exists a function*

   $$\boldsymbol{\varrho} \in H^1(0, \mathsf{T}; \mathbf{V}^*) \cap L^2(0, \mathsf{T}; \mathbf{V}) \cap L^\infty(0, \mathsf{T}; L^2(\Omega, \mathbb{R}^2)) \cap C^0([0, \mathsf{T}]; L^2(\Omega; \mathbb{R}^2)) \,, \tag{4.104a}$$

   which satisfies

   $$\int_{Q_\mathsf{T}} \left(\partial_t \boldsymbol{\varrho} \cdot \mathbf{v} + \widehat{\mathsf{K}}_{\mathrm{D}}(\boldsymbol{\varrho}, \theta) \nabla \boldsymbol{\varrho} : \nabla \mathbf{v} \right) \mathrm{d}x \, \mathrm{d}t = 0 \quad \textit{for all } \mathbf{v} \in L^2(0, \mathsf{T}; \mathbf{V}). \tag{4.104b}$$

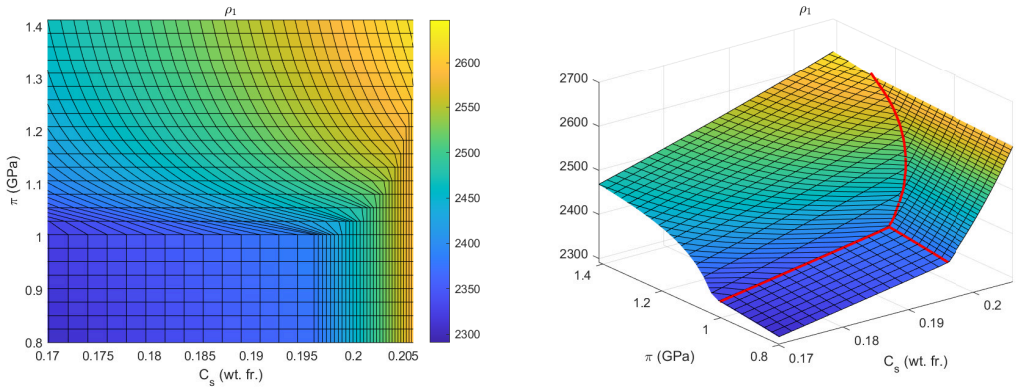

Figure 4.7: Plots of the total mass density $\tilde{\varrho}_1 = \tilde{\varrho}_1(\pi, c_s, \theta)$. On the left a 2D plot showing the discretization grid resulting from an interpolation of the thermodynamic dataset. The non-differentiability points are marked with a red line in the right plot. This shows the division into three main areas $((0.8, 1)\text{GPa} \times (0.17, 0.196), (0.8, 1)\text{GPa} \times (0.196, 0.2)$ and the remaining part of the domain) delimited by two straight lines and one curve with a contact point around $(1\text{GPa}, 0.195)$. These three subdivisions and the values for which $\tilde{\varrho}_1$ is continuous but not differentiable are more clearly seen in the 3D plot on the right.

and $\boldsymbol{\varrho}(0) = \boldsymbol{\varrho_0}$.

2. *Further assume that there are constants* $0 < r_{1*} < r_1^*$ *and* $0 < r_{2*} < r_2^*$ *such that* $r_{1*} \leq \varrho_{10}(x) \leq r_1^*$ *as well as* $r_{2*} \leq \varrho_{20}(x) \leq r_2^*$ *holds true for a.e.* $x \in \Omega$ *for the initial datum* $\boldsymbol{\varrho_0} = (\varrho_{10}, \varrho_{20})^\top$. *Then for all* $t \in [0, T]$ *also a solution* $\boldsymbol{\varrho} = (\varrho_1, \varrho_2)^\top$ *satisfies* $r_{1*} \leq \varrho_1(t, x) \leq r_1^*$ *as well as* $r_{2*} \leq \varrho_2(t, x) \leq r_2^*$ *for a.e.* $x \in \Omega$.

Perusal of Assumptions (4.100) & (4.103) for Thermodynamical Rock Data

Firstly we recall that system (4.2) is written in terms of $\mathbf{q} = (\pi, c_s)^\top$, i.e., in terms of the pressure π and the concentration of silica in the solid c_s. A close inspection of the thermodynamical rock data sets reveals that the introduction of this additional complexity causes the resulting mass densities to have regions of non-invertibility and non-differentiability, as it can be seen in Figures 4.7 and 4.8 for the mass densities $\tilde{\varrho}_1$ and $\tilde{\varrho}_2$. This is in analogy to the kink in the thermodynamical data of model (4.1) shown in Figure 4.6. More precisely, we see in Figure 4.7 that the total mass density $\tilde{\varrho}_1$ is strictly monotonously increasing with respect to pressure and silica-content, but that kinks arise in the region of the antigorite-olivine phase transition discussed in Figure 4.3. Similarly, also Figure 4.8 shows a monotone behavior of the total silica-mass density $\tilde{\varrho}_2$ in pressure and silica-content, also with kinks arising at the antigorite-olivine phase transition. Obviously, within this region assumptions (4.99) and (4.100) are not satisfied.

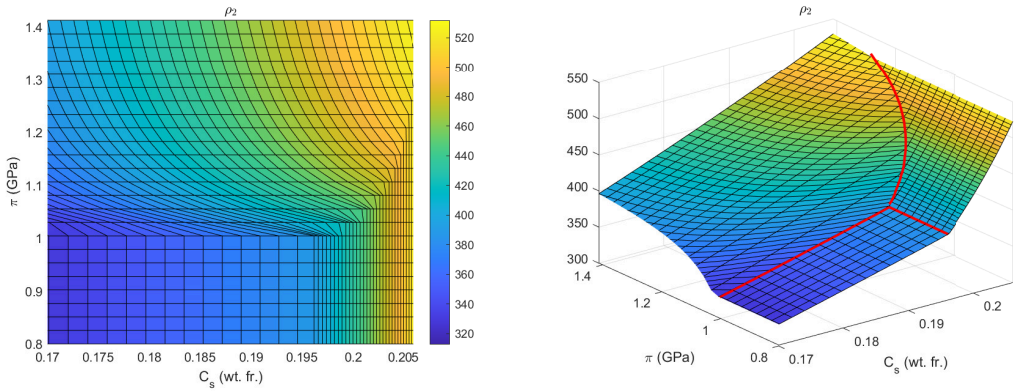

Figure 4.8: Plots of the total mass density of silica $\tilde{\varrho}_2 = \tilde{\varrho}_2(\pi, c_s, \theta)$. On the left a 2D plot showing the discretization grid resulting from an interpolation of the thermodynamic dataset. The non-differentiability points are marked with a red line in the right plot. This shows the division into three main areas (the same of $\tilde{\varrho}_1$ shown in Figure 4.7). These three subdivisions and the values for which $\tilde{\varrho}_2$ is continuous but not differentiable are more clearly seen in the 3D plot on the right.

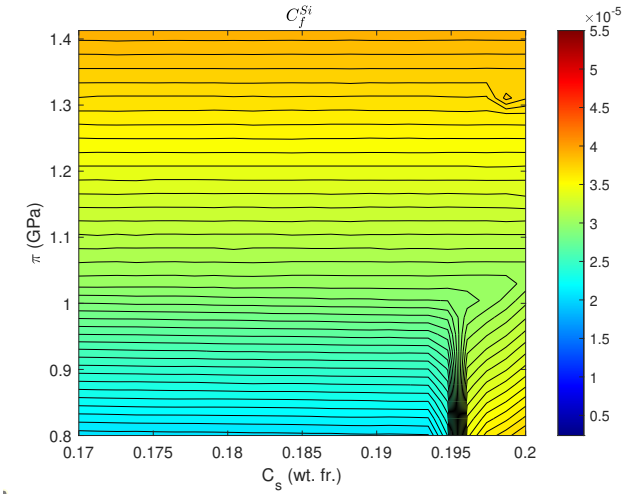

Figure 4.9: The figure shows isolevels for the function $\tilde{c}_f(\pi, \tilde{c}_s)$ at $\theta = 480°C$. One can see that in most parts of the considered domain we have $\partial c_f / \partial c_s = 0$ which translates to no diffusion occurring in the system. However it is worth noticing that there is a small area in the bottom right corner where this condition is not met. In addition, a discontinuity point where the lines are more dense can be seen around $c_s \approx 0.195$. This discontinuity would, i.e., invalidates assumption (4.103a)

Additionally we point out that in (4.2) the gradient of the silica concentration in the fluid $\tilde{c}_f$ drives the diffusion process. Hence, it would be natural to chose $\tilde{c}_f$ as a variable.

However, as Figure 4.9 reveals, in wide areas of the data range $\tilde{c}_f$ is constant with respect to c_s, so that the function is not invertible in these areas. This is the reason why system (4.96) is written in terms of the variables π and c_s. Indeed, such plateau regions followed by kinks as in Figure 4.9 are common in thermodynamical rock data sets. They are also predicted in Guy (1993) in the case of non-convex thermodynamical functions, which is again closely related to phase stability.

As can be seen from (4.97), in regions where $\partial\tilde{c}_f/\partial c_s = 0$, diffusion of silica is absent and the mathematical classification of the PDE system becomes unclear. Similar to Section 4.5.1 one may also try here to confine the initial data to a data range that ensures the validity of assumptions (4.100) and (4.103). Then the results of Theorem 4.5.3 would also guarantee that solutions are confined to that data range for all times $t \in (0, T]$. However, as can be seen from (4.97) the positive definiteness of $\widehat{K}_D$, and hence the classification of the PDE system, is not solely linked to the positive definiteness of the Jacobian $D_{\mathbf{q}}\tilde{\boldsymbol{\varrho}}$ but also to the values of the material constants κ, μ, and D_c contributing to the non-symmetric coefficient matrix $\widetilde{K}$ in (4.97).

These material constants are, in fact, the main contributors, together with $\partial\tilde{c}_f/\partial c_s$ and $\partial\tilde{c}_f/\partial\pi$, to the parabolicity of the system. In the literature, see e.g. Watson and Wark (1997), it is discussed that potential values for D_c and μ range from 10^{-8} to 10^{-10} $m^2\,s^{-1}$ and 10^{-4} Pa s while for the permeability κ one finds 10^{-17} to 10^{-14} m^2 see e.g. (Manning and Ingebritsen, 1999). An unprecise tuning of the system might lead to fail the assumption (4.103b). This is exemplary seen in Figure 4.10, where we have plotted the eigenvalues of $\mathrm{sym}\hat{K} = 1/2(\hat{K} + \hat{K}^\top)$. In the considered range of pressure and concentration it turns out that its smallest eigenvalue is negative whereas the largest eigenvalue is positive. In fact, the uniform positive definiteness of $\widehat{K}$, i.e., a lower bound as in (4.103b), is equivalent to $\mathrm{sym}\hat{K}$ being positive definite. As a further difficulty it turns out that the computation of the thermodynamical data set is highly sensitive to the total composition and therefore to the function $\tilde{c}_f$. This creates approximation errors in the plateau region where $\partial\tilde{c}_f/\partial c_s = 0$ that may cause backward diffusion in the system.

Different strategies can be deployed to circumvent this problem: the interpolation of the approximated $\tilde{c}_f$ function could be constructed to ensure that $\partial\tilde{c}_f/\partial c_s = 0 > \delta > 0$. Alternatively, more sophisticated and invasive solutions rely on extensions of the system that account for further geophysical phenomena that could help mitigate this behavior. One possibility is to include more species and phases, which would lead to a change in the landscape of $\tilde{c}_f$, possibly avoiding a plateau of the previous type. In general, non-convex regions in the energy landscape can produce $\partial\tilde{c}_f/\partial c_s = 0$ of different signs, indicating that phase separation is taking place. In such a case, higher-order derivatives as in the Cahn-

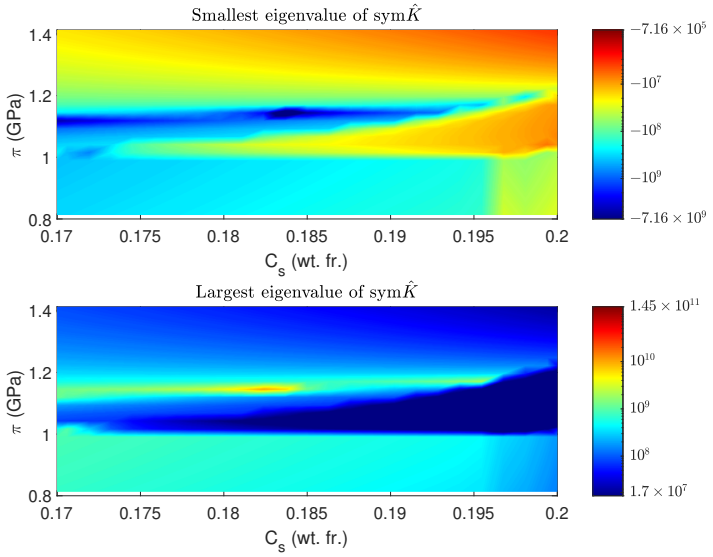

Figure 4.10: The figure shows the eigenvalue for the symmetrized operator sym$\hat{K} = 1/2(\hat{K} + \hat{K}^\top)$ for θ =480 °C. For the considered range of pressure and concentration the smallest eigenvalue is well kept below 0 while the largest is clearly positive.

Hilliard model might help to ensure the mathematical well-posedness of the problem.

4.6 Acknowledgements

AZ, KH, DP, JV, TJ, and MT gratefully acknowledge the funding by the DFG-Collaborative Research Centre 1114 *Scaling cascades in complex systems*, project # 235221301, C09 *Dynamics of rock dehydration on multiple scales*. DP gratefully acknowledges the funding by the DFG-Priority Programme 2171 *Dynamic Wetting of Flexible, Adaptive, and Switchable Substrates* by project # 422792530. DP and MT also thank the Berlin Mathematics Research Center MATH+ and the Einstein Foundation Berlin for the financial support within the Thematic Einstein Semester *Energy-based mathematical methods for reactive multiphase flows* and by project AA2-9.

References

S. Angiboust, T. Pettke, J. C. M. De Hoog, B. Caron, and O. Oncken. Channelized Fluid Flow and Eclogite-facies Metasomatism along the Subduction Shear Zone. *J. Petrol.*, 55(5):883–916, 2014. ISSN 0022-3530. doi:10.1093/petrology/egu010.

D. Aregba-Driollet, F. Diele, and R. Natalini. A Mathematical Model for the Sulphur Dioxide Aggression to Calcium Carbonate Stones: Numerical Approximation and Asymptotic Analysis. *SIAM J. Appl. Math.*, 64(5):1636–1667, 2004. ISSN 0036-1399. doi:10.1137/S003613990342829X.

L. E. Baker, A. C. Pierce, and K. D. Luks. Gibbs Energy Analysis of Phase Equilibria. *Society of Petroleum Engineers Journal*, 22(05):731–742, 1982. ISSN 0197-7520. doi:10.2118/9806-PA.

A. Beinlich, T. John, J. C. Vrijmoed, M. Tominaga, T. Magna, and Y. Y. Podladchikov. Instantaneous rock transformations in the deep crust driven by reactive fluid flow. *Nat. Geosci.*, 13(4):307–311, 2020. ISSN 1752-0908. doi:10.1038/s41561-020-0554-9.

W. Bloch, T. John, J. Kummerow, P. Salazar, O. S. Krüger, and S. A. Shapiro. Watching Dehydration: Seismic Indication for Transient Fluid Pathways in the Oceanic Mantle of the Subducting Nazca Slab. *Geochem. Geophys. Geosystems*, 19(9):3189–3207, 2018. ISSN 1525-2027. doi:10.1029/2018GC007703.

C. M. Breeding and J. J. Ague. Slab-derived fluids and quartz-vein formation in an accretionary prism, Otago Schist, New Zealand. *Geology*, 30(6):499–502, 2002. ISSN 0091-7613. doi:10.1130/0091-7613(2002)030<0499:SDFAQV>2.0.CO;2.

S. Chen, R. C. Hin, T. John, R. Brooker, B. Bryan, Y. Niu, and T. Elliott. Molybdenum systematics of subducted crust record reactive fluid flow from underlying slab serpentine dehydration. *Nat. Commun.*, 10(1):4773, 2019. ISSN 2041-1723. doi:10.1038/s41467-019-12696-3.

M. Clément, J. A. Padrón-Navarta, and A. Tommasi. Interplay between fluid extraction mechanisms and antigorite dehydration reactions (val malenco, italian alps). *J. Petrol.*, 60(10):1935–1962, 2020. ISSN 0022-3530. doi:10.1093/petrology/egz058.

J. A. Connolly. A primer in Gibbs energy minimization for geophysicists. *Petrology*, 25(5):526–534, 2017.

O. Coussy. *Poromechanics*. John Wiley & Sons, 2004. ISBN 978-0-470-09270-5.

M. Dreher and A. Jüngel. Compact families of piecewise constant functions in. *Nonlinear Analysis: Theory, Methods & Applications*, 75(6):3072–3077, 2012. ISSN 0362546X. doi:10.1016/j.na.2011.12.004.

W. Ehlers. Challenges of porous media models in geo- and biomechanical engineering including electro-chemically active polymers and gels. *Int J Adv Eng Sci Appl Math*, 1(1):1–24, 2009. ISSN 0975-0770. doi:10.1007/s12572-009-0001-z.

P. J. Flory. Thermodynamics of High Polymer Solutions. *The Journal of Chemical Physics*, 10(1):51–61, 1942. ISSN 0021-9606. doi:10.1063/1.1723621.

M. Grmela and H. C. Öttinger. Dynamics and thermodynamics of complex fluids. I. Development of a general formalism. *Phys. Rev. E*, 56(6):6620–6632, 1997.

B. Guy. Mathematical revision of Korzhinskii's theory of infiltration metasomatic zoning. *Eur. J. Mineral.*, pages 317–340, 1993. ISSN ,. doi:10.1127/ejm/5/2/0317.

P. Herms, T. John, R. J. Bakker, and V. Schenk. Evidence for channelized external fluid flow and element transfer in subducting slabs (Raspas Complex, Ecuador). *Chemical Geology*, 310–311:79–96, 2012. ISSN 0009-2541. doi:10.1016/j.chemgeo.2012.03.023.

K. Huber, J. C. Vrijmoed, and T. John. Formation of Olivine Veins by Reactive Fluid Flow in a Dehydrating Serpentinite. *Geochem Geophys Geosyst*, 23(6):e2021GC010267, 2022. ISSN 1525-2027, 1525-2027. doi:10.1029/2021GC010267.

M. L. Huggins. Solutions of Long Chain Compounds. *The Journal of Chemical Physics*, 9(5):440, 1941. ISSN 0021-9606. doi:10.1063/1.1750930.

T. John, R. Klemd, J. Gao, and C.-D. Garbe-Schönberg. Trace-element mobilization in slabs due to non steady-state fluid–rock interaction: Constraints from an eclogite-facies transport vein in blueschist (Tianshan, China). *Lithos*, 103(1):1–24, 2008. ISSN 0024-4937. doi:10.1016/j.lithos.2007.09.005.

T. John, N. Gussone, Y. Y. Podladchikov, G. E. Bebout, R. Dohmen, R. Halama, R. Klemd, T. Magna, and H.-M. Seitz. Volcanic arcs fed by rapid pulsed fluid flow through subducting slabs. *Nat. Geosci.*, 5(7):489–492, 2012. ISSN 1752-0908. doi:10.1038/ngeo1482.

P. Koukkari and R. Pajarre. Calculation of constrained equilibria by Gibbs energy minimization. *Calphad*, 30(1):18–26, 2006. ISSN 0364-5916. doi:10.1016/j.calphad.2005.11.007.

R. F. Krause. *Growth, Modelling and Remodelling of Biological Tissue*. doctoralThesis, 2014.

C. E. Manning and S. E. Ingebritsen. Permeability of the continental crust: Implications of geothermal data and metamorphic systems. *Rev. Geophys.*, 37(1):127–150, 1999. ISSN 1944-9208. doi:10.1029/1998RG900002.

M. Marcus and V. J. Mizel. Every superposition operator mapping one Sobolev space into another is continuous. *Journal of Functional Analysis*, 33(2):217–229, 1979. ISSN 0022-1236. doi:10.1016/0022-1236(79)90113-7.

A. Mielke. A gradient structure for reaction–diffusion systems and for energy-drift-diffusion systems*. *Nonlinearity*, 24(4):1329, 2011. ISSN 0951-7715. doi:10.1088/0951-7715/24/4/016.

A. Mielke and E. Rohan. Homogenization of elastic waves in fluid-saturated porous media using the biot model. *Math. Models Methods Appl. Sci.*, 23(05):873–916, 2013. ISSN 0218-2025. doi:10.1142/S0218202512500637.

A. Mielke and T. Roubíček. *Rate-Independent Systems: Theory and Application*, volume 193 of *Applied Mathematical Sciences*. Springer New York, New York, NY, 2015. ISBN 978-1-4939-2705-0 978-1-4939-2706-7. doi:10.1007/978-1-4939-2706-7.

A. Mielke, M. A. Peletier, and A. Stephan. EDP-convergence for nonlinear fast–slow reaction systems with detailed balance. *Nonlinearity*, 34(8):5762–5798, 2021. ISSN 0951-7715, 1361-6544. doi:10.1088/1361-6544/ac0a8a.

V. Orava, O. Souček, and P. Cendula. Multi-phase modeling of non-isothermal reactive flow in fluidized bed reactors. *Journal of Computational and Applied Mathematics*, 289:282–295, 2015. ISSN 0377-0427. doi:10.1016/j.cam.2015.01.012.

H. C. Öttinger and M. Grmela. Dynamics and thermodynamics of complex fluids. II. Illustrations of a general formalism. *Phys. Rev. E*, 56(6):6633–6655, 1997.

J. A. Padrón-Navarta, A. Tommasi, C. J. Garrido, V. L. Sánchez-Vizcaíno, M. T. Gómez-Pugnaire, A. Jabaloy, and A. Vauchez. Fluid transfer into the wedge controlled by high-pressure hydrofractur-

ing in the cold top-slab mantle. *Earth Planet. Sci. Lett.*, 297(1):271–286, 2010. ISSN 0012-821X. doi:10.1016/j.epsl.2010.06.029.

O. Plümper, T. John, Y. Y. Podladchikov, J. C. Vrijmoed, and M. Scambelluri. Fluid escape from subduction zones controlled by channel-forming reactive porosity. *Nature Geosci*, 10(2):150–156, 2017. ISSN 1752-0908. doi:10.1038/ngeo2865.

L. H. Rüpke, J. P. Morgan, M. Hort, and J. A. D. Connolly. Serpentine and the subduction zone water cycle. *Earth Planet. Sci. Lett.*, 223(1):17–34, 2004. ISSN 0012-821X. doi:10.1016/j.epsl.2004.04.018.

C. Spandler, T. Pettke, and D. Rubatto. Internal and External Fluid Sources for Eclogite-facies Veins in the Monviso Meta-ophiolite, Western Alps: Implications for Fluid Flow in Subduction Zones. *Journal of Petrology*, 52(6):1207–1236, 2011. ISSN 0022-3530. doi:10.1093/petrology/egr025.

E. M. Syracuse, P. E. van Keken, and G. A. Abers. The global range of subduction zone thermal models. *Physics of the Earth and Planetary Interiors*, 183(1):73–90, 2010. ISSN 0031-9201. doi:10.1016/j.pepi.2010.02.004.

S. Taetz, T. John, M. Bröcker, C. Spandler, and A. Stracke. Fast intraslab fluid-flow events linked to pulses of high pore fluid pressure at the subducted plate interface. *Earth and Planetary Science Letters*, 482:33–43, 2018. ISSN 0012-821X. doi:10.1016/j.epsl.2017.10.044.

P. E. van Keken, B. R. Hacker, E. M. Syracuse, and G. A. Abers. Subduction factory: 4. Depth-dependent flux of H2O from subducting slabs worldwide. *J. Geophys. Res. Solid Earth*, 116(B1), 2011. ISSN 2156-2202. doi:10.1029/2010JB007922.

E. B. Watson and D. A. Wark. Diffusion of dissolved SiO_2 in H_2O at 1 GPa, with implications for mass transport in the crust and upper mantle. *Contrib. Mineral. Petrol.*, 130(1):66–80, 1997. doi:10.1007/s004100050350.

A. Zafferi and M. Thomas. Mathematical analysis of a porous-media model for rock-dehydration processes. *WIAS Prepr.*, 2023.

A. Zafferi, D. Peschka, and M. Thomas. GENERIC framework for reactive fluid flows. *ZAMM - J. Appl. Math. Mech. Z. Für Angew. Math. Mech.*, 103(7):e202100254, 2022. ISSN 1521-4001. doi:10.1002/zamm.202100254.

E. Zeidler. *Nonlinear functional analysis and its applications*. Springer-Verlag, New York, 1985. ISBN 978-0-387-90914-1.

Chapter 5

Conclusions

Dehydration of subducted oceanic lithosphere in subduction zones has been the subject of intense research for many years. Slab dehydration at depths of several tens of kilometers prevents direct observation, so numerical modeling is needed as a powerful tool to investigate dehydration mechanisms. Combining these numerical models with natural rock data from fully hydrated serpentinites as precursor rocks for subduction is a powerful method for investigating the formation of channelized vein networks during dehydration.

The results of this dissertation show the existence of self-similar chemical heterogeneities in the distribution of iron and silica in serpentinites from the sub-millimeter up to the meter scale, and likely even beyond. These heterogeneities manifest themselves as textural and mineralogical differences at the small scale and as lithological differences at the kilometer scale. Consequently, these scale-invariant patterns of chemical heterogeneities lead to a similar dehydration behavior of the slab at all scales. Pulse-like fluid production occurs at each scale with increasing fluid production rates towards the terminus of a dehydration reaction. These fluid production peaks emerge even in the case of the simplest chemical system possible to describe serpentinites with the effects of Fe-Mg partitioning. Additional peaks form in the case of more complex chemistry, thus even enhancing the effects of peaked fluid production.

The self-similar chemical heterogeneities also enhance the evolution of a channelized vein network during dehydration. SiO_2-poor domains liberate a SiO_2-poor fluid («1 wt. % SiO_2) that flows along fluid pressure gradients into silica-richer parts of the rock once the percolation threshold is reached. Here, reactive fluid flow can trigger mineral reactions without the necessity of a subduction-related increase in P-T conditions. The influx of a low-silica fluid into a pre-existing vein structure can induce antigorite breakdown and lead to the formation of an almost olivine-pure mineral assemblage within the vein with significant

amounts of antigorite stable in the host rock. Thus, SiO_2-metasomatism can lead to the formation of olivine-rich veins in an antigorite-rich host rock, similar to the veins observed in the Erro Tobbio meta-serpentinites.

The system of equations used for the reactive fluid flow model has successfully been reformulated in terms of GENERIC (General Equations of Non-Equilibrium Reversible–Irreversible Coupling). It is the first application of GENERIC in a geological context, and in particular in the case of rock dehydration. The analysis shows a kink in the coefficient function Khat at the phase transition between antigorite and olivine. In addition, the analysis can prove the existence of a weak solution if the initial conditions are chosen strictly outside the kink.

Chapter 6

Outlook: Towards the Slab Scale – Fluid Escape from a Dehydrating Slab by Reactive Porosity Waves

6.1 Introduction

The previous chapters have shown the role of chemical heterogeneities and reactive fluid flow for the onset of dehydration and the subsequent evolution towards an interconnected vein network. The models presented so far do not consider gravitational effects because the processes act on small length scales. However, gravitational effects must be considered on larger scales. Including gravitational effects introduces buoyancy forces acting on the porous medium, leading to solid compaction and fluid expulsion from the pore network (Figure 3.1).

In the case of brittle deformation of the surrounding rock, fluid expulsion by hydraulic fracturing can occur when the fluid pressure exceeds the yield strength of the surrounding rock. Hydraulic fractures provide a transient highly porous fluid pathway that can facilitate rapid fluid expulsion. Another possible mechanism for fluid expulsion are porosity waves (Yarushina and Podladchikov, 2015; Räss et al., 2014, 2018). Spontaneous and self-propagating porosity waves occur in fluid-saturated porous rocks undergoing viscoelastoplastic deformation and can transfer fluid upward through the rock column. At the head of a porosity wave, fluid overpressure causes decompaction, allowing the porosity to migrate further upward. At the tail of the porosity wave, underpressure leads to compaction and closure of the porosity.

Rock rheology influences the morphology of porosity waves. Thus, decompaction weakening describes the phenomenon that decompaction happens on shorter timescales than compaction, resulting in channeling instability and an elongated shape of the propagating

porosity wave Connolly and Podladchikov (2007); Omlin et al. (2018). Recently, porosity wave models have also been used to explain vertical chimney structures in sedimentary basins (Yarushina et al., 2022) and possible fluid-escape pipes during CO_2 storage (Johnson et al., 2024) in Norway.

In many cases, mechanical models need to be coupled with the effects of reactive transport (e.g. Bessat et al., 2022; Khakimova and Podladchikov, 2024). Intrinsic chemical heterogeneities have a first-order effect on the composition of the fluid liberated by dehydration reactions. Since the solid and fluid are in thermodynamic equilibrium, intrinsic chemical heterogeneities cause variations in fluid chemistry, which can in turn change the bulk composition when fluid flow occurs in the porous network. Thus, reactive fluid flow is important when modeling the dynamic evolution of porosity and permeability in rocks. Mineral reactions triggered by reactive fluid flow can lead to drastic changes in the solid density and, hence, to volumetric changes. In addition, dissolution-precipitation changes can have a drastic effect on the fluid density. To properly incorporate these density changes into numerical models, it is necessary to incorporate thermodynamic models into the purely mechanical models.

The model presented takes an important step in this direction and includes two main improvements compared to previous models. Firstly, mechanics and thermodynamical data are fully coupled by using thermodynamic lookup tables. The model can consider changes in fluid and solid densities, as well as the associated mineral reactions and volumetric changes in the full P-T-X range (Figure 6.4). Secondly, the model uses mappings of intrinsic chemical heterogeneities in a natural rock sample as input. This approach is challenging because the rock compositions, and thus important variables in the model, may have steep gradients in certain areas of the model. In addition, significant improvements in the numerical scheme result in shorter runtime and allow running the model without the necessity for access to high-performance computing infrastructure. Combining fully coupled Thermo-Hydro-Mechanical-Chemical (THMC) models with compositional data from natural rocks is therefore a logical and promising next step in studying the dynamic porosity evolution during rock dehydration.

In the context of this thesis, this model combines the findings from the previous chapters and combines them into a fully coupled model that combines the findings about reactive transport (Chapters 3 and 4 with the need for mechanical effects due to the larger length scale and the multiscale dataset from Chapter 2.

6.2 Model

Our mathematical model is based on the formulation by Yarushina et al. (2015); Yarushina and Podladchikov (2015), in which the authors provide a detailed derivation of the equations.

For completeness, we present a short derivation of the equations used in our model. A list of all symbols and units is given in Table 6.1. To close the system of equations, a thermodynamic model of pre-computed lookup tables is needed. Details about how the lookup tables were calculated are given in Section 6.2.1.

6.2.1 Mathematical Model

Here, we present a short derivation of the equations used in our model for completeness. For an extensive derivation, see Yarushina and Podladchikov (2015); Yarushina et al. (2015). Starting with the total mass conservation for both fluid and solid

$$\frac{\partial \varrho^t}{\partial t} = -\frac{\partial}{\partial x_i}\left[\left(v_i^f - v_i^s\right)\varrho^f \phi + v_i^s \varrho^t\right] \tag{6.1}$$

with a superscript s and f referring to the solid and fluid phase, respectively, and subscript i denotes the three dimensions $i = (x, y, z)$. The total momentum conservation is given by

$$\frac{\partial}{\partial x_j}\left(-P^t \delta_{ij} + \tau_{ij}^t\right) - g_i \varrho^t = 0 \tag{6.2}$$

For viscous compaction of the solid phase, we apply the following constitutive relationship

$$\frac{\partial v_i^S}{\partial x_i} = \frac{P^f - P^t}{\eta_\phi} \tag{6.3}$$

The viscous rheology and chemical reactions lead to changes in the solid volume, which is expressed by the following equation for the total volume of the system

$$\frac{\partial v_i^s}{\partial x_i} = \frac{1}{V}\frac{d^s V}{dt} = \frac{d^s}{dt}(\ln V) \tag{6.4}$$

The fluid mass conservation is given by

$$\frac{\partial}{\partial t}\left(\varrho^f \phi\right) = -\frac{\partial}{\partial x_i}\left[\left(v_i^f - v_i^s\right)\varrho^f \phi + v_i^s \varrho^f \phi\right] \tag{6.5}$$

The fluid momentum conservation is given by Darcy's law in the form of

$$\phi\left(v_i^f - v_i^s\right) = -\frac{k}{\eta_f}\left(\frac{\partial P^f}{\partial x_i} + g_i \varrho^f\right) \tag{6.6}$$

with k being permeability and η_f fluid viscosity. Permeability is linked to porosity by the Carman-Kozeny relationship

$$k = k_0 \left(\frac{\phi}{\phi_{\text{bg}}} \right)^n \tag{6.7}$$

with k_0 and ϕ_{bg} being the background permeability and background porosity, respectively. In our model, we set $n = 3$, a value typically used for Darcy flux in porous media.

Similar to the total mass conservation [Equation (6.1)], the conservation of SiO_2 is given by

$$\frac{\partial}{\partial t} \left(rho^t C^{t,\text{SiO}_2} \right) = -\frac{\partial}{\partial x_i} \left[\left(v^f - v^s \right) \phi \varrho^f C^{f,\text{SiO}_2} + v^s \varrho^s C^{t,\text{SiO}_2} \right] \tag{6.8}$$

Conservation of the non-hydrous mass, i.e., the mass that is always bound to the solid, is given by the sum of the solid mass conservation of MgO and FeO:

$$\frac{\partial}{\partial t} \left[\varrho^s \left(1 - \phi \right) C^{s,\text{MgO+FeO}} \right] = -\frac{\partial}{\partial x_i} \left[v_i^s \varrho^s (1 - \phi) C^{s,\text{MgO+FeO}} \right] \tag{6.9}$$

Alternatively, the non-hydrous mass conservation can be expressed using the material derivative of the system volume V

$$\frac{d^s}{dt} \left[\varrho^s (1 - \phi) V C^{s,\text{MgO+FeO}} \right] = 0 \tag{6.10}$$

with d^s/dt being the material derivative with respect to the solid velocity

$$\frac{d^s}{dt} = \frac{\partial}{\partial t} + v^s \frac{\partial}{\partial x} \tag{6.11}$$

Integrating Equation (6.10) gives

$$\varrho^s (1 - \phi) V C^{s,\text{MgO+FeO}} = \varrho_0^s (1 - \phi_0) V_0 C_0^{s,\text{MgO+FeO}} \tag{6.12}$$

which can be solved for porosity

$$\phi = 1 - \frac{\varrho_0^s (1 - \phi_0) V_0 C_0^{s,\text{MgO+FeO}}}{\varrho^s V C^{s,\text{MgO+FeO}}} \tag{6.13}$$

Equation (6.13) is very similar to the equation used to calculate porosities in Chapter 2 (ref), Chapter 3 (eq. (4.2c)), and Chapter 4 (ref). However, the porosity equation used in this Chapter also accounts for the volumetric changes due to mechanical effects, which as not been captured in the previous Chapters.

Table 6.1: Reactive porosity wave model notation.

Variables and parameters			Indices, sub- and superscripts	
Symbol	Meaning	Unit		
ϱ	density	$\mathrm{kg\,m^{-3}}$	^{f}	fluid phase
C	concentration	[ ] (wt. fraction)	^{s}	solid phase
η	viscosity	Pa s	^{t}	total system (fluid + solid)
P	pressure	Pa	^{n}	Kozeny-Carman exponent
V	volume	$\mathrm{m^3}$	$_{i,j}$	spatial dimension
ϕ	porosity	[ ] (vol. fraction)	$_{0}$	reference value
v	velocity	$\mathrm{m\,s^{-1}}$		
k	permeability	$\mathrm{m^2}$		
g	gravitational constant	$\mathrm{m\,s^{-2}}$		
τ	shear stress	Pa		
T	temperature	°C		
δ	Kronecker delta			

Thermodynamic Closure Relationships

The aforementioned equations can be used to calculate porosity ϕ (6.13), fluid pressure P^f (6.1), and the SiO_2 content of the system C^{t,SiO_2} (6.5). Analog to the previous models (e.g. Chapter 3), we use pre-computed lookup tables to close the system of equations. The lookup tables contain the values for C^{f,SiO_2}, $C^{s,FeO}$, ϱ^s, and ϱ^f expressed as functions of C^{t,SiO_2}, $C^{t,MgO}$, P^f, and T.

$$C^{f,SiO_2} = C^{f,SiO_2}(C^{t,SiO_2}, C^{t,MgO}, T, P^f) \tag{6.14}$$

$$C^{s,MgO} = C^{s,MgO}(C^{t,SiO_2}, C^{t,MgO}, T, P^f) \tag{6.15}$$

$$C^{s,FeO} = C^{s,FeO}(C^{t,SiO_2}, C^{t,MgO}, T, P^f) \tag{6.16}$$

$$\varrho^s = \varrho^s(C^{t,SiO_2}, C^{t,MgO}, T, P^f) \tag{6.17}$$

$$\varrho^f = \varrho^f(C^{t,SiO_2}, C^{t,MgO}, T, P^f) \tag{6.18}$$

6.2.2 Thermodynamic Model

The lookup tables were calculated using the Thermolab software of Vrijmoed and Podladchikov (2022) in combination with the thermodynamic dataset of Holland and Powell (2004). We considered the potential solid phases antigorite, brucite, talc, orthopyroxene, olivine, and quartz, using the solution models of Evans and Frost (2021) and ideal mixing for brucite.

The lookup tables were calculated in a pressure range from 0.5 to 4 GPa and a tem-

perature range from 300 to 700 °C. All computations were performed in the full ternary FeO-MgO-SiO_2 (FMS) composition space, with H_2O available at excess. The MATLAB codes used to calculate the lookup tables are given in the thermodynamic model section below.

Figure 6.4 shows the lookup table values for C^{f,H_2O}, ϱ^s, and the abundance of olivine, antigorite, talc, and orthopyroxene in the ternary composition space at 550 °C and 3 GPa. The white crosses are plotted at the composition of each node in the 2D model shown in Figure 6.3 and demonstrate how the lookup tables are used to interpolate relevant values in P-T-X space.

At constant pressure, the fluid density in our system is a function of C^{f,SiO_2} only. Consequently, ϱ^f has the same topology in ternary composition space as the fluid composition (Figure 6.4). Fluid density and composition are strongly correlated and mainly a function of the bulk SiO_2 system, with two plateaus for low and high bulk SiO_2 contents, respectively. Such plateaus form when the fluid composition is buffered by brucite at low SiO_2 contents and by quartz at higher SiO_2 contents. Similarly, the solid density correlates with the solid H_2O content because dry phases are usually denser than hydrous phases.

6.3 Results

First, we present numerical results obtained by one-dimensional (1D) simulation before proceeding to the two-dimensional (2D) case to demonstrate the combination of sub-processes, which our coupled mathematical model is able to reproduce. A limitation of the 1D case is that it cannot capture the effects of fluid flow focusing and channeling, which is only possible considering the 2D model setup. For these purposes, we provide 2D simulations as well.

In total, three model setups are presented in this chapter: First, a 1D setup (Figure 6.1) is shown with the y-axis being depth. This simple setup demonstrates the principal fluid-solid interaction mechanisms combining reactive fluid flow and solid deformation. Next, a simplified 2D setup (Figure 6.2) is used to show fluid flow focusing, which can not be seen in the 1D case. The 2D model represents a vertical profile with depth on the y-axis and a horizontal length on the x-axis (both being non-dimensional). Finally, we show the 2D setup with the chemical mappings from Chapter 2, adding the effects of chemical heterogeneities within the domain (Figure 6.3). The initial compositions for all models are given in Table 6.2.

Table 6.2: Bulk compositions (in wt.%) for the reactive porosity wave models.

	1D (fig. 6.1)		**2D** (fig. 6.2)		**2D mappings** (fig. 6.3)	
	domain	boundary	domain	boundary	domain	boundary
SiO_2	46.0	31.3	50.0	38.8	mapping	30.0
MgO	35.0	34.3	35.0	40.0	mapping	40.0
FeO	19.0	34.4	15.0	21.2	mapping	30.0
H_2O	excess	excess	excess	excess	excess	excess

6.3.1 1D Model

Model Setup

To demonstrate the principal sub-processes capturing with the implemented coupled model, we consider the 1D case (Figure 6.1), where we use a simplified chemistry (Table 6.2). Similar to the reactive transport model in Chapter 3, the SiO_2 content is set lower at the bottom boundary to simulate the influx of a low-silica fluid. A possible source region for the fluid is another part of the rock that is relatively SiO_2-poorer and FeO-richer than the model domain. The background porosity is set to 0.1, with an increased porosity initialized at the bottom boundary, representing an upscaled vein network.

Results

Figure 6.1 shows the results of the 1D setup. The influx of a low silica fluid from the bottom boundary leads to the reaction of antigorite to olivine and brucite (e). This dehydration reaction is accompanied by a drastic increase in porosity (a) and solid density (d). The figure shows the results after several reactive porosity waves have passed through the domain and have already transformed the initially stable mineral assemblage of talc and orthopryoxene to antigorite and olivine. As the bulk SiO_2 content of the solid decreases, it becomes relatively richer in MgO and FeO. Figure 6.1d shows the fluid and solid density curves, where the fluid density is multiplied by three to show both curves on the same axis. Solid density changes drastically from approximately $2820\,kg\,m^{-3}$ to $3500\,kg\,m^{-3}$ from top to bottom, whereas the fluid density stays relatively constant. For the fluid, the decrease in density due to a lower content of dissolved silica [see Figure 6.4a] is offset by the increase in density due to increasing pressure with depth.

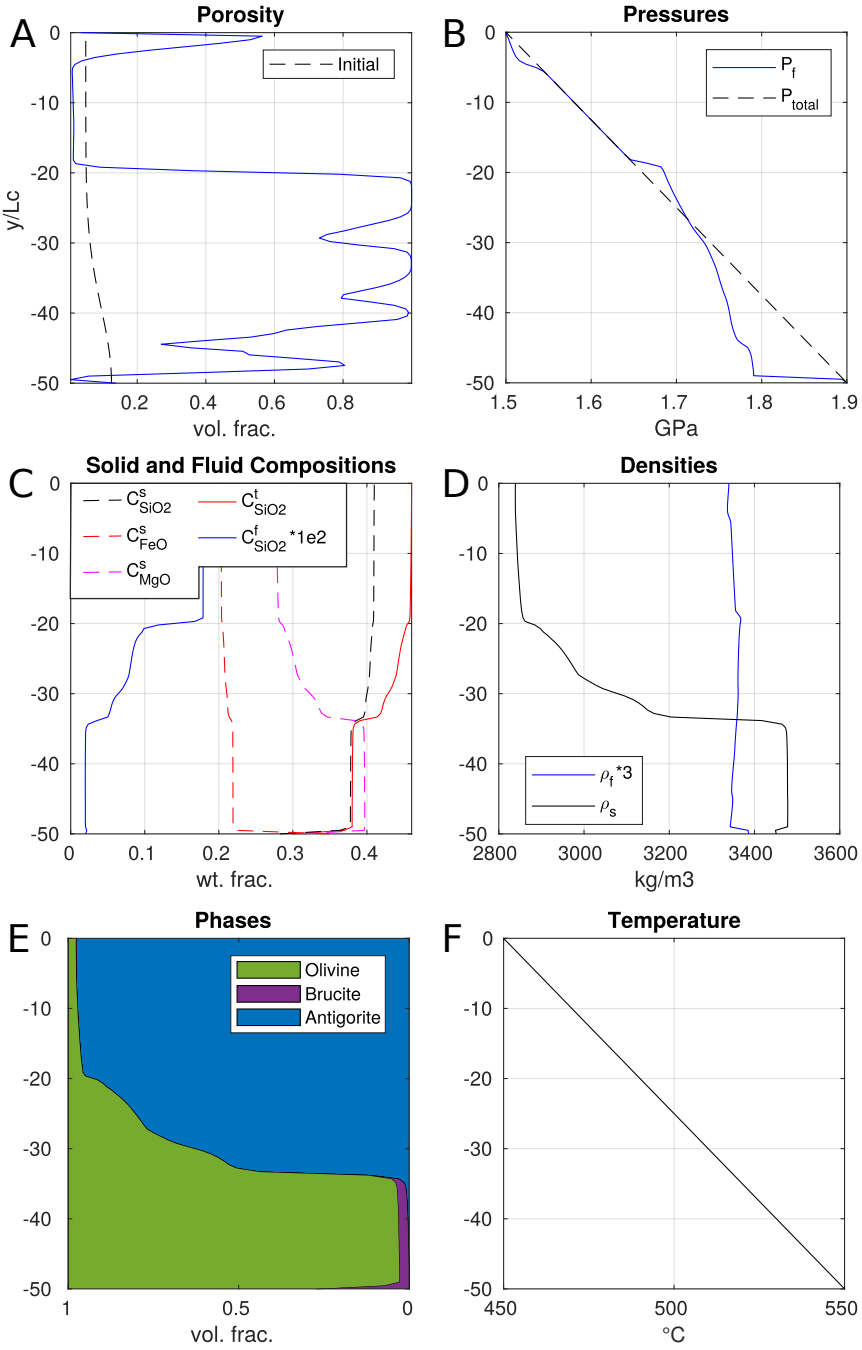

Figure 6.1: Results of a vertical 1D model. An upward traveling porosity wave causes the dehydration reaction of antigorite to olivine by a fluid pressure drop in the low-pressure tail of the porosity wave and the influx of a low-silica fluid from the bottom boundary. A steady-state temperature gradient from bottom to top is applied. Higher temperatures in the lower part of the domain result in a higher fluid density. Porosity is highest in the low-pressure tail.

6.3.2 2D Model

Setup

As input for our model in the 2D case, we use one of the chemical mappings from the multiscale dataset presented in Chapter 2. We use these mappings as representatives for slab-scale chemical heterogeneities, following the findings about the scale-independence of such heterogeneities (Chapter 2). We set a low SiO_2 content ($C_{tot} = 0.38$) as a boundary condition at the bottom boundary. Similar to the reactive transport model in Chapter 3, low SiO_2 contents at the boundary are in thermodynamic equilibrium with a low silica fluid that will then flow into the domain. Additionally, an initial high porosity domain is initialized at the bottom part of the domain, representing an existing, upscaled channelized porosity structure in the slab. A steady-state temperature gradient is initialized, with 540-590 °C from bottom to top. At these temperatures, the brucite-out reaction is terminated (see Figure 2.7), and fluid expulsion from the slab is likely to occur by compaction of the overburden.

Results

Figure 6.3 shows the results of the reactive transport model with the chemical mapping as an initial condition. The part of the chemical mapping chosen consists mainly of mesh texture and two pyroxene/talc grains in the bottom center and the top left part of the domain.

The reactive porosity wave travels from the silica-poorer mesh texture part (bottom boundary) through the silica-richer pyroxene/talc grain. Within the grain, the reactive porosity wave causes the reaction of talc to antigorite and eventually olivine, analog to the results shown in Figure 6.2.

The fluid silica content (Figure 6.3) increases as the porosity waves migrats through silica-rich pyroxene grain. Within the grain, the low silica fluid causes the reaction of pyroxene to olivine. Within the silica-richer region, mainly orthopyroxene and minor amounts of talc are stable. The low silica fluid causes the formation of olivine by the reaction of orthopyroxene to olivine and, to a lesser extent, the reaction of talc to antigorite, and of antigorite to olivine. The stability of talc and orthopyroxene is strongly temperature dependent. Thus, at lower temperatures, the latter reaction would be more pronounced.

Figure 6.4 shows the lookup table values for 550 °C and 3 GPa, the maximum P-T conditions present in the model shown in Figure 6.3. The composition of each node is plotted in the ternary diagrams, thus showing the range of the chemical heterogeneities in the model.

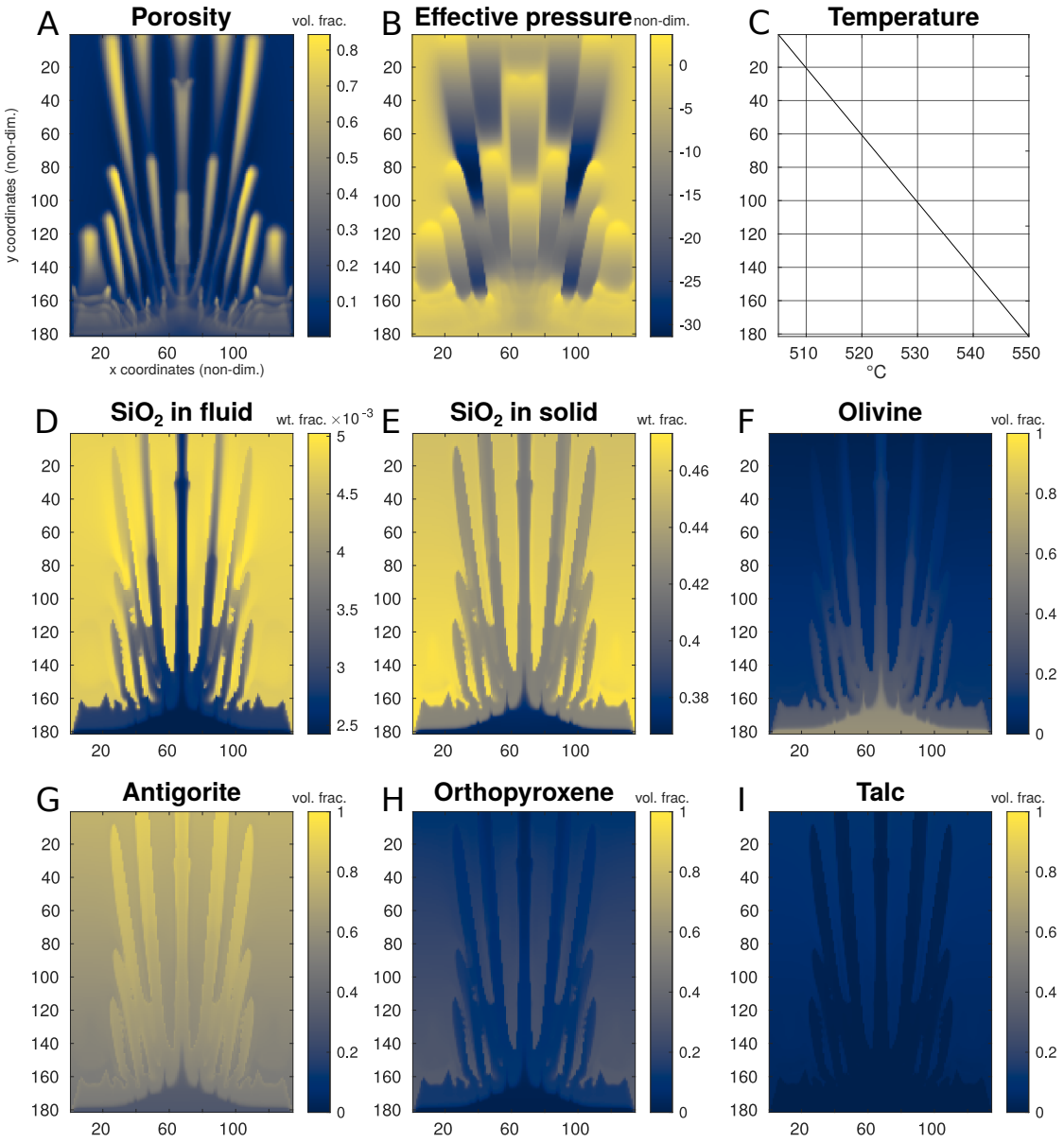

Figure 6.2: Results of the 2D model. Olivine-enriched fluid flow focusing structures form from the influx of a low-silica fluid in combination with compaction-decompaction-weakening. SiO_2 metasomatism causes the subsequent breakdown of talc to antigorite and of antigorite to olivine. y- and x-axis are depth and vertical length, respectively (both non-dimensional). A similar figure for a lower decompaction weakness factor ($R = 5$) is given in the Appendix (Figure C.1).

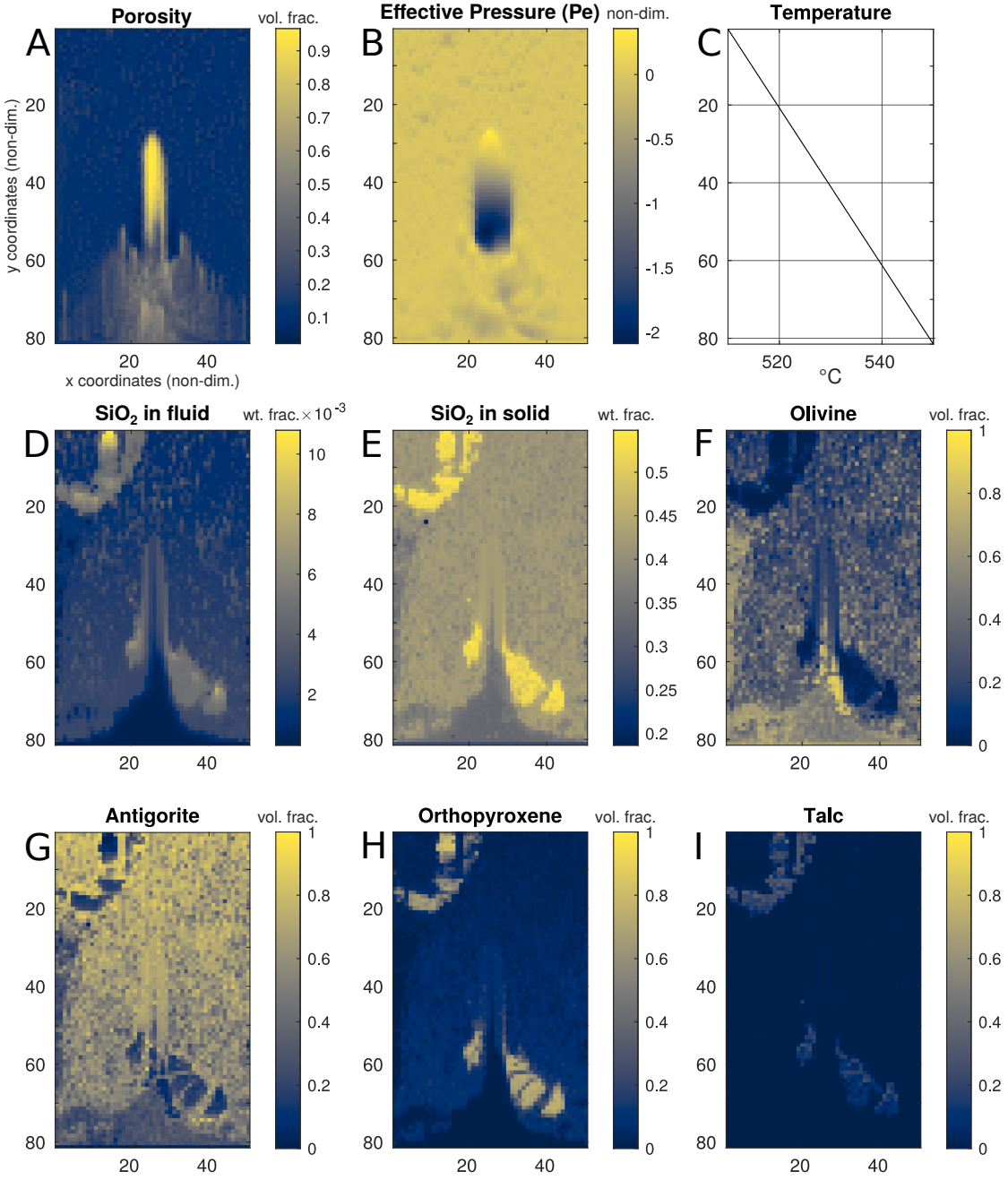

Figure 6.3: Results of the 2D model, using the chemical mapping from the multiscale dataset (index 1) as input.

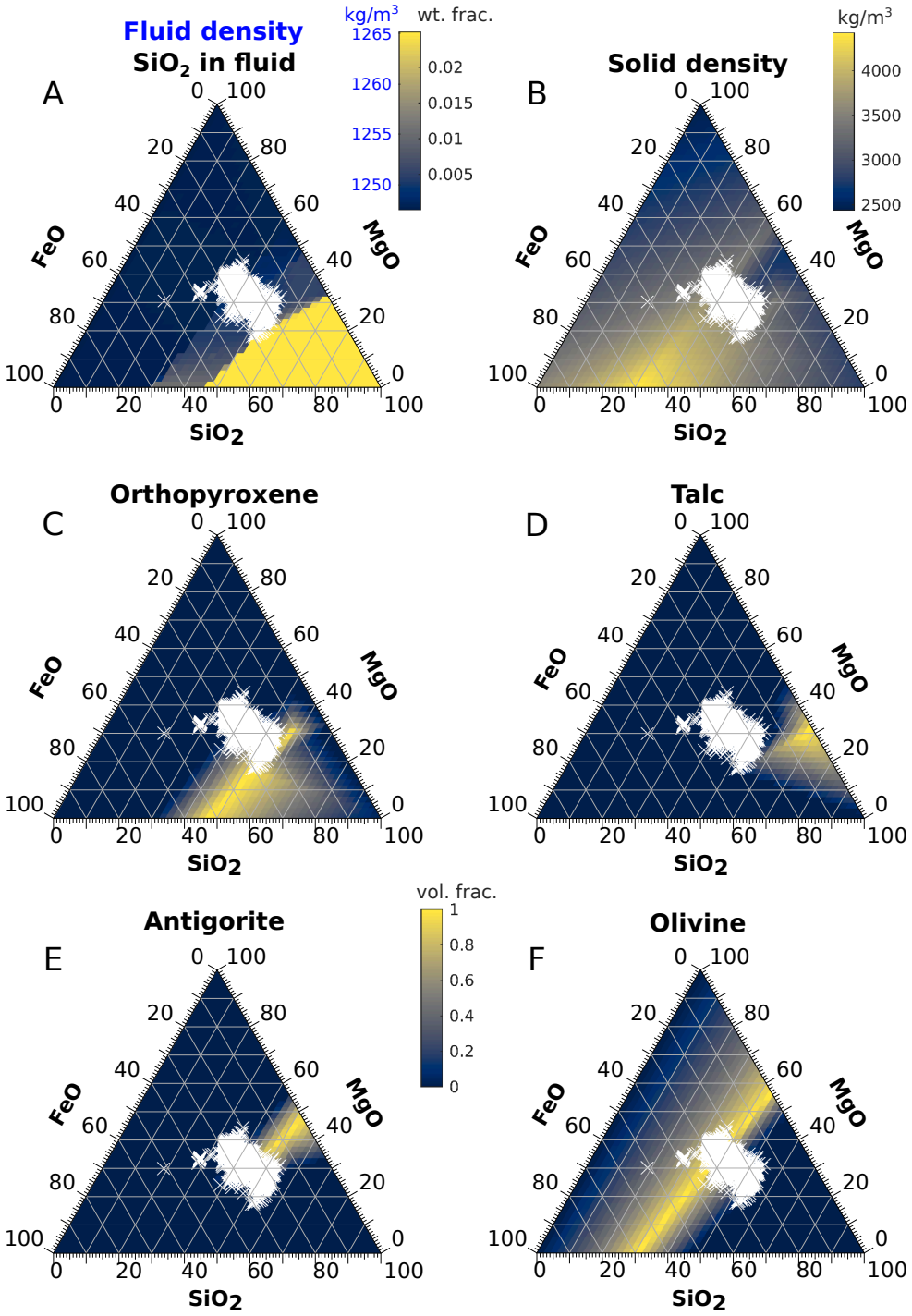

Figure 6.4: Lookup tables at 550 °C and 3 GPa, at the maximum P-T conditions of the 2D model. A: Fluid density and fluid composition have the same topology in composition space; see color bar for values of each property. C to F share the same color bar. Each white marker represents the bulk composition of a node in the 2D model.

6.4 Conclusions

The model successfully couples chemical mappings from a natural rock sample with a reactive porosity wave model. The combination of mechanical and chemical effects results in fluid flow focusing and the formation of an olivine-rich, vein-like porosity geometry. Increased computational efficiency allows running these models on local machines. Further improvement is possible by translating the codes to CUDA or Julia and the use of high-performance computing infrastructure (Omlin, 2016; Räss et al., 2022). Such a coupled THMC model can serve as a first step in combining natural rock data with state-of-the-art geodynamic models and account for the occurrence of chemical heterogeneities.

6.5 Further Outlook

Much progress has been made since the role of serpentinites in the deep volatile cycle has been recognized, and the increase in computational power in the last two decades paved the way for numerical models such as the ones presented in this dissertation. During the time of this dissertation, the Thermolab framework has evolved significantly and it will hopefully do so in the future. The work in the CRC 1114 established a common language between geoscientists and mathematicians, which can be the foundation for future collaboration. In this final section, I want to outline possible next steps to extend the work presented in this dissertation.

Regarding the multiscale dataset, further potential lies in more detailed analytical data on the meter scale. In the current thesis, this was done by using literature values, but systematic in-situ XRD measurements in the field would provide analytical data on field-scale chemical heterogeneities in the outcrop. This approach could even be upscaled to the kilometer scale by systematically sampling and analyzing larger parts of the Mirdita ophiolite. Such a strategy might reveal a large-scale chemical gradient that could affect dehydration and fluid flow channelization on the slab scale.

Extending the analytical dataset to larger scales could make a more complex chemical system necessary. In particular, including aluminum as an additional component in the thermodynamic calculations, mainly due to its effect on chlorite stability. Similarly, extending the number of aqueous species bears great potential. Especially the transport of dissolved iron could be important because of the strong dependence of olivine stability on the bulk iron content. In addition, investigating the role of single aqueous species is an additional way to extend the reactive transport models. Including multiple aqueous species also opens the way for exploring the role of redox potential for the evolution of the vein network. It

would also allow to differentiate between ferric iron and ferrous iron and therefore allow to include magnetite in the numerical models.

Finally, more advanced upscaling methods are of great interest especially because of the multiscale aspect of rock dehydration. The volumetric averaging approach used in Chapter 2 represents a first approach, yet leaves room for improvement. Here, future work could especially profit from the CRC 1114 framework and from the common language that has been established during the time of this dissertation. Applying advanced upscaling methods in combination with extended and more powerful numerical models is a promising way forward for studying rock dehydration on multiple scales and for possibly another joint publication in this field.

References

A. Bessat, S. Pilet, Y. Y. Podladchikov, and S. M. Schmalholz. Melt Migration and Chemical Differentiation by Reactive Porosity Waves. *Geochem. Geophys. Geosystems*, 23(2), 2022. ISSN 1525-2027, 1525-2027. doi:10.1029/2021GC009963.

J. A. D. Connolly and Y. Y. Podladchikov. Decompaction weakening and channeling instability in ductile porous media: Implications for asthenospheric melt segregation. *J. Geophys. Res.*, 112 (B10):B10205, 2007. ISSN 0148-0227. doi:10.1029/2005JB004213.

K. A. Evans and B. R. Frost. Deserpentinization in Subduction Zones as a Source of Oxidation in Arcs: A Reality Check. *J. Petrol.*, 62(3):egab016, 2021. ISSN 0022-3530, 1460-2415. doi:10.1093/petrology/egab016.

T. J. B. Holland and R. Powell. An internally consistent thermodynamic data set for phases of petrological interest: An internally consistent thermodynamic data set. *J. Metamorph. Geol.*, 16 (3):309–343, 2004. ISSN 02634929, 15251314. doi:10.1111/j.1525-1314.1998.00140.x.

J. R. Johnson, R. van Noort, J. Rahman, L. H. Wang, and V. Yarushina. Impact of injection rate for CO2 storage within sedimentary basins, a multidisciplinary analysis of focused fluid flow. 42, 2024.

L. Khakimova and Y. Podladchikov. Modeling Multicomponent Fluid Flow in Deforming and Reacting Porous Rock. 32(1), 2024.

S. Omlin. *Development of Massively Parallel near Peak Performance Solvers for Three-Dimensional Geodynamic Modelling*. PhD thesis, Université de Lausanne, Lausanne, 2016.

S. Omlin, L. Räss, and Y. Y. Podladchikov. Simulation of three-dimensional viscoelastic deformation coupled to porous fluid flow. *Tectonophysics*, (746):695–701, 2018.

L. Räss, V. M. Yarushina, N. S. Simon, and Y. Y. Podladchikov. Chimneys, channels, pathway flow or water conducting features - an explanation from numerical modelling and implications for CO2 storage. *Energy Procedia*, 63:3761–3774, 2014. ISSN 18766102. doi:10.1016/j.egypro.2014.11.405.

L. Räss, N. S. C. Simon, and Y. Y. Podladchikov. Spontaneous formation of fluid escape pipes

from subsurface reservoirs. *Sci Rep*, 8(1):11116, 2018. ISSN 2045-2322. doi:10.1038/s41598-018-29485-5.

L. Räss, I. Utkin, T. Duretz, S. Omlin, and Y. Y. Podladchikov. Assessing the robustness and scalability of the accelerated pseudo-transient method. *Geosci. Model Dev.*, 15(14):5757–5786, 2022. ISSN 1991-9603. doi:10.5194/gmd-15-5757-2022.

J. C. Vrijmoed and Y. Y. Podladchikov. Thermolab: A Thermodynamics Laboratory for Nonlinear Transport Processes in Open Systems. *Geochem. Geophys. Geosystems*, 23(4):e2021GC010303, 2022. ISSN 1525-2027. doi:10.1029/2021GC010303.

V. M. Yarushina and Y. Y. Podladchikov. (De)compaction of porous viscoelastoplastic media: Model formulation: (DE)COMPACTION OF POROUS MEDIA. *J. Geophys. Res. Solid Earth*, 120(6): 4146–4170, 2015. ISSN 21699313. doi:10.1002/2014JB011258.

V. M. Yarushina, Y. Y. Podladchikov, and J. A. D. Connolly. (De)compaction of porous viscoelastoplastic media: Solitary porosity waves. *J. Geophys. Res. Solid Earth*, 120(7):4843–4862, 2015. ISSN 2169-9356. doi:10.1002/2014JB011260.

V. M. Yarushina, L. H. Wang, D. Connolly, G. Kocsis, I. Fæstø, S. Polteau, and A. Lakhlifi. Focused fluid-flow structures potentially caused by solitary porosity waves. *Geology*, 50(2):179–183, 2022. ISSN 0091-7613, 1943-2682. doi:10.1130/G49295.1.

Appendix A

Supporting Material for Chapter 2

Table A.1 gives all quantitative microprobe measurements taken on sample ALB09-1 (harzburgite) and sample ALB06-1 (dunite). The text in the comment column is linked to the location of the measurements on the sample, as shown in the overviews in Figures A.1 to A.3.

Additional qualitative element distribution mappings on samples ALB09-1 and ALB06-1 are shown in Figures A.9 to A.12. All mappings were performed using the JXA-8800 microprobe at Freie Universität Berlin with 15 kV beam acceleration and 50 ms beam time. All mappings have a 2 µm step size, except mapping ALB06-1-A-mesh-detail (Figure A.9 top), which has a step size of 1 µm.

Figure A.13a shows the geological map of the outcrop including tectonic structures (shear zones, joints), sampling localities, and localities of structural data (Table A.2 and fig. A.4).

Figure A.14 shows the preparation of a piece of sample ALB09-2 for the multiscale element mappings (Figure 2.5).

XRD data for sample ALB06-1 is shown in Figure A.15. Measurement was performed on July 28th, 2022, using the powder diffractometer at Freie Universität Berlin, using the wavelengths $K_{\alpha 1} = 1.5406\,\text{Å}$, $K_{\alpha 2} = 1.5444\,\text{Å}$, $K_{\beta} = 1.3923\,\text{Å}$. The powder was filed from a piece of sample ALB06-1.

Full thin section microphotographs are given for the representative dunite sample ALB06 (Figures A.5 and A.6) and the representative harzburgite sample ALB09 (Figures A.7 and A.8).

The results for the dehydration onset and porosity evolution on the centimeter, decimeter, and meter scale are shown in Figures A17, A18, and A19, respectively.

Figure A.20 shows the effect of the choice of solution model on the onset of dehydration. **??** shows the effect of H_2O fractionation along the P-T path in comparison to Figure 2.8.

Table A.1: Mineral chemical data measured on samples ALB09-1 and ALB06-1.

	Weight Percent											Comment
No.	SiO_2	MgO	FeO	CaO	Cr_2O_3	Al_2O_3	TiO_2	Na_2O	K_2O	MnO	Total	
1	41.02	49.98	8.62	0.03	0.00	0.03	0.00	0.00	0.00	0.12	99.79	ALB_09_1_Ol-1
2	40.83	50.43	8.42	0.04	0.00	0.00	0.00	0.00	0.00	0.14	99.86	ALB_09_1_Ol-2
3	40.97	49.85	8.65	0.04	0.00	0.02	0.00	0.02	0.00	0.10	99.64	ALB_09_1_Ol-3
4	41.14	50.44	8.63	0.05	0.00	0.00	0.00	0.00	0.01	0.12	100.39	ALB_09_1_Ol-4
5	54.10	18.28	1.78	24.15	0.38	0.76	0.00	0.08	0.00	0.07	99.60	ALB_09_1_Cpx-1
6	54.29	17.91	1.60	24.62	0.37	0.75	0.00	0.05	0.00	0.03	99.63	ALB_09_1_Cpx-2
7	54.14	18.17	1.81	24.08	0.42	0.72	0.00	0.10	0.00	0.05	99.48	ALB_09_1_Cpx-3
8	57.06	35.20	5.74	0.41	0.26	0.76	0.00	0.02	0.00	0.15	99.62	ALB_09_1_Opx-1
9	57.39	34.66	5.60	0.57	0.34	0.82	0.03	0.00	0.00	0.14	99.53	ALB_09_1_Opx-2
10	56.23	34.68	5.62	0.71	0.33	0.86	0.03	0.00	0.01	0.11	98.58	ALB_09_1_Opx-3
11	40.58	12.47	10.18	10.14	0.02	14.85	4.75	2.20	2.06	0.12	97.38	Hbl
12	40.56	12.50	10.07	10.11	0.00	14.86	4.66	2.29	2.11	0.05	97.20	Hbl
13	40.27	12.61	10.20	10.16	0.01	14.76	4.65	2.30	2.05	0.12	97.14	Hbl
14	40.95	47.88	10.97	0.04	0.07	0.00	0.01	0.01	0.00	0.24	100.16	olivin
15	40.80	48.02	11.04	0.03	0.09	0.00	0.00	0.00	0.00	0.25	100.23	olivin
16	41.03	48.11	11.07	0.04	0.01	0.00	0.00	0.01	0.01	0.33	100.60	olivin
17	41.00	50.11	8.52	0.03	0.00	0.01	0.02	0.00	0.00	0.07	99.75	1 ALB09_1_A_Trav1_5um
18	41.24	50.52	8.60	0.02	0.00	0.01	0.00	0.00	0.00	0.13	100.52	2 ALB09_1_A_Trav1_5um
19	41.23	50.38	8.60	0.03	0.02	0.00	0.00	0.01	0.02	0.12	100.40	3 ALB09_1_A_Trav1_5um
20	39.05	43.23	5.43	0.08	0.01	0.00	0.00	0.00	0.01	0.06	87.87	4 ALB09_1_A_Trav1_5um
21	33.48	42.34	6.37	0.10	0.02	0.00	0.00	0.03	0.00	0.07	82.40	5 ALB09_1_A_Trav1_5um
22	34.08	41.09	6.55	0.07	0.02	0.00	0.00	0.05	0.00	0.09	81.95	6 ALB09_1_A_Trav1_5um
23	34.71	40.76	6.32	0.07	0.00	0.00	0.02	0.01	0.00	0.06	81.96	7 ALB09_1_A_Trav1_5um
24	36.25	39.72	6.20	0.06	0.00	0.00	0.03	0.06	0.00	0.02	82.35	8 ALB09_1_A_Trav1_5um
25	30.96	42.15	8.51	0.10	0.02	0.00	0.00	0.01	0.00	0.10	81.84	9 ALB09_1_A_Trav1_5um
26	27.42	41.80	11.41	0.13	0.03	0.00	0.00	0.04	0.00	0.24	81.07	10 ALB09_1_A_Trav1_5um
27	31.31	42.69	7.97	0.15	0.00	0.00	0.00	0.03	0.00	0.08	82.23	11 ALB09_1_A_Trav1_5um
28	35.20	40.36	6.08	0.05	0.03	0.00	0.02	0.05	0.01	0.04	81.85	12 ALB09_1_A_Trav1_5um
29	35.49	40.38	6.02	0.06	0.00	0.00	0.00	0.04	0.00	0.02	82.01	13 ALB09_1_A_Trav1_5um
30	34.76	42.15	5.92	0.08	0.00	0.00	0.02	0.03	0.00	0.09	83.04	14 ALB09_1_A_Trav1_5um
31	38.80	45.14	7.13	0.12	0.00	0.00	0.02	0.02	0.00	0.13	91.36	15 ALB09_1_A_Trav1_5um
32	40.60	50.38	8.80	0.03	0.00	0.01	0.03	0.05	0.01	0.16	100.06	16 ALB09_1_A_Trav1_5um
33	32.40	41.01	7.42	0.12	0.00	0.00	0.02	0.06	0.00	0.08	81.10	serp_test
34	39.86	38.47	4.09	0.18	0.07	0.00	0.01	0.03	0.02	0.05	82.77	serp_test_2um
35	33.15	40.48	6.29	0.11	0.00	0.00	0.00	0.03	0.00	0.07	80.13	serp_test_5um
36	41.02	50.49	8.67	0.03	0.00	0.01	0.00	0.04	0.01	0.11	100.37	1 ALB09_1_A_Trav2_5um
37	34.62	40.84	6.57	0.09	0.00	0.02	0.01	0.01	0.00	0.05	82.20	2 ALB09_1_A_Trav2_5um
38	34.62	40.27	7.02	0.08	0.00	0.00	0.00	0.05	0.01	0.07	82.11	3 ALB09_1_A_Trav2_5um
39	33.63	40.62	6.90	0.13	0.05	0.00	0.02	0.01	0.00	0.10	81.45	4 ALB09_1_A_Trav2_5um
40	30.93	40.24	10.85	0.09	0.00	0.02	0.01	0.05	0.00	0.10	82.28	5 ALB09_1_A_Trav2_5um
41	34.60	41.73	5.96	0.08	0.00	0.00	0.01	0.02	0.00	0.07	82.46	6 ALB09_1_A_Trav2_5um
42	39.47	39.63	4.37	0.09	0.02	0.02	0.01	0.04	0.00	0.06	83.71	7 ALB09_1_A_Trav2_5um
43	38.58	49.07	8.54	0.03	0.02	0.02	0.00	0.00	0.00	0.12	96.39	8 ALB09_1_A_Trav2_5um
44	40.63	51.07	8.93	0.03	0.02	0.00	0.01	0.00	0.01	0.13	100.82	9 ALB09_1_A_Trav2_5um
45	40.73	49.32	8.88	0.03	0.00	0.00	0.00	0.00	0.00	0.10	99.06	1 ALB09_1_A_Trav3_5um
46	40.47	48.24	8.75	0.03	0.04	0.01	0.00	0.00	0.00	0.12	97.65	2 ALB09_1_A_Trav3_5um

Table continues on the next page

Table A.1: Mineral chemical data measured on samples ALB09-1 and ALB06-1.

47	41.58	48.42	8.68	0.06	0.01	0.01	0.00	0.03	0.02	0.14	98.94	3 ALB09_1_A_Trav3_5um
48	34.48	39.92	6.98	0.09	0.06	0.00	0.00	0.02	0.00	0.07	81.60	4 ALB09_1_A_Trav3_5um
49	31.71	41.51	8.71	0.06	0.00	0.00	0.00	0.06	0.00	0.11	82.16	5 ALB09_1_A_Trav3_5um
50	34.06	39.27	7.49	0.11	0.02	0.01	0.00	0.03	0.00	0.08	81.07	6 ALB09_1_A_Trav3_5um
51	36.45	39.29	5.33	0.07	0.00	0.00	0.00	0.04	0.00	0.06	81.23	7 ALB09_1_A_Trav3_5um
52	37.84	47.86	7.50	0.06	0.02	0.00	0.00	0.01	0.00	0.12	93.41	8 ALB09_1_A_Trav3_5um
53	39.94	49.03	8.61	0.04	0.00	0.00	0.00	0.02	0.00	0.07	97.70	9 ALB09_1_A_Trav3_5um
54	40.27	49.23	8.68	0.02	0.04	0.00	0.00	0.00	0.00	0.13	98.37	10 ALB09_1_A_Trav3_5um
55	41.28	49.98	8.75	0.03	0.00	0.00	0.01	0.00	0.00	0.12	100.18	1 ALB09_1_A_Trav4_5um
56	40.73	50.06	8.90	0.03	0.00	0.01	0.00	0.01	0.00	0.15	99.88	2 ALB09_1_A_Trav4_5um
57	40.81	50.95	8.65	0.02	0.01	0.00	0.02	0.02	0.00	0.11	100.59	3 ALB09_1_A_Trav4_5um
58	40.92	48.12	8.73	0.01	0.03	0.00	0.03	0.02	0.00	0.08	97.94	4 ALB09_1_A_Trav4_5um
59	39.86	44.19	4.35	0.05	0.00	0.00	0.02	0.02	0.01	0.05	88.55	5 ALB09_1_A_Trav4_5um
60	30.54	43.08	8.09	0.12	0.00	0.01	0.00	0.02	0.00	0.08	81.95	6 ALB09_1_A_Trav4_5um
61	34.67	41.08	6.03	0.05	0.01	0.02	0.00	0.02	0.00	0.02	81.90	7 ALB09_1_A_Trav4_5um
62	34.73	39.89	7.42	0.17	0.00	0.00	0.00	0.04	0.02	0.13	82.40	8 ALB09_1_A_Trav4_5um
63	36.40	40.41	5.90	0.13	0.00	0.00	0.00	0.03	0.00	0.09	82.97	9 ALB09_1_A_Trav4_5um
64	33.86	40.97	6.67	0.10	0.01	0.01	0.00	0.06	0.00	0.06	81.73	10 ALB09_1_A_Trav4_5um
65	31.57	41.92	7.60	0.10	0.01	0.00	0.01	0.04	0.00	0.09	81.34	11 ALB09_1_A_Trav4_5um
66	34.71	40.77	6.21	0.08	0.00	0.02	0.00	0.06	0.01	0.09	81.96	12 ALB09_1_A_Trav4_5um
67	33.76	40.38	6.59	0.10	0.03	0.00	0.00	0.06	0.01	0.03	80.95	13 ALB09_1_A_Trav4_5um
68	38.13	38.28	5.62	0.09	0.03	0.00	0.01	0.05	0.01	0.08	82.29	14 ALB09_1_A_Trav4_5um
69	36.01	40.10	6.52	0.19	0.00	0.00	0.00	0.02	0.01	0.12	82.98	15 ALB09_1_A_Trav4_5um
70	37.42	39.42	5.80	0.12	0.01	0.00	0.00	0.00	0.00	0.08	82.84	16 ALB09_1_A_Trav4_5um
71	37.25	39.00	5.77	0.07	0.00	0.00	0.00	0.06	0.00	0.07	82.22	17 ALB09_1_A_Trav4_5um
72	36.96	38.23	6.37	0.11	0.00	0.00	0.00	0.02	0.01	0.05	81.74	18 ALB09_1_A_Trav4_5um
73	36.34	38.84	6.55	0.11	0.01	0.00	0.01	0.06	0.00	0.08	82.00	19 ALB09_1_A_Trav4_5um
74	33.32	39.42	8.50	0.13	0.01	0.00	0.00	0.03	0.00	0.15	81.57	20 ALB09_1_A_Trav4_5um
75	38.55	38.25	5.08	0.18	0.00	0.01	0.00	0.00	0.00	0.10	82.18	21 ALB09_1_A_Trav4_5um
76	30.53	40.33	9.26	0.12	0.00	0.00	0.00	0.05	0.00	0.14	80.43	22 ALB09_1_A_Trav4_5um
77	34.65	40.49	6.75	0.05	0.00	0.00	0.01	0.09	0.00	0.05	82.10	23 ALB09_1_A_Trav4_5um
78	33.57	39.41	8.03	0.13	0.01	0.00	0.04	0.02	0.01	0.13	81.33	24 ALB09_1_A_Trav4_5um
79	32.11	40.85	8.29	0.08	0.00	0.02	0.04	0.08	0.02	0.08	81.55	25 ALB09_1_A_Trav4_5um
80	32.99	41.38	6.97	0.07	0.00	0.00	0.00	0.08	0.00	0.07	81.55	26 ALB09_1_A_Trav4_5um
81	34.05	40.02	6.80	0.09	0.00	0.00	0.00	0.07	0.00	0.01	81.04	27 ALB09_1_A_Trav4_5um
82	33.77	41.10	6.48	0.08	0.00	0.00	0.00	0.07	0.00	0.05	81.55	28 ALB09_1_A_Trav4_5um
83	34.53	39.80	6.43	0.10	0.00	0.00	0.00	0.02	0.01	0.14	81.03	29 ALB09_1_A_Trav4_5um
84	32.83	41.23	6.98	0.12	0.00	0.00	0.00	0.04	0.00	0.07	81.27	30 ALB09_1_A_Trav4_5um
85	33.78	40.58	6.81	0.09	0.00	0.00	0.00	0.05	0.00	0.06	81.37	31 ALB09_1_A_Trav4_5um
86	36.89	39.04	5.02	0.10	0.02	0.00	0.01	0.04	0.00	0.06	81.17	32 ALB09_1_A_Trav4_5um
87	40.15	35.57	4.87	0.32	0.02	0.00	0.00	0.00	0.00	0.14	81.06	33 ALB09_1_A_Trav4_5um
88	41.65	49.31	8.64	0.02	0.00	0.01	0.02	0.01	0.00	0.12	99.77	34 ALB09_1_A_Trav4_5um
89	40.76	48.25	8.60	0.03	0.01	0.02	0.00	0.01	0.00	0.13	97.81	35 ALB09_1_A_Trav4_5um
90	40.56	49.92	8.71	0.04	0.05	0.01	0.01	0.00	0.00	0.12	99.41	36 ALB09_1_A_Trav4_5um
91	40.97	49.98	8.73	0.02	0.00	0.01	0.00	0.02	0.00	0.10	99.84	37 ALB09_1_A_Trav4_5um
92	41.03	49.91	8.61	0.02	0.00	0.00	0.00	0.00	0.00	0.13	99.70	38 ALB09_1_A_Trav4_5um
93	57.02	34.21	5.59	1.15	0.30	0.84	0.00	0.02	0.00	0.15	99.27	1 ALB09_1_B_Trav1_5um
94	56.96	34.09	5.45	1.41	0.33	0.83	0.01	0.02	0.01	0.12	99.24	2 ALB09_1_B_Trav1_5um

Table continues on the next page

Table A.1: Mineral chemical data measured on samples ALB09-1 and ALB06-1.

95	57.06	33.97	5.55	1.27	0.32	0.84	0.03	0.00	0.00	0.12	99.16	3 ALB09_1_B_Trav1_5um
96	57.42	34.20	5.81	0.68	0.35	0.81	0.00	0.02	0.00	0.14	99.43	4 ALB09_1_B_Trav1_5um
97	56.16	31.01	5.68	0.72	0.32	0.86	0.00	0.00	0.01	0.16	94.93	5 ALB09_1_B_Trav1_5um
98	39.60	33.07	5.90	0.50	0.27	0.46	0.02	0.04	0.03	0.21	80.10	6 ALB09_1_B_Trav1_5um
99	39.35	34.46	6.13	1.21	0.24	0.48	0.00	0.04	0.01	0.16	82.09	7 ALB09_1_B_Trav1_5um
100	39.43	34.32	6.32	0.44	0.19	0.45	0.00	0.03	0.01	0.21	81.40	8 ALB09_1_B_Trav1_5um
101	39.46	35.33	6.51	0.35	0.08	0.42	0.02	0.03	0.01	0.14	82.34	9 ALB09_1_B_Trav1_5um
102	39.04	35.07	6.17	0.47	0.19	0.45	0.00	0.02	0.02	0.18	81.60	10 ALB09_1_B_Trav1_5um
103	38.85	35.66	6.13	0.56	0.25	0.44	0.01	0.04	0.02	0.22	82.18	11 ALB09_1_B_Trav1_5um
104	37.57	35.74	5.60	0.44	0.20	0.43	0.00	0.00	0.03	0.19	80.20	12 ALB09_1_B_Trav1_5um
105	55.38	36.52	5.69	0.73	0.28	0.79	0.01	0.00	0.01	0.11	99.50	13 ALB09_1_B_Trav1_5um
106	56.50	34.33	5.64	1.20	0.26	0.80	0.00	0.00	0.00	0.14	98.86	14 ALB09_1_B_Trav1_5um
107	57.26	34.48	5.59	1.26	0.35	0.79	0.01	0.01	0.00	0.16	99.91	15 ALB09_1_B_Trav1_5um
108	54.34	17.84	1.81	24.29	0.40	0.75	0.03	0.05	0.00	0.04	99.55	1 ALB09_1_B_Trav2_5um
109	54.43	17.95	1.77	24.37	0.35	0.71	0.01	0.10	0.01	0.02	99.72	2 ALB09_1_B_Trav2_5um
110	54.55	17.81	1.78	24.28	0.36	0.76	0.00	0.03	0.01	0.07	99.64	3 ALB09_1_B_Trav2_5um
111	53.97	17.56	1.82	24.28	0.43	0.78	0.02	0.11	0.00	0.09	99.05	4 ALB09_1_B_Trav2_5um
112	55.36	17.25	1.86	24.29	0.40	0.79	0.04	0.08	0.00	0.06	100.13	5 ALB09_1_B_Trav2_5um
113	40.75	38.09	4.84	0.28	0.02	0.10	0.00	0.01	0.01	0.04	84.14	6 ALB09_1_B_Trav2_5um
114	40.73	36.73	6.40	0.17	0.00	0.01	0.00	0.02	0.00	0.04	84.10	7 ALB09_1_B_Trav2_5um
115	41.55	35.97	5.07	0.16	0.00	0.05	0.00	0.00	0.00	0.05	82.86	8 ALB09_1_B_Trav2_5um
116	38.58	36.75	6.57	0.15	0.05	0.03	0.00	0.02	0.00	0.06	82.21	9 ALB09_1_B_Trav2_5um
117	41.10	38.21	5.14	0.13	0.03	0.06	0.00	0.03	0.01	0.01	84.72	10 ALB09_1_B_Trav2_5um
118	38.72	36.39	3.04	0.89	0.05	0.10	0.02	0.03	0.00	0.00	79.24	11 ALB09_1_B_Trav2_5um
119	54.14	18.19	1.86	24.27	0.41	0.75	0.00	0.09	0.01	0.05	99.76	12 ALB09_1_B_Trav2_5um
120	53.89	18.21	1.81	24.28	0.34	0.74	0.00	0.10	0.00	0.07	99.42	13 ALB09_1_B_Trav2_5um
121	54.09	17.87	1.80	24.41	0.38	0.73	0.02	0.08	0.00	0.09	99.47	14 ALB09_1_B_Trav2_5um
122	54.31	17.82	1.75	24.44	0.40	0.73	0.01	0.06	0.00	0.09	99.61	15 ALB09_1_B_Trav2_5um
123	57.17	34.29	5.57	0.54	0.27	0.76	0.00	0.00	0.02	0.16	98.77	1 ALB09_1_B_Trav3_5um
124	57.14	34.34	5.69	0.40	0.24	0.72	0.01	0.00	0.00	0.13	98.67	2 ALB09_1_B_Trav3_5um
125	57.25	34.13	5.65	0.34	0.17	0.70	0.00	0.02	0.00	0.11	98.37	3 ALB09_1_B_Trav3_5um
126	56.85	34.83	5.76	0.34	0.24	0.70	0.03	0.00	0.01	0.12	98.87	4 ALB09_1_B_Trav3_5um
127	57.08	33.47	5.76	0.34	0.15	0.70	0.02	0.03	0.00	0.12	97.65	5 ALB09_1_B_Trav3_5um
128	41.00	36.36	6.31	0.45	0.13	0.44	0.00	0.02	0.04	0.23	84.96	6 ALB09_1_B_Trav3_5um
129	44.90	33.24	6.33	0.41	0.44	0.65	0.02	0.03	0.03	0.18	86.23	7 ALB09_1_B_Trav3_5um
130	39.39	35.15	6.04	0.41	0.30	0.47	0.04	0.01	0.02	0.10	81.92	8 ALB09_1_B_Trav3_5um
131	38.99	35.78	6.23	0.29	0.02	0.25	0.02	0.00	0.01	0.14	81.74	9 ALB09_1_B_Trav3_5um
132	39.68	35.11	5.88	0.38	0.03	0.28	0.03	0.01	0.02	0.09	81.51	10 ALB09_1_B_Trav3_5um
133	39.30	34.23	6.10	0.41	0.03	0.38	0.01	0.05	0.02	0.20	80.72	11 ALB09_1_B_Trav3_5um
134	39.02	34.64	6.21	0.47	0.01	0.40	0.00	0.03	0.05	0.20	81.03	12 ALB09_1_B_Trav3_5um
135	38.60	34.81	6.36	0.43	0.07	0.45	0.01	0.01	0.02	0.17	80.94	13 ALB09_1_B_Trav3_5um
136	37.91	35.11	7.43	0.31	0.04	0.38	0.00	0.04	0.00	0.16	81.39	14 ALB09_1_B_Trav3_5um
137	37.73	34.98	7.97	0.27	0.01	0.33	0.01	0.03	0.01	0.20	81.53	15 ALB09_1_B_Trav3_5um
138	38.16	35.76	7.00	0.36	0.01	0.31	0.00	0.01	0.02	0.13	81.74	16 ALB09_1_B_Trav3_5um
139	38.41	34.90	6.29	0.41	0.02	0.38	0.00	0.05	0.01	0.22	80.70	17 ALB09_1_B_Trav3_5um
140	36.99	36.49	6.60	0.28	0.03	0.17	0.00	0.04	0.01	0.07	80.66	18 ALB09_1_B_Trav3_5um
141	38.33	35.11	6.32	0.47	0.05	0.33	0.01	0.05	0.02	0.20	80.88	19 ALB09_1_B_Trav3_5um
142	37.83	35.09	6.15	0.47	0.05	0.29	0.01	0.02	0.03	0.24	80.17	20 ALB09_1_B_Trav3_5um

Table continues on the next page

Table A.1: Mineral chemical data measured on samples ALB09-1 and ALB06-1.

143	38.39	35.43	5.83	0.44	0.00	0.25	0.00	0.01	0.03	0.20	80.56	21 ALB09_1_B_Trav3_5um
144	38.44	35.81	6.14	0.43	0.00	0.31	0.01	0.03	0.02	0.14	81.32	22 ALB09_1_B_Trav3_5um
145	39.02	33.48	5.99	0.42	0.02	0.31	0.00	0.02	0.01	0.13	79.38	23 ALB09_1_B_Trav3_5um
146	36.24	46.19	7.65	0.20	0.01	0.09	0.00	0.02	0.00	0.14	90.56	24 ALB09_1_B_Trav3_5um
147	40.16	49.70	8.77	0.01	0.01	0.01	0.00	0.01	0.00	0.14	98.82	25 ALB09_1_B_Trav3_5um
148	40.17	49.28	8.94	0.03	0.03	0.00	0.00	0.02	0.00	0.15	98.62	26 ALB09_1_B_Trav3_5um
149	40.57	49.82	8.86	0.01	0.00	0.01	0.00	0.02	0.00	0.15	99.45	27 ALB09_1_B_Trav3_5um
150	57.31	34.81	5.69	0.53	0.28	0.79	0.03	0.01	0.01	0.12	99.57	1 ALB09_1_C_Trav1_5um
151	57.19	34.49	5.58	0.51	0.28	0.79	0.03	0.01	0.01	0.13	99.01	2 ALB09_1_C_Trav1_5um
152	57.32	34.21	5.48	0.56	0.40	0.87	0.01	0.01	0.00	0.12	98.98	3 ALB09_1_C_Trav1_5um
153	59.09	33.22	5.63	0.56	0.38	0.89	0.00	0.01	0.00	0.13	99.91	4 ALB09_1_C_Trav1_5um
154	39.22	32.92	6.73	0.55	0.38	0.53	0.00	0.05	0.01	0.23	80.61	5 ALB09_1_C_Trav1_5um
155	40.21	33.65	6.09	0.35	0.24	0.49	0.01	0.03	0.02	0.20	81.28	6 ALB09_1_C_Trav1_5um
156	39.10	33.26	6.39	0.46	0.29	0.51	0.02	0.03	0.01	0.13	80.20	7 ALB09_1_C_Trav1_5um
157	39.13	34.06	6.27	0.44	0.25	0.51	0.00	0.02	0.01	0.17	80.85	8 ALB09_1_C_Trav1_5um
158	38.98	34.27	5.80	0.43	0.29	0.56	0.00	0.06	0.02	0.20	80.61	9 ALB09_1_C_Trav1_5um
159	39.07	34.15	5.96	0.57	0.38	0.58	0.03	0.02	0.03	0.19	80.96	10 ALB09_1_C_Trav1_5um
160	39.02	33.62	5.99	0.50	0.30	0.61	0.00	0.00	0.03	0.18	80.27	11 ALB09_1_C_Trav1_5um
161	38.91	33.46	6.06	0.49	0.37	0.61	0.01	0.03	0.03	0.21	80.19	12 ALB09_1_C_Trav1_5um
162	39.14	35.05	6.29	0.31	0.09	0.54	0.00	0.03	0.02	0.14	81.60	13 ALB09_1_C_Trav1_5um
163	39.15	34.94	6.16	0.38	0.19	0.53	0.00	0.05	0.01	0.19	81.61	14 ALB09_1_C_Trav1_5um
164	39.24	35.11	6.42	0.36	0.07	0.56	0.00	0.05	0.02	0.15	81.96	15 ALB09_1_C_Trav1_5um
165	38.79	34.66	6.09	0.38	0.09	0.59	0.00	0.02	0.01	0.14	80.78	16 ALB09_1_C_Trav1_5um
166	38.71	34.39	6.12	0.37	0.20	0.57	0.02	0.05	0.01	0.19	80.63	17 ALB09_1_C_Trav1_5um
167	38.63	35.18	6.43	0.33	0.15	0.55	0.00	0.05	0.01	0.17	81.50	18 ALB09_1_C_Trav1_5um
168	38.62	34.54	6.00	0.42	0.25	0.60	0.03	0.03	0.01	0.17	80.66	19 ALB09_1_C_Trav1_5um
169	38.59	35.44	6.43	0.41	0.01	0.53	0.01	0.05	0.01	0.15	81.63	20 ALB09_1_C_Trav1_5um
170	38.51	34.34	5.95	0.47	0.38	0.59	0.03	0.02	0.02	0.16	80.46	21 ALB09_1_C_Trav1_5um
171	38.70	35.35	6.32	0.34	0.17	0.48	0.00	0.04	0.01	0.18	81.56	22 ALB09_1_C_Trav1_5um
172	38.33	34.93	6.32	0.33	0.20	0.49	0.01	0.04	0.01	0.21	80.87	23 ALB09_1_C_Trav1_5um
173	38.42	34.83	5.86	0.56	0.33	0.58	0.02	0.04	0.01	0.16	80.81	24 ALB09_1_C_Trav1_5um
174	38.57	34.97	5.95	0.43	0.34	0.58	0.00	0.04	0.00	0.18	81.06	25 ALB09_1_C_Trav1_5um
175	38.50	35.26	5.99	0.40	0.32	0.53	0.00	0.03	0.00	0.21	81.23	26 ALB09_1_C_Trav1_5um
176	38.52	35.51	6.05	0.40	0.36	0.55	0.01	0.05	0.02	0.13	81.59	27 ALB09_1_C_Trav1_5um
177	38.40	35.17	6.35	0.82	0.38	0.54	0.03	0.00	0.00	0.19	81.88	28 ALB09_1_C_Trav1_5um
178	38.84	34.97	5.82	0.43	0.32	0.45	0.01	0.04	0.01	0.15	81.05	29 ALB09_1_C_Trav1_5um
179	38.77	35.25	5.71	0.39	0.22	0.48	0.00	0.01	0.00	0.15	80.97	30 ALB09_1_C_Trav1_5um
180	38.50	36.07	5.83	0.42	0.25	0.46	0.00	0.01	0.03	0.21	81.77	31 ALB09_1_C_Trav1_5um
181	38.48	35.29	5.84	0.49	0.26	0.41	0.00	0.05	0.02	0.18	81.01	32 ALB09_1_C_Trav1_5um
182	36.21	34.13	6.66	0.57	0.46	0.52	0.01	0.05	0.00	0.21	78.83	33 ALB09_1_C_Trav1_5um
183	36.88	35.21	6.98	0.49	0.54	0.53	0.02	0.02	0.02	0.19	80.88	34 ALB09_1_C_Trav1_5um
184	52.97	38.01	5.68	0.81	0.40	0.80	0.01	0.00	0.01	0.11	98.81	35 ALB09_1_C_Trav1_5um
185	54.62	36.81	5.63	0.79	0.45	0.90	0.02	0.00	0.01	0.13	99.35	36 ALB09_1_C_Trav1_5um
186	55.82	35.31	5.73	0.68	0.42	0.92	0.01	0.00	0.00	0.15	99.03	37 ALB09_1_C_Trav1_5um
187	56.31	34.96	5.57	0.60	0.37	0.92	0.00	0.00	0.01	0.16	98.89	38 ALB09_1_C_Trav1_5um
188	56.62	34.72	5.69	0.63	0.36	0.91	0.00	0.00	0.00	0.12	99.06	39 ALB09_1_C_Trav1_5um
189	56.58	34.73	5.77	0.60	0.40	0.96	0.00	0.00	0.02	0.15	99.21	40 ALB09_1_C_Trav1_5um
190	56.57	34.30	5.81	0.67	0.41	0.93	0.00	0.00	0.00	0.13	98.82	41 ALB09_1_C_Trav1_5um

Table continues on the next page

Table A.1: Mineral chemical data measured on samples ALB09-1 and ALB06-1.

191	56.74	34.27	5.66	0.71	0.39	0.85	0.00	0.00	0.00	0.11	98.72	1 ALB09_1_C_Trav2_5um
192	57.09	34.38	5.69	0.85	0.34	0.90	0.02	0.00	0.00	0.10	99.36	2 ALB09_1_C_Trav2_5um
193	57.08	34.19	5.73	0.76	0.40	0.86	0.03	0.01	0.00	0.11	99.18	3 ALB09_1_C_Trav2_5um
194	57.52	33.95	5.62	0.76	0.35	0.87	0.00	0.00	0.00	0.11	99.19	4 ALB09_1_C_Trav2_5um
195	48.82	36.66	5.73	1.90	0.37	0.66	0.01	0.04	0.01	0.15	94.35	5 ALB09_1_C_Trav2_5um
196	52.76	34.99	5.71	0.58	0.37	0.82	0.03	0.08	0.04	0.12	95.50	6 ALB09_1_C_Trav2_5um
197	36.93	32.74	6.70	0.40	0.47	0.46	0.00	0.03	0.01	0.18	77.92	7 ALB09_1_C_Trav2_5um
198	51.41	32.29	5.58	3.66	0.44	0.74	0.01	0.04	0.02	0.10	94.27	8 ALB09_1_C_Trav2_5um
199	39.41	33.27	6.29	1.30	0.58	0.47	0.02	0.02	0.02	0.17	81.54	9 ALB09_1_C_Trav2_5um
200	39.23	32.28	6.44	0.48	0.51	0.48	0.02	0.02	0.01	0.20	79.66	10 ALB09_1_C_Trav2_5um
201	39.31	32.28	6.44	0.40	0.48	0.45	0.00	0.04	0.02	0.16	79.58	11 ALB09_1_C_Trav2_5um
202	39.34	33.72	6.10	0.38	0.38	0.42	0.01	0.01	0.01	0.18	80.56	12 ALB09_1_C_Trav2_5um
203	39.81	33.99	5.87	1.33	0.28	0.45	0.00	0.00	0.01	0.12	81.87	13 ALB09_1_C_Trav2_5um
204	39.35	33.69	7.24	0.35	0.15	0.38	0.01	0.07	0.01	0.18	81.41	14 ALB09_1_C_Trav2_5um
205	39.58	34.01	7.24	1.22	0.09	0.39	0.00	0.06	0.02	0.15	82.74	15 ALB09_1_C_Trav2_5um
206	38.97	33.65	6.13	0.47	0.39	0.47	0.02	0.01	0.01	0.18	80.31	16 ALB09_1_C_Trav2_5um
207	38.91	35.12	7.44	0.24	0.00	0.40	0.01	0.05	0.00	0.17	82.34	17 ALB09_1_C_Trav2_5um
208	38.80	34.43	7.49	0.23	0.08	0.39	0.00	0.02	0.02	0.22	81.67	18 ALB09_1_C_Trav2_5um
209	38.77	34.76	7.22	0.29	0.18	0.42	0.02	0.01	0.01	0.22	81.89	19 ALB09_1_C_Trav2_5um
210	38.61	34.71	6.33	0.38	0.31	0.50	0.00	0.04	0.02	0.16	81.07	20 ALB09_1_C_Trav2_5um
211	38.87	34.56	6.47	0.31	0.00	0.48	0.00	0.03	0.00	0.17	80.88	21 ALB09_1_C_Trav2_5um
212	38.69	34.20	6.56	0.34	0.05	0.53	0.00	0.03	0.02	0.23	80.65	22 ALB09_1_C_Trav2_5um
213	38.76	35.17	7.32	0.25	0.00	0.40	0.00	0.02	0.01	0.17	82.10	23 ALB09_1_C_Trav2_5um
214	38.65	34.02	6.96	0.28	0.00	0.48	0.00	0.01	0.00	0.16	80.57	24 ALB09_1_C_Trav2_5um
215	38.96	34.22	6.13	0.38	0.03	0.55	0.00	0.07	0.02	0.15	80.53	25 ALB09_1_C_Trav2_5um
216	38.76	34.33	6.14	0.51	0.03	0.52	0.00	0.04	0.02	0.20	80.54	26 ALB09_1_C_Trav2_5um
217	38.76	34.58	6.89	0.33	0.00	0.47	0.02	0.02	0.02	0.19	81.27	27 ALB09_1_C_Trav2_5um
218	38.42	35.29	6.69	0.30	0.00	0.48	0.03	0.02	0.00	0.17	81.39	28 ALB09_1_C_Trav2_5um
219	38.62	34.74	6.64	0.30	0.00	0.48	0.01	0.04	0.00	0.17	81.00	29 ALB09_1_C_Trav2_5um
220	38.80	34.44	6.44	0.35	0.00	0.50	0.02	0.02	0.02	0.18	80.77	30 ALB09_1_C_Trav2_5um
221	38.59	34.69	6.18	0.38	0.01	0.53	0.01	0.01	0.02	0.16	80.57	31 ALB09_1_C_Trav2_5um
222	38.50	35.01	6.95	0.29	0.01	0.50	0.00	0.04	0.01	0.17	81.47	32 ALB09_1_C_Trav2_5um
223	38.48	35.24	6.75	0.33	0.01	0.47	0.00	0.02	0.01	0.19	81.50	33 ALB09_1_C_Trav2_5um
224	38.47	34.03	6.12	0.48	0.43	0.59	0.02	0.03	0.03	0.23	80.42	34 ALB09_1_C_Trav2_5um
225	38.81	34.29	6.12	1.48	0.53	0.51	0.00	0.04	0.04	0.22	82.02	35 ALB09_1_C_Trav2_5um
226	39.13	34.20	6.20	0.83	0.49	0.50	0.01	0.04	0.02	0.23	81.63	36 ALB09_1_C_Trav2_5um
227	38.06	34.09	6.31	0.48	0.48	0.51	0.00	0.04	0.02	0.18	80.17	37 ALB09_1_C_Trav2_5um
228	38.60	34.50	6.51	0.45	0.46	0.47	0.00	0.02	0.00	0.15	81.17	38 ALB09_1_C_Trav2_5um
229	38.50	34.48	6.16	0.47	0.48	0.50	0.02	0.01	0.03	0.18	80.83	39 ALB09_1_C_Trav2_5um
230	38.57	34.31	6.29	0.46	0.49	0.60	0.00	0.03	0.04	0.19	80.99	40 ALB09_1_C_Trav2_5um
231	38.41	35.20	6.23	0.50	0.47	0.57	0.02	0.04	0.04	0.19	81.65	41 ALB09_1_C_Trav2_5um
232	38.37	34.92	6.19	0.49	0.49	0.59	0.02	0.04	0.04	0.16	81.30	42 ALB09_1_C_Trav2_5um
233	38.26	36.09	6.31	0.48	0.49	0.60	0.02	0.04	0.04	0.17	82.50	43 ALB09_1_C_Trav2_5um
234	55.36	36.38	5.65	0.69	0.42	0.84	0.02	0.00	0.00	0.17	99.52	44 ALB09_1_C_Trav2_5um
235	56.14	35.08	5.59	0.72	0.35	0.90	0.02	0.02	0.00	0.13	98.95	45 ALB09_1_C_Trav2_5um
236	55.92	33.84	5.37	3.05	0.58	0.92	0.00	0.04	0.00	0.13	99.85	46 ALB09_1_C_Trav2_5um
237	56.37	34.52	5.60	1.10	0.35	0.84	0.01	0.01	0.02	0.13	98.94	47 ALB09_1_C_Trav2_5um
238	56.50	34.66	5.60	0.61	0.39	0.88	0.02	0.00	0.01	0.15	98.81	48 ALB09_1_C_Trav2_5um

Table continues on the next page

Table A.1: Mineral chemical data measured on samples ALB09-1 and ALB06-1.

239	56.78	34.85	5.71	0.58	0.40	0.84	0.01	0.00	0.00	0.12	99.28	49 ALB09_1_C_Trav2_5um
240	57.03	34.21	5.55	0.96	0.48	1.00	0.00	0.00	0.00	0.14	99.35	1 ALB09_1_C_Trav3_5um
241	56.64	31.16	4.90	6.12	0.52	1.07	0.01	0.03	0.00	0.09	100.53	2 ALB09_1_C_Trav3_5um
242	56.98	33.83	5.44	1.69	0.43	1.03	0.01	0.00	0.00	0.13	99.55	3 ALB09_1_C_Trav3_5um
243	57.20	34.23	5.75	0.60	0.44	0.96	0.04	0.00	0.00	0.13	99.35	4 ALB09_1_C_Trav3_5um
244	57.21	34.31	5.63	0.61	0.47	0.99	0.00	0.00	0.00	0.12	99.33	5 ALB09_1_C_Trav3_5um
245	49.85	30.41	6.12	1.73	0.39	1.01	0.02	0.01	0.00	0.15	89.69	6 ALB09_1_C_Trav3_5um
246	38.20	33.99	6.21	0.79	0.41	0.80	0.01	0.04	0.02	0.24	80.71	7 ALB09_1_C_Trav3_5um
247	39.93	34.77	5.99	1.46	0.32	0.82	0.02	0.01	0.03	0.19	83.52	8 ALB09_1_C_Trav3_5um
248	39.45	33.91	5.81	1.53	0.23	0.74	0.00	0.05	0.01	0.21	81.93	9 ALB09_1_C_Trav3_5um
249	41.93	33.53	5.33	4.75	0.43	0.74	0.00	0.04	0.02	0.16	86.94	10 ALB09_1_C_Trav3_5um
250	56.36	35.09	5.62	0.71	0.45	0.93	0.01	0.00	0.01	0.11	99.29	11 ALB09_1_C_Trav3_5um
251	56.12	35.46	5.82	0.74	0.45	0.87	0.03	0.02	0.01	0.16	99.67	12 ALB09_1_C_Trav3_5um
252	57.01	34.57	5.59	0.99	0.45	0.91	0.02	0.00	0.00	0.16	99.70	13 ALB09_1_C_Trav3_5um
253	56.30	34.31	5.46	1.33	0.48	0.90	0.00	0.00	0.00	0.15	98.92	14 ALB09_1_C_Trav3_5um
254	56.67	33.42	5.28	2.73	0.45	1.00	0.04	0.02	0.02	0.12	99.75	15 ALB09_1_C_Trav3_5um
255	56.87	34.89	5.64	0.60	0.46	0.95	0.00	0.02	0.01	0.13	99.57	16 ALB09_1_C_Trav3_5um
256	56.81	34.73	5.65	0.59	0.54	0.98	0.01	0.01	0.00	0.10	99.42	17 ALB09_1_C_Trav3_5um
257	57.00	33.32	5.43	2.92	0.43	0.97	0.00	0.00	0.00	0.14	100.21	18 ALB09_1_C_Trav3_5um
258	56.04	34.00	5.63	0.81	0.37	0.96	0.04	0.00	0.01	0.14	97.99	1 ALB09_1_C_Trav4_5um
259	56.06	33.34	5.47	1.69	0.44	0.91	0.02	0.00	0.01	0.13	98.06	2 ALB09_1_C_Trav4_5um
260	57.11	31.81	5.65	0.81	0.45	1.01	0.01	0.00	0.01	0.12	96.98	3 ALB09_1_C_Trav4_5um
261	38.51	34.85	5.77	0.29	0.32	0.76	0.03	0.04	0.01	0.20	80.76	4 ALB09_1_C_Trav4_5um
262	38.26	27.62	5.35	3.89	0.48	0.78	0.03	0.07	0.02	0.14	76.63	5 ALB09_1_C_Trav4_5um
263	42.44	34.24	5.59	3.63	0.48	0.90	0.00	0.04	0.02	0.17	87.51	6 ALB09_1_C_Trav4_5um
264	41.50	32.46	4.98	5.54	0.54	0.83	0.00	0.08	0.00	0.17	86.10	7 ALB09_1_C_Trav4_5um
265	41.18	31.57	5.20	5.10	0.61	0.81	0.00	0.06	0.00	0.20	84.71	8 ALB09_1_C_Trav4_5um
266	46.18	29.40	4.17	9.70	0.49	0.83	0.00	0.06	0.01	0.12	90.96	9 ALB09_1_C_Trav4_5um
267	54.02	26.18	3.62	11.82	0.52	0.98	0.03	0.06	0.01	0.10	97.34	10 ALB09_1_C_Trav4_5um
268	55.98	30.76	4.73	6.26	0.51	0.97	0.01	0.01	0.00	0.13	99.36	11 ALB09_1_C_Trav4_5um
269	56.31	33.17	5.03	3.12	0.45	0.97	0.02	0.01	0.00	0.12	99.20	12 ALB09_1_C_Trav4_5um
270	56.53	33.64	5.35	2.65	0.44	1.01	0.00	0.02	0.01	0.16	99.82	13 ALB09_1_C_Trav4_5um
271	56.31	32.35	5.12	3.96	0.53	0.96	0.00	0.01	0.00	0.11	99.36	14 ALB09_1_C_Trav4_5um
272	37.97	35.56	6.11	0.64	0.42	0.64	0.02	0.02	0.01	0.14	81.53	ALB09_1_C_Pt1
273	38.41	35.88	6.03	0.75	0.46	0.56	0.00	0.04	0.01	0.09	82.21	ALB09_1_C_Pt2
274	37.53	36.89	6.14	0.17	0.33	0.43	0.01	0.01	0.01	0.09	81.61	ALB09_1_C_Pt2
275	0.04	10.23	18.89	0.01	54.16	14.35	0.05	0.00	0.01	0.28	98.02	ALB09_1_C_Sp1
276	0.04	10.35	18.99	0.01	53.33	14.40	0.01	0.04	0.00	0.27	97.43	ALB09_1_C_Sp2
277	0.05	10.33	18.81	0.01	53.72	14.72	0.03	0.04	0.00	0.27	97.98	ALB09_1_C_Sp3
278	54.26	17.79	1.77	24.46	0.49	0.77	0.00	0.08	0.01	0.04	99.67	ALB09_1_C_Cpx1
279	53.68	17.68	1.65	24.58	0.49	0.76	0.03	0.09	0.00	0.10	99.05	ALB09_1_C_Cpx2
280	53.72	17.83	1.68	24.40	0.49	0.84	0.03	0.12	0.00	0.08	99.18	ALB09_1_C_Cpx3
281	40.20	49.68	8.94	0.06	0.00	0.00	0.03	0.04	0.00	0.12	99.08	1 ALB06_1_A_Trav1_5um
282	40.46	48.46	8.93	0.05	0.00	0.00	0.00	0.00	0.00	0.15	98.06	2 ALB06_1_A_Trav1_5um
283	39.79	46.33	8.85	0.06	0.00	0.04	0.02	0.00	0.01	0.17	95.28	3 ALB06_1_A_Trav1_5um
284	34.70	41.85	5.21	0.09	0.01	0.00	0.00	0.04	0.01	0.06	81.96	4 ALB06_1_A_Trav1_5um
285	31.52	41.80	7.82	0.07	0.01	0.01	0.01	0.03	0.00	0.09	81.36	5 ALB06_1_A_Trav1_5um
286	32.73	40.70	6.94	0.08	0.02	0.00	0.02	0.02	0.00	0.10	80.61	6 ALB06_1_A_Trav1_5um

Table continues on the next page

Table A.1: Mineral chemical data measured on samples ALB09-1 and ALB06-1.

287	36.99	39.42	5.17	0.06	0.00	0.00	0.02	0.03	0.00	0.06	81.76	7 ALB06_1_A_Trav1_5um
288	33.58	40.24	7.09	0.10	0.00	0.00	0.00	0.02	0.00	0.12	81.14	8 ALB06_1_A_Trav1_5um
289	36.81	39.51	4.75	0.08	0.00	0.00	0.01	0.03	0.00	0.07	81.25	9 ALB06_1_A_Trav1_5um
290	38.72	50.88	8.81	0.05	0.00	0.01	0.02	0.00	0.01	0.11	98.60	10 ALB06_1_A_Trav1_5um
291	40.41	49.79	8.81	0.06	0.00	0.01	0.03	0.00	0.00	0.08	99.19	11 ALB06_1_A_Trav1_5um
292	40.21	49.76	8.87	0.05	0.00	0.00	0.00	0.00	0.01	0.13	99.02	1 ALB06_1_A_Trav2_5um
293	40.20	49.67	8.76	0.05	0.01	0.00	0.00	0.03	0.01	0.12	98.85	2 ALB06_1_A_Trav2_5um
294	39.67	41.65	5.35	0.14	0.00	0.00	0.00	0.01	0.01	0.09	86.93	3 ALB06_1_A_Trav2_5um
295	36.78	38.70	4.92	0.04	0.00	0.00	0.00	0.03	0.00	0.04	80.51	4 ALB06_1_A_Trav2_5um
296	30.28	42.48	8.11	0.10	0.00	0.01	0.00	0.03	0.00	0.09	81.09	5 ALB06_1_A_Trav2_5um
297	33.44	40.46	6.68	0.15	0.04	0.00	0.00	0.02	0.00	0.15	80.94	6 ALB06_1_A_Trav2_5um
298	34.90	40.27	5.16	0.10	0.03	0.01	0.01	0.02	0.01	0.03	80.53	7 ALB06_1_A_Trav2_5um
299	33.24	41.36	6.24	0.08	0.00	0.00	0.02	0.05	0.01	0.09	81.08	8 ALB06_1_A_Trav2_5um
300	34.74	40.20	5.90	0.10	0.00	0.00	0.00	0.02	0.00	0.05	80.99	9 ALB06_1_A_Trav2_5um
301	36.67	43.38	5.92	0.11	0.00	0.00	0.00	0.00	0.00	0.09	86.18	10 ALB06_1_A_Trav2_5um
302	41.04	48.01	8.74	0.05	0.00	0.00	0.00	0.01	0.00	0.17	98.02	11 ALB06_1_A_Trav2_5um
303	40.55	49.88	8.84	0.05	0.01	0.00	0.01	0.00	0.01	0.15	99.50	12 ALB06_1_A_Trav2_5um
304	40.74	49.78	8.87	0.04	0.00	0.00	0.00	0.03	0.00	0.11	99.57	1 ALB06_1_A_Trav3_5um
305	41.04	49.20	9.01	0.03	0.00	0.00	0.00	0.00	0.00	0.09	99.38	2 ALB06_1_A_Trav3_5um
306	41.22	45.06	7.07	0.05	0.00	0.00	0.00	0.00	0.00	0.12	93.51	3 ALB06_1_A_Trav3_5um
307	37.21	39.63	5.02	0.06	0.00	0.01	0.00	0.03	0.01	0.03	81.99	4 ALB06_1_A_Trav3_5um
308	31.30	41.68	8.34	0.09	0.04	0.00	0.00	0.04	0.00	0.14	81.64	5 ALB06_1_A_Trav3_5um
309	34.56	39.89	7.85	0.07	0.00	0.00	0.00	0.07	0.00	0.11	82.55	6 ALB06_1_A_Trav3_5um
310	33.95	38.53	7.84	0.04	0.02	0.01	0.01	0.05	0.01	0.08	80.52	7 ALB06_1_A_Trav3_5um
311	35.13	39.49	7.21	0.05	0.00	0.00	0.00	0.04	0.00	0.08	82.01	8 ALB06_1_A_Trav3_5um
312	34.36	37.85	5.70	0.11	0.00	0.00	0.01	0.08	0.00	0.04	78.15	9 ALB06_1_A_Trav3_5um
313	38.16	39.14	4.72	0.10	0.00	0.01	0.02	0.04	0.00	0.04	82.22	10 ALB06_1_A_Trav3_5um
314	31.88	40.74	8.17	0.06	0.00	0.00	0.00	0.04	0.01	0.09	80.99	11 ALB06_1_A_Trav3_5um
315	29.98	41.74	9.66	0.10	0.02	0.00	0.00	0.07	0.00	0.13	81.70	12 ALB06_1_A_Trav3_5um
316	33.19	41.05	6.83	0.07	0.00	0.00	0.00	0.02	0.00	0.05	81.21	13 ALB06_1_A_Trav3_5um
317	34.28	39.88	6.66	0.24	0.03	0.00	0.00	0.03	0.00	0.10	81.21	14 ALB06_1_A_Trav3_5um
318	39.95	39.89	4.53	0.15	0.00	0.00	0.00	0.02	0.00	0.09	84.64	15 ALB06_1_A_Trav3_5um
319	40.93	49.86	8.60	0.03	0.00	0.00	0.00	0.00	0.00	0.16	99.58	16 ALB06_1_A_Trav3_5um
320	40.83	49.43	8.68	0.05	0.00	0.02	0.00	0.03	0.00	0.15	99.19	1 ALB06_1_A_Trav4_5um
321	41.31	49.22	8.79	0.05	0.01	0.00	0.00	0.03	0.00	0.12	99.54	2 ALB06_1_A_Trav4_5um
322	41.02	49.62	8.83	0.06	0.02	0.01	0.00	0.00	0.00	0.13	99.68	3 ALB06_1_A_Trav4_5um
323	40.88	49.32	8.85	0.07	0.01	0.00	0.00	0.00	0.01	0.12	99.26	4 ALB06_1_A_Trav4_5um
324	38.19	38.43	4.87	0.09	0.01	0.00	0.00	0.00	0.00	0.07	81.65	5 ALB06_1_A_Trav4_5um
325	34.36	40.27	6.45	0.09	0.02	0.00	0.00	0.06	0.00	0.10	81.35	6 ALB06_1_A_Trav4_5um
326	32.50	40.05	7.79	0.07	0.00	0.00	0.00	0.04	0.00	0.12	80.57	7 ALB06_1_A_Trav4_5um
327	33.34	39.83	7.68	0.05	0.01	0.01	0.01	0.07	0.00	0.08	81.08	8 ALB06_1_A_Trav4_5um
328	32.68	39.88	8.08	0.07	0.00	0.00	0.01	0.06	0.00	0.06	80.84	9 ALB06_1_A_Trav4_5um
329	30.26	41.52	8.62	0.12	0.00	0.00	0.00	0.02	0.00	0.09	80.62	10 ALB06_1_A_Trav4_5um
330	34.13	39.90	6.92	0.06	0.00	0.00	0.04	0.03	0.00	0.07	81.15	11 ALB06_1_A_Trav4_5um
331	37.53	39.00	4.88	0.06	0.02	0.02	0.01	0.02	0.00	0.06	81.60	12 ALB06_1_A_Trav4_5um
332	33.53	41.39	5.79	0.07	0.00	0.01	0.00	0.07	0.00	0.09	80.94	13 ALB06_1_A_Trav4_5um
333	32.77	41.17	6.94	0.08	0.00	0.02	0.02	0.05	0.00	0.02	81.06	14 ALB06_1_A_Trav4_5um
334	32.60	40.57	7.38	0.07	0.01	0.00	0.02	0.06	0.01	0.06	80.78	15 ALB06_1_A_Trav4_5um

Table continues on the next page

Table A.1: Mineral chemical data measured on samples ALB09-1 and ALB06-1.

335	31.71	40.60	7.54	0.08	0.00	0.00	0.02	0.03	0.00	0.09	80.07	16 ALB06_1_A_Trav4_5um
336	33.83	40.58	6.58	0.08	0.02	0.01	0.00	0.06	0.00	0.07	81.22	17 ALB06_1_A_Trav4_5um
337	34.33	40.45	5.84	0.08	0.00	0.00	0.00	0.05	0.00	0.05	80.79	18 ALB06_1_A_Trav4_5um
338	32.85	40.90	6.82	0.08	0.03	0.00	0.00	0.05	0.00	0.08	80.81	19 ALB06_1_A_Trav4_5um
339	33.96	41.14	5.61	0.11	0.00	0.01	0.02	0.01	0.00	0.08	80.94	20 ALB06_1_A_Trav4_5um
340	32.45	41.66	6.07	0.12	0.00	0.00	0.00	0.06	0.00	0.07	80.43	21 ALB06_1_A_Trav4_5um
341	38.83	52.24	8.62	0.05	0.00	0.00	0.00	0.00	0.00	0.13	99.87	22 ALB06_1_A_Trav4_5um
342	39.96	48.76	8.85	0.34	0.00	0.00	0.00	0.01	0.00	0.17	98.08	23 ALB06_1_A_Trav4_5um
343	38.69	51.29	8.74	0.08	0.00	0.01	0.04	0.03	0.00	0.14	99.01	24 ALB06_1_A_Trav4_5um
344	40.65	49.95	8.90	0.07	0.02	0.01	0.01	0.00	0.00	0.16	99.78	25 ALB06_1_A_Trav4_5um
345	40.68	49.95	8.85	0.05	0.01	0.00	0.00	0.02	0.00	0.12	99.66	1 ALB06_1_A_Trav5_5um
346	41.49	49.11	8.65	0.06	0.00	0.00	0.00	0.00	0.01	0.11	99.43	2 ALB06_1_A_Trav5_5um
347	41.10	49.80	8.78	0.06	0.00	0.00	0.00	0.01	0.00	0.15	99.90	3 ALB06_1_A_Trav5_5um
348	42.83	47.96	8.62	0.07	0.00	0.00	0.00	0.00	0.01	0.12	99.60	4 ALB06_1_A_Trav5_5um
349	37.74	56.14	8.72	0.07	0.04	0.00	0.01	0.00	0.00	0.09	102.81	5 ALB06_1_A_Trav5_5um
350	34.91	41.85	5.48	0.11	0.00	0.01	0.00	0.00	0.00	0.12	82.49	6 ALB06_1_A_Trav5_5um
351	34.96	40.08	6.39	0.08	0.00	0.00	0.01	0.06	0.00	0.08	81.65	7 ALB06_1_A_Trav5_5um
352	35.81	40.26	6.21	0.05	0.02	0.01	0.00	0.04	0.00	0.05	82.46	8 ALB06_1_A_Trav5_5um
353	33.84	41.32	6.95	0.15	0.02	0.00	0.01	0.01	0.00	0.07	82.37	9 ALB06_1_A_Trav5_5um
354	31.71	40.61	8.90	0.09	0.00	0.01	0.00	0.04	0.00	0.09	81.46	10 ALB06_1_A_Trav5_5um
355	33.19	40.04	7.75	0.08	0.00	0.00	0.00	0.06	0.00	0.10	81.20	11 ALB06_1_A_Trav5_5um
356	35.36	39.59	6.27	0.08	0.00	0.00	0.01	0.01	0.00	0.07	81.40	12 ALB06_1_A_Trav5_5um
357	33.35	41.34	6.84	0.06	0.00	0.02	0.00	0.04	0.00	0.05	81.69	13 ALB06_1_A_Trav5_5um
358	35.62	41.39	4.46	0.07	0.01	0.00	0.00	0.04	0.00	0.03	81.62	14 ALB06_1_A_Trav5_5um
359	40.20	50.62	8.69	0.07	0.00	0.00	0.01	0.00	0.01	0.14	99.74	15 ALB06_1_A_Trav5_5um
360	40.68	50.18	8.92	0.06	0.00	0.00	0.00	0.00	0.00	0.17	100.01	16 ALB06_1_A_Trav5_5um
361	40.58	49.88	8.85	0.06	0.00	0.01	0.00	0.04	0.00	0.14	99.56	17 ALB06_1_A_Trav5_5um
362	41.09	49.53	8.93	0.04	0.03	0.03	0.02	0.00	0.00	0.14	99.81	1 ALB06_1_B_Trav1_5um
363	41.16	49.56	9.01	0.10	0.01	0.00	0.00	0.01	0.00	0.16	100.01	2 ALB06_1_B_Trav1_5um
364	40.66	48.32	8.93	0.06	0.04	0.00	0.02	0.00	0.00	0.14	98.18	3 ALB06_1_B_Trav1_5um
365	42.13	48.51	8.93	0.07	0.00	0.00	0.00	0.03	0.00	0.10	99.77	4 ALB06_1_B_Trav1_5um
366	41.53	49.91	8.94	0.06	0.04	0.00	0.00	0.00	0.00	0.16	100.64	5 ALB06_1_B_Trav1_5um
367	36.47	39.39	5.62	0.12	0.00	0.01	0.00	0.00	0.01	0.10	81.71	6 ALB06_1_B_Trav1_5um
368	34.44	41.22	6.33	0.09	0.02	0.01	0.00	0.02	0.00	0.07	82.20	7 ALB06_1_B_Trav1_5um
369	34.10	39.93	7.16	0.08	0.00	0.00	0.02	0.04	0.00	0.14	81.47	8 ALB06_1_B_Trav1_5um
370	34.43	40.39	7.11	0.06	0.00	0.01	0.04	0.06	0.01	0.09	82.19	9 ALB06_1_B_Trav1_5um
371	33.92	39.26	7.77	0.07	0.01	0.01	0.00	0.02	0.00	0.06	81.13	10 ALB06_1_B_Trav1_5um
372	29.53	40.01	11.58	0.09	0.01	0.01	0.01	0.02	0.00	0.16	81.41	11 ALB06_1_B_Trav1_5um
373	30.20	41.08	9.39	0.08	0.00	0.00	0.02	0.06	0.01	0.09	80.93	12 ALB06_1_B_Trav1_5um
374	34.39	39.67	7.16	0.06	0.03	0.00	0.00	0.08	0.00	0.10	81.50	13 ALB06_1_B_Trav1_5um
375	37.95	37.19	6.48	0.06	0.01	0.01	0.02	0.06	0.00	0.04	81.81	14 ALB06_1_B_Trav1_5um
376	27.22	41.19	10.59	0.16	0.02	0.00	0.00	0.02	0.01	0.19	79.39	15 ALB06_1_B_Trav1_5um
377	26.96	43.56	11.42	0.09	0.00	0.00	0.00	0.02	0.01	0.24	82.30	16 ALB06_1_B_Trav1_5um
378	40.47	39.35	3.88	0.04	0.00	0.00	0.01	0.00	0.00	0.04	83.80	17 ALB06_1_B_Trav1_5um
379	36.98	39.14	5.06	0.08	0.00	0.00	0.00	0.00	0.01	0.08	81.35	18 ALB06_1_B_Trav1_5um
380	27.46	43.91	10.60	0.20	0.01	0.00	0.00	0.04	0.00	0.17	82.39	19 ALB06_1_B_Trav1_5um
381	31.17	40.74	8.83	0.09	0.00	0.00	0.00	0.04	0.01	0.11	80.98	20 ALB06_1_B_Trav1_5um
382	34.68	40.27	6.86	0.06	0.04	0.00	0.01	0.08	0.01	0.04	82.03	21 ALB06_1_B_Trav1_5um

Table continues on the next page

Table A.1: Mineral chemical data measured on samples ALB09-1 and ALB06-1.

383	30.63	41.30	9.29	0.14	0.00	0.00	0.00	0.04	0.00	0.17	81.57	22 ALB06_1_B_Trav1_5um
384	29.56	41.39	10.13	0.14	0.01	0.00	0.00	0.03	0.01	0.15	81.41	23 ALB06_1_B_Trav1_5um
385	33.02	41.36	7.88	0.13	0.00	0.00	0.00	0.02	0.01	0.12	82.53	24 ALB06_1_B_Trav1_5um
386	37.34	39.32	5.62	0.12	0.01	0.00	0.00	0.02	0.00	0.09	82.52	25 ALB06_1_B_Trav1_5um
387	33.10	40.87	7.21	0.17	0.03	0.00	0.00	0.05	0.00	0.15	81.58	26 ALB06_1_B_Trav1_5um
388	37.41	38.83	5.09	0.14	0.00	0.00	0.02	0.00	0.00	0.09	81.58	27 ALB06_1_B_Trav1_5um
389	30.07	42.28	8.19	0.18	0.00	0.01	0.01	0.00	0.00	0.16	80.90	28 ALB06_1_B_Trav1_5um
390	36.17	38.86	6.42	0.04	0.01	0.00	0.02	0.07	0.00	0.01	81.60	29 ALB06_1_B_Trav1_5um
391	38.99	39.69	4.36	0.06	0.00	0.00	0.01	0.04	0.00	0.08	83.24	30 ALB06_1_B_Trav1_5um
392	34.29	40.69	7.68	0.06	0.01	0.00	0.01	0.05	0.00	0.12	82.91	31 ALB06_1_B_Trav1_5um
393	35.56	39.28	6.64	0.04	0.00	0.00	0.00	0.05	0.00	0.05	81.62	32 ALB06_1_B_Trav1_5um
394	33.08	40.18	7.70	0.07	0.00	0.00	0.01	0.03	0.00	0.08	81.15	33 ALB06_1_B_Trav1_5um
395	33.66	37.12	6.99	0.09	0.02	0.01	0.00	0.04	0.00	0.08	78.02	34 ALB06_1_B_Trav1_5um
396	33.44	42.76	6.25	0.08	0.00	0.00	0.01	0.03	0.00	0.08	82.64	35 ALB06_1_B_Trav1_5um
397	37.16	47.86	6.21	0.07	0.00	0.00	0.01	0.02	0.01	0.10	91.44	36 ALB06_1_B_Trav1_5um
398	40.40	51.22	8.75	0.06	0.00	0.00	0.00	0.00	0.00	0.12	100.55	37 ALB06_1_B_Trav1_5um
399	39.13	53.84	8.80	0.07	0.00	0.03	0.02	0.02	0.00	0.15	102.05	38 ALB06_1_B_Trav1_5um
400	40.60	50.26	8.73	0.05	0.00	0.00	0.01	0.00	0.00	0.13	99.79	39 ALB06_1_B_Trav1_5um
401	40.54	50.40	8.65	0.05	0.03	0.00	0.02	0.01	0.01	0.12	99.83	40 ALB06_1_B_Trav1_5um
402	0.00	8.44	22.76	0.00	55.68	10.16	0.06	0.03	0.00	0.43	97.56	ALB06_1_C_Spinel1
403	0.02	8.63	22.57	0.00	55.55	10.22	0.10	0.00	0.01	0.35	97.45	ALB06_1_C_Spinel2
404	0.00	8.55	22.64	0.00	55.96	10.02	0.06	0.00	0.00	0.33	97.57	ALB06_1_C_Spinel3
405	54.03	17.38	1.44	25.39	0.26	0.64	0.00	0.08	0.01	0.05	99.27	ALB06_1_C_Cpx1
406	53.83	17.22	1.36	25.36	0.30	0.60	0.02	0.10	0.01	0.01	98.80	ALB06_1_C_Cpx2
407	54.39	17.65	1.40	25.39	0.29	0.58	0.02	0.08	0.00	0.02	99.83	ALB06_1_C_Cpx3
408	40.72	49.67	8.96	0.06	0.04	0.01	0.00	0.00	0.01	0.10	99.57	ALB06_1_C_olivine1
409	40.80	49.94	9.07	0.06	0.00	0.00	0.00	0.01	0.00	0.12	99.99	ALB06_1_C_olivine2
Min.	0.004	8.44	1.36	0	0	0	0	0	0	0		
Max.	59.09	56.14	22.76	25.39	55.96	14.86	4.75	2.30	2.17	0.43		
Avg.	40.43	37.92	6.82	1.61	0.95	0.59	0.04	0.04	0.02	0.13		
σ	9.37	8.29	2.48	5.11	6.58	1.95	0.4	0.19	0.18	0.06		

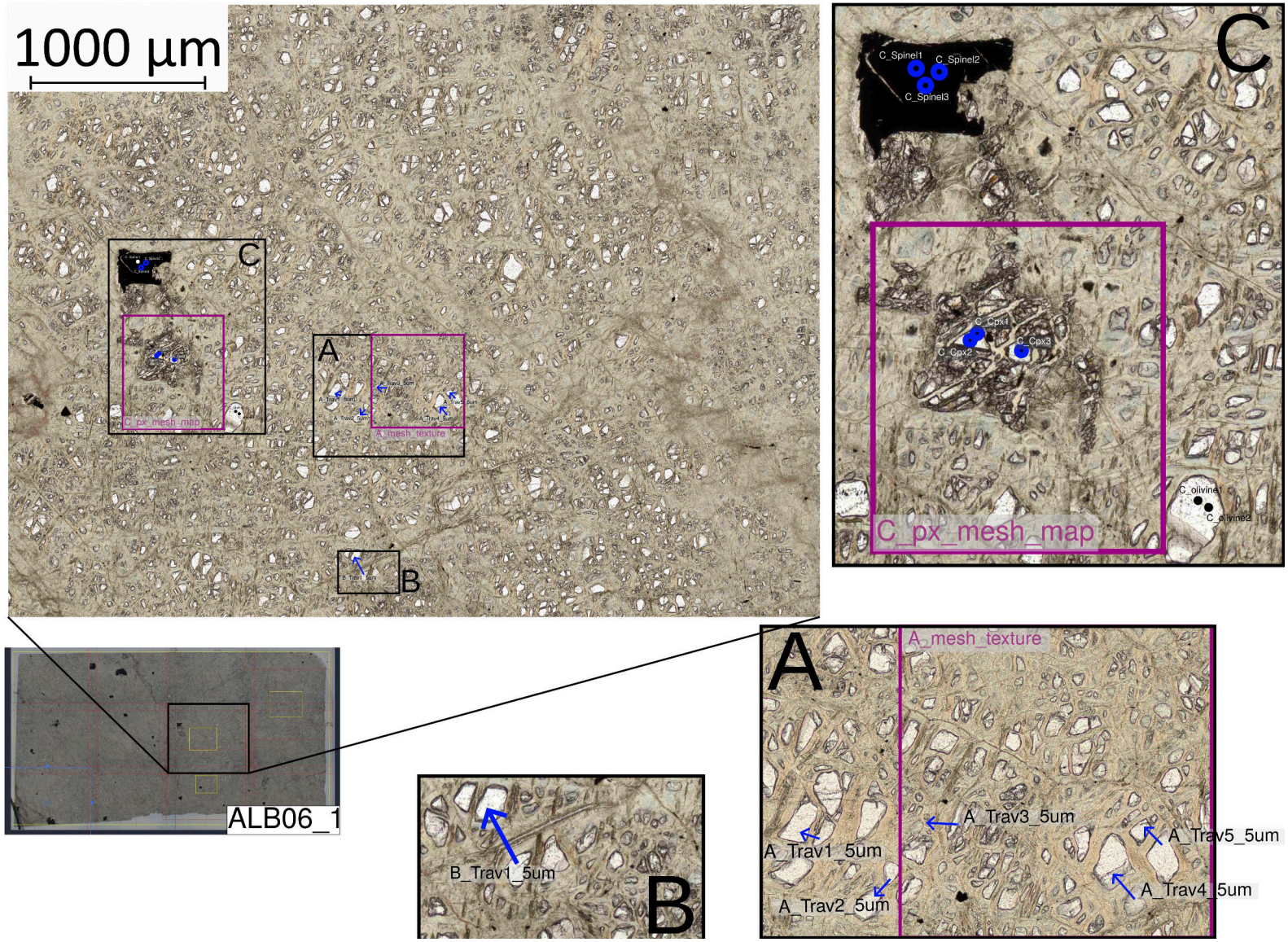

Figure A.1: Loality of microprobe element mappings *A_mesh_texture* and *C_px_mesh_map*, and the quantitative mineral chemistry points (Figure A.3). For mapping results, see Figures A.9 and A.10.

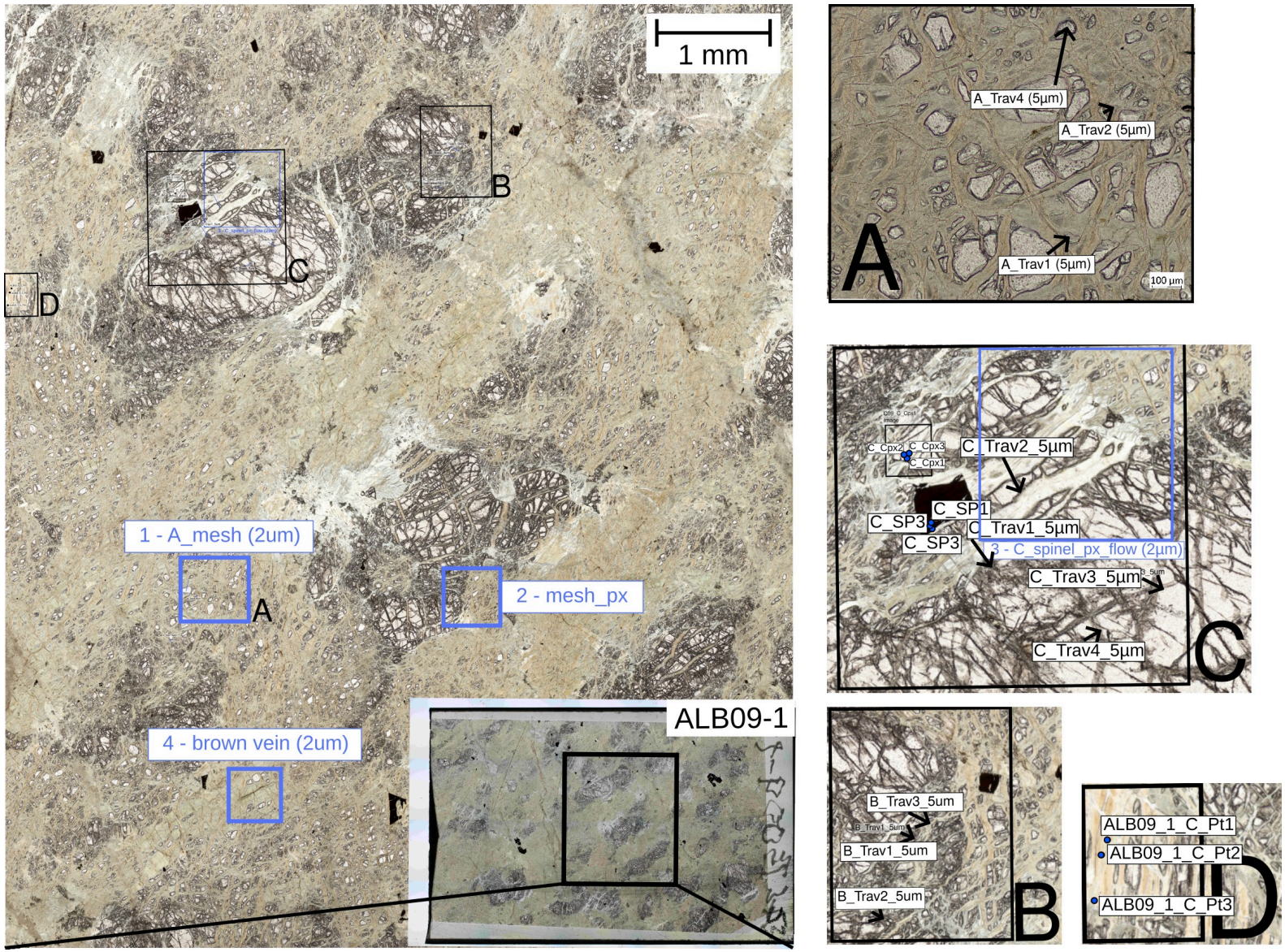

Figure A.2: Loality of microprobe element mappings *1 - A_mesh (2um)*, *2 - mesh_px*, *3 - C_spinel_px_flow (2um)*, and *4 - brown vein (2um)*, and the quantitative mineral chemistry points (Figure A.3). For mapping results, see Figures A.11 and A.12.

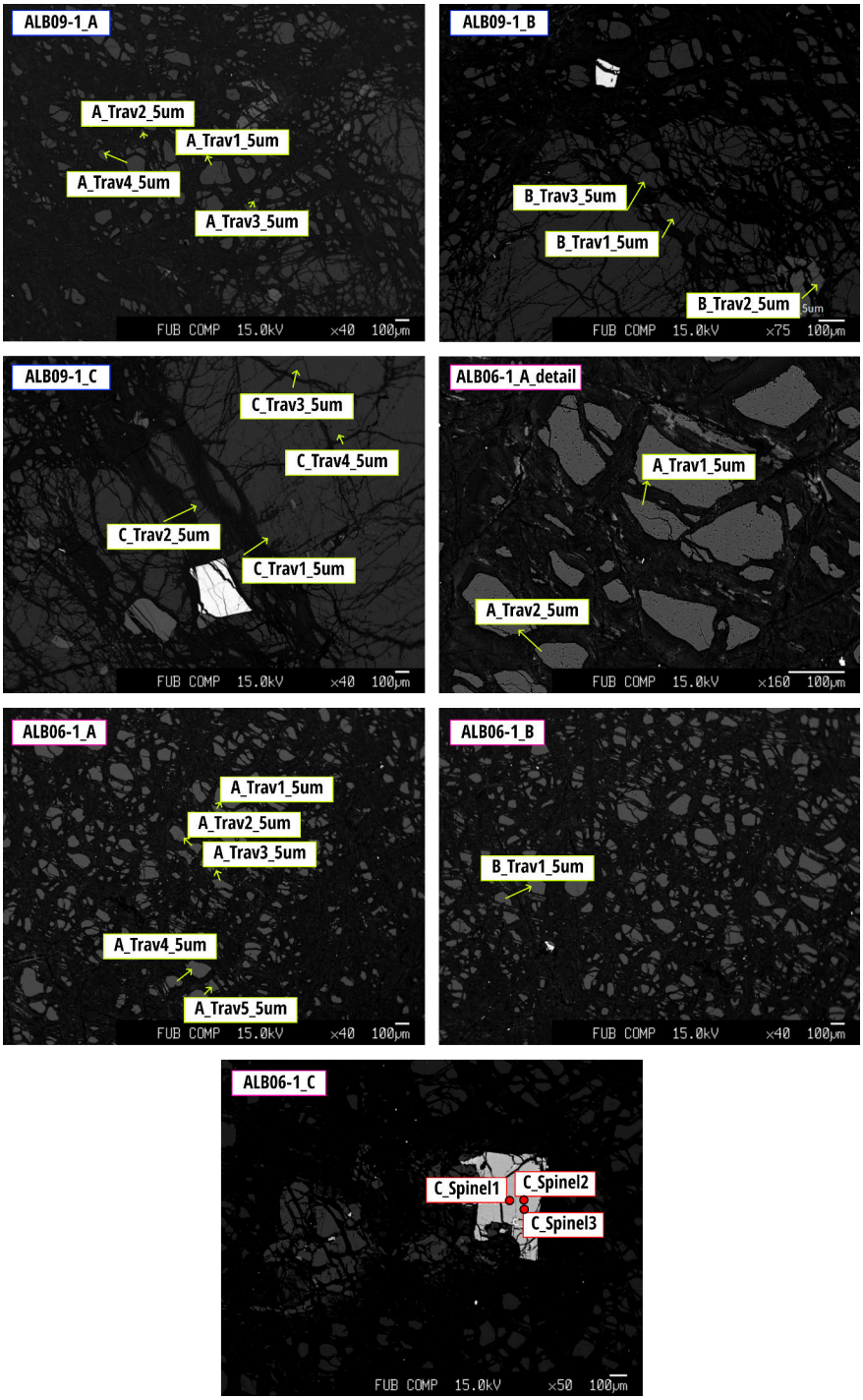

Figure A.3: Backscatter images with locations of chemical mineral data points in Table A.1.

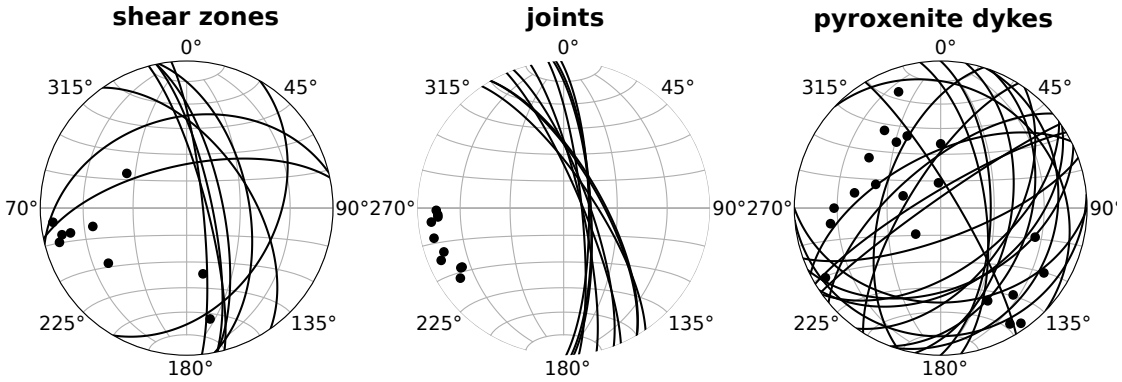

Figure A.4: Stereoplots from data in Table A.2.

Table A.2: Structural measurements of shear zones, joints, pyroxenite bands, and pyroxenite dykes taken at the Mirdita ophiolite outcrop. Figure A.13a shows the location of the measurements at the outcrop.

ID	strike	dip	type	ID	strike	dip	type
SZ1	348	70	shear zone	PX1	235	80	pyroxenite dyke
SZ2	258	66	shear zone	PX1	235	85	pyroxenite dyke
SZ3	30	39	shear zone	PX1	239	81	pyroxenite dyke
SZ3	256	38	shear zone	PX1	329	81	pyroxenite dyke
SZ3	325	55	shear zone	PX2	314	20	pyroxenite dyke
SZ3	349	55	shear zone	PX2	360	62	pyroxenite dyke
SZ3	348	76	shear zone	PX2	18	22	pyroxenite dyke
SZ5	345	79	shear zone	PX2	65	45	pyroxenite dyke
SZ5	354	81	shear zone	PX2	20	39	pyroxenite dyke
KL6	358	80	joint	PX2	352	65	pyroxenite dyke
KL6	357	75	joint	PX2	197	57	pyroxenite dyke
KL7	326	74	joint	PX3	243	60	pyroxenite dyke
KL7	356	75	joint	PX3	212	72	pyroxenite dyke
KL1	359	76	joint	PX4	230	66	pyroxenite dyke
KL2	330	70	joint	PX5	35	50	pyroxenite dyke
KL4	354	80	joint	PX5	54	55	pyroxenite dyke
KL5	347	80	joint	PX5	10	50	pyroxenite dyke
KL5	337	80	joint	PX5	90	36	pyroxenite dyke
KL5	340	76	joint	PX6	56	45	pyroxenite dyke
KL5	330	69	joint	PX7	85	14	pyroxenite dyke
SB1	318	60	pyroxenite dyke	PX7	70	73	pyroxenite dyke
SB3	329	60	pyroxenite dyke	PX8	58	80	pyroxenite dyke
SB3	331	71	pyroxenite dyke	SB5	358	33	pyroxenite dyke
PX4	338	76	pyroxenite dyke	SB5	338	85	pyroxenite dyke

Figure A.5: Full thin section photography of sample ALB06-1 (serpentinized dunite).

Figure A.6: Full thin section photography of sample ALB06-2 (serpentinized dunite).

Figure A.7: Full thin section photography of sample ALB09-1 (serpentinized harzburgite).

Figure A.8: Full thin section photography of sample ALB09-2 (serpentinized harzburgite).

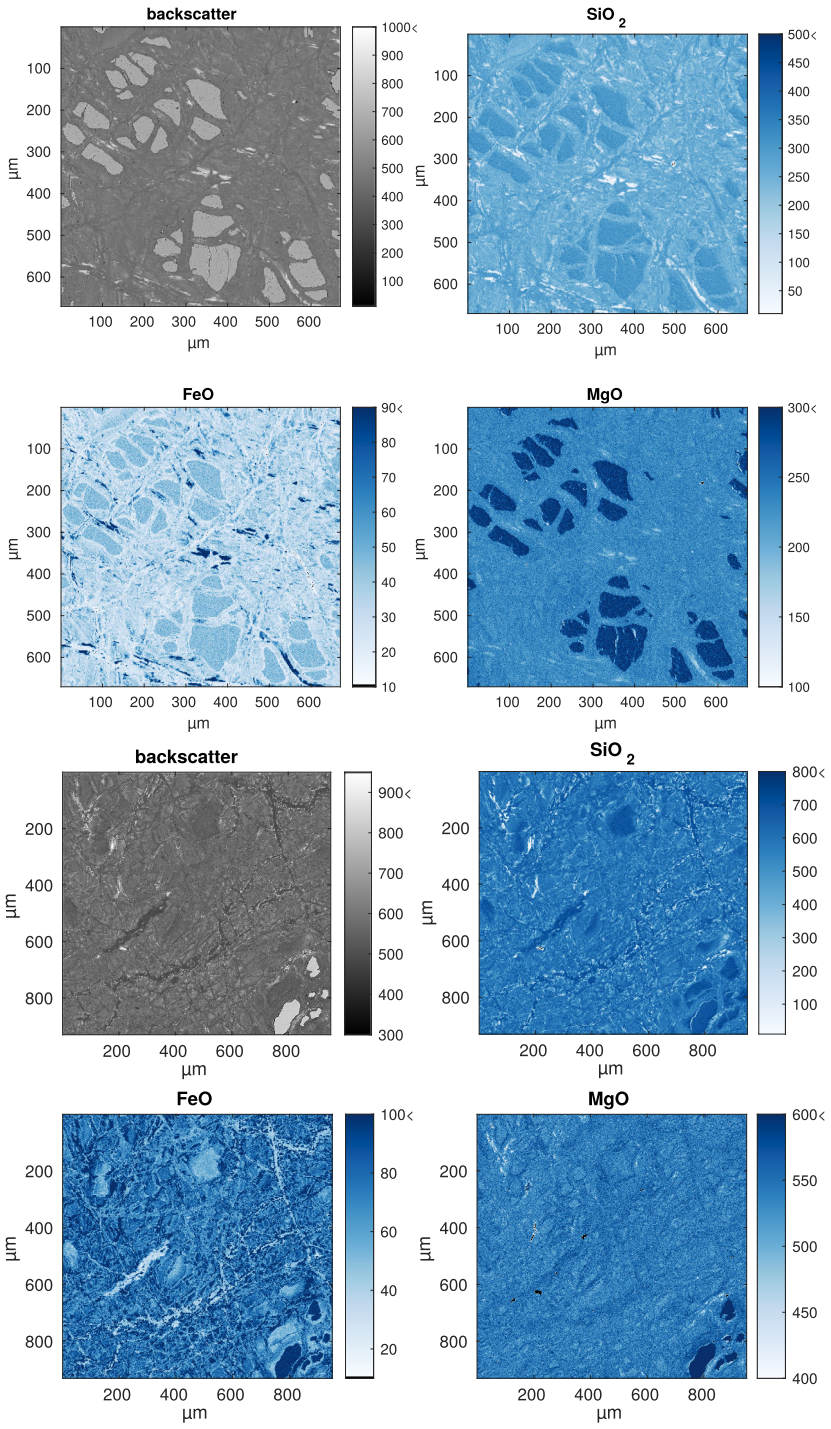

Figure A.9: Qualitative chemical element mappings (microprobe). Top: ALB06-1-A-mesh-1um in counts. Bottom: Raman mapping area. For location on sample, see Figure A.1.

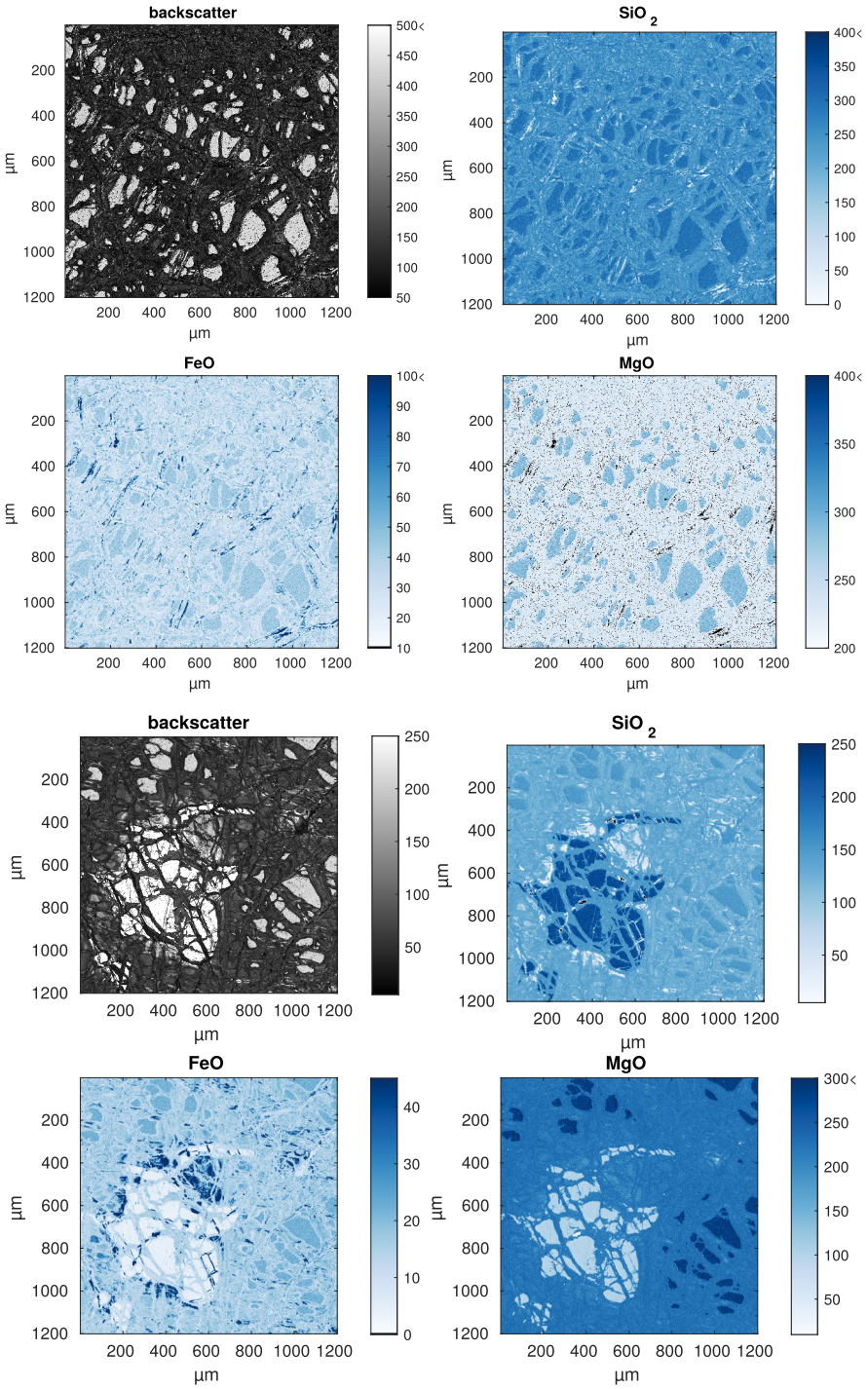

Figure A.10: Qualitative chemical element mappings (microprobe). Top: ALB06-1-A-mesh-texture. Bottom: ALB06-1-C-px-mesh. Both mappings are given in counts. For location on sample, see Figure A.1.

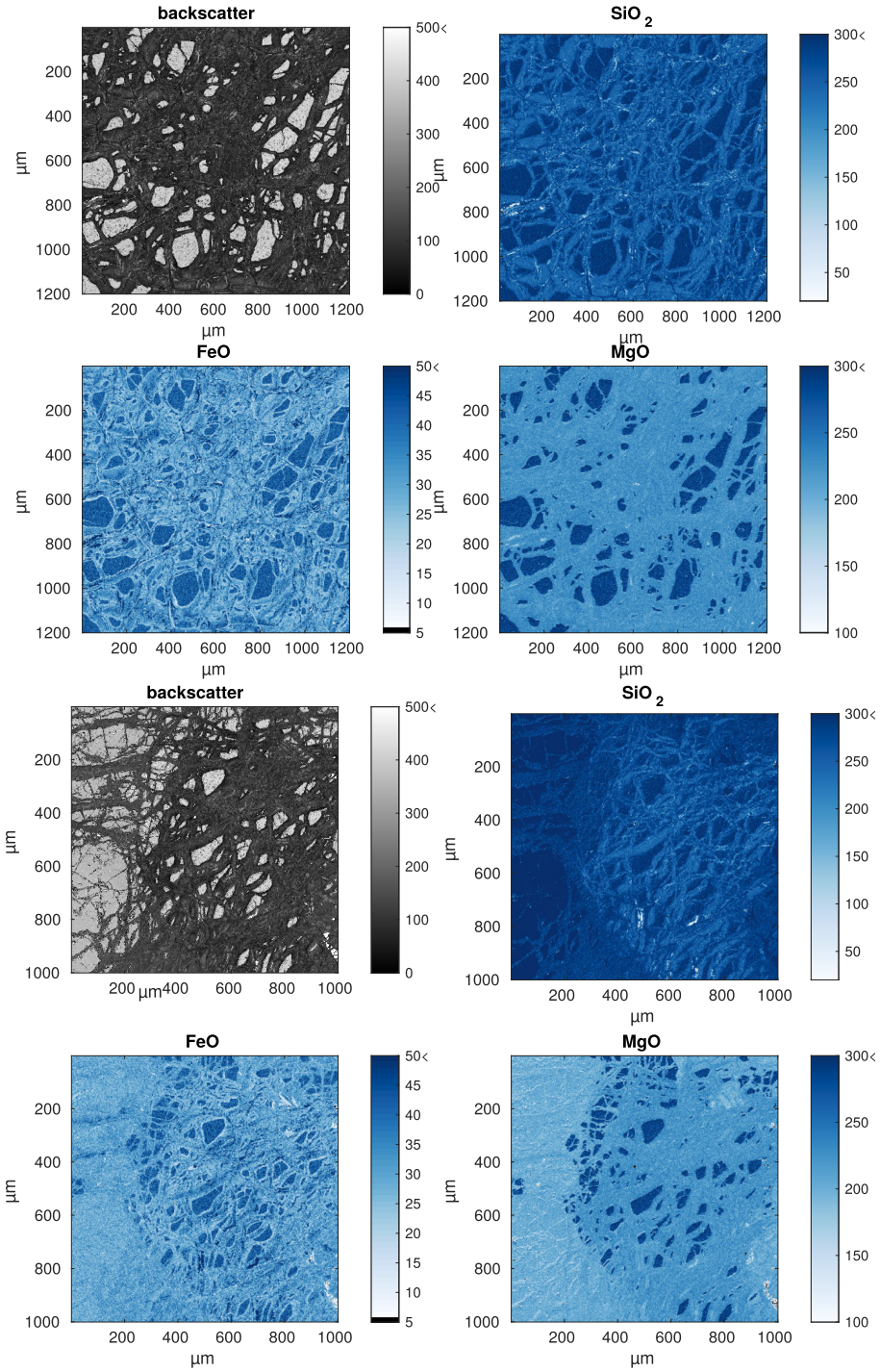

Figure A.11: Qualitative chemical element mappings (microprobe). Top: ALB09-1-A-mesh. Bottom: ALB09-1-mesh-px. Both mappings are given in counts. For location on sample, see Figure A.2.

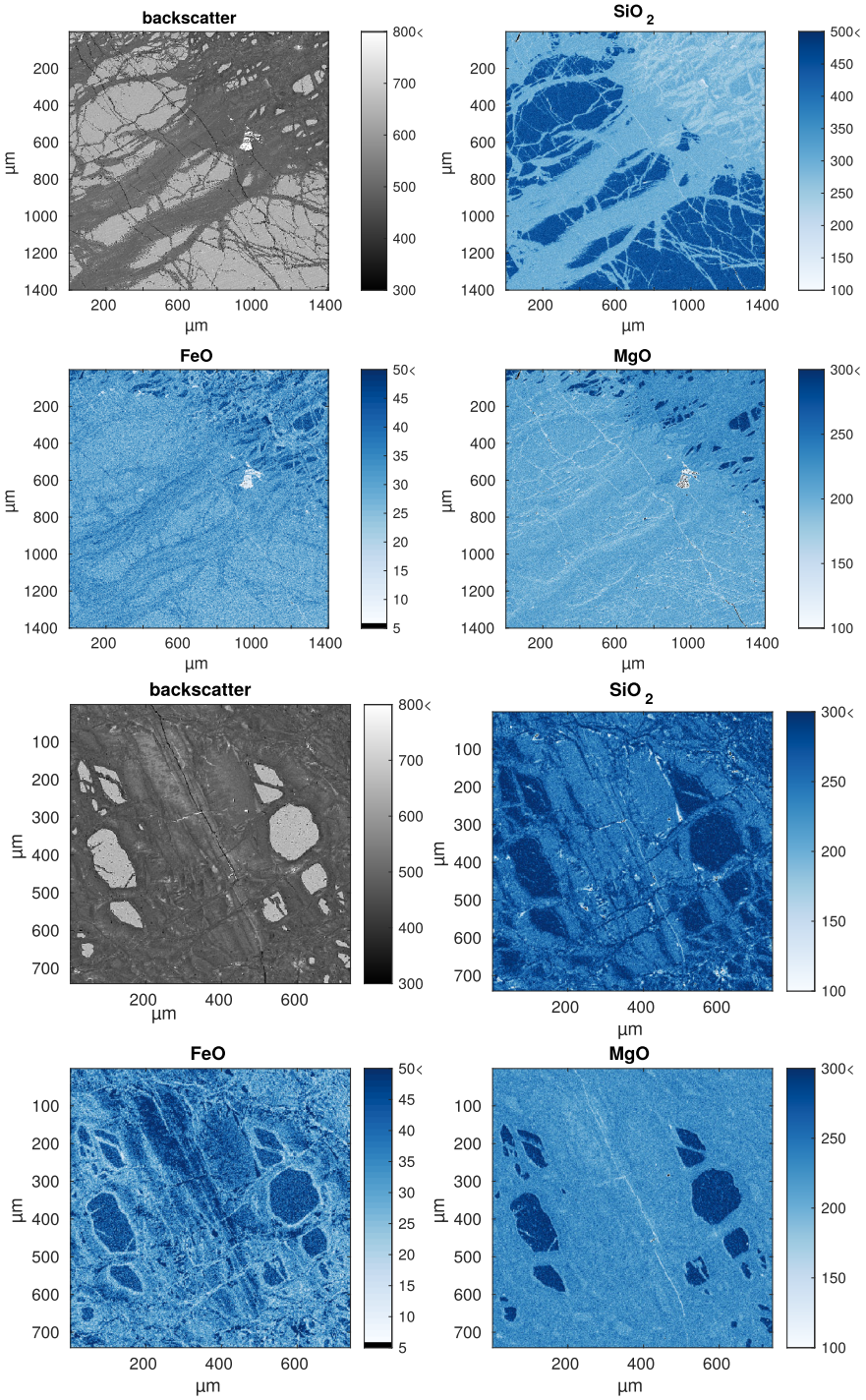

Figure A.12: Qualitative chemical element mappings (microprobe). Top: ALB09-1-A-brown-vein. Bottom: ALB09-1-spinel-px-flow. Both mappings are given in counts. For location on sample, see Figure A.2.

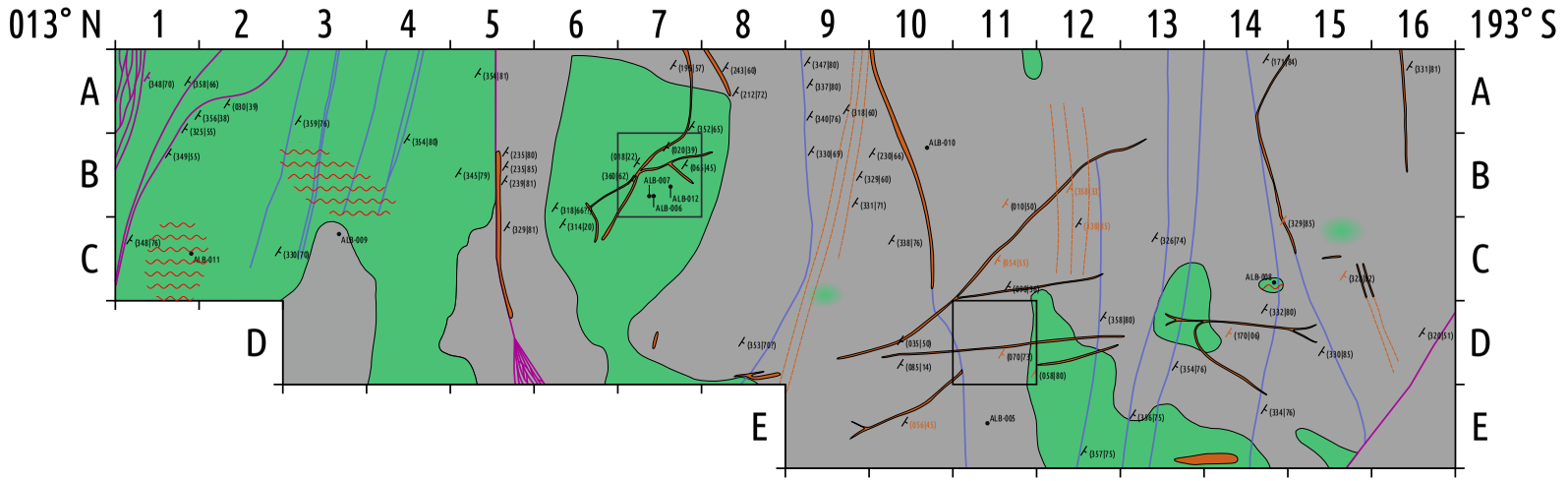

(a) Outcrop map with locations of structural orientation measurements (Table A.2) and sampling localities. Squares indicate the meter scale geological mappings. The meter scale mapping for the representative harzburgite area is given below. pink: shear zones; blue: joints; the rest of the legend is the same as in Figure 2.2. Orientation measurements are given in Table A.2.

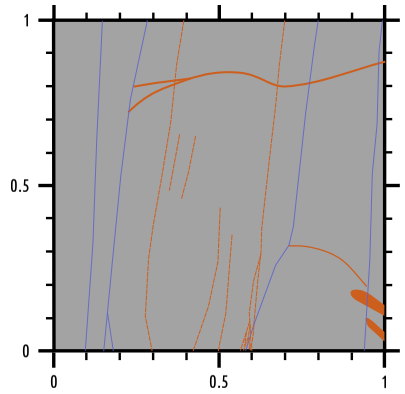

(b) Meter scale mapping of section D11.

Figure A.13: Geological maps with localities of sampling and structural measurements.

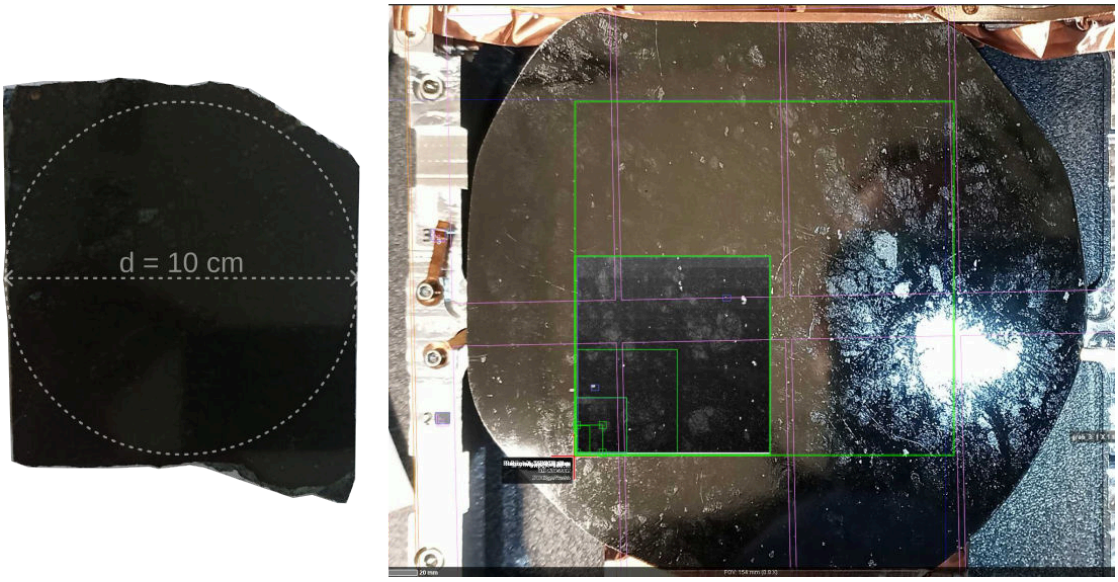

Figure A.14: Left: The piece of sample ALB09-1 on which the multiscale chemical mappings were taken. The dashed circle with a diameter of 10 cm shows the carbon-coated area (right). Right: Coated sample in the SEM sample holder with superimposed BSE images. The green rectangles show the position of the multiscale chemical mappings.

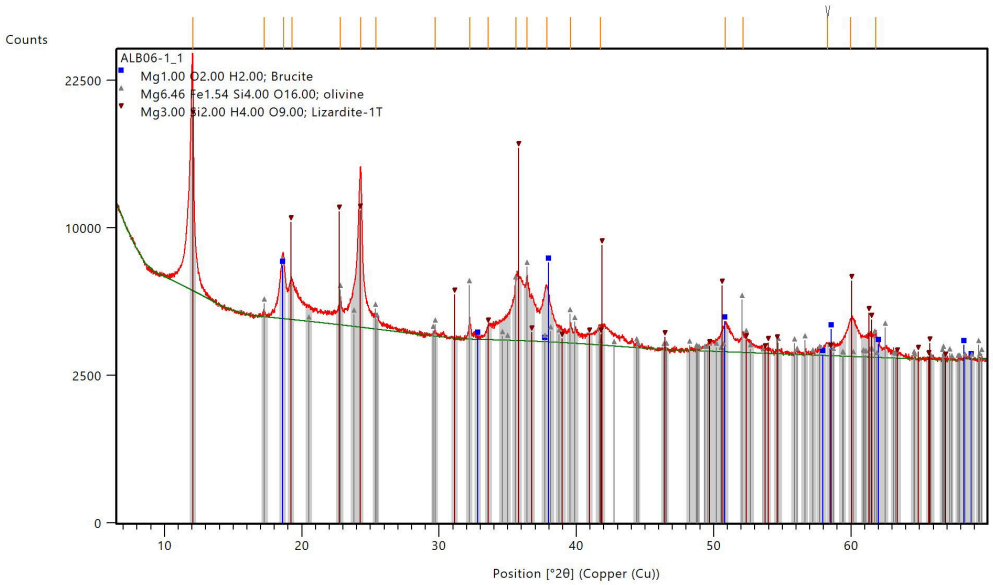

Figure A.15: XRD data for dunite sample ALB06-1, measured on July 22nd, 2022.

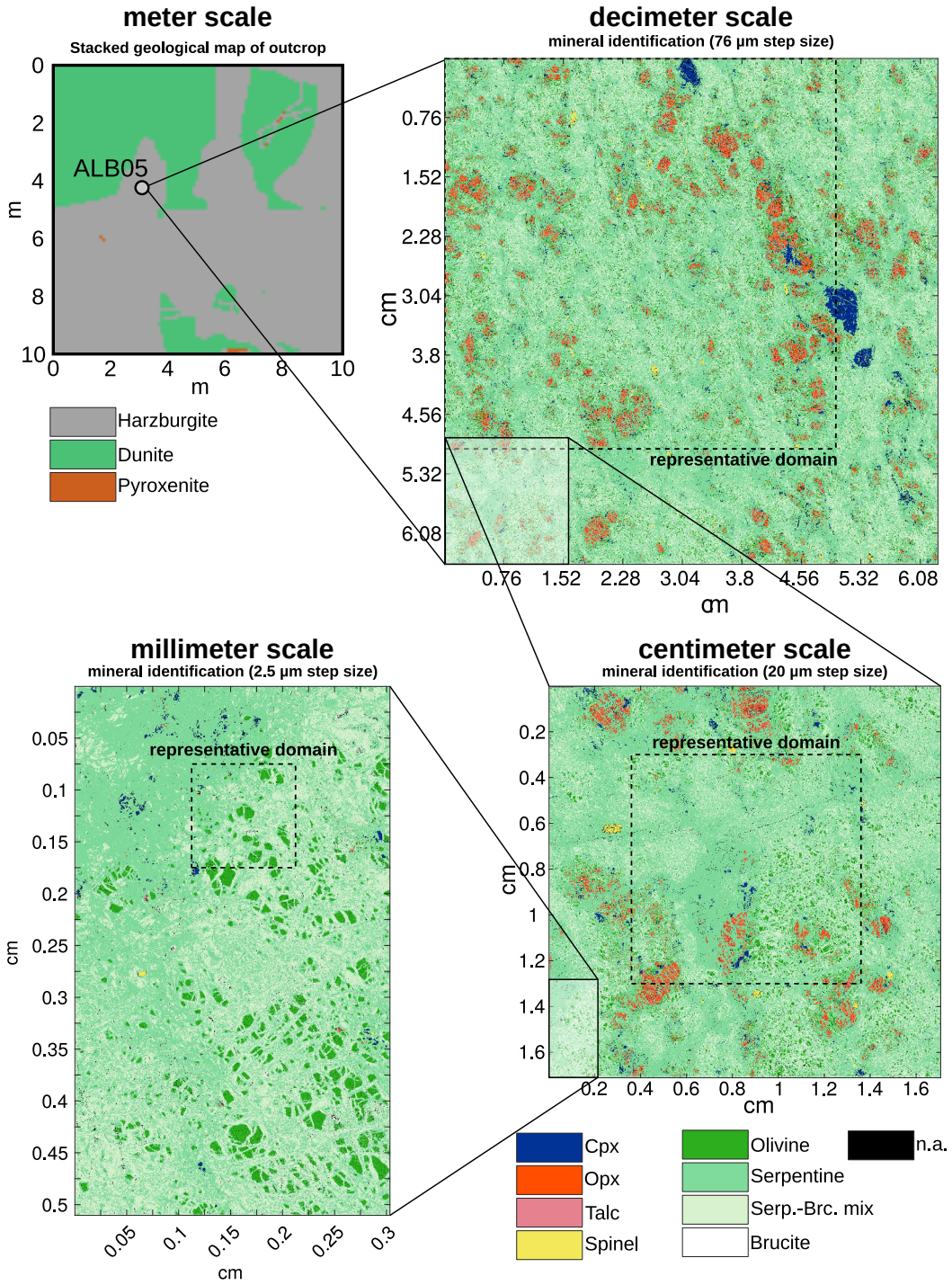

Figure A.16: Mineral classification for the three representative scales used in the chapter. The mineral classification is performed by the MATLAB codes Listing B.1 and Listing B.2. For the results of the meter, decimeter, and centimeter scale, see Figures A. 19c, A. 18c, and A. 17c, respectively.

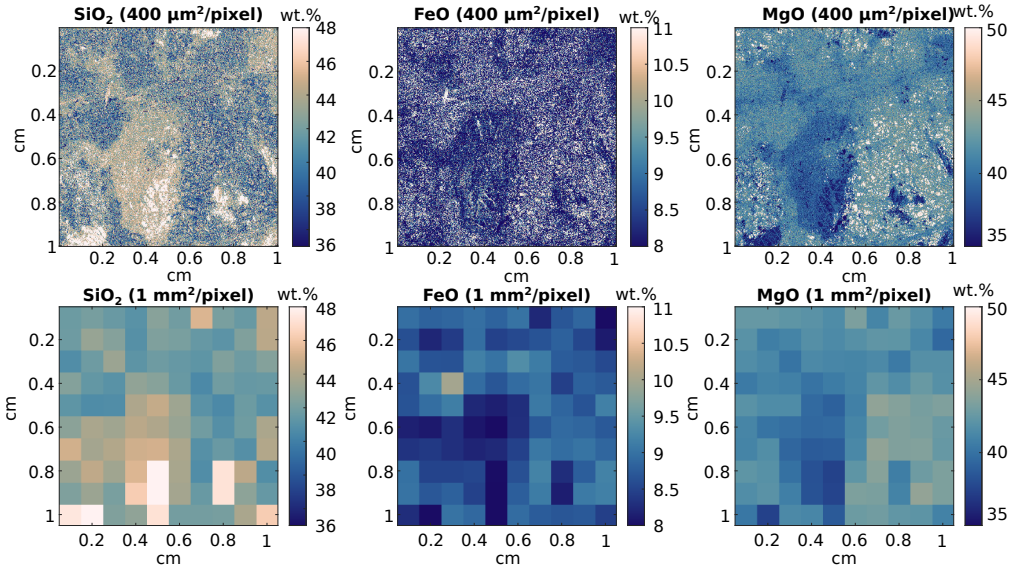

(a) Centimeter scale chemical mapping

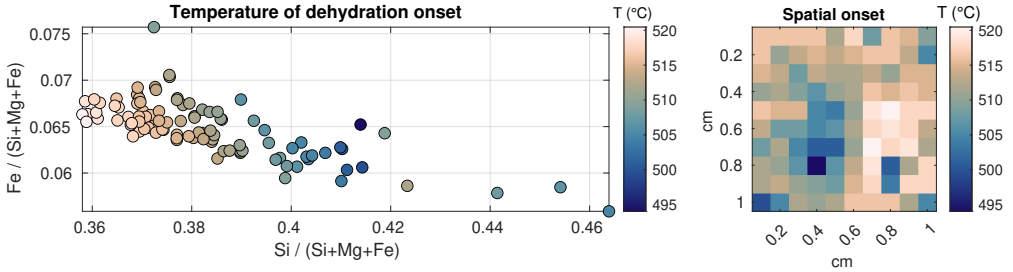

(b) Centimeter scale dehydration onset

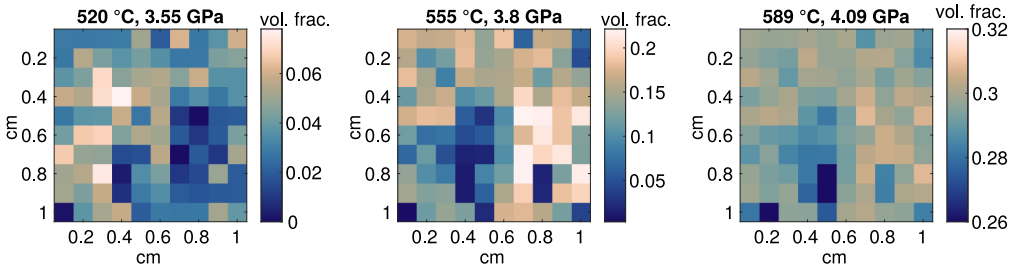

(c) Centimeter scale porosity evolution

Figure A.17: Results of thermodynamic and porosity calculations for the centimeter scale dataset

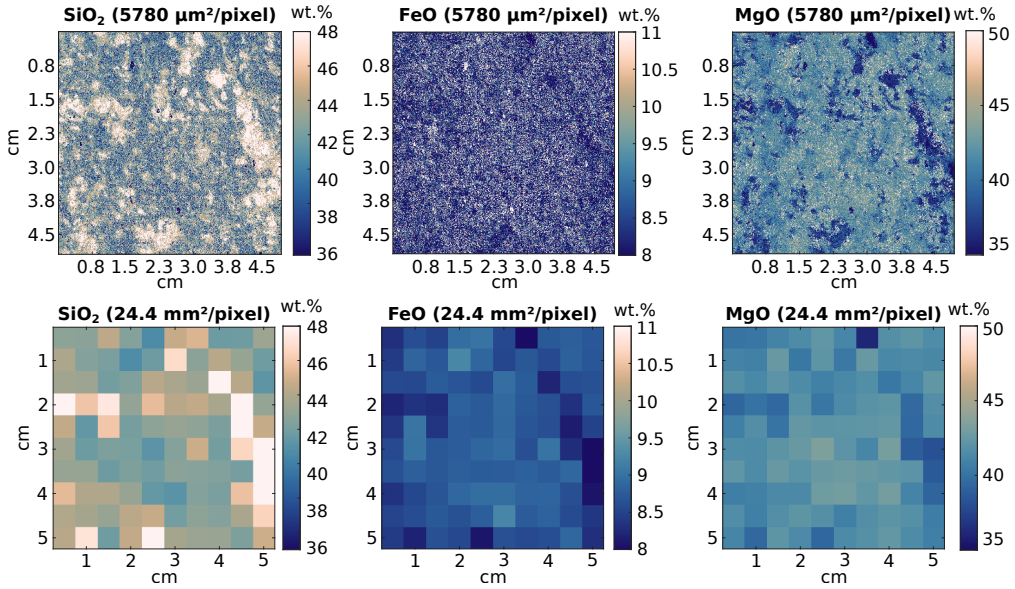

(a) Decimeter scale chemical mapping

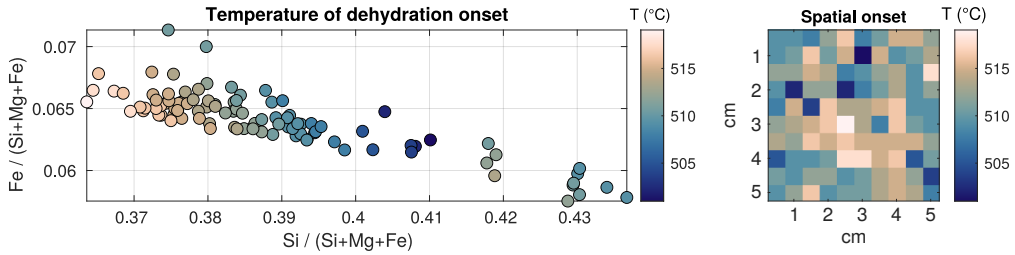

(b) Decimeter scale dehydration onset

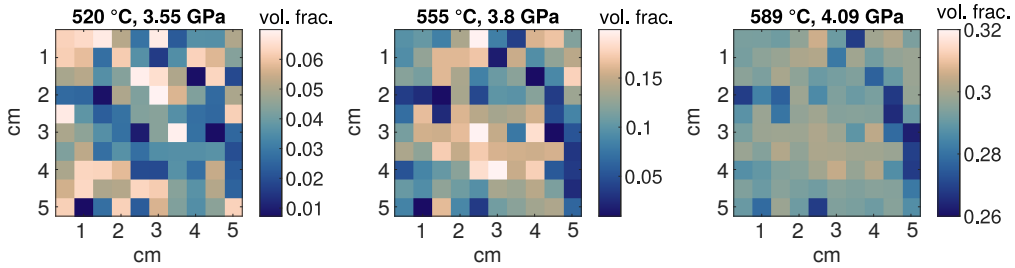

(c) Decimeter scale porosity evolution

Figure A.18: Results of thermodynamic and porosity calculations for the decimeter scale dataset.

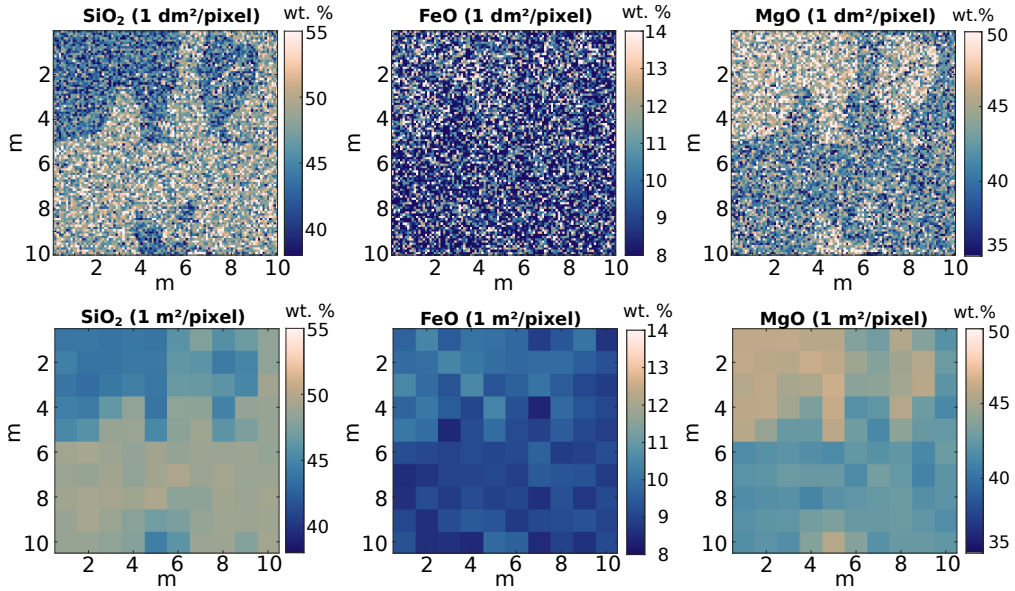

(a) Rearranged geological map with assigned bulk composition variations

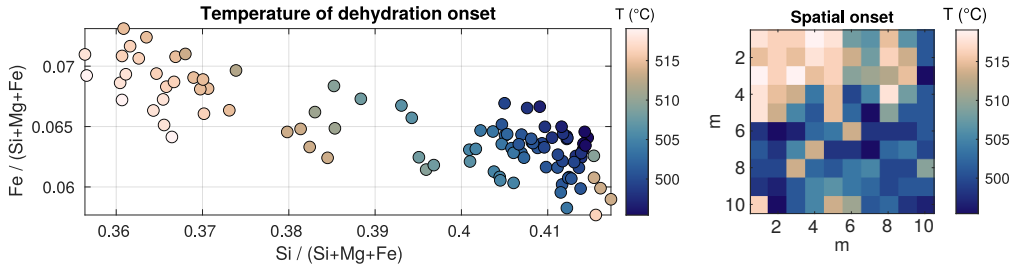

(b) Meter scale dehydration onset

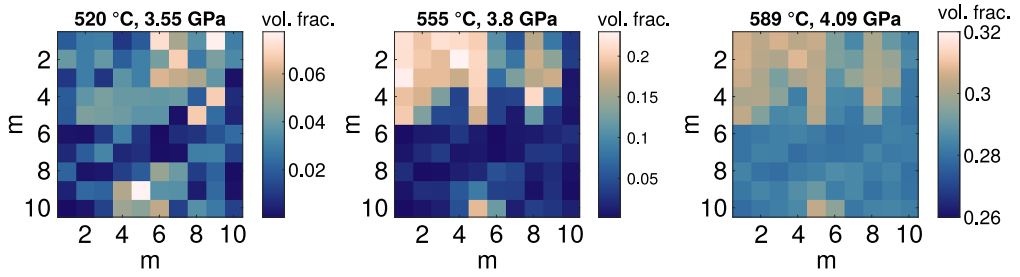

(c) Meter scale porosity evolution

Figure A.19: Results of thermodynamic and porosity calculation for the meter scale dataset (outcrop).

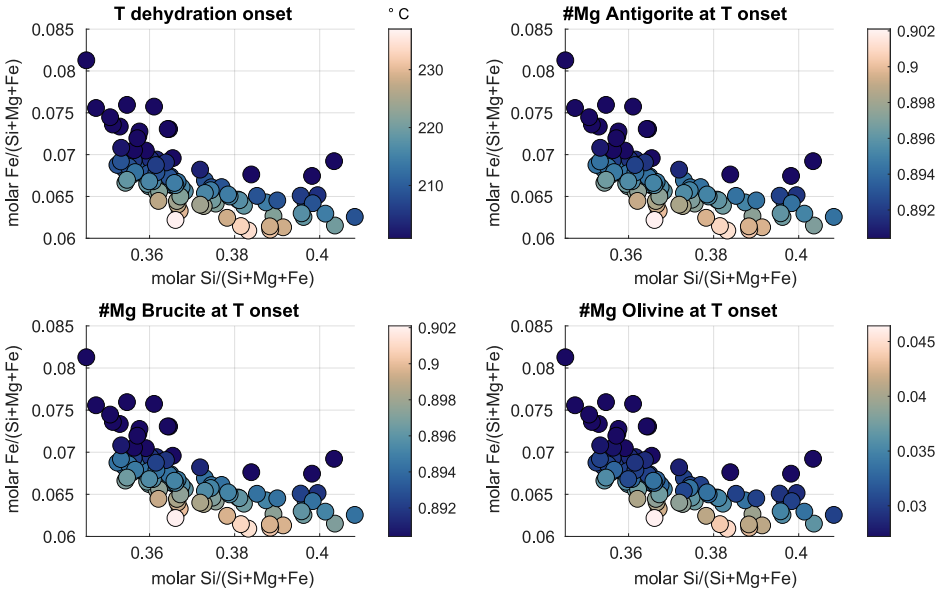

(a) Using solution models of Holland et al. (2018)

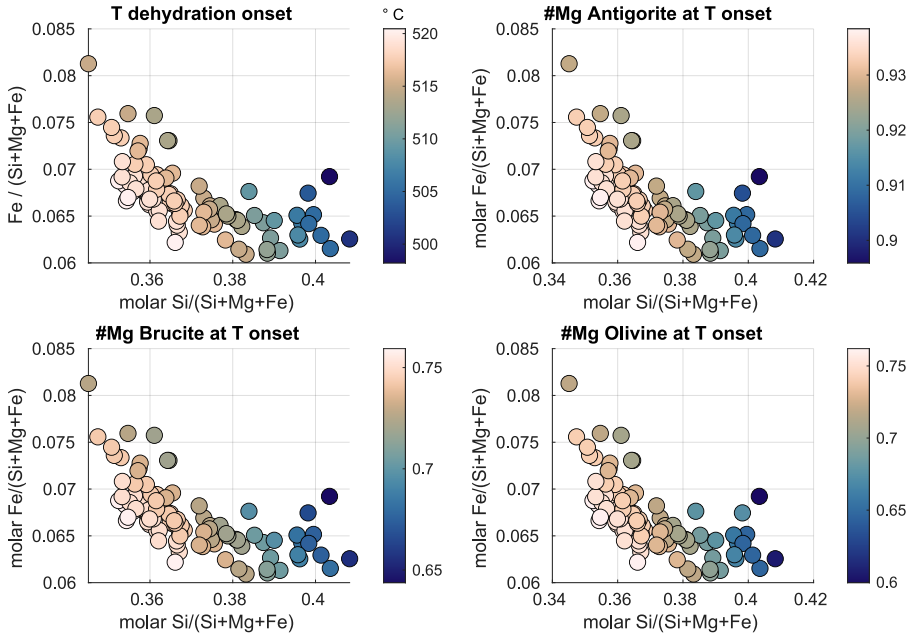

(b) Using solution models of Evans and Frost (2021)

Figure A.20: Temperature for the stability of first olivine and phase compositions for the millimeter scale dataset for different solution models.

Appendix B

MATLAB Codes to Generate the Multiscale Dataset for Chapter 2

Here, the MATLAB codes to generate the multiscale dataset from Chapter 2 are listed. The multiscale dataset contains the raw data and results from thermodynamic calculations and is also available online at https://zenodo.org/records/10368961 (Huber, 2023). For visualization, I used the scientific colormaps of Fabio Crameri (Crameri, 2023).

- `a1_load_data.m` (Listing B.2) loads the chemical mappings and performs mineral classifications.
- `a2_EDS_select_texture_areas_and_coarse.m` (Listing B.3) allows to select areas of interest (textures), to define a thermodynamic domain size, and to coarsen the texture for upscaling, using volumetric averaging.
- `a3_prepare_outcrop_map.m` (Listing B.4) loads the rearranged outcrop map and assigns chemical heterogeneities to the lithologies, based on the natural range of bulk rock variations in peridotites.
- `b1_tl_minimizer_postprocessing_EDS.m` (Listing B.6) is the Thermolab (Vrijmoed and Podladchikov (2022), using the version of November 16, 2023) code to perform Gibbs energy minimization for every pixel along a pre-defined subduction zone P-T path.
- `b2_tl_minimizer_postprocessing_outcrop.m` (Listing B.5) Gibbs energy minimization for the outcrop data.

- `b_create_lookup_tables.m` (Listing B.7) post-processes the results from the Gibbs energy minimization calculations and creates lookup tables.
- `get_PTpath_fun.m` (Listing B.8) is a function to create a P-T path from a thermal model in the Supplementary Information of Syracuse et al. (2010).

Generate upper and lower compositional limits to perform a mineral classification

```
clear
%% List of minerals and colors
phs_id = {'Olivine','Serpentine','SerpBrucMix', 'Brucite', 'Cpx','Opx','Talc','Spinel'};
colors = {'#000000','#1B7837','#4EB265','#CAE0AB','#f7f7f7','#762a83 ','#d6604d','#5385bc','#f7f056'};
cmap   = validatecolor(colors, 'multiple'); % generate colormap
ele    = {'Si', 'Mg' , 'Fe', 'Ca', 'Al', 'Cr', 'O' };

%% classification limits (wt.%)
% OLIVINE      Si     Mg    Fe     Ca    Al    Cr    O
ind(1,:,1) = [19   ,  28   ,  5   ,   0 ,   0 ,   0 , 30 ]; % min
ind(2,:,1) = [30   ,  32   , 15   ,   1 ,  10 ,   0 , 60 ]; % max
% SERPENTINE   Si     Mg    Fe     Ca    Al    Cr    O
ind(1,:,2) = [19   ,  10   ,  0   ,   0 ,   0 ,   0 , 30 ];
ind(2,:,2) = [25   ,  28   , 15   ,   1 ,  10 ,   0 , 60 ];
% SERP-BRC-MIX Si    Mg    Fe     Ca    Al    Cr    O
ind(1,:,3) = [ 7   ,  12   ,  4   ,   0 ,   0 ,   0 , 20 ];
ind(2,:,3) = [19   ,  40   , 20   ,   1 ,  10 ,   0 , 60 ];
% BRUCITE      Si     Mg    Fe     Ca    Al    Cr    O
ind(1,:,4) = [ 0   ,   5   , 10   ,   0 ,   0 ,   0 , 40 ];
ind(2,:,4) = [ 7   ,  45   , 30   ,   0 ,  10 ,   0 , 60 ];
% CPX          Si     Mg    Fe     Ca    Al    Cr    O
ind(1,:,5) = [23   ,   0   , 0    ,   2 ,   0 ,   0 , 35 ];
ind(2,:,5) = [31   ,  20   , 10   ,  25 ,  10 ,   0 , 60 ];
% OPX          Si     Mg    Fe     Ca    Al    Cr    O
ind(1,:,6) = [24   ,  21   , 0    ,   0 ,   0 ,   0 , 40 ];
ind(2,:,6) = [31   ,  28   , 15   ,   2 ,  10 ,   0 , 60 ];
% TALC         Si     Mg    Fe     Ca    Al    Cr    O
ind(1,:,7) = [28   ,  15   ,  0   ,   0 ,   0 ,   0 , 30 ];
ind(2,:,7) = [35   ,  23   , 10   ,   1 ,  10 ,   0 , 60 ];
% SPINEL       Si     Mg    Fe     Ca    Al    Cr    O
ind(1,:,8) = [ 0   ,   0   , 10   ,   0 ,   0 ,  10 , 16 ];
ind(2,:,8) = [10   ,  25   , 40   ,   1 ,  10 ,  70 , 40 ];
%% save
save mineral_classification_limits
```

Listing B.1: `mineral_classification_limits.m`

Load EDS mappings and perform mineral classification ()

```
% this script
% 1) loads the chemical mappings (EDS data)
```

```
% 2) performs a mineral classification based on the thresholds in
% EDS_data/mineral_classification_limits
% 3) converts the mappings from elements to oxides
% 4) stores the results in a structure ALB19


clear,clf,cnt=0;
load ./data/EDS_data/mineral_classification_limits
%
ele          = {'Si', 'Mg'  ,'Fe','Ca','Al','Cr', 'O'};
noxy         = [ 2      1     1    1    3/2 3/2    0  ];
molm         = molmass_fun(ele);
el2ox        = (molm + noxy'.*molm(strcmp(ele,'O')))./molm;
%
mapping_dir = './data/EDS_data/ALB05_Hz/';

for res = [2.5 5 10 20 38 76]
    cnt=cnt+1;
    clear Cmaps_ox Cmaps_ele
    if res == 76
        res         = 76; % stepsize in mu
        timestamp   = '4610113032023'; % in name of .csv file
        name        = 'ALB05_full_76mu';
        indx = [10 12];
        indy = [14 10];
    elseif res == 38
        res        = 38;
        timestamp = '50103132023';
        name       = 'ALB05_full_38mu';
        indx = [10 18];
        indy = [10 10];
    elseif res == 20
        res        = 20;
        timestamp = '283211342023';
        name       = 'ALB05_full_20mu';
        indx = [10 12];
        indy = [8   5];
    elseif res == 10
        res        = 10;
        timestamp = '165010442023';
        name       = 'ALB05_full_10mu';
        indx = [10 13];
        indy = [15 10];
    elseif res == 5
        res        = 5;
        timestamp = '494310442023';
        name       = 'ALB05_full_5mu';
        indx = [15 13];
        indy = [20 15];
    elseif res == 2.5
        res        = 2.5;
```

```
        timestamp = '27389542023';
        name      = 'ALB05_full_2-5mu';
        indx = [14 139];
        indy = [24  20];
    end

% load maps and convert to elements
for i = 1:length(ele)
    Cmaps_ele(:,:,i) = readmatrix([mapping_dir num2str(res) 'mu/' ele{i} '_'
        timestamp '.csv']); % given in element wt.%
    Cmaps_ox(:,:,i)  = Cmaps_ele(:,:,i)*el2ox(i); % convert to oxide wt.%
end

%% crop and store
Cmaps_ox        = Cmaps_ox (indx(1):end-indx(2),indy(1):end-indy(2),:);
Cmaps_ele       = Cmaps_ele(indx(1):end-indx(2),indy(1):end-indy(2),:);

% store in ALB structure
ALB19.ALB05_full(cnt).maps_ele        = Cmaps_ele;
ALB19.ALB05_full(cnt).maps_ox         = Cmaps_ox;
ALB19.ALB05_full(cnt).res             = res;
ALB19.ALB05_full(cnt).ele             = ele;
ALB19.ALB05_full(cnt).el2ox           = el2ox;

disp(res)
end
save data/ALB19_dataset ALB19
```

Listing B.2: a1_load_data.m

Select regions of interest and perform coarsening.

```
% in this script, one can select regions of interest (defined by indx and
% indy, the x and y indices of the region, respectively). These regions are
% coarsened and stored seperately in the ALB19 structure.

clear,clf
load data/ALB19_dataset

%%
resolutions = [2.5 5 10 20 38 76];
cmap        = crameri('lapaz');
el2ox       = ALB19.ALB05_full(1).el2ox;

for mapind = [1 4 6]
for itexture = 1:3

    % 2.5 mu mapping: 400x400 pixel = 1 mm2
    if mapind==1
        if itexture == 1 %
            texture    = 'mm_representative';
            XFe3       = 0;
```

```
            frac       = 0;
            res        = 2.5;
            resc       = 100; % coarse resolution (thermodynamic domain size in um)
            indx       = 300:700;
            indy       = 450:850;
        else
            break
        end

    % 20 mu mapping: 500x500 pixel = 1 cm2
    elseif mapind==4
        if itexture==1 % representative 1x1 cm domain for cm-scale
            texture    = 'cm_representative';
            XFe3       = 0;
            frac       = 0;
            res        = 20;
            resc       = 1000; % coarse resolution (thermodynamic domain size in um
                )
            indx       = 150:650;
            indy       = 180:680;
        else
            break
        end

    % 76 mu mapping
    elseif mapind==6
        if itexture == 1 % representative 5x5 cm domain for dm-scale
            texture    = 'dm_representative';
            XFe3       = 0;
            frac       = 0;
            res        = 76;
            resc       = 760*6.5; % coarse resolution (thermodynamic domain size in
                 um)
            indx       = 1:658;
            indy       = 1:658;
        elseif itexture == 2
            texture    = 'dm_representative_oxidized';
            XFe3       = 0.6259;
            frac       = 0;
            res        = 76;
            resc       = 760*6.5; % coarse resolution (thermodynamic domain size in
                 um)
            indx       = 1:658;
            indy       = 1:658;
        elseif itexture == 3
            texture    = 'dm_representative_fractionated';
            XFe3       = 0;
            frac       = 1;
            res        = 76;
            resc       = 760*6.5; % coarse resolution (thermodynamic domain size in
                 um)
```

```
            indx       = 1:658;
            indy       = 1:658;
        else
            break
        end

    end

% coarsening
dx                  = resc/res; % number of pixels in 1 dimension that are being merged
Cmaps_in            = ALB19.ALB05_full(mapind).maps_ele(indx,indy,:); % select a part of the entire mapping


%%
Cmaps_coarse        = coarsening_fun(Cmaps_in,dx);
Cmaps_coarse_ox     = reshape(reshape(Cmaps_coarse,[],length(el2ox)).*el2ox',size(Cmaps_coarse));
selected_area_coords = [indy(1) indx(1) indx(end)-indx(1) indy(end)-indy(1)];


% ticks
[nx , ny , ~] = size(Cmaps_coarse);
[nx2, ny2, ~] = size(Cmaps_in);  % nx2=100; ny2=100; % when outcrop
xvec_coarse   = (1:nx)*res*1e-4; % ticks in cm
yvec_coarse   = (1:ny)*res*1e-4;
tcks.tx       = 100:100:nx2;
tcks.ty       = 100:100:ny2;
tcks.txc      = 2:2:10;
tcks.tyc      = 2:2:10;


% plotting
figure(1),clf,tiledlayout(2,2),colormap(cmap)
nexttile([2,1]),imagesc(ALB19.ALB05_full(mapind).maps_ele(:,:,1)),clim([12 25]),title('Si full mapping') % full mapping
hold on
rectangle('Position',selected_area_coords)
axis image
hold off


nexttile,imagesc(Cmaps_in    (:,:,1)), axis image,clim([12 25]), title('Si selected domain') % selected region in original resolution
colorbar('location','eastoutside')
[ny,nx]=size(Cmaps_in(:,:,1));
ticks_x = 100:100:nx; xticks(ticks_x);
ticks_y = 100:100:ny; yticks(ticks_y);
xl = round(xticks*res*1e-4,3); xticklabels(xl); xlabel('cm') % x axis labels in cm
yl = round(yticks*res*1e-4,3); yticklabels(yl); ylabel('cm') % y axis labels in cm
```

```
114
115 nexttile,imagesc(Cmaps_coarse(:,:,1)), axis image,colorbar('location','eastoutside
        ') , title('Si coarse map') % coarsened
116 [ny,nx]=size(Cmaps_coarse(:,:,1));
117 ticks_x = 2:2:nx; xticks(ticks_x);
118 ticks_y = 2:2:ny; yticks(ticks_y);
119 xl = round(xticks*resc*1e-4,3); xticklabels(xl); xlabel('cm') % x axis labels in
        cm
120 yl = round(yticks*resc*1e-4,3); yticklabels(yl); ylabel('cm') % y axis labels in
        cm
121 drawnow,pause(0.1)
122
123
124 % add to existing structure
125 ALB19.ALB05_full(mapind).resc                              = resc;
126 ALB19.ALB05_full(mapind).textures.(texture).XFe3           = XFe3;
127 ALB19.ALB05_full(mapind).textures.(texture).frac           = frac;
128 ALB19.ALB05_full(mapind).textures.(texture).ticks          = tcks;
129 ALB19.ALB05_full(mapind).textures.(texture).maps_coarse    = Cmaps_coarse;
130 ALB19.ALB05_full(mapind).textures.(texture).maps_coarse_ox = Cmaps_coarse_ox;
131 ALB19.ALB05_full(mapind).textures.(texture).maps_ele       = Cmaps_in;
132 ALB19.ALB05_full(mapind).textures.(texture).indx           = indx;
133 ALB19.ALB05_full(mapind).textures.(texture).indy           = indy;
134 ALB19.ALB05_full(mapind).textures.(texture).selected_area  = selected_area_coords;
135
136     end
137 end
138
139 % save
140 save data/ALB19_dataset ALB19
141
142 %% coarsening function; average composition within given domain
143 function [mean_comp] = coarsening_fun(maps, dx)
144
145 dy = dx;
146
147 % numer of steps
148 nx = floor(size(maps,1)/dx);
149 ny = floor(size(maps,2)/dy);
150
151 % preallocate
152 mean_comp = zeros(nx,ny,size(maps,3));
153
154 % get mean composition of every section
155 for ix = 1:nx
156     for iy = 1:ny
157
158         % indices of current section
159         x_ind  = ((ix-1)*dx + 1):ix*dx;
160         y_ind  = ((iy-1)*dy + 1):iy*dy;
161
```

```
        % compositional data within this section
        data    = maps(x_ind,y_ind,:);

        % flatten and take mean
        data_f = reshape(data,[],size(maps,3));
        data_m = mean(data_f,1);

        % store into array
        mean_comp(ix,iy,:) = data_m;

        % one line mean_comp(:,ix,iy) = mean(reshape(  maps(:,((ix-1)*dx+1):ix*dx
            ,((iy-1)*dy+1):iy*dy) ,size(maps,1),[]) ,2);
    end
end
end
```

Listing B.3: a2_EDS_select_texture_areas_and_coarse.m

Assign chemical heterogeneities to outcrop mapping.

```
clear,clf,colormap(crameri('lapaz'))
load data/ALB19_dataset % load outcrop image and convert to grayscale
outcrop_rgb  = imread('data/Outcrop_data/outcrop_map_10x10_m.png');
[nx,ny,~]    = size(outcrop_rgb);
outcrop_gsc  = rgb2gray(outcrop_rgb);
outcrop_gsc  = outcrop_gsc(:);

% color of each lithology in grayscale image
cind_hzb = 255; % harzburgite color index
cind_dun = 179; % dunite color index
cind_pyx = 226; % pyroxenite color index

% mean composition for each lithology and standard deviation
%         SiO2    MgO   FeO
ele    = {'Si', 'Mg', 'Fe'}; %
mu.Hzb = [ 49    42,    9 ]; % mean harzburgite composition (oxides)
mu.Dun = [ 44    46    10 ]; % mean dunite composition (oxides)
mu.Pyx = [ 56    35     5 ]; % mean pyroxenite composition (oxides)
sigma  = [  4     4     3 ]; % standard deviation

% Preallocate
Cmaps_ox = zeros(nx*ny,length(ele));
% assign normal distributed random values // Niu et al. (2004), Fig. 1 & 2
for i = 1:length(ele)
    Cmaps_ox(outcrop_gsc==cind_hzb, i) = normrnd(mu.Hzb(i), sigma(i), length(find(
        outcrop_gsc==cind_hzb)), 1);
    Cmaps_ox(outcrop_gsc==cind_dun, i) = normrnd(mu.Dun(i), sigma(i), length(find(
        outcrop_gsc==cind_dun)), 1);
    Cmaps_ox(outcrop_gsc==cind_pyx, i) = normrnd(mu.Pyx(i), sigma(i), length(find(
        outcrop_gsc==cind_pyx)), 1);
end

```

```
% coarsening
Cmaps_ox        = reshape(Cmaps_ox,nx,ny,length(ele)); % reshape to 2D
Cmaps_ox_coarse = coarsening_fun(Cmaps_ox,nx/10);      % coarsen

%% create structure and save
ALB19.outcrop.Cmaps_ox        = Cmaps_ox;        % 1 dm resolution
ALB19.outcrop.Cmaps_ox_coarse = Cmaps_ox_coarse; % 1 m resolution
ALB19.outcrop.ele             = ele;             %
ALB19.outcrop.res             = 1e5^2;           %
% save
save data/ALB19_dataset ALB19

%% plotting
figure(1),clf,tiledlayout(2,3); colormap(crameri('lapaz'))
% original mappings
for i = 1:length(ele)
    nexttile, imagesc(Cmaps_ox(:,:,i)), axis image, colorbar,title([ele(i), ' dx = 1dm'])
end
% coarsened mappings
for i = 1:length(ele)
    nexttile, imagesc(Cmaps_ox_coarse(:,:,i)), axis image, colorbar ,title([' dx = 1m'])
end

%% coarsening function; average composition within given domain
function [mean_comp] = coarsening_fun(maps, dx)
dy = dx;
% numer of steps
nx = floor(size(maps,1)/dx);
ny = floor(size(maps,2)/dy);
% preallocate
mean_comp = zeros(nx,ny,size(maps,3));
% get mean composition of every section
for ix = 1:nx
    for iy = 1:ny
        % indices of current section
        x_ind  = ((ix-1)*dx + 1):ix*dx;
        y_ind  = ((iy-1)*dy + 1):iy*dy;
        % compositional data within this section
        data   = maps(x_ind,y_ind,:);
        % flatten and take mean
        data_f = reshape(data,[],size(maps,3));
        data_m = mean(data_f,1);
        % store into array
        mean_comp(ix,iy,:) = data_m;
        % alternative: one line
        % mean_comp(:,ix,iy) = mean(reshape(  maps(:,((ix-1)*dx+1):ix*dx ,((iy-1)*dy+1):iy*dy) ,size(maps,1),[]) ,2);
    end
end
```

```
78 end
```

Listing B.4: a3_prepare_outcrop_map.m

Thermolab code for Gibbs energy minimization and postprocessing (outcrop).

```
1  clear,clf
2  %% load
3  load atomweight, load tl_dataset,  % thermolab
4  load data/ALB19_dataset_v3
5
6  mapped_elements = {'Si','Mg','Fe'};
7
8  Cmaps_coarse    = ALB19.outcrop.Cmaps_ox_coarse;
9  Cmaps_coarse    = reshape(Cmaps_coarse(:,:,1:3),100,3);
10 Cmaps_coarse_wt = Cmaps_coarse./ALB19.ALB05_full(1).el2ox(1:3)'; % convert to
       element wt.%
11
12 tds = 1e9;
13 % input
14 sz          = 'data/mmc14/D80/N_Antilles'; % subduction zone
15 theta       = 42.4; % degree, subduction angle
16 convergence = 17.9; % km/Ma, convergence rate
17 % [T_Cel, P_GPa, ~, ~] = get_PTpath_fun(sz, theta, convergence, [200 650], 400);
18 [T_Cel, P_GPa, ~, ~] = get_PTpath_fun(sz, theta, convergence, [450 620], 200);
19 T           = T_Cel + 273.15 ; % Kelvin
20 P           = P_GPa*1e9;       % Pascal
21 XFe3   = 0;
22 Cname   = [    mapped_elements                    'H' , 'O'];
23 noxy    = [ 2   ,    1   ,  (1-XFe3)*1+XFe3*3/2, 1/2 ,  0 ]; % add oxygen for Fe ->
       stabilize magnetite
24 for ic = 1:length(Cname)
25     c_ind(ic) = find(strcmp(elements,Cname(ic)));
26 end
27 molm  = atomwt5(c_ind)*1e-3;
28 % system composition
29 Cmaps_mol        = reshape(Cmaps_coarse_wt,[],length(mapped_elements)) ./ molm(1:
       end-2)'; % convert wt.% to moles
30 Nsys0            = Cmaps_mol*1e-3; % Si, Mg, Fe
31 N_H0             = 10; % hydrogen
32 frac             = 0;
33 % phases
34 fluid    = 'H2O,tc-ds633';
35 phs_name = {'Lizardite','Antigorite','Brucite','Talc','Olivine','Orthopyroxene','
       per,tc-ds633','q,tc-ds633',fluid};
36 td       = init_thermo(phs_name,Cname,'solution_models_EF21');
37 % solution model resolutions
38 for i = 1:length(phs_name)
39     td(i).dz(:) = 1/15;
40 end
41 td(strcmp(phs_name, 'Orthopyroxene')).dz(:) = 1/15;
42 p                = props_generate(td);     % generate endmember proportions
```

```
43 options.nref     = 50; % max number of iterations 30
44 options.eps_dg   = 1e-12; % tolerance to stop iterations when difference between
       global gibbs minimimum is below this
45 options.dz_tol   = 1e-14; % tolerance to stop iterations when z window becomes
       below this
46 options.z_window = ones(size(phs_name))*0.065; % the window over which the refined
        grid is generated 0.085
47 options.dz_fact  = ones(size(phs_name))*4; % the factor to determine new dz
       spacing, the larger, the more pseudocompounds 10
48 options.ref_fact = 1.6; % the factor to control how the z_window is narrowed each
       iteration, the larger, the smaller the z window over which new grid is
       generated 2
49 options.disp_ref = 0;  % display refinement iterations
50 options.solver   = 0;
51 % preallocate
52 nPT             = length(T);
53 nX              = size(Nsys0, 1);
54 preall_dims     = [nX, nPT];
55 pc_id_all       = cell(preall_dims);
56 p_all           = cell(preall_dims);
57 alph_all        = cell(preall_dims);
58 Npc_all         = cell(preall_dims);
59 asm_id          = cell(preall_dims);
60 phase_modes     = cell(preall_dims);
61 rhos            = cell(preall_dims);
62 rhof            = cell(preall_dims);
63 cwt_solid       = cell(preall_dims);
64 Npc_cell        = cell(preall_dims);
65 Cwt_cell        = cell(preall_dims);
66 % postprocessing tolerance
67 solv_tol        = 100;
68 % Gibbs minimization
69 tic
70 parfor iX = 1:nX
71     Nsys      = [Nsys0(iX,:), N_H0, 0];
72     Nsys(end) = Nsys*noxy';
73     T_iX      = T;
74     P_iX      = P;
75     for iPT = 1:nPT
76         % minimization
77         [alph_all{iX}{iPT},Npc_all{iX}{iPT},pc_id_all{iX}{iPT},p_all{iX}{iPT}] =
               tl_minimizer(T_iX(iPT),P_iX(iPT),Nsys,phs_name,p,td,options);
78
79         % postprocessing
80         [pc_id,phi,Cwt,Npc,rho,mu,p_out,phiw] = postprocess_fun(T_iX(iPT),P_iX(iPT
               ),td,alph_all{iX}{iPT},Npc_all{iX}{iPT},molm,p_all{iX}{iPT},pc_id_all{
               iX}{iPT},phs_name,solv_tol,'CORK','S14');
81         % prepare
82         fluid_id_iPT            =  strcmp(phs_name(pc_id), fluid);
83         solid_id_iPT            = ~strcmp(phs_name(pc_id), fluid);
84         asm_id_iPT              = zeros(1, length(phs_name));
```

```
85          phase_modes_iPT         = zeros(1, length(phs_name));
86          Npc_iPT                 = zeros(length(Cname), length(phs_name));
87          asm_id_iPT(pc_id)       = pc_id;
88          phase_modes_iPT(pc_id) = phi;
89          Npc_iPT(:,pc_id)        = Npc;
90          % store results in cells
91          asm_id{iX}{iPT}         = asm_id_iPT;
92          phase_modes{iX}{iPT}    = phase_modes_iPT;
93          Cwt_solid{iX}{iPT}      = Cwt(:,solid_id_iPT)*phiw(solid_id_iPT)/sum(Cwt(:,
                solid_id_iPT)*phiw(solid_id_iPT));
94          rhos{iX}{iPT}           = rho(solid_id_iPT)'*phi(solid_id_iPT)/sum(phi(
                solid_id_iPT));
95          rhof{iX}{iPT}           = rho(fluid_id_iPT);
96          Npc_cell{iX}{iPT}       = Npc_iPT;
97          % fractionation
98          if ~isempty(find(fluid_id_iPT, 1))
99              % total moles of every component in the fluid
100             Nfluid = alph_all{iX}{iPT}(fluid_id_iPT)*Npc(:, fluid_id_iPT);
101             % update system composition
102             Nsys          = Nsys - Nfluid'*frac; % substract fluid composition from
                    system composition
103             Nsys(Nsys<0) = 0; % // should not be needed
104             Nsys(end)     = Nsys*noxy'; % oxygen correction // should not be needed
105         end
106     end
107     % output progress
108     disp([iX/nX])
109 end
110 cpu = toc
111 % create lookup tables
112 run b_create_lookup_tables.m
113 % save
114 save data/ALB19_dataset_v3 ALB19
```

Listing B.5: `b2_tl_minimizer_postprocessing_outcrop.m`

Thermolab code for Gibbs energy minimization and postprocessing (chemical mappings).

```
1  clear,clf, cnt=0;
2  %% load
3  load atomweight, load tl_dataset
4  load data/ALB19_dataset
5  %% Input
6  % consider these elements
7  mapped_elements = {'Si','Mg','Fe'};
8  % loop through all scales and textures
9  for mapind = [1 4 6]
10 textures = fieldnames(ALB19.ALB05_full(mapind).textures);
11
12 for itex = 1:length(textures)
13 texture_char = char(textures(itex))  % select texture
14
```

```
% preprocessing
XFe3   = ALB19.ALB05_full(mapind).textures.(texture_char).XFe3;
Cname  = [    mapped_elements                    'H' , 'O'];
noxy   = [ 2   ,    1   ,  (1-XFe3)*1+XFe3*3/2, 1/2 ,  0 ];
for ic = 1:length(Cname)
    c_ind(ic) = find(strcmp(elements,Cname(ic)));
end
molm      = atomwt5(c_ind)*1e-3;
% input
sz          = 'data/mmc14/D80/N_Antilles'; % subduction zone
theta       = 42.4; % degree, subduction angle (Table 3, Syracuse et al. 2010)
convergence = 17.9; % km/Ma, convergence rate  (Table 3, Syracuse et al. 2010)
[T_Cel, P_GPa, ~, ~] = get_PTpath_fun(sz, theta, convergence, [450 620], 200);
T           = T_Cel + 273.15 ; % convert to Kelvin
P           = P_GPa*1e9;       % convert to Pascal
% bulk compositions
Cmaps_coarse_wt = ALB19.ALB05_full(mapind).textures.(texture_char).maps_coarse
    (:,:,ismember(ALB19.ALB05_full(mapind).ele,mapped_elements));
Cmaps_mol = reshape(Cmaps_coarse_wt,[],length(mapped_elements)) ./ molm(1:end-2)';
     % convert wt.% to moles
Nsys0     = Cmaps_mol*1e-3; % Si, Mg, Fe
N_H0      = 10; % H
frac      = ALB19.ALB05_full(mapind).textures.(texture_char).frac;  %
    fractionation factor; 0 = nothing, 1 = all
% phases
fluid     = 'H2O,tc-ds633';
phs_name  = {'Lizardite','Antigorite','Brucite','Talc','Olivine','Orthopyroxene','
    per,tc-ds633','q,tc-ds633','mt,tc-ds633',fluid};
td        = init_thermo(phs_name,Cname,'solution_models_EF21');
% solution model resolutions
for i = 1:length(phs_name)
    td(i).dz(:) = 1/15;
end
p                = props_generate(td);     % generate endmember proportions
options.nref     = 50; % max number of iterations 30
options.eps_dg   = 1e-12; % tolerance to stop iterations when difference between
    global gibbs minimimum is below this
options.dz_tol   = 1e-14; % tolerance to stop iterations when z window becomes
    below this
options.z_window = ones(size(phs_name))*0.065; % the window over which the refined
     grid is generated 0.085
options.dz_fact  = ones(size(phs_name))*4; % the factor to determine new dz
    spacing, the larger, the more pseudocompounds 10
options.ref_fact = 1.6; % the factor to control how the z_window is narrowed each
    iteration, the larger, the smaller the z window over which new grid is
    generated 2
options.disp_ref = 0;  % display refinement iterations
options.solver   = 0;
% preallocate
nPT            = length(T);
nX             = size(Nsys0, 1);
```

```
preall_dims     = [nX, nPT];
pc_id_all       = cell(preall_dims);
p_all           = cell(preall_dims);
alph_all        = cell(preall_dims);
Npc_all         = cell(preall_dims);
asm_id          = cell(preall_dims);
phase_modes     = cell(preall_dims);
rhos            = cell(preall_dims);
rhof            = cell(preall_dims);
cwt_solid       = cell(preall_dims);
Npc_cell        = cell(preall_dims);
Cwt_solid       = cell(preall_dims);
% postprocessing tolerance
solv_tol        = 100;
% Gibbs minimization
tic
parfor iX = 1:nX
    Nsys      = [Nsys0(iX,:), N_H0, 0]; % add hydrogen to bulk composition
    Nsys(end) = Nsys*noxy';             % oxygen stochiometric
    % Nsys      = Nsys + [0 0 0 0 0.]*0.01;
    T_iX      = T;                      % temperature array
    P_iX      = P;                      % pressure array
    for iPT = 1:nPT
        % minimization
        [alph_all{iX}{iPT},Npc_all{iX}{iPT},pc_id_all{iX}{iPT},p_all{iX}{iPT}] =
            tl_minimizer(T_iX(iPT),P_iX(iPT),Nsys,phs_name,p,td,options);
        % postprocessing
        [pc_id,phi,Cwt,Npc,rho,mu,p_out,phiw] = postprocess_fun(T_iX(iPT),P_iX(iPT
            ),td,alph_all{iX}{iPT},Npc_all{iX}{iPT},molm,p_all{iX}{iPT},pc_id_all{
            iX}{iPT},phs_name,solv_tol,'CORK','S14');
        % prepare
        fluid_id_iPT           =  strcmp(phs_name(pc_id), fluid);
        solid_id_iPT           = ~strcmp(phs_name(pc_id), fluid);
        asm_id_iPT             = zeros(1, length(phs_name));
        phase_modes_iPT        = zeros(1, length(phs_name));
        Npc_iPT                = zeros(length(Cname), length(phs_name));
        asm_id_iPT(pc_id)      = pc_id;
        phase_modes_iPT(pc_id) = phi;
        Npc_iPT(:,pc_id)       = Npc;
        % store results in cellsfind(rhof{iX}(:))
        asm_id{iX}{iPT}        = asm_id_iPT;
        phase_modes{iX}{iPT}   = phase_modes_iPT;
        Cwt_solid{iX}{iPT}     = Cwt(:,solid_id_iPT)*phiw(solid_id_iPT)/sum(Cwt(:,
            solid_id_iPT)*phiw(solid_id_iPT));
        rhos{iX}{iPT}          = rho(solid_id_iPT)'*phi(solid_id_iPT)/sum(phi(
            solid_id_iPT));
        rhof{iX}{iPT}          = rho(fluid_id_iPT);
        Npc_cell{iX}{iPT}      = Npc_iPT;
        % fractionation (set frac = 1 in l. 45 to apply)
        if ~isempty(find(fluid_id_iPT, 1))
            % total moles of every component in the fluid
```

```
            N_ff = alph_all{iX}{iPT}(fluid_id_iPT)*Npc(:, fluid_id_iPT);
            % substract fluid composition from system composition
            Nsys         = Nsys - N_ff'*frac;
            Nsys(Nsys<0) = 0;
            Nsys(end) = Nsys*noxy';
        end

    end
end
% create lookup tables
disp('create lookup tables')
run b_create_lookup_tables
end
end
save data/ALB19_dataset ALB19
```

Listing B.6: `b1_tl_minimizer_postprocessing_EDS.m`

Generate lookup tables from Gibbs energy minimization results.

```
%% convert minimization results to cell arrays
% preallocate
asm_id_tab      = zeros(nX, nPT*length(phs_name));
rhos_tab        = zeros(nX, nPT);
rhof_tab        = zeros(nX, nPT);
phase_modes_tab = zeros(nX, length(phs_name)*nPT);
Cwt_solid_tab   = zeros(nX, length(Cname), nPT);
Npc_tab         = zeros(nX, length(Cname), nPT*length(phs_name));
% convert cells from minimization to matrix arrays
for iX = 1:nX
    asm_id_tab(iX,:)      = cell2mat(asm_id{iX});
    rhos_tab(iX,:)        = cell2mat(rhos{iX});
    if frac>0 % fluid might not be stable when fractionation is on
        rhof_iX = cell2mat(rhof{iX}(:));
        rhof_tab(iX,1:length(rhof_iX)) = rhof_iX;
    else
        rhof_tab{iX}      = cell2mat(rhof{iX});
    end
    phase_modes_tab(iX,:) = cell2mat(phase_modes{iX});
    Cwt_solid_tab(iX,:,:) = cell2mat(Cwt_solid{iX});
    Npc_tab(iX,:,:)       = cell2mat(Npc_cell{iX});
end
Npc_tab         = reshape(Npc_tab        , [nX, length(Cname), length(phs_name),
    nPT]);
phase_modes_tab = reshape(phase_modes_tab, [nX, length(phs_name), nPT]);

%% solid composition and stable mineral assemblage
% kick out non-stable phases and get mineral assemblage in solid
solid_id        = ~strcmp(phs_name,fluid);
vol_frac_solids = phase_modes_tab(:,solid_id,:)./sum(phase_modes_tab(:,solid_id,:)
    , 2);
stable_id       = find(sum(sum(vol_frac_solids, 1), 3) > 0);
```

```
vol_frac_solids = vol_frac_solids(:,stable_id,:);
solid_names     = phs_name(stable_id);
% XH and XO in solid
Cs_H_tab        = squeeze(Cwt_solid_tab(:,strcmp(Cname, 'H'),:));
Cs_O_tab        = squeeze(Cwt_solid_tab(:,strcmp(Cname, 'O'),:));

%% Temperature for dehydration onset // first occurence of non-hydrous phase
non_hydrous_id  = ismember(solid_names, {'Olivine'; 'Orthopyroxene'});
sum_non_hydrous_modes = squeeze(sum(vol_frac_solids(:,non_hydrous_id,:), 2));
% find index of first non-hydrous phase
ind_onset       = arrayfun(@(iX) find(sum_non_hydrous_modes(iX,:)>0, 1, 'first'),
    1:nX);
ind_ref         = ind_onset - 1; % last fully hydrated assemblage
% Temperature for dehydration onset
Tin             = T(ind_onset)-273.15;  % Celsius

%% porosity and fluid production
rhon0      = zeros(nX, 1);
FP         = zeros(nX, length(T));
phi        = zeros(nX, length(T));
phi0       = 0;
rhon       = rhos_tab.*(1-Cs_H_tab-Cs_O_tab);
for iX = 1:nX
    if frac>0
        for iPT = 2:length(T)
            rhon0 = rhon(iX, iPT-1); % previous PT as reference point
            dphidT(iX,iPT) = 1 - (rhon0*(1-phi0))./rhon(iX,iPT);
        end
        phi(iX,:) = cumsum(dphidT(iX,:));
    else
        rhon0(iX) = rhon(iX, ind_ref(iX)); % last fully hydrated assemblage
        phi(iX,:) = 1 - (rhon0(iX)*(1-phi0))./rhon(iX,:);
    end
    phi(phi<0) = 0;
    FP(iX,:) = rhof_tab(iX,:).*phi(iX,:); % kg H2O released per m3 rock
end

%% Molar #Mg = Mg/(Mg+Fe)
molar_FeMg  = squeeze(Npc_tab(:,strcmp(Cname,'Mg'),stable_id,:)./(Npc_tab(:,strcmp
    (Cname,'Mg'),stable_id,:) + Npc_tab(:,strcmp(Cname,'Fe'),stable_id,:)));
% #Mg at temperature of dehydration onset for every phase
molar_FeMg_Tin = zeros(nX, length(solid_names));
for iX = 1:nX
    molar_FeMg_Tin(iX,:) = molar_FeMg(iX,:,ind_onset(iX));
end

%% Bulk composition full system
Nsys_all        = [Nsys0, ones(nX,1)*N_H0, zeros(nX,1)];
Nsys_all(:,end) = Nsys_all*noxy';

%% add lookup tables (lut) to data structure
```

```
if exist('Cmaps_coarse', 'var') == 1
    % outcrop data
    ALB19.outcrop.lut.asm_id       = asm_id_tab;
    ALB19.outcrop.lut.Npc          = Npc_tab;
    ALB19.outcrop.lut.Cwt_solid    = Cwt_solid_tab;
    ALB19.outcrop.lut.Tin          = Tin;
    ALB19.outcrop.lut.ind_onset    = ind_onset;
    ALB19.outcrop.lut.phi          = phi;
    ALB19.outcrop.lut.XFe3         = XFe3;
    ALB19.outcrop.lut.FP           = FP;
    ALB19.outcrop.lut.stable_id    = stable_id;
    ALB19.outcrop.lut.solid_names  = solid_names;
    ALB19.outcrop.lut.solid_modes  = vol_frac_solids;
    ALB19.outcrop.lut.rhos         = rhos_tab;
    ALB19.outcrop.lut.rhof         = rhof_tab;
    ALB19.outcrop.lut.T            = T;
    ALB19.outcrop.lut.P            = P;
    ALB19.outcrop.lut.Cname        = Cname;
    ALB19.outcrop.lut.Nsys         = Nsys_all;
    ALB19.outcrop.lut.nMg_mol      = molar_FeMg;
    ALB19.outcrop.lut.nMg_mol_Tin  = molar_FeMg_Tin;

else
    % chemical mappings
    ALB19.ALB05_full(mapind).textures.(texture_char).lut.asm_id       = asm_id_tab
        ;
    ALB19.ALB05_full(mapind).textures.(texture_char).lut.Npc          = Npc_tab;
    ALB19.ALB05_full(mapind).textures.(texture_char).lut.Cwt_solid    =
        Cwt_solid_tab;
    ALB19.ALB05_full(mapind).textures.(texture_char).lut.Tin          = Tin;
    ALB19.ALB05_full(mapind).textures.(texture_char).lut.ind_onset    = ind_onset;
    ALB19.ALB05_full(mapind).textures.(texture_char).lut.phi          = phi;
    ALB19.ALB05_full(mapind).textures.(texture_char).lut.XFe3         = XFe3;
    ALB19.ALB05_full(mapind).textures.(texture_char).lut.FP           = FP;
    ALB19.ALB05_full(mapind).textures.(texture_char).lut.stable_id    = stable_id;
    ALB19.ALB05_full(mapind).textures.(texture_char).lut.solid_names  =
        solid_names;
    ALB19.ALB05_full(mapind).textures.(texture_char).lut.solid_modes  =
        vol_frac_solids;
    ALB19.ALB05_full(mapind).textures.(texture_char).lut.rhos         = rhos_tab;
    ALB19.ALB05_full(mapind).textures.(texture_char).lut.rhof         = rhof_tab;
    ALB19.ALB05_full(mapind).textures.(texture_char).lut.T            = T;
    ALB19.ALB05_full(mapind).textures.(texture_char).lut.P            = P;
    ALB19.ALB05_full(mapind).textures.(texture_char).lut.Cname        = Cname;
    ALB19.ALB05_full(mapind).textures.(texture_char).lut.Nsys         = Nsys_all;
    ALB19.ALB05_full(mapind).textures.(texture_char).lut.nMg_mol      = molar_FeMg
        ;
    ALB19.ALB05_full(mapind).textures.(texture_char).lut.nMg_mol_Tin  =
        molar_FeMg_Tin;
end
```

Listing B.7: b_create_lookup_tables.m

Generate a P-T path from Supplementary Information of

```
% returns temperature T (C), pressure P (GPa), depth z (km) and time (Ma)
% for a subduction zone (sz_name) with a subduction angle theta from the
% compilation of Syracuse et al. (2010).
% [T, P_GPa, z_km, t_Ma] = get_PTpath_fun(sz_name, theta, con_rate, range, nPT)
% Specify a (temperature) range to select only parts of the P-T path.
% Use nPT to set the resolution using interp1
% [T, P_GPa, z_km, t_Ma] = get_PTpath_fun(sz_name, theta, con_rate, [], [])
% returns the full range in the resolution set by the supplementary data of
% Syracuse et al. (2010)
function [T, P_GPa, z_km, t_Ma] = get_PTpath_fun(sz_name, theta, con_rate, range,
    nPT)
% constants for unit conversion
a2s     = 60*60*24*365; % years to seconds
% cma2ms  = 1e-2/a2s;     % cm/a to m/s
kmMa2ms = 1e3/(a2s*1e6);
s2Ma    = 1e-6/a2s;  % seconds to million years
% load data and consider Moho data only
d       = load([sz_name '.txt']);
d_moho = d(d(:,1)==7, :, :, :); % Moho data
% retrieve temperature and calculate lithostatic pressure P
rho     = 3300;                 % mantle density (kg/m3)
g       = 9.81;                 % gravitational constant (m/s2)
depth   = d_moho(:,3)*1e3;      % depth (m)
P       = depth*rho*g;          % pressure (Pa)
T       = d_moho(:,4);          % temperature (deg. Celsius)
%
if exist('range','var') == 1
    inds = range(1)<T & T<range(2); % set desired range of P-T path
    T     = T(inds);
    P     = P(inds);
    depth = depth(inds);
end
nT = length(T);
if exist('nPT','var') == 1
    P     = interp1(1:nT, P    , linspace(1,nT, nPT));
    depth = interp1(1:nT, depth, linspace(1,nT, nPT));
    T     = interp1(1:nT, T    , linspace(1,nT, nPT));
end
dP   = diff(P);
dzdt = con_rate*kmMa2ms*sind(theta); % m/s
dPdt = dzdt * rho * g; % Pa/s
dt   = dP/dPdt;  % s
t    = cumsum(dt); % time integral, Ma
% convert
t_Ma    = t*s2Ma; % convert to Ma
P_GPa   = P*1e-9; % convert to GPa
```

```
z_km     = depth*1e-3;

% dphidt = diff(d.lut.phi,1,2)./dt; % 1/s
% depth2  = dzdt*t; % m, alternative way to calculate depth
```

Listing B.8: `get_PTpath_fun.m`

References

F. Crameri. Scientific colour maps. Zenodo, 2023.

K. A. Evans and B. R. Frost. Deserpentinization in Subduction Zones as a Source of Oxidation in Arcs: A Reality Check. *J. Petrol.*, 62(3):egab016, 2021. ISSN 0022-3530, 1460-2415. doi:10.1093/petrology/egab016.

T. J. B. Holland, E. C. R. Green, and R. Powell. Melting of Peridotites through to Granites: A Simple Thermodynamic Model in the System KNCFMASHTOCr. *Journal of Petrology*, 59(5):881–900, 2018. ISSN 0022-3530. doi:10.1093/petrology/egy048.

K. Huber. Data, multiscale dataset and supplementary information for 'Pulsed fluid release from subducting slabs caused by a scale-invariant dehydration process', 2023.

E. M. Syracuse, P. E. van Keken, and G. A. Abers. The global range of subduction zone thermal models. *Physics of the Earth and Planetary Interiors*, 183(1):73–90, 2010. ISSN 0031-9201. doi:10.1016/j.pepi.2010.02.004.

J. C. Vrijmoed and Y. Y. Podladchikov. Thermolab: A Thermodynamics Laboratory for Nonlinear Transport Processes in Open Systems. *Geochem. Geophys. Geosystems*, 23(4):e2021GC010303, 2022. ISSN 1525-2027. doi:10.1029/2021GC010303.

Appendix C

MATLAB Codes and Supporting Material for Chapter 6

MATLAB Codes

1D Reactive Porosity Wave Model

```
clear all, figure(1), clf, colormap jet
load lookup_tables
count       = 0;
rhof0       = rhof_tab(2,1,1,1);
rhos_tab    = rhos_tab/rhof0;
rhof_tab    = rhof_tab/rhof0;
Ly_Lc       = 50;
P0          = P_4d(1,1,1,1);
P_4d        = P_4d/P0*Ly_Lc;
%% Physics
% dimentionally independent
k_mu        = 1e0;   % [m2/Pa/s] Permeability/fluid viscosity
eta_phi0    = 1e0;   % [Pa*s] bulk viscosity
rhos0g      = 1e0;   % [Pa/m] rho*g
% dimensionless
phi0        = 0.05;  % background porosity
phia        = 1.5;   % amplitude of anomaly
npow        = 3;     % Cozeny-Carman exponent
R           = 1e1;   % decompaction weakening
% useful dep shorcuts
Lc0         = sqrt(k_mu*eta_phi0); % [m]
Pc          = rhos0g*Lc0; % [Pa]
timec       = Pc/k_mu/rhos0g/rhos0g*phi0; % [s] Pc[Pa]/k_mu[m2/Pa/s]/rhos0g[Pa/m]/
    rhos0g[Pa/m]
% dimentionally dependent
dT          = 100;        % [deg C] temperature
```

```
g           = rhos0g/rhos_tab(1,1,1,1);
Ly          = Ly_Lc*Lc0;  % [m] y length
lam         = 15*Lc0;     % wave lenght
yc          = -Ly;        % location of the perturbation
tt          = 6e5*timec;  % number of time steps
relk        = 1*(1 - 5e-2);
rele        = 1*(1 - 5e-2);
% numerics
ny          = 100;  % dimless
nout        = 10;   % dimless
niter       = 1e4;  % dimless
err         = 1e-2; % dimless
count       = 0;
CFL         = 0.99; % Courant-Friedrichs-Lewy criterion
CFL2        = 1e-1; % Courant-Friedrichs-Lewy criterion
w           = pi/Ly;
% Preprocessing
dy          = Ly/(ny-1); % [m] y grid spacing
y           = -Ly:dy:0;  % [m] y vector
% Initial conditions
Pt          = (min(P_4d(:))+max(P_4d(:)))/2 + (min(P_4d(:))-max(P_4d(:)))/5/Ly*y;
    % [Pa] lithostatic pressure; Pt=Pf*phi+Ps*(1-phi)
Pf          = Pt;      % [Pa] lithostatic pressure
Pe          = Pf - Pt; % [Pa] effective pressure
qy          = 0*diff(Pe); % Darcy flux
phi         = phi0*(1+phia*exp( -( (y-yc)/lam ).^2 )); % porosity anomaly
eta_phi     = eta_phi0*ones(size(Pe)); % viscosity
k_etaf      = k_mu*(phi/phi0).^npow;   % permeability/viscosity
time        = 0;
Volume      = ones(size(phi));      % volume
qye         = zeros(1,ny+1);
Vye         = zeros(1,ny+1);
phi_0       = phi;                  % initial porosity
Pe0         = Pe;
qy0         = qy;
CtSiO2      = 0.46*ones(size(phi)); % bulk SiO2 composition
CtMgO       = 0.35*ones(size(phi)); % bulk MgO composition
Temp        = 500-50/Ly*y;          % initial temperature
% interpolate thermodynamic closure relationships from lookup tables
CfSiO2      = interpn(CsysSiO2_4d,CsysMgO_4d,P_4d,T_4d,Cf_SiO2_tab,CtSiO2,CtMgO,Pe
    +Pt,Temp);
CsSiO2      = interpn(CsysSiO2_4d,CsysMgO_4d,P_4d,T_4d,Cs_SiO2_tab,CtSiO2,CtMgO,Pe
    +Pt,Temp);
CfSiO20     = CfSiO2;
CsSiO20     = CsSiO2;
% action
it = 0;
while time <= tt
    it       = it + 1;
    % physical process
    phi_old    = phi;    % porosity from previous timestep
```

```
74      Volume_old = Volume; % volume from previous timestep
75      % boundary condition
76      CtSiO2(1:1) = 0.3;
77      % interpolate from lookup table
78      CfSiO2  = interpn(CsysSiO2_4d, CsysMgO_4d, P_4d, T_4d, Cf_SiO2_tab, CtSiO2,
            CtMgO, Pe+Pt, Temp);
79      CsFeO   = interpn(CsysSiO2_4d, CsysMgO_4d, P_4d, T_4d, Cs_FeO_tab , CtSiO2,
            CtMgO, Pe+Pt, Temp);
80      CsMgO   = interpn(CsysSiO2_4d, CsysMgO_4d, P_4d, T_4d, Cs_MgO_tab , CtSiO2,
            CtMgO, Pe+Pt, Temp);
81      CsSiO2  = interpn(CsysSiO2_4d, CsysMgO_4d, P_4d, T_4d, Cs_SiO2_tab, CtSiO2,
            CtMgO, Pe+Pt, Temp);
82      rhos    = interpn(CsysSiO2_4d, CsysMgO_4d, P_4d, T_4d, rhos_tab   , CtSiO2,
            CtMgO, Pe+Pt, Temp);
83      rhof    = interpn(CsysSiO2_4d, CsysMgO_4d, P_4d, T_4d, rhof_tab   , CtSiO2,
            CtMgO, Pe+Pt, Temp);
84      for iter = 1:niter %iter
85          % Update for iterations
86          Pe_old       = Pe;
87          qy_old       = qy;
88          eta_phi_old  = eta_phi;
89          k_etaf_old   = k_etaf;
90          % porosity
91          if it == 1
92              phirhoCsim0    = (1 - phi).*rhos.*(CsMgO+CsFeO).*Volume;
93              phirhoCsimMgO0 = (1 - phi).*rhos.* CsMgO       .*Volume;
94          end
95          phi    = 1 - phirhoCsim0./(Volume.*(CsMgO+CsFeO).*rhos);
96          CtMgO  = phirhoCsimMgO0./(Volume.*(1-phi).*rhos);
97          % all properties
98          lam_p    = ( 1e-4 + (it==1)*1e-1 )*Pc;
99          Rsmooth  = (1 + 0.5*(1/R-1)*(1+tanh(Pe/lam_p)));
100         eta_phi  = exp((1-rele)*log( eta_phi0*(phi0./phi).*Rsmooth) + rele*log(
                eta_phi));
101         k_etaf   = exp((1-relk)*log(     k_mu*(phi /phi0).^npow    ) + relk*log(
                k_etaf ));
102         % solid divergence
103         divVs    = Pe./eta_phi ;
104         % times
105         dt_phys  = CFL2*min(phi./(1e-20+abs(divVs))); % CFL - physical time for
                phi//compaction time step
106         % local and optimal
107         dmp1        = 1./(1./eta_phi); %eta_phi;
108         dmp2        = k_etaf;
109         Damp        = -1+sqrt(1+1./sqrt(precond_max(dmp2.*dmp1)).^2/w^2);
110         De_opt      = (1+2./Damp);
111         tau1_dt     = 1./sqrt(De_opt)./sqrt(Damp+2)./sqrt(Damp)./w./dmp1/dy/CFL;
112         tau2_dt     = 1/(CFL*dy)^2./tau1_dt;
113         % Volume
114         Volume      = exp(log(Volume_old) + dt_phys*divVs);
115         % fluid momentum
```

```
        dqy          = -qy - (diff(Pe)/dy - av(rhos-rhof)*g).*av(dmp2);
        qy           = qy + dqy./(1+av(dmp2).*av(tau2_dt));
        % solid and fluid mass conservation
        dPe          = -Pe(2:end-1) - diff(qy)/dy.*dmp1(2:end-1);
        Pe(2:end-1) =  Pe(2:end-1) + dPe./(1+dmp1(2:end-1).*tau1_dt(2:end-1));
        % errors
        errPe        = max(abs(Pe-Pe_old))/(1e-20+max(abs(Pe)));
        errqy        = max(abs(qy-qy_old))/(1e-20+max(abs(qy)));
        % break condition
        if max(abs([errPe;errqy]))<err && iter>2,break,end
        if max(abs([errPe;errqy]))<err && iter>2,break,end
    end % iter
    iters(it) = iter;
    % Concentrations
    rhot  = rhof.*phi + rhos.*(1-phi); % total density
    Dm    = 1e-6;
    qye(2:end-1)    = 1e1*qy; % effective Darcy flux
    Vye(2:end-1)    = av(cumsum(divVs));
    dCtdt           = 1*diff(av(rhof.*phi).*Dm.*diff(CfSiO2)/dy)/dy...
        -             1*rhof(2:end-1).*Vgrad(CfSiO2,qye,dy)...
        -             0*rhot(2:end-1).*Vgrad(CtSiO2,Vye,dy);
    CtSiO2(2:end-1) = (CtSiO2(2:end-1).*rhot(2:end-1) + dCtdt*dt_phys)./rhot(2:end
        -1);
    time     = time + dt_phys;
    nits(it) = iter;
    if mod(it,nout)==0
        count = count + 1;
        % interpolate phase modes
        for iph=1:size(modes_tab,5)
            phi_phases(:,:,iph) = interpn(CsysSiO2_4d,CsysMgO_4d,P_4d,T_4d,squeeze
                (modes_tab(:,:,:,:,iph)),CtSiO2,CtMgO,Pe+Pt,Temp);
        end
        stable_id = sum(squeeze(phi_phases),1)>0;

        % create figure
        figure(1), clf, tiledlayout(2,3,'tilespacing','tight'),
        set(gca,'fontsize',10),

        % porosity
        nexttile, plot(phi,y, 'b', phi_0,y, 'k--'),
        title('Porosity'),xlabel(''),ylabel('y/Lc'),axis tight, grid on,
        xlabel('vol. frac.'), legend('','Initial')
        % effective and total pressure
        nexttile, plot((Pe+Pt)*P0/Ly_Lc,y, 'b',(Pe0+Pt)*P0/Ly_Lc,y,'k--'),
        title('Pressures'),xlabel(''),axis tight, grid on, legend('P_f','P_{total}
            '), xlabel('GPa')
        % fluid and solid compositions
        nexttile,
        plot(CtSiO2,y,'r-', CfSiO2*1e2,y, 'b',CsSiO2,y, 'k--', CsFeO,y,'r--',
            CsMgO,y,'m--'),
        xlabel('wt. frac.'), grid on, title('Solid and Fluid Compositions'),
```

```
        legend('C^t_{SiO2}','C^f_{SiO2}*1e2','C^s_{SiO2}', 'C^s_{FeO}', 'C^s_{MgO}
            ','location','north')
        % fluid and solid densities
        nexttile, plot(rhof*rhof0*3,y, 'b',rhos*rhof0,y, 'k'),
        xlabel('kg/m3'), grid on
        % temperature
        nexttile, plot(Temp,y, 'b'),
        title('Temperature'), xlabel('deg C'),axis tight, grid on

        % output time
        time/timec
    end
end
%% functions
function F_av = av(F)
F_av = (F(1:end-1) + F(2:end))/2;
end
function A_exp = expy(A)
A_exp = [A(1),A,A(end)];
end
function Ap = precond_max(A)
Ap     = A;
Ap     = max(Ap(1:end-1),Ap(2:end));
Ap     = max(Ap(1:end-1),Ap(2:end));
Ap     = expy(Ap);
end
function Ap = precond_min(A)
Ap     = A;
Ap     = min(Ap(1:end-1),Ap(2:end));
Ap     = min(Ap(1:end-1),Ap(2:end));
Ap     = expy(Ap);
end
function  dT = Vgrad(T,Vy,dy)
dT                    =(max(0,Vy(2:end-2)).*diff(T(1:end-1))/dy ...
    +                  min(0,Vy(3:end-1)).*diff(T(2:end  ))/dy);
end
```

Listing C.1: HmC_PW_1D.m

2D Reactive Porosity Wave Model

```
clear; figure(1); clf; colormap jet
load lookup_tables % lookup tables
rhof0    = rhof_tab(2,1,1,1); % reference value
rhos_tab = rhos_tab/rhof0;    % rescale solid density
rhof_tab = rhof_tab/rhof0;    % rescale fluid density
P0       = P_4d(1,1,1,1);     % reference value
Ly_Lc    = 100;               % rescaling factor
P_4d     = P_4d/P0*Ly_Lc;     % rescale
```

```
%% Physics
% dimentionally independent
k_mu      = 1e0;                    % [m2/Pa/s] permeability/fluid viscosity
eta_phi0  = 1e0;                    % [Pa*s]    bulk viscosity
rhos0g    = 1e0;                    % [Pa/m]    rho*g
% dimensionless
phi0      = 0.1;                    % [vol. frac.] background porosity
phia      = 3;                      %              amplitude of anomaly
npow      = 3;                      % Cozeny-Carman exponent
R         = 5e1;                    % decompaction weakening
Lx_Ly     = 1/2;                    % x/y length ratio
% useful scales
Lc0       = sqrt(k_mu*eta_phi0);    % [m]
Pc        = rhos0g*Lc0;             % [Pa]
timec     = Pc/k_mu/rhos0g/rhos0g*phi0;
% dimensionally dependent
dT        = 100;                    % [degC] temperature
g         = rhos0g/rhos_tab(1,1,1,1); % gravity
Ly        = Ly_Lc*Lc0;     % [m] y length
Lx        = Lx_Ly*Ly;      % [m] x length
lam       = 10*Lc0;        % wave length
yc        = -Ly;           % [m] y centered
xc        = 0*Lx;          % [m] x centered
tt        = 6e5*timec;     % total number of time steps
CFL       = 0.99;          % Courant-Friedrichs-Lewy criterion
CFL2      = 1e-1/2;        % Courant-Friedrichs-Lewy criterion
w         = pi/Ly;
relk      = 1*(1 - 5e-2); % relaxation parameter
rele      = 1*(1 - 5e-2); % relaxation parameter
%% numerics
ny        = 101;            % number of y gridpoints
nx        = fix(Lx_Ly*ny); % number of x gridpoints
nout      = 10;             % output (dimless)
niter     = 1e4;            % maximum number of iterations (dimless)
err       = 1e-3;           % convergence limit (dimless)
count     = 0;              % counter
%% preprocessing
dx       = Lx/(nx-1);       % x spacing
dy       = Ly/(ny-1);       % y spacing
[x,y]    = ndgrid(-Lx/2:dx:Lx/2,-Ly:dy:0); % grid
%% initial conditions
Pt       = zeros(nx, ny);  % preallocate total pressure
Pt       = (min(P_4d(:))+max(P_4d(:)))/1.5 + (min(P_4d(:))-max(P_4d(:)))/5/Ly*y;
Pf       = Pt;                % fluid pressure
Pe       = Pf - Pt;           % [Pa] effective pressure
% preallocation
qx       = 0*diff(Pe,1,1);    % Darcy flux (x-direction)
qy       = 0*diff(Pe,1,2);    % Darcy flux (y-direction)
qxe      = zeros(nx+1,ny  );  % effective Darcy flux
qye      = zeros(nx  ,ny+1);  % effective Darcy flux
Vxe      = zeros(nx+1,ny  );
```

```
Vye      = zeros(nx   ,ny+1);
% chemo
% from chemical mappings [scale=[1:6], x_indices, y_indices]
[CtSiO2r, CtMgOr, CtFeOr] = get_initial_comps(1, [2:nx+2], [2:ny+2]);
CtSiO2   = CtSiO2r(2:end,2:end);
CtMgO    = CtMgOr(2:end,2:end) ;
CtMgO(CtMgO<1e-2) = 1e-2; CtMgO(CtMgO>0.40) = 0.40;
CtSiO2(CtSiO2>0.55) = 0.55; %CtSiO2(CtSiO2<1e-2) = 1e-2;
% pre-defined
% CtMgO    = ones(nx,ny)*0.35;       % initial bulk MgO content
% CtSiO2   = ones(nx,ny)*0.50;       % initial bulk SiO2 content
% CtFeO    = ones(nx,ny)*0.15;       % initial bulk FeO content
Temp     = 500-50/Ly*y;              % initial temperature
% interpolate thermodynamic closure relationships from lookup tables
CfSiO2   = interpn(CsysSiO2_4d, CsysMgO_4d, P_4d, T_4d, Cf_SiO2_tab, CtSiO2, CtMgO,
     Pe+Pt, Temp);
CsFeO    = interpn(CsysSiO2_4d, CsysMgO_4d, P_4d, T_4d, Cs_FeO_tab , CtSiO2, CtMgO,
     Pe+Pt, Temp);
CsMgO    = interpn(CsysSiO2_4d, CsysMgO_4d, P_4d, T_4d, Cs_MgO_tab , CtSiO2, CtMgO,
     Pe+Pt, Temp);
CsSiO2   = interpn(CsysSiO2_4d, CsysMgO_4d, P_4d, T_4d, Cs_SiO2_tab, CtSiO2, CtMgO,
     Pe+Pt, Temp);
rhos     = interpn(CsysSiO2_4d, CsysMgO_4d, P_4d, T_4d, rhos_tab    , CtSiO2, CtMgO,
     Pe+Pt, Temp);
rhof     = interpn(CsysSiO2_4d, CsysMgO_4d, P_4d, T_4d, rhof_tab    , CtSiO2, CtMgO,
     Pe+Pt, Temp);
Dm       = 1e-6;
Pec      = 1;
Volume   = ones(size(Pt));         % initial volume
phirhoCsim0 = phi0*rhos.*(CsMgO+CsFeO).*Volume; % non-volatile density
phi      = 1 - phirhoCsim0./(Volume.*(CsMgO+CsFeO).*rhos); % initial porosity
phi      = phi0*(1+phia*exp(-((x-xc)/lam ).^2 -((y-yc)/lam ).^2)); % porosity
    anomaly
k_etaf   = k_mu*(phi/phi0).^npow; % permeability factor
eta_phi  = ones(nx, ny)*eta_phi0; % preallocate
it1      = 1;                      % first timestep
time     = 0;                      % time
nt       = 1000000;                % total number of timesteps
phi_ini  = phi(fix(ny/2),:);       % initial vertical porosity profile
Pe_ini   = Pe(fix(ny/2),:);        % initial vertical effective pressure
it       = 0;                      % timestep
indl     = [ny-10:ny];             % indices
ind      = [1:ny-20];              % indices
%% ACTION
while time <= tt
    it = it + 1; % time
    %% store old
    phi_old      = phi;     % porosity from previous timestep
    Volume_old   = Volume;  % volume from previous timestep
    % low SiO2 at bottom boundary
    CtSiO2(:,1) = 0.3;
```

```
104     % interpolate from lookup tables
105     CfSiO2 = interpn(CsysSiO2_4d, CsysMgO_4d, P_4d,T_4d, Cf_SiO2_tab, CtSiO2,
            CtMgO, Pe+Pt, Temp);
106     CsFeO  = interpn(CsysSiO2_4d, CsysMgO_4d, P_4d,T_4d, Cs_FeO_tab , CtSiO2,
            CtMgO, Pe+Pt, Temp);
107     CsMgO  = interpn(CsysSiO2_4d, CsysMgO_4d, P_4d,T_4d, Cs_MgO_tab , CtSiO2,
            CtMgO, Pe+Pt, Temp);
108     CsSiO2 = interpn(CsysSiO2_4d, CsysMgO_4d, P_4d,T_4d, Cs_SiO2_tab, CtSiO2,
            CtMgO, Pe+Pt, Temp);
109     rhos   = interpn(CsysSiO2_4d, CsysMgO_4d, P_4d,T_4d, rhos_tab   , CtSiO2,
            CtMgO, Pe+Pt, Temp);
110     rhof   = interpn(CsysSiO2_4d, CsysMgO_4d, P_4d,T_4d, rhof_tab   , CtSiO2,
            CtMgO, Pe+Pt, Temp);
111     %% iter
112     for iter = 1:niter
113         Pe_old      = Pe;
114         qy_old      = qy;
115         qx_old      = qx;
116         eta_phi_old = eta_phi;
117         k_etaf_old  = k_etaf;
118         % porosity
119         if it == 1 % first timestep
120             phirhoCsim0    = (1 - phi).*rhos.*(CsMgO+CsFeO).*Volume;
121             phirhoCsimMgO0 = (1 - phi).*rhos.* CsMgO       .*Volume;
122         end
123         phi           = 1 - phirhoCsim0./(Volume.*(CsMgO+CsFeO).*rhos);
124         phi(:,indl)   = exp((1-relk)*log(phi(:,indl)) + relk*log(phi0));
125         phi(phi>0.99) = 0.99;
126         CtMgO         = phirhoCsimMgO0./(Volume.*(1-phi).*rhos);
127         % all properties
128         lam_p   = ( 1e-4 + (it==1)*1e-1 )*Pc;
129         Rsmooth = (1 + 0.5*(1/R-1)*(1+tanh(Pe/lam_p)));
130         eta_phi = exp((1-rele)*log( eta_phi0*(phi0./phi).*Rsmooth) + rele*log(
                eta_phi));
131         k_etaf  = exp((1-relk)*log(     k_mu*(phi /phi0).^npow   ) + relk*log(
                k_etaf ));
132         % solid divergence
133         divVs   = Pe./eta_phi;
134         % times CFL; physical time for phi;  compaction time step
135         dt_phys = CFL2*min(min(phi./(1e-20+abs(divVs))));
136         % local and optimal
137         dmp1    = eta_phi;
138         dmp2    = k_etaf;
139         Damp    = -1+sqrt(1+1./sqrt(precond_max(dmp2).*precond_max(dmp1)).^2/w^2);
140         De_opt  = (1+2./Damp);
141         tau1_dt = 1./sqrt(De_opt)./sqrt(Damp+2)./sqrt(Damp)./w./precond_max(dmp1)/
                dy/CFL;
142         tau2_dt = 1/(CFL*dy)^2./tau1_dt*2; % ! factor 2 in 2D !
143         % Volume
144         Volume  = exp(log(Volume_old) + dt_phys*divVs);
145         % Fluid momentum
```

```
146         dqx      = -qx - (diff(Pe,1,1)/dx).*avx(dmp2);
147         qx       =  qx + dqx./(1+avx(dmp2).*avx(tau2_dt));
148         dqy      = -qy - (diff(Pe,1,2)/dy - avy(rhos-rhof)*g).*avy(dmp2);
149         qy       =  qy + dqy./(1+avy(dmp2).*avy(tau2_dt));
150         % solid and fluid mass conservation
151         dPe      = -Pe(2:end-1,2:end-1) - (diff(qx(:,2:end-1),1,1)/dx + diff(qy(2:
                end-1,:),1,2)/dy).*dmp1(2:end-1,2:end-1);
152         Pe(2:end-1,2:end-1) =  Pe(2:end-1,2:end-1) + dPe./(1+dmp1(2:end-1,2:end-1)
                .*tau1_dt(2:end-1,2:end-1));
153         Pe(:, [end])    = 0; % top boundary
154         Pe([1 end], :) = 0; % left and right boundaries
155         % errors
156         errPe    = max(abs(dPe))/(1e-20+max(abs(Pe(2:end-1,2:end-1))));
157         errqy    = max(abs(dqy))/(1e-20+max(abs(qy)));
158         if max(abs([errPe;errqy]))<err && iter>2, break, end
159         if sum(isnan(Pe(:))) > 0, disp('break'), break, end
160     end
161     %% store
162     rhot = rhof.*phi + rhos.*(1-phi);
163     if iter == 1, rhot_old = rhot; Ct_old = CtSiO2;end
164     Pec  = 5e1;
165     Dm   = 1e-6;
166     qxe(2:end-1,:) = qx*Pec;
167     qye(:,2:end-1) = qy*Pec;
168     Vxe(2:end-1,:) = avx(cumsum(divVs,1));
169     Vye(:,2:end-1) = avy(cumsum(divVs,2));
170     dCtdt = 0*diff(avx(rhof(:,2:end-1).*phi(:,2:end-1)).*Dm.*diff(CfSiO2(:,2:end
            -1),1,1)/dx,1,1)/dx ...
171         +   0*diff(avy(rhof(2:end-1,:).*phi(2:end-1,:)).*Dm.*diff(CfSiO2(2:end
                -1,:),1,2)/dy,1,2)/dy...
172         -   1*rhof(2:end-1,2:end-1).*Vgrad(CfSiO2,qxe,qye,dx,dy)...
173         -   0*rhot(2:end-1,2:end-1).*Vgrad(CtSiO2,0*Vxe,Vye,dx,dy);
174     CtSiO2(2:end-1,2:end-1) = (CtSiO2(2:end-1,2:end-1).*rhot(2:end-1,2:end-1) +
            dCtdt*dt_phys)./rhot(2:end-1,2:end-1);
175     time     = time + dt_phys;
176     nits(it) = iter;
177     %% postprocessing
178     if mod(it,nout) == 0
179     y1d = y(fix(nx/2), ind);
180     % interpolate phase modes
181     figure(1), clf
182     phi_phases = zeros(nx, ny, size(modes_tab, 5)); % preallocate
183     for iph = 1:size(modes_tab,5) % interpolate phase modes
184         phi_phases(:,:,iph) = interpn(CsysSiO2_4d,CsysMgO_4d,P_4d,T_4d,squeeze(
                modes_tab(:,:,:,:,iph)),CtSiO2,CtMgO,Pe+Pt,Temp);
185     end
186     % porosity
187     nexttile, pcolor(x(:,ind),y(:,ind),phi(:,ind)),
188     shading flat,colorbar,axis image, title('phi')
189     % effective pressure
190     nexttile, pcolor(x(:,ind),y(:,ind),Pe (:,ind)),
```

```
    shading flat,colorbar,axis image, title('Pe')
    % vertical mineral assemblage profile
    nexttile, area(y1d,squeeze(phi_phases(fix(nx/2), ind, :))),
    camroll(90) , ylim([0 1]), xlim([-Ly 0]), legend(solid_names,'Location','best'
        ), ylabel('Vol frac []'), title('Phases'), axis tight
    % temperature
    nexttile, pcolor(x(:,ind), y(:,ind), Temp(:,ind)),
    shading flat, axis image, colorbar, title('Temperature')
    % phase modes
    for iph = find(ismember(solid_names, {'Olivine','Orthopyroxene', 'Antigorite',
         'Talc'}))
        nexttile, pcolor(x(:,ind),y(:,ind),squeeze(phi_phases(:,ind, iph))),
            shading flat, title(solid_names(iph)), colorbar, axis image
    end
    % fluid and solid compositions
    nexttile, pcolor(x(:,ind),y(:,ind),CfSiO2(:,ind));
    shading flat,colorbar,axis image; title('CfSiO2')
    nexttile, pcolor(x(:,ind),y(:,ind),CsSiO2(:,ind));
    shading flat,colorbar,axis image; title('CsSiO2')
    nexttile, pcolor(x(:,ind),y(:,ind),CsMgO (:,ind));
    shading flat,colorbar,axis image; title('CsMgO')
    nexttile, pcolor(x(:,ind),y(:,ind),CsFeO (:,ind));
    shading flat,colorbar,axis image; title('CsFeO')
    % output timestep and number of iterations
    disp([it iter])
    end
end
%% functions
function A_av = av4(A)
   A_av = 0.25 * (A(1:end - 1, 1:end - 1) ...
      + A(1:end - 1, 2:end) ...
      + A(2:end, 1:end - 1) ...
      + A(2:end, 2:end));
end

function A_av = avx(A)
   A_av = 0.5 * (A(1:end - 1, :) + A(2:end, :));
end

function A_av = avy(A)
   A_av = 0.5 * (A(:, 1:end - 1) + A(:, 2:end));
end
function Ap = precond(A)
   Ap = A;
   Ap = max(max(max(Ap(1:end - 1, 1:end - 1), Ap(1:end - 1, 2:end)) ...
      , Ap(2:end, 1:end - 1)), Ap(2:end, 2:end));
   Ap = max(max(max(Ap(1:end - 1, 1:end - 1), Ap(1:end - 1, 2:end)) ...
      , Ap(2:end, 1:end - 1)), Ap(2:end, 2:end));
   Ap = expx(expy(Ap));
end
function A_exp = expx(A)
```

```
239     A_exp = [A(1, :); A; A(end, :)];
240 end
241 function A_exp = expy(A)
242     A_exp = [A(:, 1), A, A(:, end)];
243 end
244 function P = LF(P, LFP)
245     npow = 4;
246     Pmax = max(P(:));
247     P = P / Pmax;
248     laplP = zeros(size(P));
249     laplP(2:end - 1, 2:end - 1) = diff(P(:, 2:end - 1) .^ npow / npow, 2, 1) ...
250         + diff(P(2:end - 1, :) .^ npow / npow, 2, 2);
251     P = P + LFP * laplP;
252     P(:, [1 end]) = 1 * P(:, [2 (end - 1)]);
253     P([1 end], :) = 1 * P([2 (end - 1)], :);
254     P = P * Pmax;
255 end
256 function  T = adv(Told,T,Vx,Vy,dx,dy,dt)
257 dTdt                =-(max(0,Vx(2:end-2,2:end-1)).*diff(T(1:end-1,2:end-1),1,1)/
        dx ...
258     +                   min(0,Vx(3:end-1,2:end-1)).*diff(T(2:end  ,2:end-1),1,1)/
            dx ...
259     +                   max(0,Vy(2:end-1,2:end-2)).*diff(T(2:end-1,1:end-1),1,2)/
            dy ...
260     +                   min(0,Vy(2:end-1,3:end-1)).*diff(T(2:end-1,2:end  ),1,2)/
            dy);
261 T(2:end-1,2:end-1)   = Told(2:end-1,2:end-1)  + dTdt*dt;
262 end
263 function  dT = Vgrad(T,Vx,Vy,dx,dy)
264 dT                    =(max(0,Vx(2:end-2,2:end-1)).*diff(T(1:end-1,2:end-1),1,1)/
        dx ...
265     +                   min(0,Vx(3:end-1,2:end-1)).*diff(T(2:end  ,2:end-1),1,1)/
            dx ...
266     +                   max(0,Vy(2:end-1,2:end-2)).*diff(T(2:end-1,1:end-1),1,2)/
            dy ...
267     +                   min(0,Vy(2:end-1,3:end-1)).*diff(T(2:end-1,2:end  ),1,2)/
            dy);
268 end
269 function Ap = precond_max(A)
270 Ap      = A;
271 Ap      = max(max(max(Ap(1:end-1,1:end-1) ,Ap(1:end-1,2:end)) ...
272     ,             Ap(2:end  ,1:end-1)),Ap(2:end  ,2:end));
273 Ap      = max(max(max(Ap(1:end-1,1:end-1) ,Ap(1:end-1,2:end)) ...
274     ,             Ap(2:end  ,1:end-1)),Ap(2:end  ,2:end));
275 Ap      = expx(expy(Ap));
276 end
277 function Ap = precond_min(A)
278 Ap      = A;
279 Ap      = min(min(min(Ap(1:end-1,1:end-1) ,Ap(1:end-1,2:end)) ...
280     ,             Ap(2:end  ,1:end-1)),Ap(2:end  ,2:end));
281 Ap      = min(min(min(Ap(1:end-1,1:end-1) ,Ap(1:end-1,2:end)) ...
```

```
    ,                Ap(2:end   ,1:end-1)),Ap(2:end   ,2:end));
Ap      = expx(expy(Ap));
end
function [CtSiO2, CtMgO, CtFeO] = get_initial_comps(scale, indsx, indsy)
% load chemical mappings
load oxide_maps
% assign data for the selected scale
if ~isempty(indsx) && ~isempty(indsy)
    CtSiO2 = oxide_maps(scale).map(indsx, indsy, strcmp(oxide_maps(scale).ele, 'Si
        '));
    CtMgO  = oxide_maps(scale).map(indsx, indsy, strcmp(oxide_maps(scale).ele, 'Mg
        '));
    CtFeO  = oxide_maps(scale).map(indsx, indsy, strcmp(oxide_maps(scale).ele, 'Fe
        '));
else
    CtSiO2 = oxide_maps(scale).map(:,:, strcmp(oxide_maps(scale).ele, 'Si'));
    CtMgO  = oxide_maps(scale).map(:,:, strcmp(oxide_maps(scale).ele, 'Mg'));
    CtFeO  = oxide_maps(scale).map(:,:, strcmp(oxide_maps(scale).ele, 'Fe'));
end
% avoid compositions close to 0
CtSiO2(CtSiO2<1e-3) = 1e-3;
CtFeO (CtFeO<1e-3)  = 1e-3;
CtMgO (CtMgO<1e-3)  = 1e-3;
% normalize pixels with sum > 1
chksum        = CtSiO2 + CtMgO + CtFeO;
normalizeMask = chksum > 1;
CtSiO2(normalizeMask) = CtSiO2(normalizeMask)/max(chksum(:));
CtFeO (normalizeMask) = CtFeO (normalizeMask)/max(chksum(:));
CtMgO (normalizeMask) = CtMgO (normalizeMask)/max(chksum(:));
end
```

Listing C.2: `HmC_PW_2D.m`

Thermolab Code to Calculate the Lookup Tables of the Reactive Porosity Wave Model

```
% Thermolab Gibbs energy minimizer and postprocessing to calculate lookup tables
    for the reactive porosity wave model in ternary P-T-X space
% Thermolab version: November 10, 2023
% github: https://github.com/hansjcv/Thermolab
clear, clf
run_name = 'lookup_tables'; % name of lookup tables
% temperature, pressure, and composition input
T  = [450:25:600] + 273.15; % temperatures (K)
P  = [0.5:0.5:4.0] * 1e9; % pressures (GPa)
X1 = 0:0.05:1; % fractions of component 1
X2 = 0:0.05:1; % fractions of component 2
tic % set timer
% loop over all temperatures
```

```
for iT = 1:length(T) % for low resolutions, commenting out the iT loop is possible
    T_iT  = T(iT); % fixed temperature
    [C1_2d, C2_2d] = ndgrid(X1, X2); % create grid of independent components
    C3_2d = 1 - C1_2d - C2_2d; % component 3 is not independent
    XH2O  = 1.2; % moles of H2O added to bulk composition
    % Phases and components
    fluid    = 'Fluid (SiO2)'; % fluid phase
    phs_name = {fluid, 'Antigorite', 'Orthopyroxene', 'Talc', 'Brucite', 'Olivine',
        'per,tc-ds633', 'q,tc-ds633'}; % solid phases
    Cname    = {'Si', 'Mg', 'Fe', 'H', 'O'}; % chemical components
    td = init_thermo(phs_name, Cname, 'solution_models_EF21'); % create dataset
    % pseudocompound resolution
    td(strcmp(phs_name, 'Fluid (SiO2)')).dz(:)  = 1/1e4;
    td(strcmp(phs_name, 'Antigorite')).dz(:)    = 1/6;
    td(strcmp(phs_name, 'Talc')).dz(:)          = 1/4;
    td(strcmp(phs_name, 'Brucite')).dz(:)       = 1/4;
    td(strcmp(phs_name, 'Olivine')).dz(:)       = 1/6;
    td(strcmp(phs_name, 'Orthopyroxene')).dz(:) = 1/4;
    p = props_generate(td); % generate dataset
    % pre-processing
    %       Si Mg Fe H  O
    noxy   = [2 1 1 1/2 0]; % oxygen atoms in oxide
    % molar composition of component
    Nsys1  = [1 0 0 0 2];
    Nsys2  = [0 1 0 0 1];
    Nsys3  = [0 0 1 0 1];
    NH2O   = [0 0 0 2 1];
    molm   = molmass_fun(Cname);
    % molar mass of components
    molm1  = Nsys1 * molm;
    molm2  = Nsys2 * molm;
    molm3  = Nsys3 * molm;
    % total moles of components
    C1_mol = C1_2d / molm1;
    C2_mol = C2_2d / molm2;
    C3_mol = C3_2d / molm3;
    % mole fractions of components
    X1_nd  = C1_mol ./ (C1_mol + C2_mol + C3_mol);
    X2_nd  = C2_mol ./ (C1_mol + C2_mol + C3_mol);
    X3_nd  = C2_mol ./ (C1_mol + C2_mol + C3_mol);
    % Consider only unique ternary compositions
    id     = X1_nd(:) + X2_nd(:) <= 1;
    X1_nd = X1_nd(id);
    X2_nd = X2_nd(id);
    % Prepare arrays for minimization
    [~, Pnd, Tnd] = ndgrid(X1_nd(:), P, T_iT); % P, T array for each ternary
        composition
    X1_nd = repmat(X1_nd(:), length(P), length(T_iT));
    X2_nd = repmat(X2_nd(:), length(P), length(T_iT));
    nPTX  = length(X1_nd(:)); % number of minimizations
    % Options
```

```
62    options.nref     = 80; % max number of iterations
63    options.eps_dg   = 1e-12; % tolerance for global Gibbs energy minimum
          differences
64    options.dz_tol   = 1e-14; % tolerance for when z window; stop if smaller
65    options.z_window = ones(size(phs_name)) * 0.085; % window for refined grid
66    options.dz_fact  = ones(size(phs_name)) * 1.5; % new dz spacing
67    options.ref_fact = 1.25; % how the z_window is narrowed each iteration. larger:
           smaller z window over which new grid is generated
68    options.disp_ref = 1; % show refinement graphically
69    options.solver   = 0; % solver option. 0 = linprog
70    solv_tol         = 100; % tolerance to group pseudocompounds
71    % Preallocate cells for parallel loop
72    alph_all         = cell(nPTX, 1); % pseudocompound abundances
73    Npc_all          = cell(nPTX, 1); % phase composition
74    pc_id_ref        = cell(nPTX, 1); % phase ID
75    p_ref            = cell(nPTX, 1); %
76    g_min            = cell(nPTX, 1); % Gibbs energy minimum
77    phs_modes_cell   = cell(nPTX, 1); % phase modes
78    Cf_cell          = cell(nPTX, 1); % fluid composition
79    Cs_cell          = cell(nPTX, 1); % solid composition
80    rhof_tab_cell    = cell(nPTX, 1); % fluid density
81    rhos_tab_cell    = cell(nPTX, 1); % solid density
82
83    %%  Gibbs energy minimization and postprocessing
84    parfor iPTX = 1:nPTX
85       % System composition
86       Nsys = Nsys1 * X1_nd(iPTX) + Nsys2 * X2_nd(iPTX) + Nsys3 * (1 - X1_nd(iPTX)
             - X2_nd(iPTX)) + NH2O * XH2O;
87       % Gibbs minimization
88       [alph_all{iPTX}, Npc_all{iPTX}, pc_id_ref{iPTX}, p_ref{iPTX}, g_min{iPTX}] =
              tl_minimizer(Tnd(iPTX), Pnd(iPTX), Nsys, phs_name, p, td, options);
89       % Postprocessing function
90       [pc_id, phi, Cwt, Npc, rho, mu, p_out, phiw, g, alph] = postprocess_fun(Tnd(
             iPTX), Pnd(iPTX), td, alph_all{iPTX}, Npc_all{iPTX}, molm, p_ref{iPTX},
             pc_id_ref{iPTX}, phs_name, solv_tol, 'CORK', 'S14');
91       % Preallocate local arrays
92       phs_modes_iPT = zeros(1, length(phs_name));
93       asm_id_iPT    = zeros(1, length(phs_name));
94       % Stable assemlage ID
95       asm_id_iPT(pc_id) = pc_id;
96       asm_id_cell{iPTX} = asm_id_iPT; % Store pc_id as a cell
97       % Phase modes
98       phs_modes_iPT(pc_id) = phi;
99       phs_modes_cell{iPTX} = phs_modes_iPT;
100      % Properties of fluid and solid phase
101      fluid_id = strcmp(phs_name(pc_id), fluid);
102      solid_id = ~strcmp(phs_name(pc_id), fluid);
103      % Fluid and solid composition
104      Cf_cell{iPTX} = Cwt(:, fluid_id) * phiw(fluid_id) / sum(Cwt(:, fluid_id) *
             phiw(fluid_id));
```

```
105         Cs_cell{iPTX} = Cwt(:, solid_id) * phiw(solid_id) / sum(Cwt(:, solid_id) *
                phiw(solid_id));
106         % Fluid and solid density
107         rhos_tab_cell{iPTX} = rho(solid_id)' * phi(solid_id) / sum(phi(solid_id));
108         rhof_tab_cell{iPTX} = rho(fluid_id)' * phi(fluid_id) / sum(phi(fluid_id));
109
110         % Output progress
111         disp([T_iT - 273.15, iPTX / nPTX])
112     end
113
114     %% create lookup tables
115     % convert cells to matrices
116     asm_id     = cell2mat(asm_id_cell);
117     phs_m odes = cell2mat(phs_modes_cell);
118     Cf         = cell2mat(Cf_cell);
119     Cs         = cell2mat(Cs_cell);
120     rhof       = cell2mat(rhof_tab_cell);
121     rhos       = cell2mat(rhos_tab_cell);
122     % reshape and permute
123     Cf     = reshape(Cf, length(Cname), nPTX); Cf = permute(Cf, [2, 1]);
124     Cs     = reshape(Cs, length(Cname), nPTX); Cs = permute(Cs, [2, 1]);
125     asm_id = reshape(asm_id, length(phs_name), nPTX); asm_id = permute(asm_id, [2,
            1]);
126     % identify stable phases and kick out phases that are not present
127     solid_id        = find(~strcmp(phs_name, fluid));
128     solid_names     = phs_name(solid_id);
129     vol_frac_solids = phs_modes(:, solid_id) ./ sum(phs_modes(:, solid_id), 2);
130     stable_id       = sum(vol_frac_solids) > 0;
131     solid_names     = solid_names(stable_id);
132     vol_frac_solids = vol_frac_solids(:, stable_id);
133     % reshape into ternary array
134     nX1 = length(X1); nX2 = length(X2);
135     nT = length(T_iT); nP = length(P);   nC = length(Cname);
136     Csys1_2d   = C1_2d; % component 1 (SiO2)
137     Csys2_2d   = C2_2d; % component 2 (MgO)
138     [x2d, y2d] = cart2bary(C1_2d, C2_2d); % convert to barycentric
139     id2d       = repmat(id, nP * nT, 1); % ternary ID for all P-T conditions
140
141     % stable mineral assemblage
142     asm_id_all = zeros(nX1 * nX2 * nP * nT, length(phs_name)); % preallocate
143     asm_id_all(id2d, :) = asm_id; % assign stable assemblage id
144     asm_id = reshape(asm_id_all, nX1 * nX2, nP, nT, length(phs_name));
145     % show phase diagram
146     %figure(1), clf,
147     %tl_psection(x2d,y2d, Cname, squeeze(asm_id(:,1,1,:)), phs_name, 1);
148     % prepare lookup table variables
149     % preallocate in complete X1-X2-T-P space
150     Cf_all              = nan(nX1 * nX2 * nT * nP, nC);
151     Cs_all              = nan(nX1 * nX2 * nT * nP, nC);
152     phs_modes_all       = nan(nX1 * nX2 * nT * nP, length(phs_name));
153     vol_frac_solids_all = nan(nX1 * nX2 * nT * nP, length(solid_names));
```

```
    rhos_all             = nan(nX1 * nX2 * nT * nP, 1);
    rhof_all             = nan(nX1 * nX2 * nT * nP, 1);
    % assign values in ternary X space using id2d index vector
    Cf_all(id2d, :)              = Cf;
    Cs_all(id2d, :)              = Cs;
    phs_modes_all(id2d, :)       = phs_modes;
    vol_frac_solids_all(id2d, :) = vol_frac_solids;
    rhof_all(id2d)               = rhof;
    rhos_all(id2d)               = rhos;
    % reshape into dimensions X1-X2-P-T
    Cf        = reshape(Cf_all, [nX1, nX2, nP, nT, nC]);
    Cs        = reshape(Cs_all, [nX1, nX2, nP, nT, nC]);
    phs_modes = reshape(phs_modes_all, [nX1, nX2, nT, nP, length(phs_name)]);
    % convert element fracs. to oxides fracs.
    %        Si Mg Fe  H  O
    noxy = [2 1 1 1/2 0]; % number of oxyagen atoms in oxide
    % constants to convert element wt.frac. to oxide wt.frac.
    el2ox = (molm' + noxy .* molm(strcmp(Cname, 'O'))) ./ molm';
    % convert element frac. to oxide frac. and reshape
    Cs_all_ox = Cs_all(:, 1:end - 1) .* el2ox(1:end - 1);
    Cf_all_ox = Cf_all(:, 1:end - 1) .* el2ox(1:end - 1);
    Cs_all_ox = reshape(Cs_all_ox, [nX1, nX2, nP, nT, nC - 1]);
    Cf_all_ox = reshape(Cf_all_ox, [nX1, nX2, nP, nT, nC - 1]);
    % store in lookup tables
    Cf_SiO2_tab(:,:,:,iT) = Cf_all_ox(:,:,:,:,strcmp(Cname,'Si'));
    Cs_SiO2_tab(:,:,:,iT) = Cs_all_ox(:,:,:,:,strcmp(Cname,'Si'));
    Cs_MgO_tab (:,:,:,iT) = Cs_all_ox(:,:,:,:,strcmp(Cname,'Mg'));
    Cs_FeO_tab (:,:,:,iT) = Cs_all_ox(:,:,:,:,strcmp(Cname,'Fe'));
    Cs_H2O_tab (:,:,:,iT) = Cs_all_ox(:,:,:,:,strcmp(Cname,'H'));
    modes_tab  (:,:,:,iT, :) = reshape(vol_frac_solids_all, [nX1, nX2, nP, nT,
        length(solid_names)]);
    rhof_tab   (:,:,:,iT) = reshape(rhof_all, [nX1, nX2, nP, nT]);
    rhos_tab   (:,:,:,iT) = reshape(rhos_all, [nX1, nX2, nP, nT]);
end
% output runtime
cpu = toc
%% create a 4D grid for interpolation in transport code
[CsysSiO2_4d, CsysMgO_4d, P_4d, T_4d] = ndgrid(X1, X2, P/1e9, T-273.15);
%% save lookup tables
save(run_name, 'modes_tab', 'Cs_SiO2_tab', 'Cs_H2O_tab', 'Cs_MgO_tab', 'Cs_FeO_tab
    ', 'Cf_SiO2_tab', 'rhof_tab', 'rhos_tab', 'solid_names', 'CsysSiO2_4d', '
    CsysMgO_4d', 'P_4d', 'T_4d', 'T', 'P', 'X1', 'X2', 'Cname', 'phs_name', '
    asm_id', 'el2ox', 'x2d', 'y2d', 'C1_2d', 'C2_2d', 'phs_modes')
```

Listing C.3: Thermolab_RPWLookupTables.m

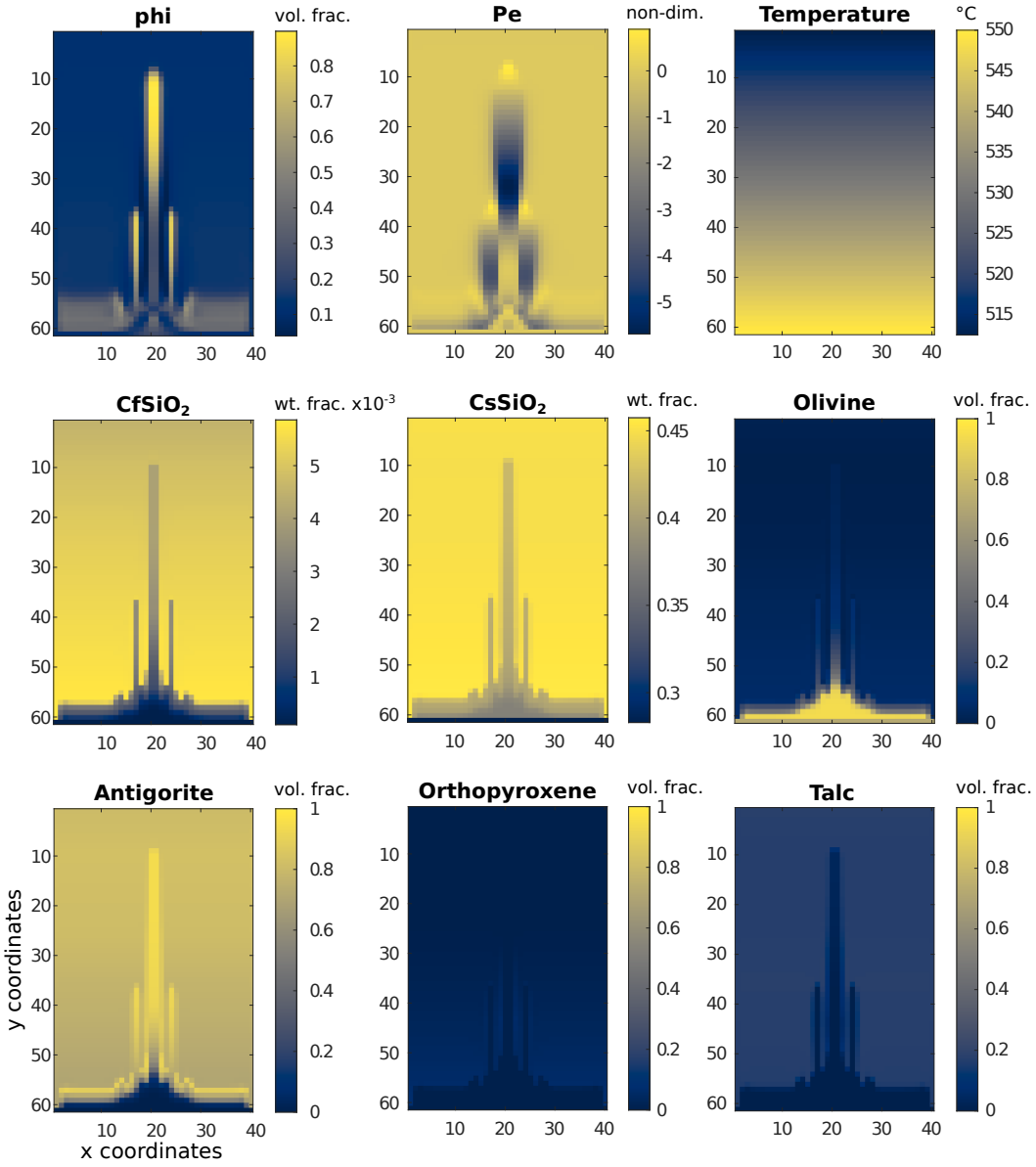

Figure C.1: A different setup for the 2D model. The number and width of fluid flow focusing structures can be controlled by changing the (de-)compaction weakness factor R. A lower R value ($R = 5$) leads to the formation of fewer channels compared to Figure 6.2.

Appendix D

Related Publications and Conference Contributions

Publications

- K. Huber, J. C. Vrijmoed, and T. John. Formation of Olivine Veins by Reactive Fluid Flow in a Dehydrating Serpentinite. Geochem. Geophys. Geosystems, 23(6):e2021GC010267, 2022. doi: 10.1029/2021GC010267.
- A. Zafferi, K. Huber, D. Peschka, J. Vrijmoed, T. John, and M. Thomas. A porous-media model for reactive fluid-rock interaction in a dehydrating rock. Journal of Mathematical Physics, 64(9):091504, 2023. ISSN 0022-2488. doi: 10.1063/5.0148243.
- K. Huber, T. John, J. C. Vrijmoed, J. Pleuger, X. Zhong (XXXX): Pulsed fluid release from subducting slabs caused by a scale-invariant dehydration process *(submitted to Earth and Planetary Science Letters, accepted with major revisions)*

First Author Conference Contributions

- Poster presentation at DMG Sektionstreffen Mineralogie-Petrologie 2019 at Heidelberg University
- K. Huber, T. John, J. C. Vrijmoed (2020): Modeling serpentinite dehydration on multiple scales constrained by field observations. *EGU General Assembly (Vienna)*
- K. Huber, J. C. Vrijmoed, T. John (2023): Serpentinite dehydration as a multiscale process. *EGU General Assembly (Vienna)*

- K. Huber, J. C. Vrijmoed, T. John, E. Schwarzenbach (2023): Upscaling of chemical and petrophysical rock properties for modeling serpentinite dehydration using a multiscale dataset. *Goldschmidt2023 (Lyon)*
- K. Huber, J. C. Vrijmoed, L. Khakimova, Y. Y. Podladchikov, T. John (2023): Reactive Porosity Waves as a Fluid Flow Focusing Mechanism. *GeoBerlin 2023 (Berlin)*